THE SEPARATION OF SIGNALS AND BACKGROUND IN A NUCLEON DECAY EXPERIMENT

Giles David Barr, Keble College, Oxford

Submitted for the degree of Doctor of Philosophy

Michaelmas Term 1987

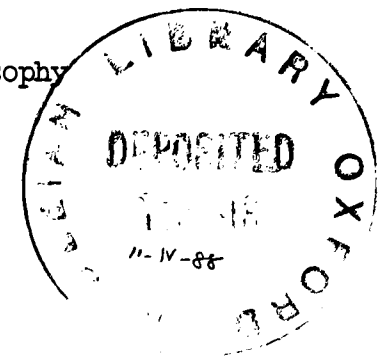

Abstract

Two aspects of the problems encountered in searching for nucleon decay in the Soudan 2 detector are discussed.

The types of event which are expected are discussed. The most common are induced by gamma rays from the naturally occurring radioactive isotopes in the cavern rock. A calculation has been developed to predict the rates of such events in the detector and the results agree well when compared with measurements made underground. Some radioactive events cause Compton scattering in the wireplane region of the detector and prohibit the use of a simple multiplicity trigger. Such events have been studied. An electronic trigger system has been designed which will achieve a factor of 10^3 rejection of these events while remaining efficient for even the most difficult modes of proton decay (75% for $p \rightarrow K^+\nu$). It is predicted that radioactive triggers will occur at less than 3Hz when the full detector is operating.

The neutrino induced background to proton decay has been simulated. The neutrino flux at the detector caused by cosmic ray induced showers in the atmosphere has been predicted. A comprehensive low energy (0.2 GeV to 20 GeV) Monte-Carlo neutrino event generator has been developed as a tool for background studies to proton decay. The reinteraction of proton decay or neutrino interaction products in the parent nucleus is discussed. It is found that these reinteractions are quite probable, except for K^+ and K^o particles. Data from a low energy neutrino beam experiment has been studied and it is deduced that in some cases, the events seen in the detector will contain visible tracks associated with the disintegration of the parent nucleus. A background estimate for the mode $p \rightarrow K^+\nu$ from the neutrino interaction $\nu n \rightarrow \mu^- p$ is presented.

To My Parents

CONTENTS

ABSTRACT
CONTENTS
ACKNOWLEDGMENTS
PREFACE

1. STABILITY OF MATTER 1

1.1 Introduction
1.2 The Standard Model
1.3 Grand Unified Theories - SU(5)
1.4 Supersymmetry
1.5 Sub-structure of Quarks and Leptons
1.6 Gravity, The Planck Scale and Superstrings
1.7 The Matter Antimatter Asymmetry In The Universe
1.8 Conclusion

2. EXPERIMENTAL SEARCHES FOR PROTON DECAY 18

2.1 Water Cerenkov Detectors
2.2 Tracking Calorimeter Detectors

3. THE SOUDAN 2 DETECTOR 24

3.1 Principle of Operation
3.2 Detector Construction
3.3 Instrumentation
3.4 The Analogue Signal Processing
3.5 The Digital Readout Electronics
3.6 The Readout Sequence
3.7 Appearance of Data from the Detector
3.8 Distribution of Particle Range in the Detector
3.9 The Veto Shield
3.10 Summary

4. NATURAL RADIOACTIVITY 39

4.1 Physical Processes Which Will Be Observed In An Underground Detector
4.2 Natural Radioactivity
4.3 The Gamma Emissions of Potassium-40 and the Daughters of the Natural Decay Chains
4.4 The Gamma Rays Emitted From The Walls Of The Cavern
4.5 Photon Penetration of the Detector
4.6 Electron Ranges
4.7 Expected Singles Rates in a Main Detector Module
4.8 Singles Rates in the Complete Detector
4.9 Compton Electrons In The Wireplane Regions
4.10 Properties Of Photon Induced Electron Events In The Wireplanes
4.11 Summary

5. TRIGGERING 76

5.1 Introduction
5.2 Desirable Triggering Properties
5.3 The Edges Trigger
5.4 Details of Implementation
5.5 Trigger Response to Radioactive and Noise Events
5.6 Trigger Response to Monte Carlo Proton Decay Events
5.7 Refinements
5.8 Earlier Triggering Schemes
5.9 Summary

6. THE FLUX OF ATMOSPHERIC NEUTRINOS AT UNDERGROUND DETECTORS 99

6.1 Introduction
6.2 The Flux of Primary and Secondary Cosmic Rays at the Top of the Atmosphere
6.3 Solar Modulation
6.4 The Hydrogen Spectrum at Solar Minimum
6.5 The Helium Spectrum
6.6 The flux of nucleons bound in nuclei of $Z \geqslant 3$
6.7 The Low Energy Flux at Solar Maximum
6.8 Proton Yields
6.9 Neutron Yields
6.10 The Earth's Magnetic Field - Penetration probabilities
6.11 The neutrino flux at each detector site
6.12 Comparison of Calculated Muon Fluxes with Experimental Data
6.13 Other Possible Souroes of Neutrinos

7. NEUTRINO INTERACTIONS ON FREE NUCLEONS 124

7.1 Introduction
7.2 The Kinematics of Neutrino Nucleon Interactions
7.3 Elastic and quasielastic neutrino Nucleon Scattering
7.4 Neutrino Induced Resonance Production
7.5 The Inelastic Contribution to the Neutrino Cross Section
7.6 Predicted Neutrino Event Rates in Underground Detectors
7.7 Summary

8. NUCLEAR EFFECTS AND A BACKGROUND CALCULATION FOR THE PROTON DECAY MODE $p \rightarrow K^{+}\nu$ 152

8.1 Interaction of Elementary Particles with Nuclear Matter
8.2 Interactions of Pions in Nuclear Matter
8.3 Interactions of Other Particles in Nuclear Matter
8.4 Nuclear breakup
8.5 The Signature of the Proton Decay Mode $p \rightarrow K^{+}\nu$
8.6 The Neutrino Background to the Decay Mode $p \rightarrow K^{+}\nu$
8.7 Conclusions

9. SUMMARY AND CONCLUSIONS 173

APPENDICES 176

A. The Soudan 2 Collaboration, List of Collaborators
B. The Density of the Detector and Range Momentum Graphs

Acknowledgments

I would like to thank the many people whose help has made this thesis possible. My supervisor, John Cobb has been very patient and helpful and I thank him for all the time he has given me. I would also like to thank Tom Gaisser, Earl Peterson, Tegid Jones, Don Perkins, Gino Saitta, Nick West and the rest of the Soudan 2 collaboration for their help and guidance during my work in Oxford and at the mine. I am indebted to the Athens Pisa Padova Wisconsin collaboration who have supplied me with a data summary tape of their neutrino oscillation search experiment at CERN.

I would also like to thank the friends I have made in the department and at Keble who have made my time at Oxford most enjoyable. There are too many to mention all by name, but I particularly enjoyed the company of Harry, Jaime, Lucy. Sue, Janet, Duncan, Ian, Seth, Rod and Steve Brindle.

I am indebted to the SERC who have supported me while doing this research. I would like to thank the SERC, Oxford Nuclear Physics, Keble College, Argonne National Laboratory and the Bartol Research Institute for supplying me with travel funds.

I would like to thank mum for her careful typing of this thesis.

PREFACE

The experimental evidence for the stability of the proton is increasing each year. There are about three large detectors currently operating. This thesis describes the theoretical reasons for expecting that the nucleon is unstable in chapter 1. The currently operating detectors are briefly reviewed in chapter 2. A new large detector, Soudan 2 is about to start operating. This detector is described in chapter 3.

The first major topic of this thesis is the design of the trigger system. Chapter 4 starts with a brief discussion of the different types of events and the signals they produce in the detector. The trigger must analyse the data coming from the detector and indicate when an event must be recorded. Radioactive hits themselves are of no interest and must be ignored by the trigger. Chapter 4 continues with a detailed consideration of the features of radioactive events and their rates which are needed in the consideration of the trigger design. A triggering algorithm which can be implemented in electronic hardware has been designed. This trigger is discussed in chapter 5. The chapter continues with an investigation of the response of the trigger to radioactive and simulated proton decay events.

The second topic which this thesis addresses is the background to proton decay from neutrino induced signals. The problem is that neutrinos from atmospheric cascades interact in the detector and produce a signal which is compatible with a proton decay event (typically 1 GeV of energy is released). This topic is the single most difficult part of searching for proton decay signals once the detector is operating, since

it requires a detailed knowlege of several low energy processes which cannot be accuratly described by current theories. Chapter 6 presents a calculation which has been done in collaboration with T. K. Gaisser and T. Stanev of the Bartol Research Foundation in Newark, DE. of the predicted atmospheric neutrino fluxes at the detector site.

The next step is to model the interactions of these neutrinos in the detector material. The two major problems are that there are no complete models which predict the topologies of 1 GeV neutrino events and the corrections due to rescattering in the parent nucleus are significant. The first of these topics is tackled in chapter 7 where a Monte Carlo generator has been developed using a combination of resonance and deep inelastic interactions and may be used to simulate the complete spectrum of neutrino events. Chapter 8 briefly investigates the effects which change the appearance of the event caused by the parent nucleus. The interaction length of hadrons in nuclear matter is estimated. Some neutrino data from CERN has been used to investigate the possibility that nuclear breakup may occur and be visible in the detector. Finally the background of the decay mode $p \rightarrow K^{+}\bar{\nu}$ from quasielastic neutrino events is calculated as an example of the use of the results of the above work.

Chapter 1

STABILITY OF MATTER

1.1 Introduction

Over the past century, many particles have been discovered. In most cases, these are short lived. They decay into lighter particles, liberating kinetic energy from the excess mass. The decay processes obey the law of electric charge conservation, the total charge of the products is equal to the charge of the initial particle. This is a consequence of gauge invariance which is an important part of the field theories which describe particle physics. The lightest particles, the neutral photon and neutrino and the charged electron are stable, there is nothing lighter they can decay into. There is one other particle, the proton (and also the neutron when bound in a nucleus) which has not been seen to decay.

Table 1.1 shows the masses and decay modes of the lighter particles, there are more than twenty particles which are lighter than the proton, and yet it has not been observed to decay. The proton is the lightest of the baryons. As a convenient way of remembering that it does not decay, the concept of baryon number conservation is used. Unlike charge conservation, there is no underlying invariance principle which requires this conservation law, it is only used in order to describe what has been experimentally observed. There seems to be no fundamental reason for the proton to be stable.

At the quark level, the stability of the proton is assured by forbidding reactions in which a quark changes to either an antiquark or a lepton. Quarks may only be produced or destroyed with a corresponding

Particle		Type	Mass (MeV)	Electric Charge	Baryon Number	Principle Decay Mode
Photon	γ	Boson	0	0	0	None Known
Neutrino	ν	Lepton	0 (?)	0	0	None Known
Electron	$e^{\pm}$	Lepton	0.511	± 1	0	None Known
Muon	$\mu^{\pm}$	Lepton	105.7	± 1	0	$\mu^{\pm} \mapsto e^{\pm} + \nu + \bar{\nu}$
Pion	$\pi^{\pm}$	Meson	139.6	± 1	0	$\pi^{\pm} \mapsto \mu^{\pm} + \nu/\bar{\nu}$
	π^0	Meson	135.0	0	0	$\pi^0 \mapsto \gamma\gamma$
Kaon	$K^{\pm}$	Meson	493.7	± 1	0	$K^{\pm} \mapsto \mu^{\pm} + \nu/\bar{\nu}$
	K_S^0	Meson	497.7	0	0	$K_S^0 \mapsto \pi^+ + \pi^-$
	K_L^0	Meson	497.7	0	0	$K_L^0 \mapsto \pi + \pi + \pi$
Proton	p	Baryon	938.3	$+1$	$+1$	None Known
Antiproton	$\bar{p}$	Baryon	938.3	-1	-1	None Known
Neutron	n	Baryon	939.6	0	$+1$	$n \mapsto p + e^- + \bar{\nu}$
Antineutron	$\bar{n}$	Baryon	939.6	0	-1	$\bar{n} \mapsto \bar{p} + e^+ + \nu$
Lambda	Λ^0	Baryon	1115.6	0	$+1$	$\Lambda^0 \mapsto p + \pi^-$
Antilambda	$\bar{\Lambda}^0$	Baryon	1115.6	0	-1	$\bar{\Lambda} \mapsto \bar{p} + \pi^+$

Table 1.1 Properties of some of the known particles.

antiquark. These features are part of the standard model which successfully describes all the particle interactions which have been seen at accelerators.

In this chapter, I will first briefly describe the standard model, in particular, how it is made from the separate theories of the fundamental forces of nature. I will then survey some of the extensions to the model which have been proposed. In the cases described, the new theories provide a mechanism for the proton to decay. I will conclude the chapter with a discussion of the experimental observation that the universe contains a matter/antimatter imbalance. It has been proposed that this may be reconciled with the big bang model if the proton is unstable. Detailed descriptions of these topics can be found in the references at the end of this chapter.

1.2 The Standard Model

The spin 1/2 fermions in the standard model may be grouped according to the following properties.

(1) Colour: The particles are red, blue, green or colourless. The colourless particles are known as leptons and the coloured ones are called quarks.

(2) Helicity: Particles are either left handed (spin in opposite direction to motion) or right handed (spin in same direction as motion). For massive particles, the direction of motion can be changed simply by changing Lorentz frames, so helicity is not a conserved quantity. Massless particles always have the same direction relative to their spins, - their helicities are conserved.

(3) Weak Isospin: The particles are assigned a third component of weak isospin (T_3). The up quark and neutrino have $T_3 = +1/2$ and the down quark and electron have $T_3 = -1/2$.

(4) Electric Charge: Each of the particles has an electric charge. These are multiples of 1/3 of the electron charge.

Each of the particles described above has a corresponding antiparticle with opposite colour, helicity, charge and T_3. In addition there are three generations of particles, the first containing the particles mentioned above. The other generations seem to contain exact replicas, differing only in their mass. A summary of the different types of particle is shown in table 1.2.

The different properties of the particles govern the way in which the forces of nature act upon them. Indeed the only way we can perceive the particles is by virtue of these forces. The properties mentioned above are only distinguished because they modify the forces which act upon them. There are two forces which are important at the elementary particle scale, the strong force described by quantum chromodynamics

Particles

T_3	Left Handed				Right Handed				
	Colourless	Red	Green	Blue	Colourless	Red	Green	Blue	
$+\frac{1}{2}$	ν_e	u_L	u_L	u_L		u_R	u_R	u_R	1st
$-\frac{1}{2}$	e_L^-	d_L	d_L	d_L	e_R^-	d_R	d_R	d_R	generation
$+\frac{1}{2}$	ν_μ	c_L	c_L	c_L		c_R	c_R	c_R	2nd
$-\frac{1}{2}$	μ_L^-	s_L	s_L	s_L	μ_R^-	s_R	s_R	s_R	generation
$+\frac{1}{2}$	ν_τ	t_L	t_L	t_L		t_R	t_R	t_R	3rd
$-\frac{1}{2}$	τ_L^-	b_L	b_L	b_L	τ_R^-	b_R	b_R	b_R	generation

Antiparticles

T_3	Left Handed				Right Handed				
	Colourless	Anti-Red	Anti-Green	Anti-Blue	Colourless	Anti-Red	Anti-Green	Anti-Blue	
$+\frac{1}{2}$		$\bar{u}_L$	$\bar{u}_L$	$\bar{u}_L$	$\bar{\nu}_e$	$\bar{u}_R$	$\bar{u}_R$	$\bar{u}_R$	1st
$-\frac{1}{2}$	e_L^+	$\bar{d}_L$	$\bar{d}_L$	$\bar{d}_L$	e_R^+	$\bar{d}_R$	$\bar{d}_R$	$\bar{d}_R$	generation
$+\frac{1}{2}$		$\bar{c}_L$	$\bar{c}_L$	$\bar{c}_L$	$\bar{\nu}_\mu$	$\bar{c}_R$	$\bar{c}_R$	$\bar{c}_R$	2nd
$-\frac{1}{2}$	μ_L^+	$\bar{s}_L$	$\bar{s}_L$	$\bar{s}_L$	μ_R^+	$\bar{s}_R$	$\bar{s}_R$	$\bar{s}_R$	generation
$+\frac{1}{2}$		$\bar{t}_L$	$\bar{t}_L$	$\bar{t}_L$	$\bar{\nu}_\tau$	$\bar{t}_R$	$\bar{t}_R$	$\bar{t}_R$	3rd
$-\frac{1}{2}$	τ_L^+	$\bar{b}_L$	$\bar{b}_L$	$\bar{b}_L$	τ_R^+	$\bar{b}_R$	$\bar{b}_R$	$\bar{b}_R$	generation

Table 1.2 Elementary Particles in the Standard Model.

(QCD) and the electroweak force. At low energies, the electroweak force can be decomposed into two separate aspects, the electromagnetic force and the weak force. A fourth force, gravity is very weak, it can be neglected at the elementary particle level.

The strong force couples to the colour of the particles. The leptons which are colourless are neutral to the strong force, they do not interact. Quarks are the only fermions which interact in QCD. The interaction between two quarks takes place by the exchange of a vector boson called a gluon (see fig 1.1a). QCD describes the strong force using the mathematical group SU(3). SU(3) describes the symmetry properties of the three colours - the theory is invariant under a transformation of colour fields as governed by the SU(3) group structure. One of the features of this group structure is that it allows the gluon which is exchanged to transfer the colour charge between the quarks (fig 1.1b) - a red quark can become a green quark when it is interacted upon by the strong force. This can be illustrated

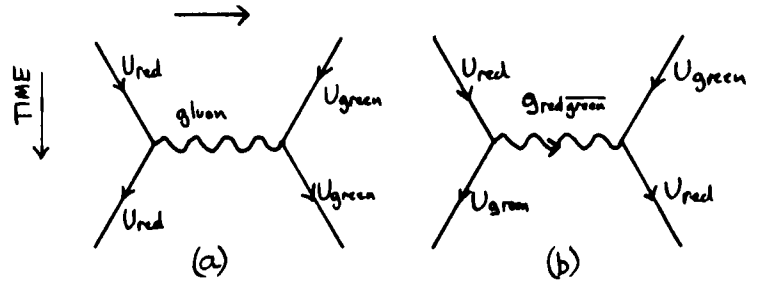

Fig 1.1 The Strong Interaction

mathematically by interacting a triplet of red green and blue quarks of the same types with an SU(3) matrix representing the gluon field.

$$\begin{pmatrix} d_R \\ d_G \\ d_B \end{pmatrix} \rightarrow \begin{pmatrix} G_1+G_2 & G_{\bar{R}G} & G_{\bar{R}B} \\ G_{\bar{G}R} & G_1+G_2 & G_{\bar{G}B} \\ G_{\bar{B}R} & G_{\bar{B}G} & G_1+G_2 \end{pmatrix} \begin{pmatrix} d_R \\ d_G \\ d_B \end{pmatrix}$$

Since the colour of a quark may be changed by a gluon, it follows that gluons also carry colour charge, so gluons can also interact in QCD. In SU(3) there are six colour changing gluons and two which are themselves colour neutral which mediate interactions as in fig 1.1a where no colour charge is transferred.

The weak force is similar, it is described by the mathematical group SU(2). In this case, the particles with right handed helicities do not interact. The left handed particles are grouped into weak isospin doublets. Particles within one group have the same colour. For example, some groups are

$$\begin{pmatrix} \nu_L \\ e_L^- \end{pmatrix}, \quad \begin{pmatrix} u_L^{Red} \\ d_L^{Red} \end{pmatrix}, \quad \begin{pmatrix} u_L^{Green} \\ d_L^{Green} \end{pmatrix}$$

Once again the particles interact with each other by the emission and absorption of gauge bosons, in this case the W^+, W^- and W^o . The interaction can either leave the particle identity unchanged, or it can change to the other member in the group, see fig 1.2. Again, the gauge bosons carry weak charge, and so may self interact.

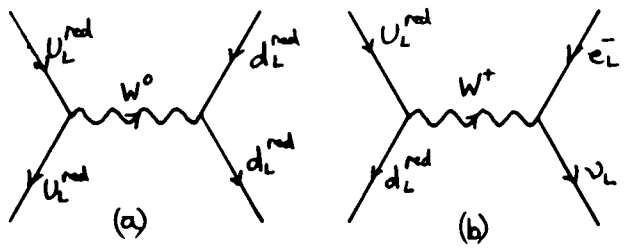

Fig 1.2 The Weak Interaction

The electromagnetic force couples to the electric charge. The theoretical description of the electromagnetic force, quantum electrodynamics (QED) is based on the group U(1). In the same way as in

the strong and the weak forces, the electromagnetic force acts by transferring a gauge boson, the V^o. In contrast to the other two forces, QED acts on groups of only one particle, the emission of a V^o cannot change the identity of the particle. In addition, the V^o itself does not carry electric charge, so there are no self interactions. The neutrino which is electrically neutral does not couple to the electromagnetic force.

Each force has a coupling constant which governs the strength of the force. A particle is allowed to emit a virtual gauge boson and then reabsorb it within the time governed by the uncertainty principle. A particle is surrounded by a 'cloud' of such virtual particles which shield the 'bare' properties (charge etc.). Low energy interactions do not penetrate this shield, whereas high energy interactions do. The effect of this is that the strength of the interaction, the coupling constant, depends on the energy scale of the interaction. The coupling constant is said to run. Fig 1.3 shows how the coupling constants for

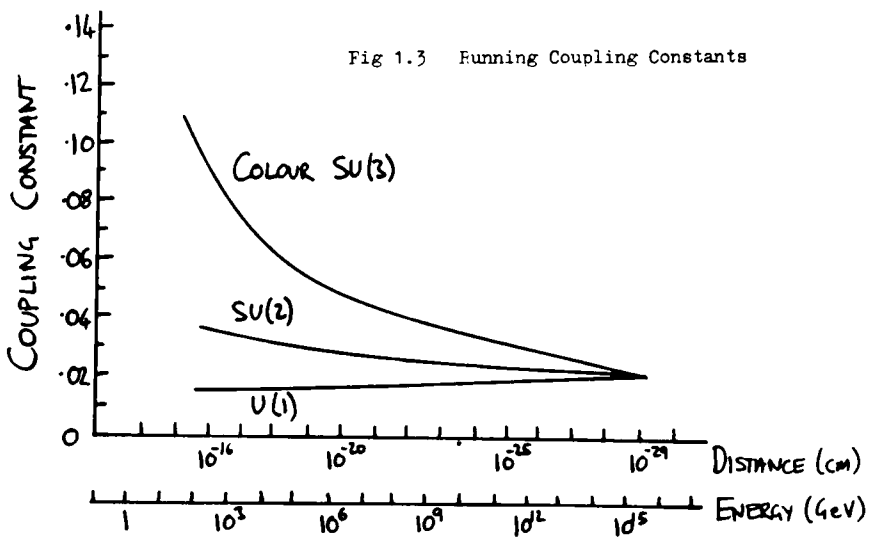

Fig 1.3 Running Coupling Constants

the strong, electromagnetic and weak forces change with energy. The strong and weak coupling constants get smaller whereas the electromagnetic force becomes stronger at higher energies. At an energy of 10^{15} GeV the three couplings become equal. This is referred to as the Grand Unification mass. It is possible that at these energies, the three forces can be described by a single grand unified theory which changes, at low energy, into three aspects which we perceive as

different forces.

So far, the weak and electromagnetic interactions have been successfully combined. Treating QCD as a separate theory, this combination is now known as the standard model. Where predictions can be made, it always agrees with data from accelerator experiments.

The weak and electromagnetic interactions are described jointly by a product of the two groups SU(2) x U(1). This combined electroweak theory contains the four gauge bosons the W^+, W^-, W^o and V^o. Since the subgroups SU(2) and U(1) adequately describe low energy phenomena separately, the more general SU(2) x U(1) symmetries are not visible at low energy. The scheme used to hide this symmetry at low energies, spontaneous symmetry breaking has the effect of mixing the W^o and V^o particles to give the experimentally observed γ and Z^o. The symmetry breaking also gives masses to the W^+, W^- and Z^o while leaving the γ massless. This scheme also requires the existence of a currently unobserved massive scalar particle, the Higgs.

1.3 Grand Unified Theories - SU(5)

The standard model contains no mechanism which changes a quark to a lepton, since there are no SU(3) or SU(2) particle groups containing both leptons and quarks. This makes the lowest qqq baryon, the proton, stable. A natural extension to the standard model, it would seem, is to try to combine the QCD and electroweak aspects of the theory. In most such attempts, groups of particles are assigned containing both quarks and leptons. A consequence of this is that, in these theories, the stability of the proton is no longer assured.

One of the schemes for unifying QCD with the electroweak theory is to construct a gauge theory from a larger group which has subgroups SU(3) and SU(2) x U(1) which can be identified with the current standard model. Again some form of symmetry breaking at low energy will be needed so that only the subgroups are recognised. The simplest such

group to choose is SU(5). In the minimal SU(5) theory, the particles are arranged in a group of 5 and a group of 10 - $\{\bar{d}_{RGB}, e^-, \nu_e\}$ and $\{d_{RGB}, u_{RGB}, \bar{u}_{RGB}, e^+\}$. These groups contain left handed particles. There are similar groups for the right handed particles. The SU(5) interaction matrix is shown below for the group of 5.

$$\begin{pmatrix} d_L^R \\ d_L^G \\ d_L^B \\ \nu_e \\ e_L^- \end{pmatrix} \longrightarrow \left(\begin{array}{ccc|cc} G_1+G_2+Z^0+\gamma & G_{\bar{G}R} & G_{\bar{B}R} & X_R^{-4/3} & X_R^{-1/3} \\ G_{\bar{R}G} & G_1+G_2+Z^0+\gamma & G_{\bar{B}G} & X_G^{-4/3} & X_G^{-1/3} \\ G_{\bar{R}B} & G_{\bar{G}B} & G_1+G_2+Z^0+\gamma & X_B^{-4/3} & X_B^{-1/3} \\ \hline X_{\bar{R}}^{4/3} & X_{\bar{G}}^{4/3} & X_{\bar{B}}^{4/3} & Z^0 & W^- \\ X_{\bar{R}}^{1/3} & X_{\bar{G}}^{1/3} & X_{\bar{B}}^{1/3} & W^+ & Z^0+\gamma \end{array}\right) \begin{pmatrix} d_L^R \\ d_L^G \\ d_L^B \\ \nu_e \\ e_L^- \end{pmatrix}$$

The SU(3) QCD subgroup appears in the top left, the weak SU(2) subgroup in the bottom right, and the U(1) subgroup along the leading diagonal. The off diagonal positions represent 12 new X vector bosons. These mediate reactions in which a quark turns into a lepton or vice versa. The SU(5) symmetry must be badly broken, since there is no experimental evidence for interactions involving the X which would mediate, for example, proton decay (fig 1.4). Some symmetry breaking

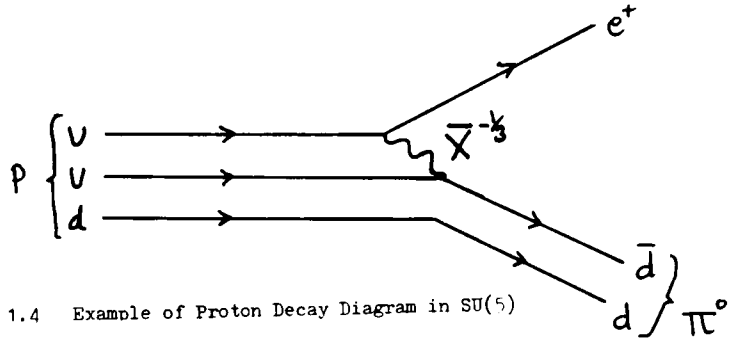

Fig 1.4 Example of Proton Decay Diagram in SU(5)

schemes give the X a mass comparable with the unification mass, which suppresses proton decay. One can calculate the approximate proton decay lifetime. Dimensional arguments suggest

$$\Upsilon_p \sim \frac{A M_X^4}{\alpha_g^2 M_p^5}$$

Where the factor M_X^4 is introduced by the X exchange propagator. α_g is the coupling constant at the unification scale ($\sim 1/40$) and A contains details of matrix elements. Assuming A = 1 and $M_X = 10^{15}$GeV, $\Upsilon_p = 6 \times 10^{31}$ years. A more precise minimal SU(5) model calculation (see

Ross(1984)) yields $1/\Gamma(p \to e^+\pi^0) = 4.5 \times 10^{29\pm1.7}$ years $= 2 \times 1/\Gamma(n \to e^+\pi^-)$. Table 1.3 gives values for other modes.

Final State f	$e^+\rho^0$	$e^+\omega$	$\bar{\nu}_e\pi^+$	μ^+K^0	$e^+\eta$
$\Gamma_f/\Gamma(p \to e^+\pi^0)$	0.11	0.10	0.4	0.03-0.1	0.01-0.08

Table 1.3 Ratio of proton decay half widths to the $p \to e^+\pi^0$ decay width from Ross (1984) predicted by minimal SU(5).

1.4 Supersymmetry

In SU(5) and similar theories, the symmetry groups are limited to particles with the same spin. The principle of supersymmetric theories is to impose a symmetry between fermions and bosons. Each quark and lepton has a supersymmetric spin zero spartner and each gauge boson, the photon, gluons, W Z and the graviton (the mediator of gravity) all have supersymmetric fermion partners. The Higgs (scalar) is also given a spin 1/2 counterpart, the Higgsino. Unfortunately none of the elementary particles have supersymmetric partners which are identifiable with anything currently known, so all the supersymmetric partners must be somehow hidden. One way of arranging this is for them to have a higher mass than their particle counterparts which requires that supersymmetry is broken.

In most supersymmetric theories, a multiplicative quantum number known as R parity is conserved, R = +1 for particles and R = -1 for supersymmetric particles. This has the consequence that supersymmetric particles are created and destroyed in pairs. Some of the interaction vertices involving supersymmetric particles can be constructed by taking a standard model vertex and replacing two of the lines with their supersymmetric counterparts, for example see fig 1.5.

It is possible in a supersymmetric theory for proton decay to be mediated by exchange of a supersymmetric Higgs as in fig 1.6. Lifetimes

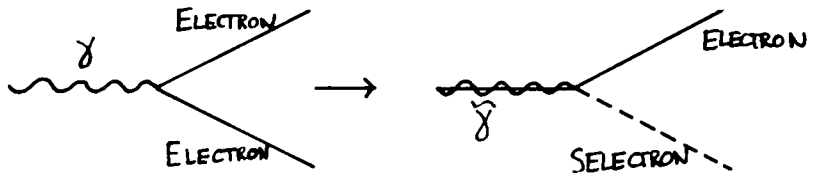

Fig 1.5 Standard Model Vertex

Supersymmetric Vertex

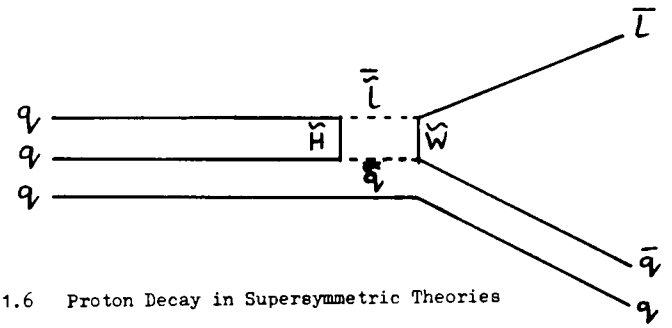

Fig 1.6 Proton Decay in Supersymmetric Theories

as short as those of SU(5) can be predicted, although modifications to the theory can increase the lifetime substantially. Decay into products in higher generations are preferred. Predicted branching ratios from a minimal supersymmetric theory are shown in table 1.4. The most likely modes are $p \to K^+ \bar{\nu}_\tau$ and $n \to K^0 \bar{\nu}_\tau$. $N \to K\mu$ is less likely and $N \to e^+ \pi^0$ is suppressed.

	$\tilde{H}_1, \tilde{H}_2$ exchange & Wino exchange	$\tilde{H}_1, \tilde{H}_2$ exchange & gluino exchange
$p \to \bar{\nu} K^+$	0.55	~1
$n \to \bar{\nu} K^0$	1	~1
$p \to \mu^+ K^0$	$\sim 2\times10^{-3}$ to 2×10^{-4}	~1

Table 1.4 Relative ratios for baryon decays into Strange particles. Non-strange modes are suppressed. From Ross (1984).

1.5 Sub-structure of Quarks and Leptons

A puzzle about nature is that it has three generations of quarks and leptons. The (u, d, e, ν_e) particles are all that are needed to make atoms, and all that we see in classical physics, and yet, the whole structure is duplicated twice more to produce the (s, c, μ, ν_μ) family

and the (t, b, Υ, ν_τ) family. It is not known why this duplication exists, the standard model gives no clues.

One possible way to explain it is to conceive the quarks and leptons as composites of more fundamental particles. This idea is not new, it has worked very successfully in unravelling the properties of the atom as a composite of electrons and a nucleus, the nucleus as a composite of protons and neutrons, and the protons and neutrons as being made from combinations of quarks. Then the higher generations of quarks and leptons could just be excited states of the 'ground states' u, d, e, and ν_e .

One problem which is encountered is that in order for the substructure of say the electron, to have remained hidden to all experiments to date, it must be on a scale less than about 10^{-16}cm, this means that the energy is on a scale >100 GeV. It is hard then to conceive of how such particles can produce excited states, which we see as the 2nd and 3rd fermion generations separated by as little as 0.1 GeV. I will now describe one of the schemes for the constituents which has been proposed.

The model has just two species of the fundamental building block, the rishon, the T rishon has electric charge +1/3 and the V rishon is electrically neutral. Each rishon comes in three colours, which will appear as the colours of the composite quarks, and in three 'hyper colours', see fig 1.7. The hypercolours are used analogously to the way colour is used in QCD to bind the rishons together to produce quarks and leptons. Since hypercolour is not seen in the composite particles, only rishon combinations which produce hypercolourless singlets are allowed. Each rishon is accompanied by an antirishon which carries opposite charge, colour and hypercolour. All the particles in the first generation are formed by combining the rishons in groups of three, see fig 1.8. The higher generations are just excited rishon states of the corresponding first generation states.

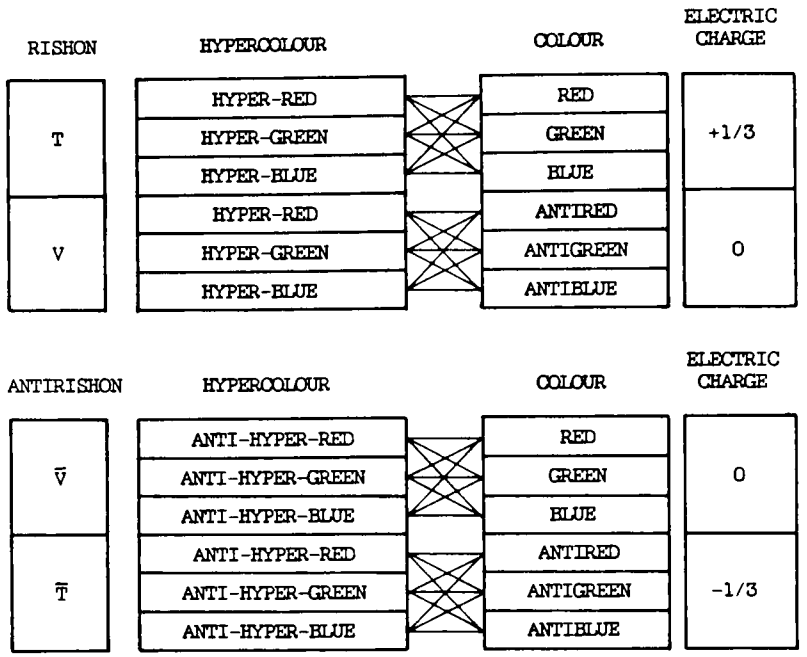

Fig 1.7 Rishon Properties

RISHON COMBINATION	PARTICLE	COLOUR	ELECTRIC CHARGE
TTT	e^+	COLOURLESS	+1
TTV	u	RED GREEN BLUE	+2/3
TVV	$\bar{d}$	ANTIRED ANTIGREEN ANTIBLUE	+1/3
VVV	ν_e	COLOURLESS	0
$\bar{V}\bar{V}\bar{V}$	$\bar{\nu}_e$	COLOURLESS	0
$\bar{V}\bar{V}\bar{T}$	d	RED GREEN BLUE	-1/3
$\bar{V}\bar{T}\bar{T}$	$\bar{u}$	ANTIRED ANTIGREEN ANTIBLUE	-2/3
$\bar{T}\bar{T}\bar{T}$	e^-	COLOURLESS	-1

Fig 1.8 Elementary Particles formed from Rishons

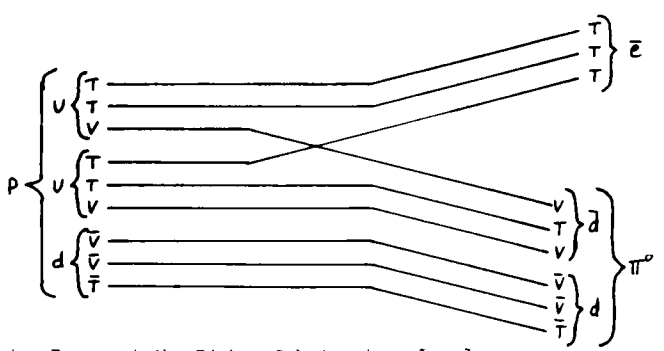

Fig 1.9 Proton Decay at the Rishon Substructure Level

Fig 1.9 shows a conjectured proton decay event at the rishon substructure level. The interaction proceeds by the exchange of a rishon pair in two of the quarks. This type of exchange interaction is familiar in Yukawa type pion exchange in nucleon interactions.

1.6 Gravity, The Planck Scale and Superstrings

One problem in attempts to construct a quantum theory of gravity (which is a prerequisite for including it in any grand unified theory) concerns the gravitational self energy of a particle. A structureless elementary particle of mass m occupies a region of space λ as governed by the uncertainty relation

$$mc^2 = \frac{\hbar c}{\lambda} \qquad (1)$$

But the gravitational energy is

$$V_{gr} = \frac{Gm^2}{\lambda} \qquad (2)$$

So the gravitation self energy increases faster than the rest mass at higher energy scales. This becomes important on an energy scale characterised by the Planck Mass, this is the mass at which the gravitational energy is equal to the rest mass. Equating (1) and (2) and solving for m

$$m = \frac{\hbar c}{G}$$

inserting values for $\hbar$, c and G, one finds.

	Planck mass	$= m_{pl}$	$= 1.22 \times 10^{22}$	MeV
also	Planck length	$= \hbar c/m_{pl}\, c^2$	$= 1.6 \times 10^{-33}$	cm
and	Planck time	$= \hbar/m_{pl}$	$= 5.4 \times 10^{-44}$	seconds

It is quite interesting to consider a particle whose mass is greater than the Planck mass, it will have a gravitational energy greater than its rest mass and will collapse and form a black hole.

Anything it emits will not be able to overcome its gravitational attraction. Any grand unified theory which includes gravity must be able to describe such objects. There must be some new physics at the Planck scale.

The only properties of a black hole which can be measured by an outside observer are its mass, its angular momentum and its charge. The baryon number of the black hole is unknown, because there is no force coupling to baryon number. Since it is impossible to know what the baryon number is, it is not meaningful to try and conserve it. It is possible to imagine a process where a proton might decay by emission of a virtual black hole, which then decays into products with zero baryon number. Estimates of such a process yield proton lifetimes of order 10^{40} years.

There are powerful models and ideas which are currently being developed to describe quantum gravity. The latest is Superstrings, in which the universe exists in a 10 dimensional space, 6 of which are compacted, ie they curl back on each other and are only visible at scales of the Planck length. The topology of the six compacted dimensions is called the Calabi-Yau manifold.

Some of the properties of the superstring theory are:

(1) It contains gravity. The particles of the theory are created by resonant modes of strings on the Calabi-Yau manifold, it contains an infinite set of massive particles with masses $\sim$Mp and a finite set of almost massless particles.

(2) It contains a GUT, which is consistent in 10 dimensions only if it has an SO(32) or $E_8 \times E_8'$ gauge group. Parity violation in 4 dimensions is only possible with the $E_8 \times E_8'$ group, which contains all the traditional GUT groups, E_6, SO(10) and SU(5).

(3) The superstring contains supersymmetry.

(4) It may solve the generation problem, the topology of the Calabi-

Yau manifold may determine the number of generations of fermions.

Many papers are published each week on the development of superstrings but so far it has not been developed sufficiently to allow any experimentally verifiable predictions to be made at all.

1.7 The Matter Antimatter Asymmetry In The Universe

Despite nature's apparent symmetry between particles and antiparticles as seen in accelerator experiments, the stars and galaxies around us are made up predominantly of matter, rather than antimatter. This asymmetry is not only seen on the earth, but also in the cosmic rays observed to fall on the earth which have originated all over the galaxy.

Current theories of how the universe began are based on a big bang, an instant in time some 10^{10} years ago when the universe was compressed in a single, very high temperature point. Since then the universe has expanded and cooled. One to the successes of the theory is that a background radiation characteristic of a black body of 2.73K is measured. This radiation is thought to be the residual radiation from the big bang in the still cooling, expanding universe.

In the big bang model, at the very early stages of the universe, the temperature was high enough for particles and gauge bosons to freely interconvert. As the temperature decreased, the heavier particles would 'freeze out' ie it would no longer be energetically favourable to generate them, they would annihilate with their antiparticle partners and not reappear. In all this, there is no mechanism which will produce a collection of matter to be left over to make the stars and galaxies. This is a problem for both particle physics and astrophysics. There are three possible solutions:

(1) The universe started at the time of the big bang with more matter than antimatter.

(2) Antimatter galaxies exist in other parts of the universe - there is no asymmetry. (Current experimental evidence does not support this idea.)

(3) There is some mechanism which, while the universe cooled would leave an excess of matter over antimatter.

A mechanism which would produce the third solution is baryon number non-conservation, combined with CP violation. In the early universe, some of the quarks and antiquarks would decay to produce leptons. Furthermore, through CP violation, they would do so at different rates, which would then leave a residue of quarks (and electrons) when all the antiquarks and positrons were frozen out. The proton decay could easily be mediated by a heavy vector boson X, which would be readily produced in the early universe. At present day temperatures, the proton is long lived, the process would be inhibited by the large energy required to create the X.

1.8 Conclusion

The fact that the proton is so stable is reason enough in itself to want to extend the measurement of the stability to the limits of experimental possibility. The above discussions have shown that it is desirable to have an unstable proton in order to construct the elegant theories described. The theorists need more information from experiment in order to indicate which is the correct way to proceed in the development of the theories. This data is particularly hard to come by, since all measurements up to now agree with the rather cumbersome standard model. Proton stability is one of the few experimentally

accessible observations which, if found will indicated that the standard model is inadequate. This thesis describes some of the physics involved in the experimental measurement of proton decay.

References

The community of theoretical physicists has produced a profusion of literature on the subjects in this chapter. Overviews of the topics can be found in the following.

G. G. Ross "Grand Unified Theories"
Benjamin/Cummings (Menlo Park, California) (1984)

D. H. Perkins "Proton Decay Experiments"
Ann Rev Nucl Part Sci (1984) 34 1

H. Georgi "A Unified Theory of Elementary Particles and Forces"
Scientific American (April 1981) p40

H. E. Haber and G. L. Kane "Is Nature Supersymmetric ?"
Scientific American (June 1986) p42

F. Wilczek "The Cosmic Asymmetry between Matter and Antimatter"
Scientific American (Dec 1980) p60

H. Harari "The Structure of Quarks and Leptons"
Scientific American (April 1983) p48
also Harari H. Phys Lett 86B 83 (1979)
Shupe M. A. Phys Lett 86B 87 (1979)
Harari H. and Seiberg N. Phys Lett 98B 269 (1981)
Phys Lett 100B 41 (1981)

V. A. Kuzmin "GUTs and Cosmology"
Proc 1985 CERN/JNIR Summer School CERN 86-03 2 356

J. Ellis "Supersymmetry"
Proc 1985 CERN/JNIR Summer School CERN 86-03 2 325

J. Ellis "Superphysics"
Proc 1986 CERN Summer School CERN 87-02 276

G. 't Hooft "Quantum Black Holes"
Talk given at the 1986 CERN Summer School

More detailed papers are referenced in the above.

Chapter 2

EXPERIMENTAL SEARCHES FOR PROTON DECAY

With the recent developments in unified theories, the experimental study of nucleon decay has become more interesting. Early experiments which show that the lifetime is at least 10^{30} years are reviewed by Perkins [1]. One approach is to look for the production of rare isotopes caused by the decay of one of the protons in a parent nucleus. This type of measurement is independent of the mode of decay.

More recent experiments have been designed to search for proton decay at the $10^{31} - 10^{33}$ years level. The experiments attempt to detect the products of the decay as they pass through the surrounding matter and reconstruct the mass and momentum of the original proton. A large number of measurements are recorded for each event. These are analysed to determine if they are consistent with the expected signatures of each possible decay mode.

Since the nucleon lifetime is known to be long, the detectors must monitor a sufficiently large quantity of nucleons such that a few may decay per year of operation. This requires that many hundreds of tons of matter are instrumented (one kiloton of any material contains 6×10^{32} nucleons). Two complementary experimental techniques have been used, (1) Water Cerenkov detectors and (2) Tracking 'calorimeter' detectors. The detectors must record sufficient data on each event to distinguish it from the backgrounds which are discussed in this thesis. As mentioned in chapter 4, the detectors are constructed underground to shield them from cosmic ray muons.

2.1 Water Cerenkov Detectors

Water Cerenkov detectors consist of a volume of water surrounded by photomultiplier tubes (see fig 2.1). There are currently two major experiments of this type operating, the IMB detector in Ohio, USA and the Kamiokande experiment in Japan. The water volume serves the dual purpose of a sample of nucleons which are monitored and as a means of detecting relativistic charged particles through the emission of Cerenkov light. As indicated in fig 2.2 the Cerenkov cone will intersect the plane of photomultiplier tubes in an elliptical ring, the width of the ring depends on the track length. The direction may be obtained from the shape of the ellipse and the relative times of firing of the PM tubes. Some sample Cerenkov rings are shown in fig 2.3. For proton decay events, several rings will be produced and must be separately reconstructed.

Some of the key features of this type of detector are:

1. The detector response is uniform, it doesn't depend on the particle direction.

2. Direction of particle motion along track can be unambiguously determined.

3. One in 9 of the nucleons are not bound in the detector, these can be used to search for nucleon decay without the need to correct for a parent nucleus.

4. Muon decays are detectable as delayed ($2.2\,\mu s$) pulses.

One of the drawbacks of the technique is that the particle must be travelling above the Cerenkov threshold to be detected. Particles must be travelling with velocity $\beta >$ (refractive index)$^{-1}$ = 0.75. This is suitable for recording electrons and photons, but heavier particles such as kaons are only indirectly detectable from their decay products. The detector is ideal for searching for the SU(5) preferred modes where light particles are emitted, eg $p \rightarrow e^{+}\pi^{0}$, but observing the supersymmetric

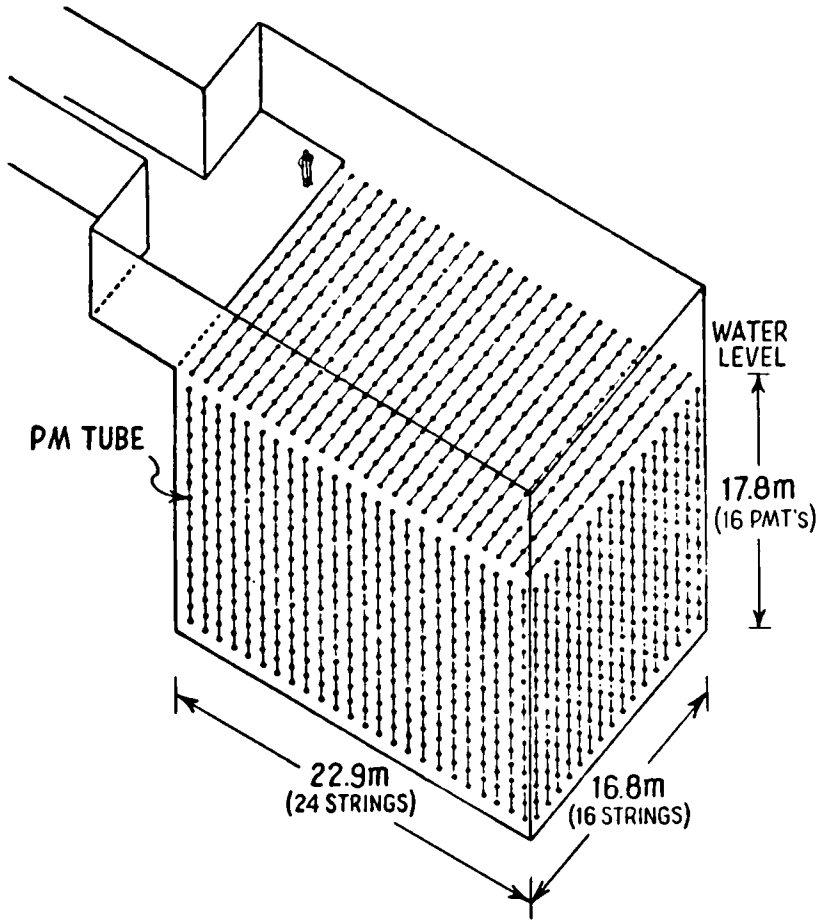

Fig 2.1 IMB Water Čerenkov Proton Decay Detector

Fig 2.2 Reconstruction of Čerenkov Rings

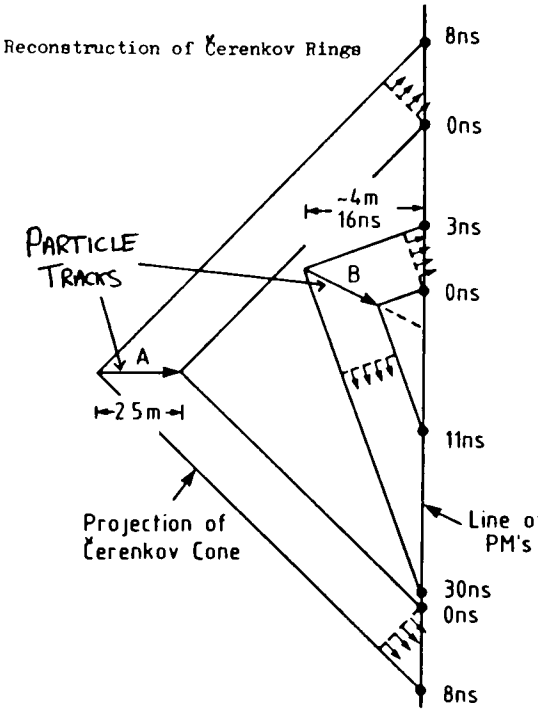

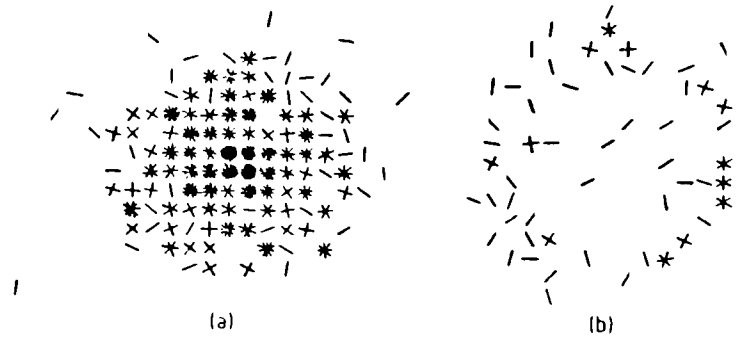

Fig 2.3 Sample Čerenkov Rings (a) Muon Crossing IMB Detector
(b) Muon Stopping in Water
The number of crossing lines at each point indicates photomultiplier pulse height.

preferred modes is more difficult, since not all the products can be directly detected (for example $p \rightarrow K^+ \bar{\nu}_\tau$).

Recent published results [2] indicate that $\Upsilon/B\ (p \rightarrow e^+\pi^o)$ is greater than 2.5×10^{32} years. This is in clear contradiction with the predictions of minimal SU(5) discussed in section 1.3. Further improvements in the proton lifetime limit from these detectors is limited by their inability to differentiate proton decay events from neutrino induced background.

2.2 Tracking Calorimeter Detectors

A different technique for detecting proton decay is to instrument a large mass of dense material, such as iron, with counter detectors, such as proportional or drift tubes. The charged products of a nucleon decay in the dense material ionizes the atoms of the material along its track. The counters are used to sample the ionisation of the tracks. When read out, the data yields measurements of the track positions. The event topology appears directly as in a bubble chamber photograph. The different detectors which have been built differ both in the material which is used and in the type of counter used to instrument the mass. The Soudan 2 detector is made from iron and is instrumented by plastic drift tubes. This detector will be described in detail in Chapter 3. Some of the features of this approach to proton decay detection are:

1. The data output is similar to a picture of the topology of the event - reconstruction of complex topologies is possible.

2. Vertex and track positions can be measured accurately.

3. The detector is sensitive to heavy particles such as kaons which would be below threshold in a Cerenkov detector.

4. Particles can be identified by ionisation loss (where recorded) and by scattering.

5. The detectors can be modular which allows a small section of them to be exposed to an accelerator beam for studying the characteristics of known particles.

6. Muon charge can be measured, since a negative muon will be absorbed in the heavy nuclei, the observation of a decay electron indicates positive charge.

7. The detectors will distinguish particles emitted from a secondary scatter, a separate vertex will be observed.

Table 2.1 summarises the experiments currently in progress to search for proton decay. For a recent review of results from these experiments, see [8].

References

[1] D. H. Perkins Ann Rev Nucl Part Sci 34 (1984) 1

[2] R. M. Bionta et al. Phys Rev Lett 51 (1983) 27
Blewitt et al. Phys Rev Lett 55 (1985) 2114

[3] K. Hirata et al. Proc 1987 Intl. Symp. on Lepton and Photon interactions at High Energies, Hamburg (preprint UT-ICEPP-87-04)
M Takita et al. Phys Rev D 34 (1986) 902

[4] M. R. Krishnaswamy et al. Phys Lett 106B (1981) 339
M. R. Krishnaswamy et al. Phys Lett 115B (1982) 349

[5] G. Battistoni et al. Nucl. Instr. Meth. 202 (1982) 459
G. Battistoni et al. Phys Lett 118B (1982) 461
G. Battistoni et al. Phys Lett 133B (1983) 454

[6] J. Bartelt et al. Phys Rev Lett 50 (1983) 50

[7] R. Barloutaud et al. Proc ICOBAN 1982 Bombay p143
C. Paulot. Frejus Collaboration note·Tp/R-13/87

[8] R. Barloutaud Proc. 8th WOGU Syracuse (1987)

Experiment	Location	Depth (mwe)	Dimensions (m)	Mass* (tons)	Sample material	Detection method	Operational	Reference
IMB	Cleveland Ohio USA	1570	23x18x17	7000 (3300)	Water	Water Cerenkov (2400 PM tubes)	1981 ***	[2]
Kamiokande	Kamioka Japan	2700	16x15.6 ϕ Cylindrical	3000 (880)	Water	Water Cerenkov (1000 PM tubes)	1983 **	[3]
KGF	Kolar Gold Fields India	7600	6x4x4	140	1.2cm thick steel	Proportional Counters	1980	[4]
NUSEX	Mont Blanc Road Tunnel	5000	3.5 cubic	150	1cm thick steel	Resistive Streamer Tubes	1982	[5]
Soudan 1	Soudan Mine N Minnesota	1800	3x3x2	32	Iron/Concrete	Proportional Tubes	1980	[6]
Frejus	Frejus Tunnel France/Italy	4400	6x6x13	1000	0.3cm steel sheets	Flash tubes & Geiger planes	1984	[7]
Soudan 2	Soudan Mine N Minnesota	2200	5x8x16	1000	0.16cm steel sheets	Hexagonal array of plastic drift tubes	1988	

* Fiducial in brackets

** Upgraded to Kamiokande 2 in late 1986 by addition of phototubes to lower the neutrino energy threshold.

*** Upgraded to IMB-3, light collection efficiency of PMT's improved

Table 2.1 Operational Proton Decay Detectors.

Chapter 3

THE SOUDAN 2 DETECTOR

The Soudan 2 experiment is being carried out by a collaboration from the universities of Oxford, Minnesota and Tufts and by Argonne National Laboratory and the Rutherford Appleton Laboratory. The detector is currently being installed in a purpose built experimental hall 2400 feet underground (2200 mwe) on the 27th level of the Tower-Soudan Iron Mine in North Minnesota. The rock overburden absorbs the flux of cosmic ray muons (see chapter 6) which would continually illuminate the detector had it been built on the surface.

3.1 Principle of Operation

The detector consists of 1200 tonnes of 1.6 mm thick steel sheets instrumented by some 2000 km of plastic drift tube. The detector is subdivided into 256 individually gas sealed modules 1m x 1m x 2.5m (vertical) which are stacked into the complete detector as an 8 x 16 x 2 (high) block (fig 3.1). The steel is made into corrugated sheets and stacked so as to form a honeycomb cell structure. Each cell is instrumented with a plastic drift tube of diameter 1.6cm (fig 3.2). The drift tubes extend the full 1 metre length of the module stack. The centre of each tube is held at -10 kV and the ends at ground potential. A constant current flows down the tubes, from the centre to the ends. This establishes a uniform axial electric field in each half tube. The volume of each module is maintained in an atmosphere of argon and carbon

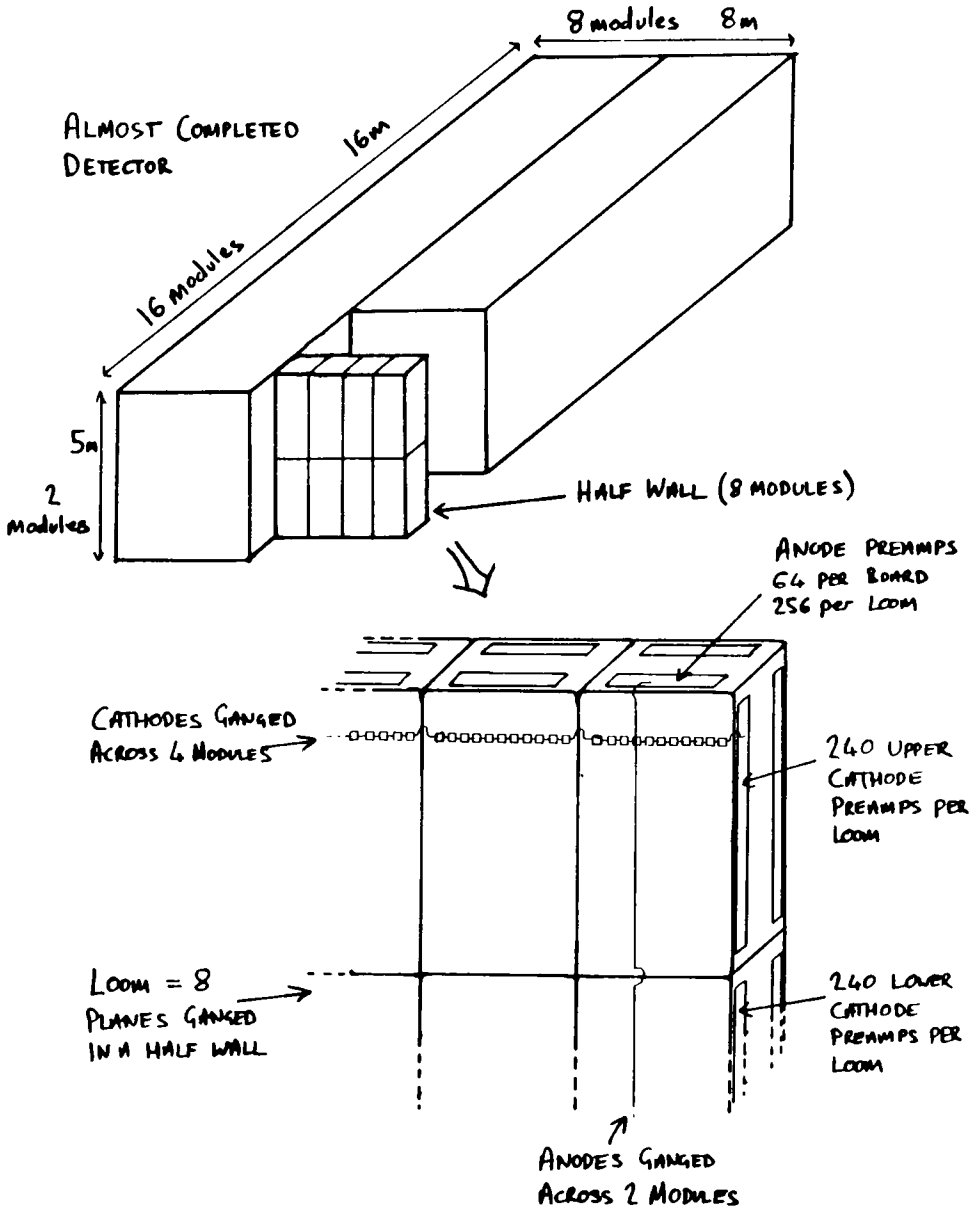

Fig 3.1 The Soudan 2 detector showing modular construction.

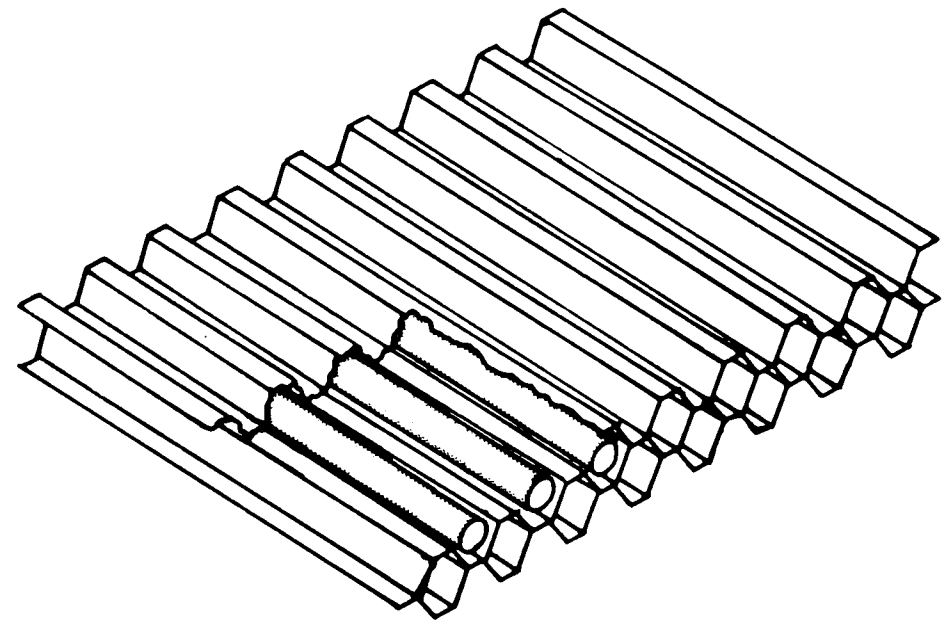

Fig 3.2 Corrugated steel stack instrumented with plastic drift tubes.

dioxide at atmospheric pressure. The oxygen concentration is kept below 3ppm. A charged particle which slows down in the detector will deposit a fraction of its energy by ionising the argon gas within the tubes. The ionisation will drift to the ends of the tube where it is picked up and converted into electric signals. The maximum distance over which electrons are drifted is 50 cm.

A 50 micron diameter anode wire runs vertically the length of the module 10 mm from the end of each line of tubes (fig 3.3). The wire is held at about +2.2kV and is used to collect the ionisation which has drifted down the tubes. The wire operates as a proportional counter and gives gas amplification such that the total charge induced is proportional to the number of electrons which drift to the end of the tube. A cathode pad (figs 3.3 and 3.4) is situated 5 mm beyond the anode wire. During the avalanche process, a signal whose magnitude is a fraction of that collected on the anode is induced on the cathode pad. The cathode pads are mounted on a printed circuit board and are bussed horizontally. By matching a pulse on an anode and cathode pair at a specific time, the exact tube location and drift time of an ionisation deposit in the tubes can be determined. This information is used to construct the full (x,y,z) location of the ionisation.

Each module contains 63 anodes in the 'x' direction and 240 cathode strips in the vertical 'y' direction. The tubes run in the 'z' direction.

3.2 Detector Construction

In practice, the tubes are constrained in a mylar 'bandolier' (fig 3.5). This insulates the high drift potential of the tube from the steel which is held at ground potential. Copper strips on the insides of the mylar sheets feed current to all the tubes. The bandolier is made from two sheets of mylar which are laminated to form pockets which hold the tubes. In addition to the -10kV on the centre and ground on the

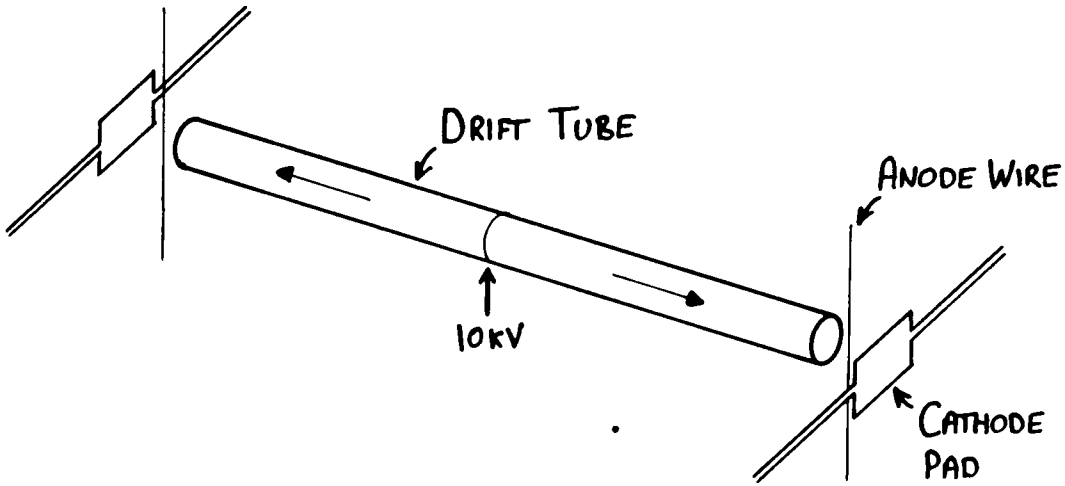

Fig 3.3 Instrumentation of a Drift Tube. The drift field is from the middle outwards. The ends of the tube are held at ground potential (not shown).

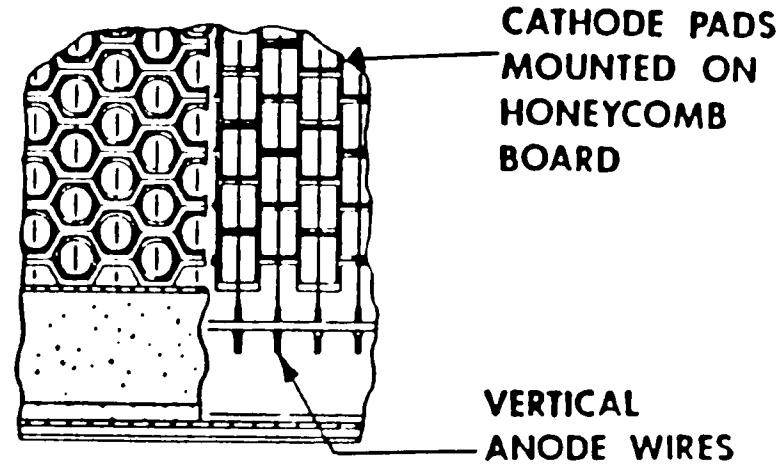

Fig 3.4 Detail of wireplane construction showing bussing of anodes and cathodes. The left hand side of the diagram shows the positions of the ends of the tubes

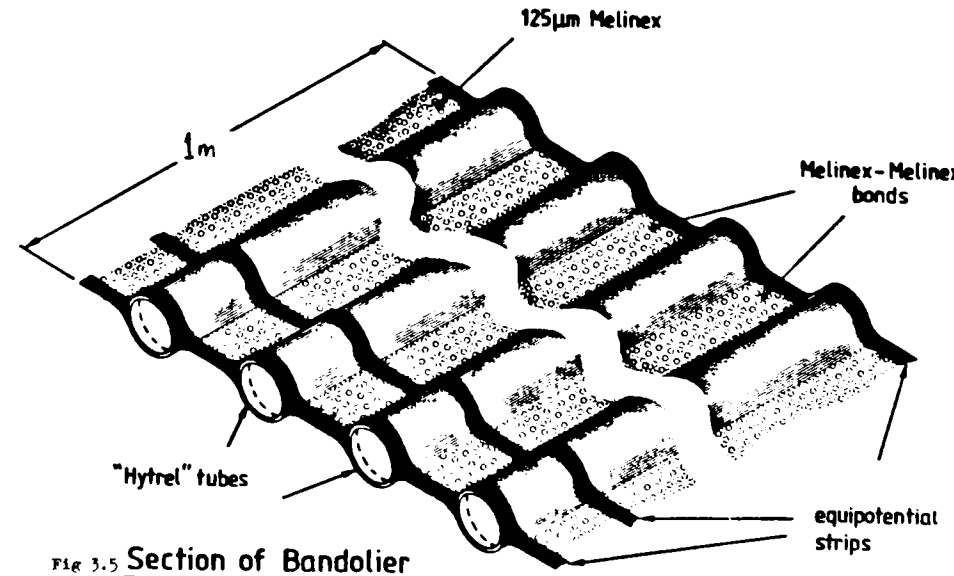

Fig 3.5 Section of Bandolier

edges, nine further traces feed intermediate voltages to points on each half tube to compensate for leakage currents through the mylar to the steel and to maintain a uniform voltage along the tube.

The anodes and cathode pads are mounted onto a 'wireplane' which is fastened to the face of the stack with the anode/cathode crossing points aligned with the open ends of the tubes. There are two wireplanes for each module. The gas gain of the wires depends on the local charge per unit length, which governs local field strengths. In order to measure the ionisation information associated with each charged track the gain must be uniform to within about 10 to 20%. To accomplish this, the wireplanes must be engineered and adjusted so that the anode/cathode separation and the anode/stack face separation is controlled to 0.3 mm. Once this has been done, the residual gain variations can be calibrated.

3.3 Instrumentation

The 32,256 anode wires and 122,880 cathode strips in the complete detector are read out through a total of 5,888 channels of electronics, the bussing of many wires and pads onto one channel is accommodated at two levels.

Each module is a member of a halfwall, a group of 8 modules stacked four wide by two high (see fig 3.1). The modules are stacked with the tube axis across the short dimension of the halfwall so that each of the two major faces contains eight wireplanes. The anodes from the top module are bussed to the bottom module forming a 5m long wire and the cathodes are bussed across the 4 modules in the x direction. The collection of channels comprising 252 anode channels and 480 cathode channels are termed a 'loom' (fig 3.1). The channels from the loom are read out on three 256 channel wide data crates, one each for anodes, upper cathodes and lower cathodes.

The second level of channel fan-in is to connect the anode channels from eight separate looms into a single data crate. Similarly the cathode channels are multiplexed 8-fold. The particular scheme chosen is shown in fig 3.6. It has the property that the 8 looms served by one anode crate are each served by different cathode crates, so a tube anywhere in the detector may be uniquely located by matching the anode and cathode channels. The two levels of bussing present few problems to event reconstruction, since the interconnections are on a scale much larger than the expected size of an event. There are 8 anode data crates and 16 cathode data crates (8 for upper cathodes and 8 for lower cathodes) instrumenting the complete detector.

3.4 The Analogue Signal Processing

A block diagram of the amplification stages of the signals is shown in fig 3.7.

(1) The electrons as they encounter the anode wire produce many electron-ion pairs in the intense electric field close to the wire. The characteristic shape of the current pulses on the wire have a tail which falls as $1/(t+t_o)$ where t_o is about 11 ns. This long tail is inconvenient and is removed by later pulse conditioning.

(2) The anode signals are amplified by a current preamplifier. The preamplifier is located on the top of the top layer of modules (on the sides for cathodes) close to where the signal cables emerge from the module gas seal. The output drives the signal current down a twisted pair cable where it develops a voltage across the cable terminating resistor at the far end.

(3) An active unity gain summer combines the inputs from 8 preamplifiers and 'multiplexes' them onto a single twisted pair. The twisted pairs are driven differentially to eliminate cable

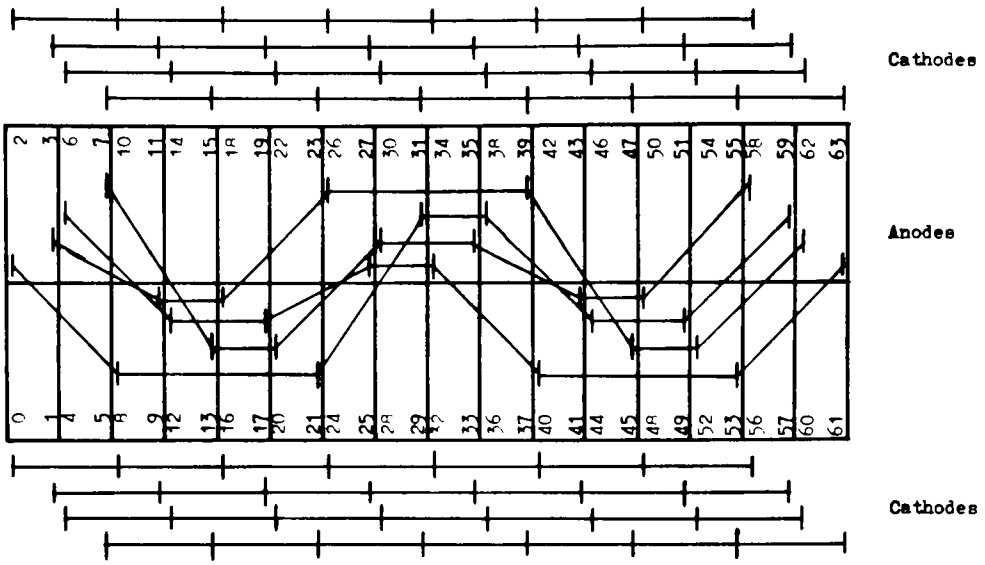

Fig 3.6 Plan view of the detector showing the multiplexing scheme. The Cathodes follow a regular pattern, the complex interconnection is on the anodes. Only half of the anode busses are shown, the others are constructed by reflection in the centre of the detector.

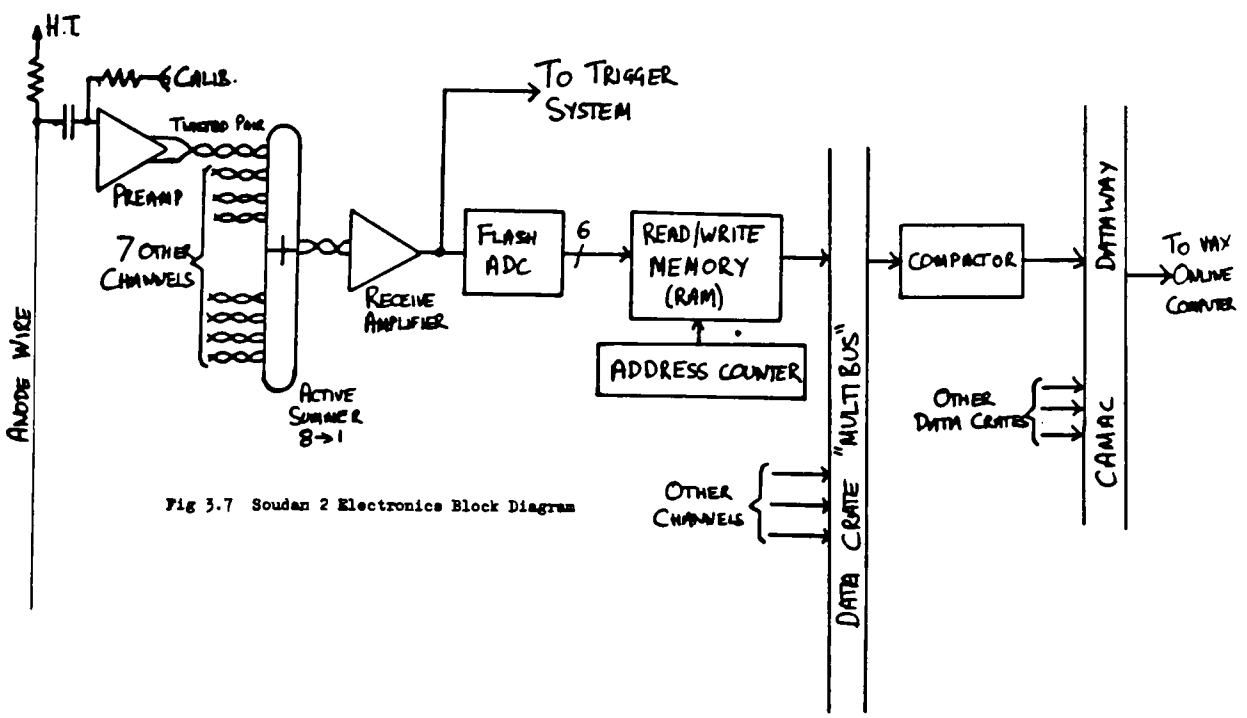

Fig 3.7 Soudan 2 Electronics Block Diagram

pickup. They carry the signals to one of the electronics rack areas around the detector.

(4) The receive amplifier contains a further two stages of amplification and also a filter. The filter emphasises the high frequency part of the response and thereby removes the slow $1/(t+t_o)$ tail in the avalanche signal.

3.5 The Digital Readout Electronics

The signals are processed in groups of 256 channels per 'Multibus' crate. Each crate is subdivided into 16 ADC cards which each contain 16 channels. Rather than logging all the data from the experiment, the detector is read out only when directed from a trigger circuit. The trigger circuit decides when an interesting event occurs and directs the readout logic to complete data taking and the entire state of the experiment is logged onto computer disk for offline analysis. The trigger decision algorithms are discussed in detail in chapter 5.

Since the detector is a drift chamber, the event occurs, then drifts in to the wireplanes where it is converted into electrical impulses on which the trigger logic operates. The trigger cannot decide to take the event until a fraction of the pulses have been received and so the hardware must retain the most recent history of the signals, which is then read out when a decision is made.

The 16 channels of information on each ADC card are buffered, flash digitised at 200ns intervals and stored in clocked RAM. The Flash ADCs provide 6 bit (0-63) output which reflects the input signal.

The system is set so that ADC 32 corresponds to a signal of 1.0V on the ADC input. One ADC count in the 0-32 range represents 31mV. The Flash ADCs can operate in bilinear mode, so that a somewhat higher step

can be used from 32-64 counts to improve the dynamic range.

The RAMs can be programmably selected to be 1024 or 512 words deep. The current RAM location is incremented as each digitisation takes place, the current data overwrites the oldest stored data.

3.6 The Readout Sequence

In addition to the 16 analogue cards, each Multibus crate contains an 8086 microprocessor and data compaction hardware. When a trigger request is received, the following sequence of events occurs:

(1) The data crate is allowed to accumulate data for a further preset time interval which is typically the full drift time and then data taking is stopped. This allows any remaining pulses after the trigger decision to drift in. The RAMs on the ADC cards now contain ADC readings for a window of 200 μs immediately before and after the trigger request.

(2) The signal occupancy of the RAM is typically less than 1% and the event is processed by a pipelined data compactor, which reads the data from the RAM and compares it with a preset threshold. The pulses which are above the threshold are stored in a FIFO memory buffer, with the channel number and pulse arrival time. This process occurs in parallel for the 24 crates. The compactor cycle takes 150 ns per RAM location. The digital threshold is typically set at 1 or 2. Latches within the trigger system are read and, under microprocessor control, channels which have been inactive for the full RAM time are not compacted.

(3) When compaction is complete, the online computer (VAX 750) reads the contents of the FIFO memory buffer from each crate and stores the event on disk. This sequence loops if there is sufficient data to overfill the FIFO memory.

3.7 Appearance of Data from the Detector

Most of the rest of this thesis will discuss the appearance of the events in the detector. I discuss here briefly the ways in which the data can be used.

The x - z view of an event may be constructed simply by plotting the magnitude of each anode channel as a function of drift time. The y - z view can be formed similarly with cathode/time signals. The x - y view must be reconstructed by pairing off pulses on anodes and cathodes. In most cases the pulses will be spread in time and this matching process may be done time slice by time slice. When many pulses appear at the same time in a local region of the detector, the matching is less straightforward and sometimes ambiguous. The three views for a typical muon event (detected on the surface of the earth) are shown in fig 3.8.

The data obtained from the detector is used as follows to obtain information on each event.

Topology : Individual tracks produced by charged particles ($\mu\pi$Kp), showers from γ, $e^{\pm}$ and $\pi^{0}(\rightarrow\gamma\gamma)$ and event vertices are identified from the 2 and 3 dimensional views of the event. The direction cosines of each particle as it emerges from the vertex can be determined.

Momentum : The momentum of each track is determined by two semi independent methods. (1) The particle will range out within the detector volume, the momentum of the particle is estimated from the measured range in the detector. Energy/range and momentum/range curves for the detector are shown in Appendix B for μ, π, K and p. (2) The detector samples the energy loss of each particle at each tube crossing along the path, the kinetic energy can be computed from the total ionisation collected.

Direction : The direction which the particle travelled along the trajectory (into or out of the vertex) is determined by two methods.

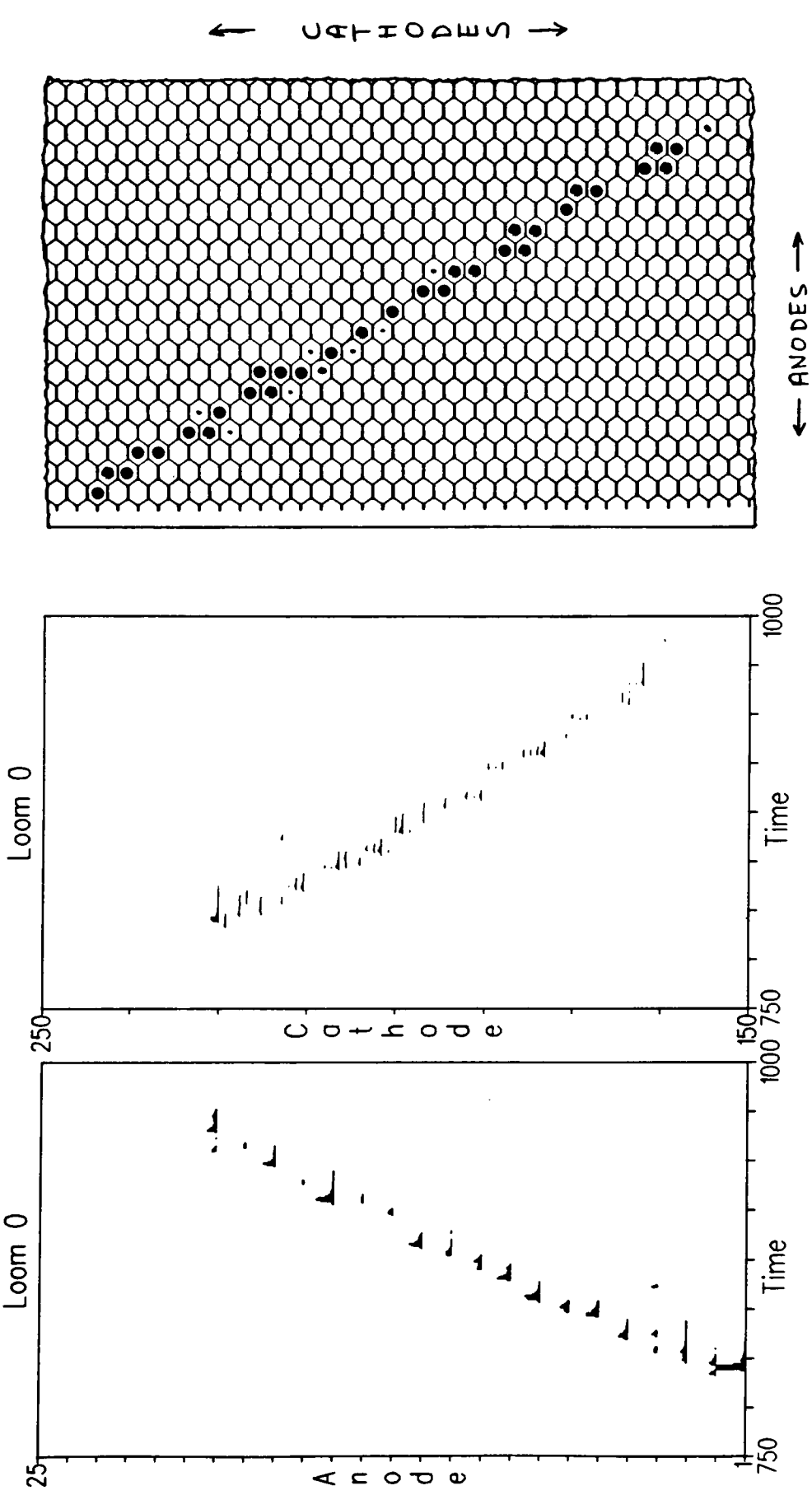

Fig 3.8 Muon in a test module on the surface
(a) Anode-Time view
(b) Cathode-Time view
(c) Anode-Cathode view

(1) The ionization loss goes as $1/\beta^2$ and so the end of the track at which the particle stops will be more heavily ionized. (2) Multiple scattering of the particle will increase at the end where it stops.

In addition any secondary interactions as the particles pass through the detector will be visible and distinguishable from the main event vertex. The way in which each particle has interacted in the detector yields information on the particle type.

3.8 Distribution of Particle Range in the Detector

The hexagonal structure of the detector makes its track measuring capabilities more uniform for different particle directions than for detectors with planar geometries. To illustrate this, a Monte-Carlo study has been carried out to determine the variation in track length distributions for a monochromatic (257 MeV) muon at different angles θ and ϕ (see inset to fig 3.10a).

The detector Monte Carlo has been developed by the collaboration, it propagates particle tracks through the honeycomb geometry in small steps and calculates the amount of energy deposited in each gas crossing. At each step, the energy loss and multiple scattering is computed and the particle may also decay or interact (in the case of pions). The EGS3 package from SLAC is used to propagate electrons and photons through the detector. It is planned to run a module in a charged particle test beam, at which point the Monte Carlo will be precisely calibrated.

Fig 3.9 shows (a) the number of tubes hit by each muon, (b) the straight line path length from start to end point and (c) the path length computed by adding up the distances between each adjacent pair of tube crossings. The distributions are made only for those tracks which remain in one module. Separate corrections must be applied to tracks which cross from one module to another. The distributions (b) and (c) are much narrower ($\sigma/r = 0.20$) than for (a) ($\sigma/r = 0.35$) and do not have

long tails which indicates that the range is a better estimate of the energy than the number of hits. There is little difference between the two methods of measuring the range. Fig 3.10 (a) shows the variations in the mean and standard deviation of the range distribution as a function of $\cos\Theta$(averaged over ϕ). The response is uniform, except close to $\cos\Theta = 1$, ie along the tube direction. Fig 3.10 (b) shows the variations as a function of ϕ(averaged over $\cos\Theta$). The width of the distribution is dependent on ϕ. The decrease in resolution at 30° corresponds to the direction where the tubes line up, separated by only a single sheet of steel. The accuracy of range measurement may be improved by tracking the muons and computing the amount of steel traversed by each. The particular energy chosen for this study is important in the study of $p \rightarrow K^{+}\nu$ proton decay. This will be discussed further in chapter 8.

3.9 The Veto Shield

The cavern is lined on all six sides by a double layer of veto tubes. This is being produced by the group at Tufts University. The tubes will be used offline to verify that there are no charged tracks entering or leaving the cavity at the time an event is seen in the main detector. This is important in two cases.

(1) Neutrons can be produced by muon induced hadronic interactions in the rock surrounding the detector. These neutrons may enter the detector and produce a contained 'neutron star' event. The shield will detect charged particle secondaries from such events. The efficiency for this is increased by installing the tubes as close to the rock walls as possible.

(2) About 8 muons a year are expected to pass through the cracks between the main detector modules undetected. Such events will be detected in the shield. This will rule out the possibility of a contained event being produced from such a muon.

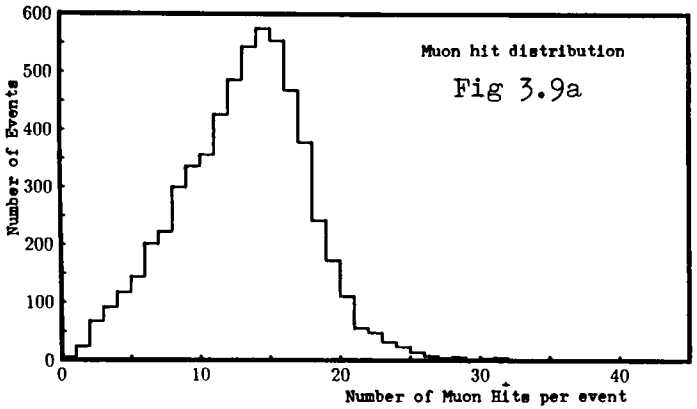

Fig 3.9a

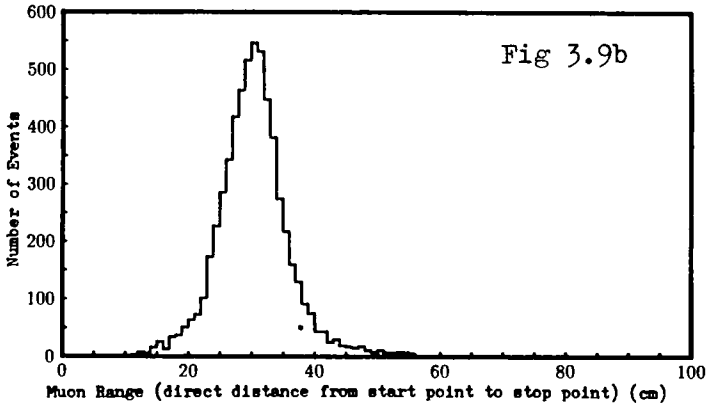

Fig 3.9b

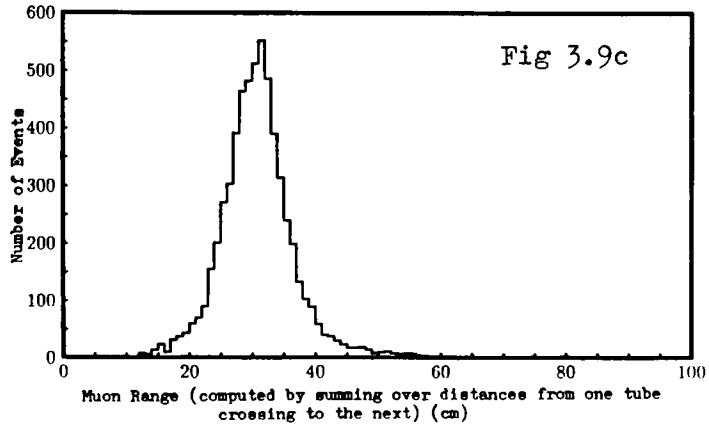

Fig 3.9c

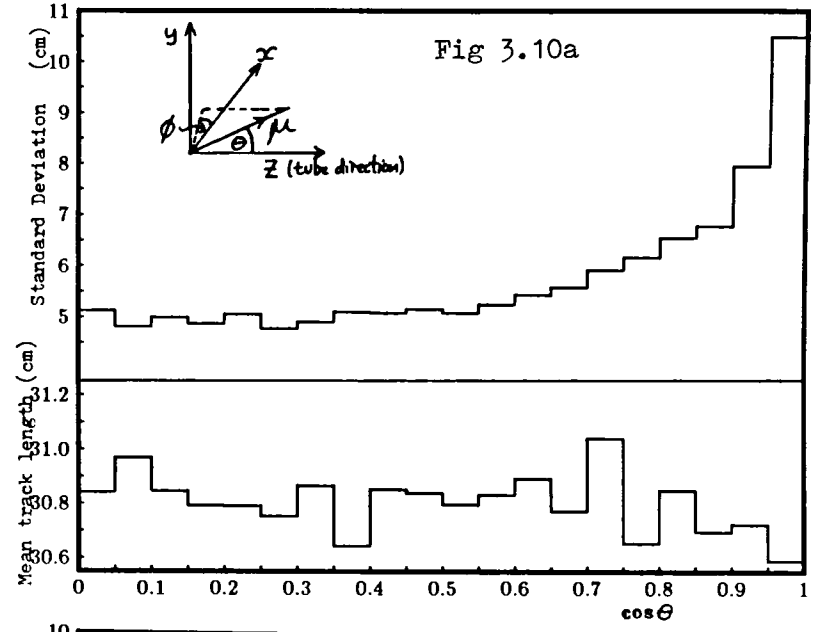

Fig 3.10a

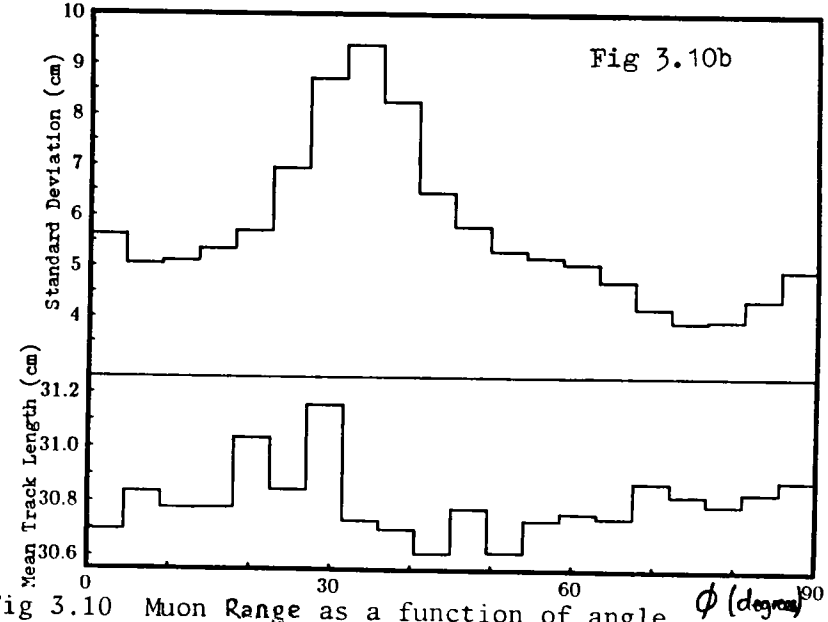

Fig 3.10b

Fig 3.10 Muon Range as a function of angle (see text)

The veto tubes are manufactured in hexagonal modules containing four tubes in each layer. The tubes are approximately 8m long with a cross section as shown in fig 3.11. Each tube contains a single wire running down its centre which is operated as a proportional counter. The four tubes in each layer are bussed together and each group of four is read out separately. The shield information is read out for each main detector trigger and used offline to veto the events.

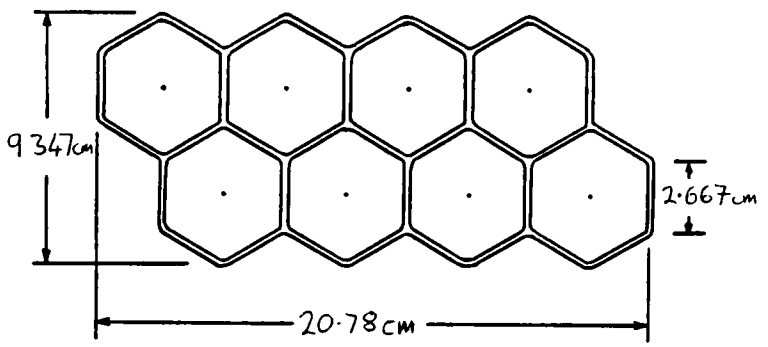

Fig 3.11 Cross section of a section of veto shield.

3.10 Summary

The Soudan 2 detector has been described. The detector uses a novel drift tube technique to instrument the mass in a hexagonal layout. The multiplexing of electronics in order to reduce the number of readout channels has been discussed. A study of the energy measuring accuracy of the detector was described for muons of total energy 257 MeV, which can be measured to 20 MeV except in a small angular range. The detector is surrounded by a double layer of veto proportional counters.

Chapter 4

NATURAL RADIOACTIVITY

The first major topic to be investigated in this thesis is the trigger system. The design and operation are held over to chapter 5. This chapter discusses in detail the signals produced by natural radioactive decay which are of no interest themselves but are a nuisance in the operation of a proton decay trigger. The chapter begins with a brief description of the appearance of radioactive signals and of the types of event which must produce a trigger. It then continues with a detailed calculation of the features and rates of radioactively induced signals in the detector which are compared with data from the mine. The final section describes an experimental verification that the events seen in the mine are produced by the radioactive processes which are considered by exposing a module to a gamma ray source.

4.1 Physical Processes Which Will Be Observed In An Underground Detector

This section presents a brief guide to the different types of physical processes which will be seen in the Soudan 2 detector underground. Except for proton decay, these events are explained by well tested physical principles. Observing these events gives a good indication that the detector is operating correctly and is sensitive to proton decay signals.

(1) Natural Radioactivity:

Long lived radioactive isotopes of naturally occurring elements are present in the rock. γ rays from the decay of these nuclei penetrate the detector mass and produce Compton electrons which will be visible as they pass through a sensitive gas region.

Radioactive events produce two distinct types of signal depending on whether the electron crosses the gas in a tube or a wireplane.

(a) If the electron crosses the gas in a tube, a single hit will be produced. The electron is unlikely to have enough energy to travel through a steel sheet and produce signals in more than one tube. The signals from more than one Compton scatter of the same photon may be seen in separate tubes.

(b) If the electron crosses the gas region of a wireplane, a signal extended over several anode channels and several cathode channels is seen (fig 4.1). The signals produced are very much larger than

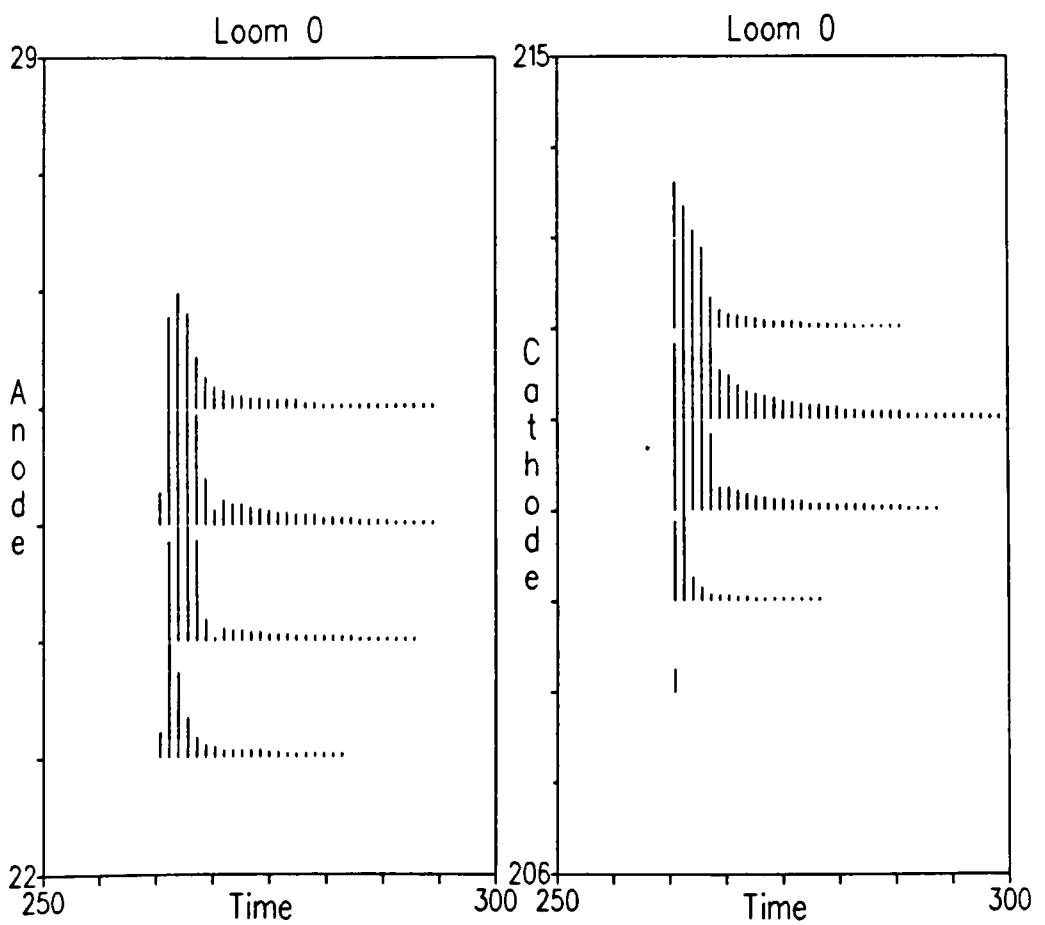

Fig 4.1 A Radioactive photon Compton Scatters in the wireplane region in a test module in the mine.

a typical minimum ionising muon pulse because of electron multiple scattering and because the gas region near the wires is larger than in a tube. Notice from fig 4.1 that all the channels fire within about 600ns of each other in both views (the ADC samples shown are taken at 200ns intervals). The rising edges on each pulse are very much faster than for the muon in fig 3.8 This is because the muon signals diffuse as they travel along the tube, while the Compton electron signals are produced immediately adjacent to the wires.

The features and expected rates of these events will be discussed in full in this chapter.

(2) Muons:

The detector is built underground so that most of the muons produced in the upper atmosphere will range out in the earth before they reach the depth of the detector (2200 mwe). The expected muon flux in the mine is $3 \times 10^{-4}/m^2/sec/sterad$ which compares to typical surface values of $110/m^2/sec/sterad$. The expected muon rate in the completed detector is about 0.5 Hz. A study of the mechanisms of muon production in the atmosphere will be presented in Chapter 6. The energy spectrum underground is considerably harder ($\langle E_\gamma \rangle \sim 200$ GeV) than on the surface, and most of the muons will not be minimum ionizing. A muon event recorded in a single underground module is shown in fig 4.2a. Recent publications [1] have claimed that the muons which point back to certain known X-ray binary stars also display the characteristic frequency and phase of the binary. This has caused a large increase in interest in muon astronomy. Muon astronomy is being studied by other members of our collaboration.

High energy muons generate bremsstralung and delta ray showers as they slow down. These are observed both originating in the detector and originating in the rock above. Fig 4.2b shows such an event observed underground. In addition muons may produce hadronic showers in underground interactions. It is possible that a stray neutron from such an interaction in the rock can interact in the detector mass. This

Fig 4.2a A muon seen in a test module underground

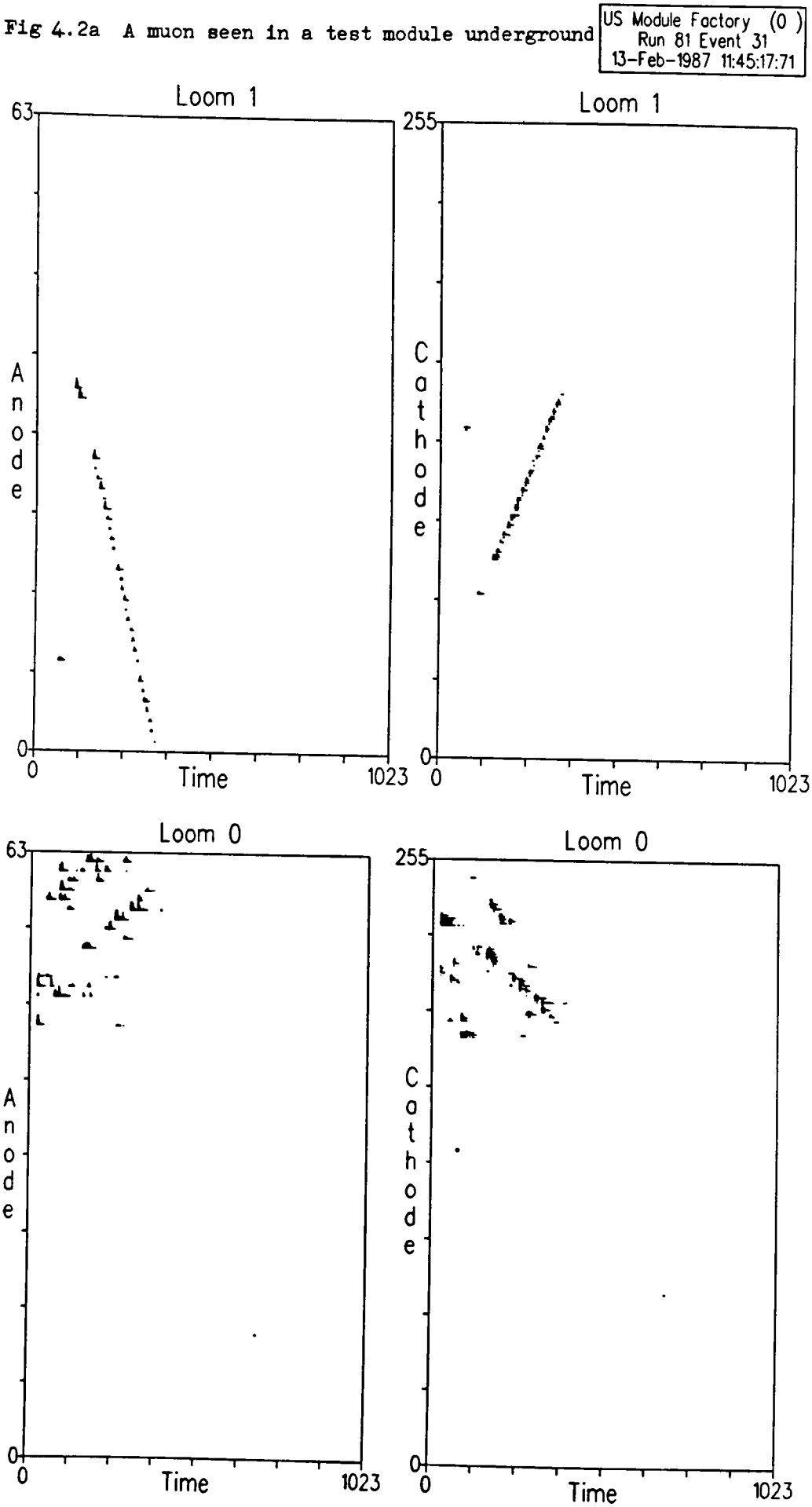

Fig 4.2b Anode-Time and Cathode-Time projections of a cascade generated in the rock immediately above the cavern and observed in a single test module in the mine.

would produce an isolated group of hits which could possibly be interpreted as a proton decay signal. Such events can be eliminated from a proton decay sample if charged products of the original interaction are detected. Our efficiency for detecting such products is considerably enhanced by the veto shield (chapter 3).

(3) Neutrinos:

Neutrinos are produced in the atmospheric cascades in association with charged lepton production. Whereas the charged particles decay or range out, the neutrino cross section is so small that most will pass all the way through the earth and out the other side. Some of the neutrinos passing through the detector will produce interactions. These will appear as an isolated vertex with a number of leaving tracks. The incoming neutrino track will not be detected. This is the principle background to proton decay. A sample simulated interaction from a 1198 MeV neutrino is shown in fig 4.3. The event crosses from one module to another through the wireplanes. The flux and interactions of neutrinos are discussed in chapters 6-8.

(4) Proton Decay Events:

Proton decay events will appear as a group of tracks appearing from a single vertex in the detector. Fig 4.4 shows a simulated $p \rightarrow K^{+}\nu$ event. Only the kaon is seen leaving the vertex (with a unique energy). The kaon produces a heavily ionizing track to its stopping position. and decays to a muon and neutrino, the muon is tracked and observed to decay to a positron. The separation of proton decay events from neutrino interactions must be done on kinematic grounds, this is discussed in chapter 8.

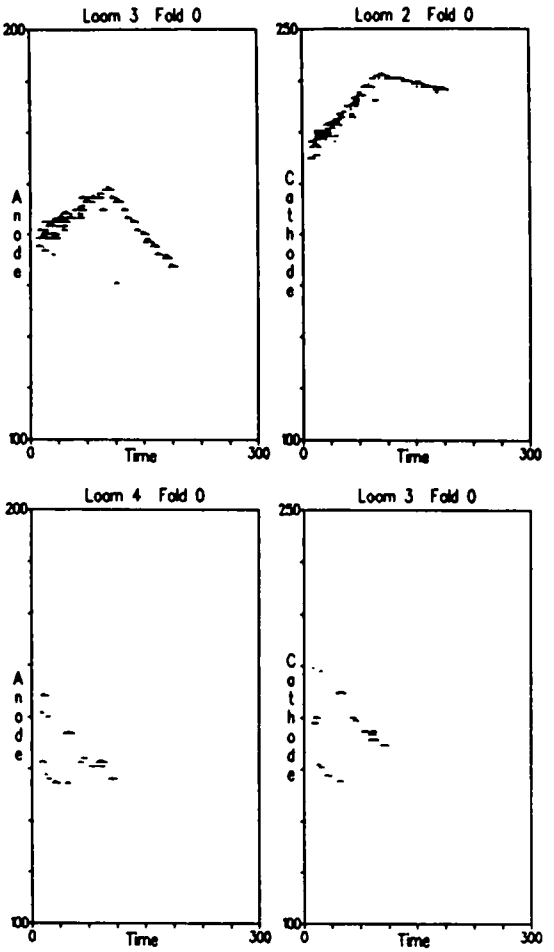

Fig 4.3 A Monte-Carlo simulated neutrino event (see text)

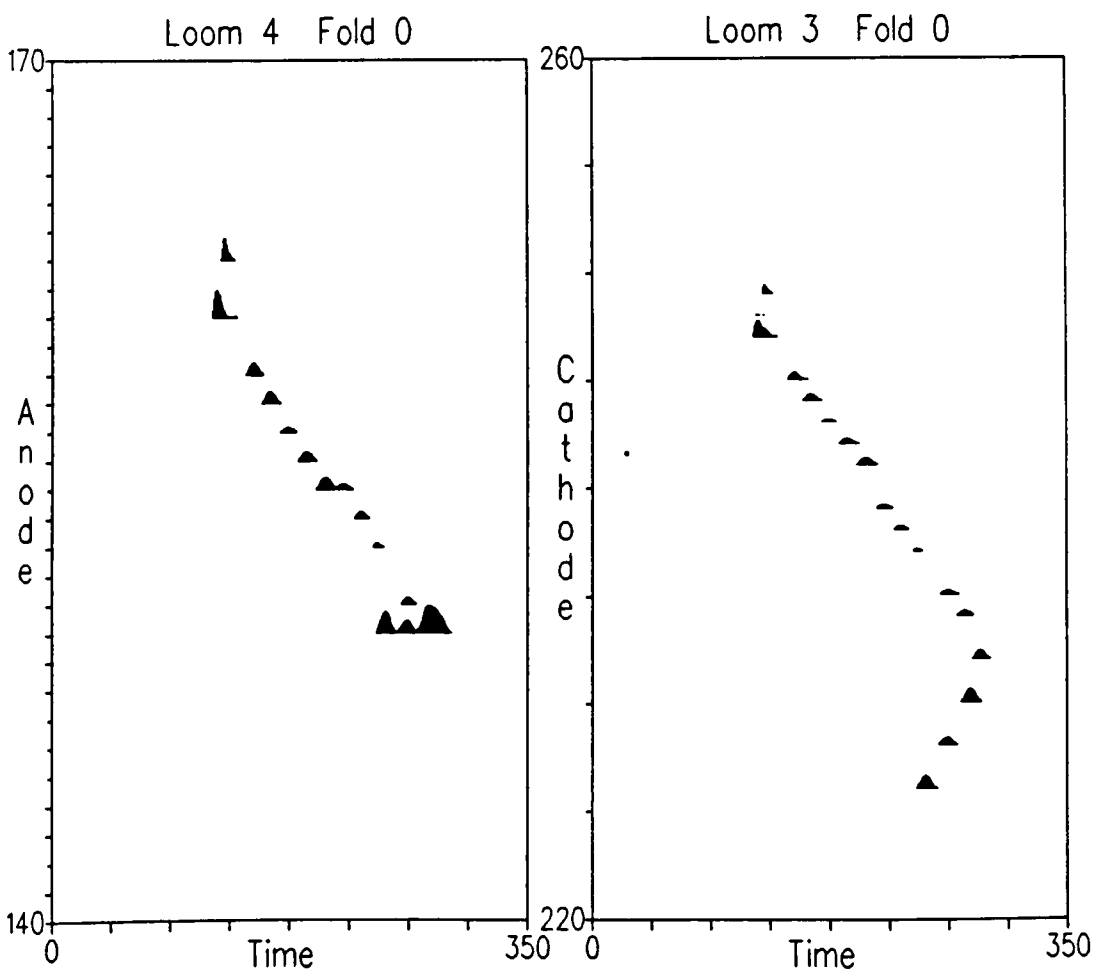

Fig 4.4 A Monte Carlo generated proton decay event. (see text)

4.2 Natural Radioactivity

The remainder of this chapter is devoted to an investigation of the signals which will appear in the detector from natural radioactive sources. This is extremely important for a proton decay experiment, since signals are five orders of magnitude more common than underground muons and eleven orders of magnitude more common than neutrino events.

There are three possible sources of radioactive nuclei,

(1) In the rock: The mine is built in a region of complex rock formation. The rock contains many elements, some of which have radioactive isotopes with lifetimes comparable to that of the earth. The known long lived naturally occurring isotopes are listed in table 4.1. Only gamma production in the rock is important since alpha and beta emissions are unable to penetrate from the bulk of the rock to the cavern walls. The most important gamma emitters present in natural rock are potassium-40 and members of the uranium-238 and thorium-232 decay chains. The decay of uranium-235 daughters are the next most important and contribute about 0.5% of the total gamma flux (see table 4.2).

(2) In the air: Radon gas is produced in the radioactive decay sequences. When it is produced it is able to move out of the rock and into the air surrounding the detector before it decays. The half life of radon is 3.8 days. Although evidence of radon gas has been found in less ventilated regions of the mine around the Soudan 1 detector [4], an efficient ventilation system ensures good circulation of air in the Soudan 2 cavity. Radon gas should not be a problem in the Soudan 2 experiment.

(3) In the detector materials: Samples of steel and Hytrel tube have been measured and contain negligible activity [4]. It is possible that the carbon dioxide contains carbon-14 which is beta unstable. A calculation has shown that if this is the case, it will be at too low a rate to be noticeable.

Parent	% Abundance	Decay Mode	Half Life (yrs)	E_γ(MeV)	n_γ%
H3	$\sim 4 \times 10^{-18}$	β^- He3	1.226×10^{1}	—	
C14	$\sim 10^{-11}$	β^- N14	5.568×10^{3}	—	
K40	0.0119	e Ar40/β^- Ca40	1.33×10^{9}	1.46	10.7%
Rb87	27.85	β^- Sr87	5.0×10^{10}	—	
In115	95.77	β^- Sn115	6.0×10^{14}	—	
La138	0.089	e Ba138/β^- Ce135	$\sim 7 \times 10^{10}$	1.44 0.79	68% 32%
Sm147	15.09	α Nd143	1.25×10^{16}	—	
Lu176	2.59	e Tb176/β^- Hf176	2.4×10^{10}	0.307 0.202 0.088	93% 80% 13%
Re187	62.93	β^- Os187	$\sim 5 \times 10^{10}$	—	
Th232	100.00	complex Pb208	1.39×10^{10}	many	
U235	0.72	complex Pb207	7.1×10^{8}	many	
U238	99.27	complex Pb206	4.5×10^{9}	many	

Table 4.1 Naturally occurring radioactive isotopes with lifetimes long compared with that of the earth.

		K40	La138	Lu176	Th232	U235	U238	Total Activity /s/g
# gammas per parent decay		0.107	1.00	1.86	2.47	2.03	2.43	
Prominent gamma energies (MeV)		1.46	1.44	0.307	2.65	1.00	0.61	
Abundance of active isotope (%)		.0119	.089	2.59	100.	0.72	99.27	
Basalts	Typical conc. (ppm)	.2%-.8%	2-5	.3-.9	.2-2.	0.1 - 0.6		0.034
	γ activity /s/gram	0.015	4×10^{-6}	9×10^{-5}	0.009	0.010		
Granites	Typical conc. (ppm)	36000	55	0.68	18	5		0.43
	γ activity /s/gram	0.11	6×10^{-5}	1×10^{-4}	0.18	0.14		
Soudan Iron Mine (greenstone)	Typical conc. (ppm)	7900	-	-	0.89	0.17		0.0390 (0.0467 incl cement cavern lining)
	γ activity /s/gram	0.0248	-	-	0.0090	0.0060		

Table 4.2 Properties and concentrations of possible γ sources in naturally occurring rock.

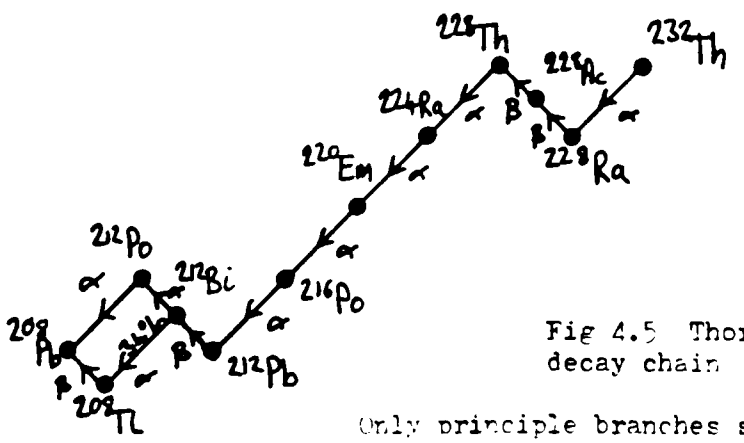

Fig 4.5 Thorium decay chain

Only principle branches shown

In summary, the strongest source of radioactive induced signals come from the gamma emission of ^{40}K and the daughters of ^{238}U and ^{232}Th in the rock surrounding the cavity.

4.3 The Gamma Emissions of Potassium-40 and the Daughters of the Natural Decay Chains

The decay scheme of thorium is shown in fig 4.5. The complete decay chain produces a total of 6 alpha and 4 beta decays. In some of these decay processes, the daughter nucleus is left in an excited state and decays by gamma emission to its ground state. Similar processes occur in the decay chain of uranium. The photon energies are typically in the 0.1 to 3 MeV energy range, the most prominent features are the bismuth-214 photopeak at 0.61 MeV in the uranium chain (47% of uranium-238 atoms will produce the photon in their decay sequences) and the thallium-208 peak at 2.615 MeV in the thorium series (35% of all parent decays). There are of the order of 50 distinct lines for each decay sequence [5]. These have been combined and binned in 0.1 MeV steps. Potassium produces only a single peak at 1.46 MeV. The properties of the three nucleides are given in table 4.2.

Keith Ruddick [4] has measured the concentrations of the radioactive substances in several rock samples from various parts of the mine, which are summarised in fig 4.6. The concentrations vary considerably from one part of the cavity to another. The average values will be multiplied by 1.2 to account for the higher activity found in the concrete aggregate used to line the cavity [4]. Typical concentrations in other types of rock from [1] are also shown in table 4.2. The activity in the mine is comparatively low.

The photon spectrum within Soudan rock is shown in fig 4.7. The dominant activity is from the potassium 1.46 MeV peak.

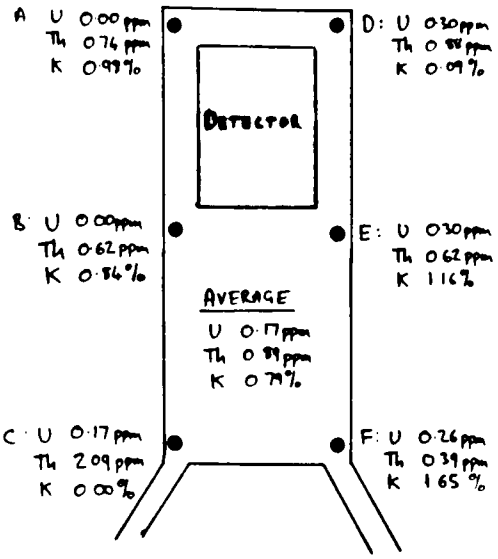

Fig 4.6 Concentrations of principle Radioactive stbstances in various locations in the Soudan 2 detector cavity. (from Ruddick)

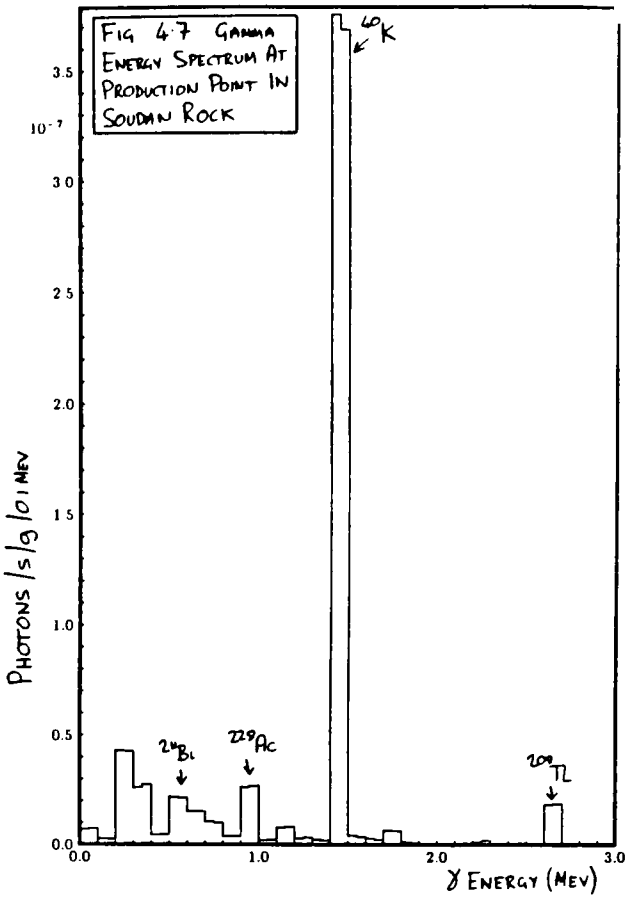

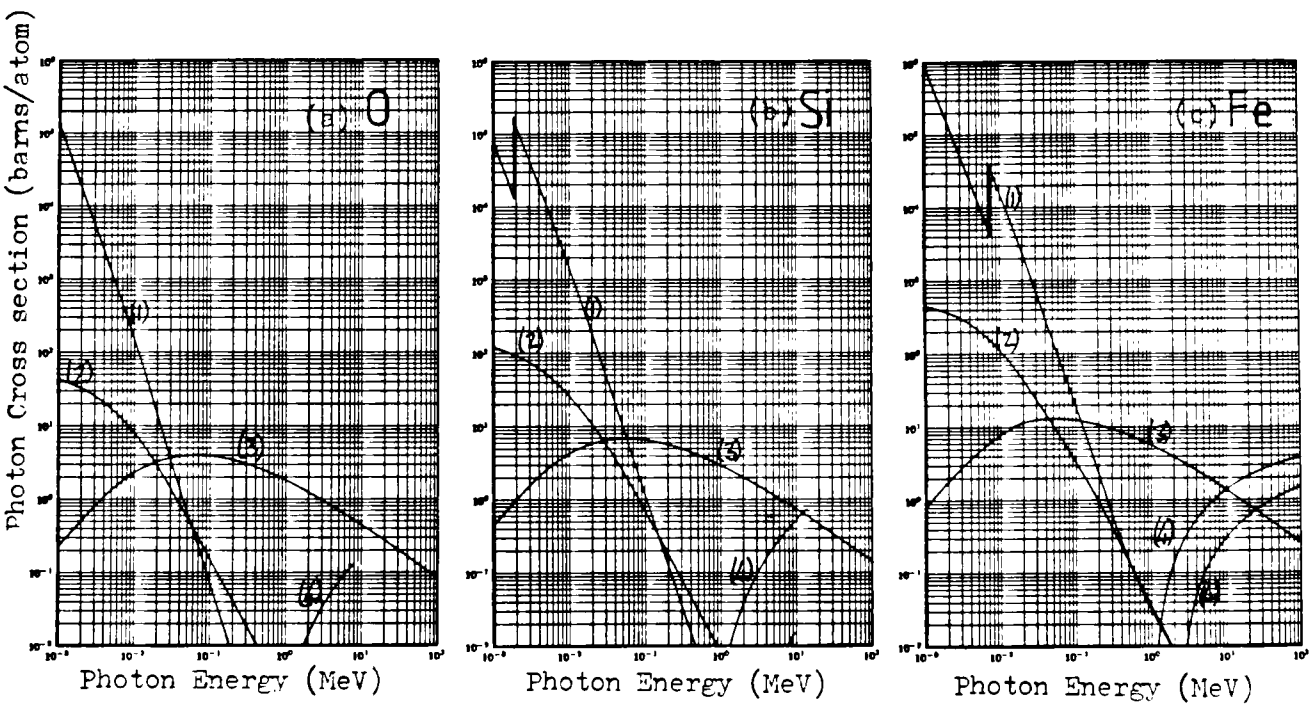

Fig 4.8 Photon Cross sections in (a) Oxygen, (b) Silicon and (c) Iron. Curves are for (1) Atomic Photo-effect, (2) Coherent Scattering (3) Compton Scattering and (4) Pair Production.

4.4 The Gamma Rays Emitted From The Walls Of The Cavern

In order to calculate the features and rates of these signals, we must follow the chain from the production of the photons in the bulk of the rock, to the final absorption of the photon in the detector bulk. Each electron which is scattered on the way will generate signals if it appears in the sensitive gas region of the detector. There are many parts to this calculation which makes the following discussion rather long.

The calculation follows similar lines to one carried out by Keith Ruddick at Minneapolis [6]. Since the calculation has many steps, it has been necessary to independently check the results of Keith's calculation. This was also necessary to educate myself in order to study the trigger design implications.

A Monte-Carlo program has been used to track gamma rays from the decay point to the surface of the rock. The various interaction cross sections of photons in rock [6] are shown in figs 4.8a & b. The cross sections in barns/atom for silicon and oxygen are combined in the ratio 1/3 : 2/3 to represent SiO_2, the principle component of rock. Contributions from other elements (eg Al) are neglected.

The most important interactions are Compton scattering and photoelectric absorption. A typical photon will Compton scatter many times, sometimes losing a little energy, occasionally a lot, until its energy falls low enough for photoelectric absorption to become probable. Pair production and coherent (Rayleigh) scattering processes have little effect, but are included in the calculation for completeness. The steps of the Monte-Carlo program are as follows.

(1) A photon energy is selected from the distribution of fig 4.7, and the photon is started at the origin, a direction is assigned isotropically.

(2) The program looks up the cross sections for the five processes shown in fig 4.8 from a table, linearly interpolating between table entries. The range of the particle is selected from an exponential distribution whose mean is the interaction length computed from the total cross section. The interaction type is selected. The interaction site is computed. Program tracking is in three dimensions.

(3) The next step depends on the interaction type selected:

(a) Compton Scattering: The final photon angle Θ is selected using the Klein - Nishina formula [7].

$$\frac{d\sigma_{KN}}{d\Omega} \propto \left[1 + k(1-\cos\Theta)\right]^{-2}\left[1 + \cos^2\Theta + \frac{k^2(1-\cos\Theta)^2}{1 + k(1-\cos\Theta)}\right]$$

for given incoming photon energy k (in units of electron masses). The distribution is strongly peaked in the forward direction at high energies and peaked forward and backward at low energies (fig 4.9). The distribution of Compton scattering angles generated in the Monte-Carlo is shown in fig 4.9c. The scattered photon energy k′ is given by kinematics from the Compton scattering formula.

$$\frac{k'}{k} = \frac{1}{1 + k(1-\cos\Theta)}$$

The scattered photon direction cosines are computed (azimuth angle selected uniformly). The energy-momentum 4-vector of the electron is also computed. The scattered photon is now tracked from step (2) above from its production point.

(b) Coherent Scattering: This is similar to Compton scattering, except that no electron is generated, so k′ = k. The Rayleigh scattering differential cross section is related to the Thompson scattering cross section by

$$\frac{d\sigma_R}{d\Omega} = \frac{d\sigma_T}{d\Omega} |F(q)|^2$$

$|F(q)|^2$ is approximately constant in the region of interest [10], and the Thompson cross section is used.

$$\frac{d\sigma_T}{d\Omega} \propto (1 + \cos^2\theta)$$

(c) Photoelectric Absorption: The photon is discarded and an electron of energy $E_e = E_\gamma - E_{K\text{shell}}$ is generated.

(d) Pair Production: The photon is discarded and two electrons produced.

Each event is tracked in the rock until the photon is discarded and the event stored in memory. The photon energy spectrum emerging from the rock (fig 4.10) is computed. To reduce the computer time needed, each event is placed at each possible depth in the rock (z). The contribution to the total flux is obtained by integrating over z (fig 4.11). The angular distribution of emerging photons (fig 4.12) is constructed in a similar way. The line indicated on figure 4.12 is obtained by a simple calculation. The flux of particles at angle θ from a given depth z is

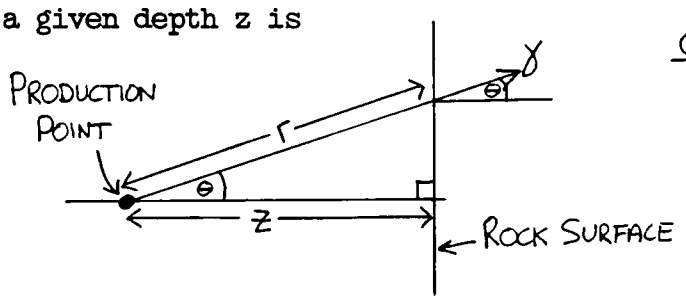

$$\frac{d^2N(\theta,z)}{d\Omega\, dz} = \frac{A e^{-\lambda r}}{4\pi} = \frac{A e^{-\lambda z/\cos\theta}}{4\pi}$$

where A is the number of particles emitted per gram of rock per second and I have assumed the path length distribution is exponential. Integrating from z = 0 to infinity.

$$\int_0^\infty \frac{d^2N(\theta,z)}{d\Omega\, dz}\, dz = \frac{dN(\theta)}{d\Omega} = \frac{A\cos\theta}{4\pi\lambda} \qquad (1)$$

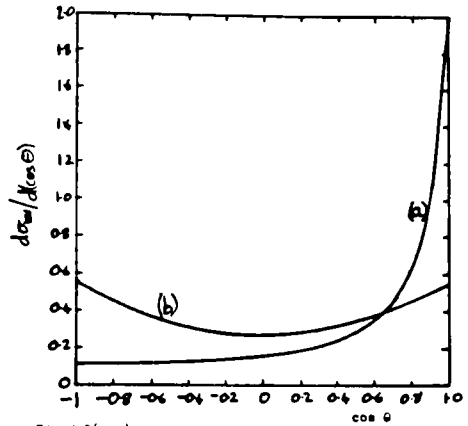

Fig 4.9(a,b) Compton scattering angular cross section from the Klein-Nishima formula (see text) (a) $k = 4m_e$ (b) $k \ll m_e$ (normalised)

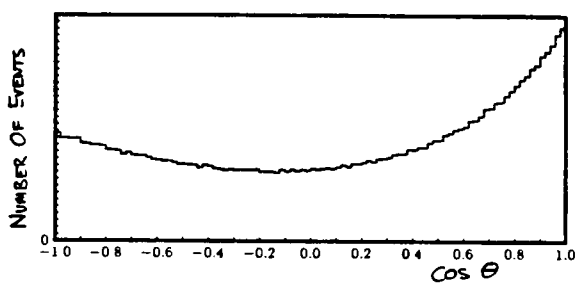

Fig 4.9(c) Angular Distribution of Final Compton Photon in the Rock Monte-Carlo

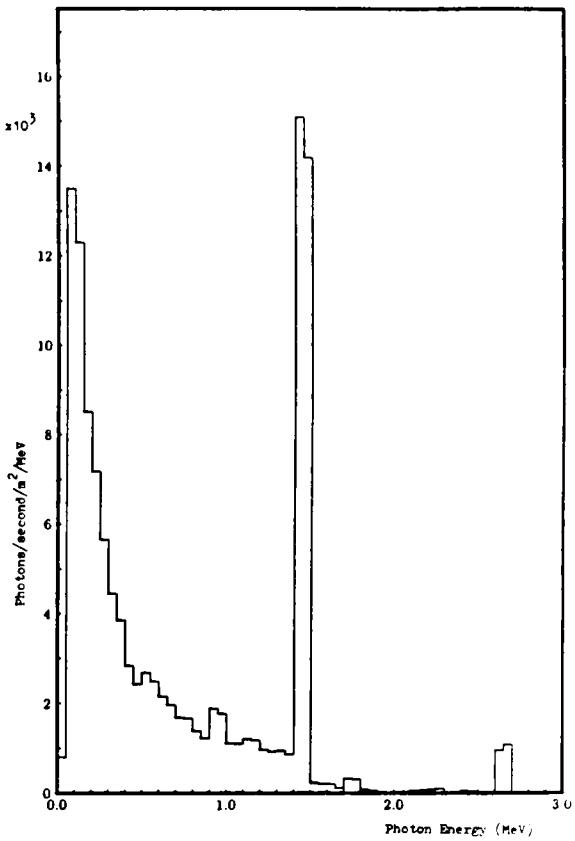

Fig 4.10 Photon spectrum at surface of rock

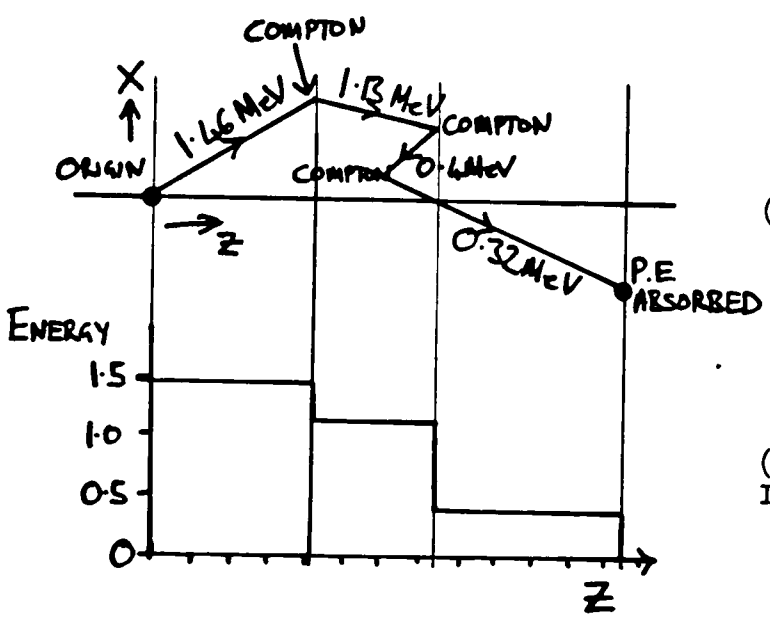

(a) Sample Event

(b) Contribution to Integral of Sample Event

Fig 4.11 Sketch showing Technique of computing integrated Photon Flux (see text)

Figs 4.13 and 4.14 show distributions obtained from the Monte Carlo calculation. The photon produces an average of 10.4 electrons before stopping (fig 4.14). The total path length (fig 4.13a) is much longer than the maximum range of the particle (fig 4.13b), since the photon zig zags from one interaction point to the next. The total range (fig 4.13b) is not an exponential, since each photon must undergo more than one interaction before stopping. The projection of the range along the z axis (fig 4.13c) is approximately exponential. The excess at low penetration distance is caused by the photons from the low end of the spectrum of fig 4.9 which are photoelectrically absorbed at their first interaction. The distribution of distance between interactions is shown in fig 4.13d.

Integrating equation (1) over forward directions, we obtain an estimate of the number of photons emitted from a $1cm^2$ area of the cavern wall per second. $$N = \int_{\phi=0}^{2\pi} \int_{\cos\theta=0}^{1} \frac{A\cos\theta}{4\pi\lambda} \, d\cos\theta \, d\phi = \frac{A}{4\lambda}$$

Using the value of A from table 2, and the mean straight line path length from fig 4.13b, $\lambda^{-1} = 43 g/cm^2$.

$$N = \frac{0.0467 \times 43}{4} = 0.502 = \text{photons/second/cm}^2$$

The value obtained from the full calculation in the Monte Carlo from fig 4.10 is

$$N = 0.611 = \text{photons/second/cm}^2$$

The difference in these numbers is a consequence of the photons moving in a zig zag path from production to stopping point, rather than moving along a straight path as assumed in the desk calculation.

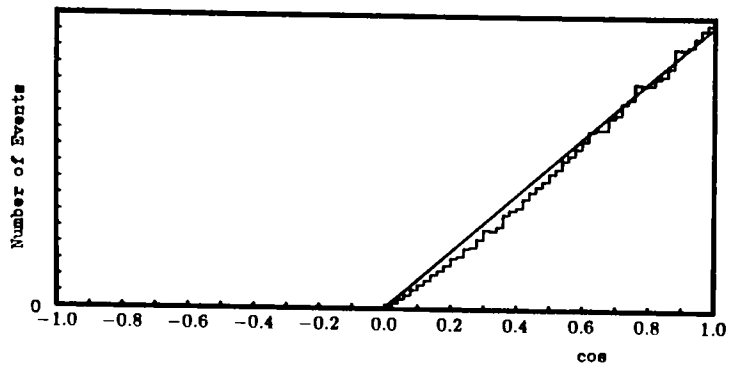

Fig 4.12 Angular Distribution of Photons Emerging From the Cavern Walls

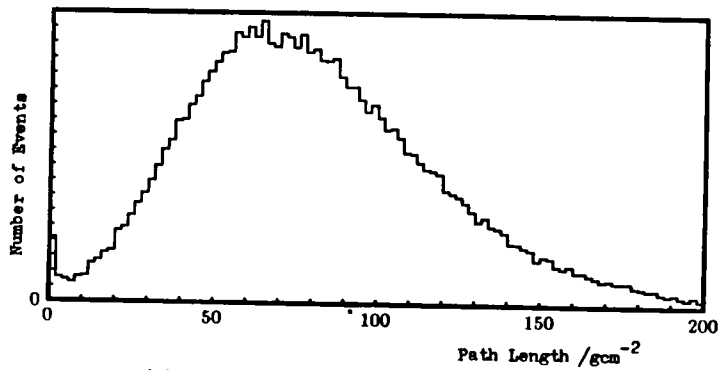

Fig 4.13(a) Total Photon Path Length Distribution in the rock

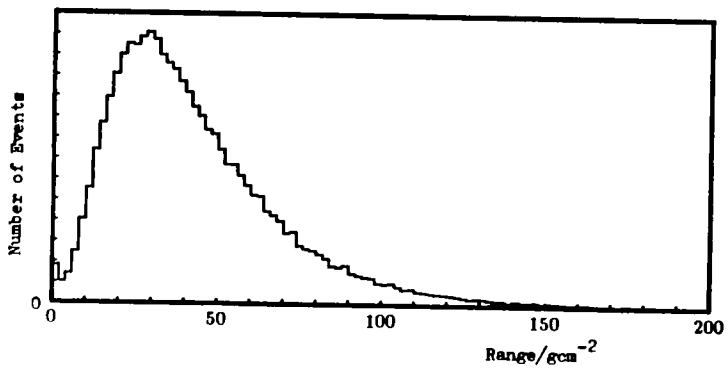

Fig 4.13(b) Maximum Photon Range from Production point in Rock

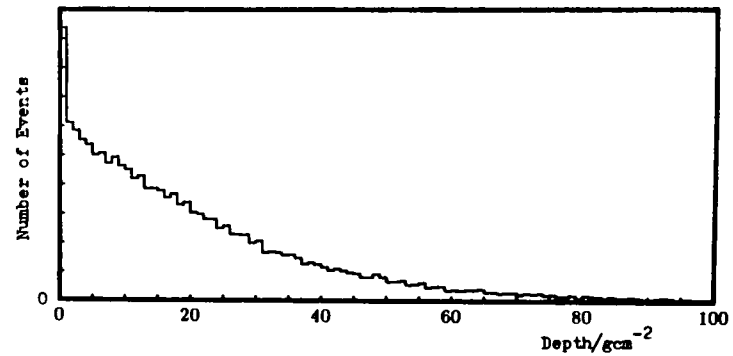

Fig 4.13(c) Maximum Distance Travelled Perpendicular to Rock Face (Penetration)

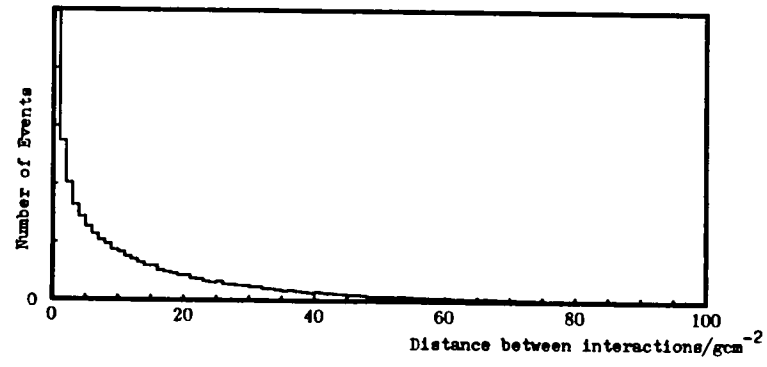

Fig 4.13(d) Distance between Interactions

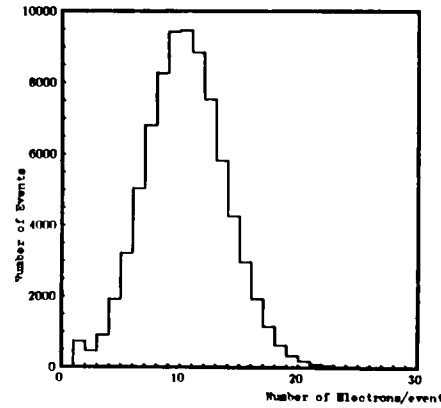

Fig 4.14 Number of Electrons Produced per Initial Photon - Rock Source Spectrum

4.5 Photon Penetration of the Detector

A second Monte-Carlo calculation has been used to simulate photon propagation inside the detector volume. The photons emitted from the rock surface are now started at the surface of the detector and tracked until they are discarded. The positions and energies of all electrons produced are recorded. In practice, this calculation is done with the same code as in the previous section, except for the following modifications.

(1) The initial photon spectrum is replaced by the output from the rock calculation (fig 4.10).

(2) The photon direction is generated according to fig 4.12.

(3) The tables of photon cross sections is replaced by the appropriate iron cross sections [6] - see fig 4.8c.

(4) The K shell energy for iron is inserted for the photoelectric simulation (=7.119 keV) [6].

(5) The photon is discarded if the photon is tracked back out of the detector.

The features of the events are similar to those of the rock calculation, figs 4.15 to 17 show distributions obtained. The number of electrons produced by the photon is reduced from a mean of 10.4 in rock (fig 4.14) to 6.0 for 1.46MeV monoenergetic photons (fig 4.16a). In iron, the photoelectric cross section is equal to the Compton cross section at a higher energy (fig 4.8c) than in either oxygen or silicon. This means that the photon will Compton scatter less times in iron before being absorbed than in rock. The electron number distribution for the spectrum of photons emerging from the rock (fig 4.16b) contains more events which produce few electrons, since some of the photons have already scattered several times in the rock.

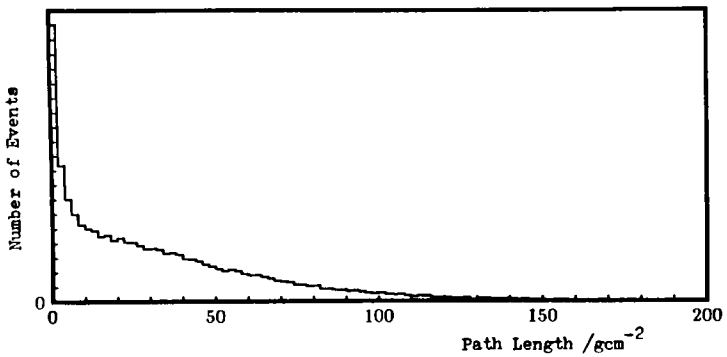

Fig 4.15(a) Total Photon Path Length Distribution in Iron

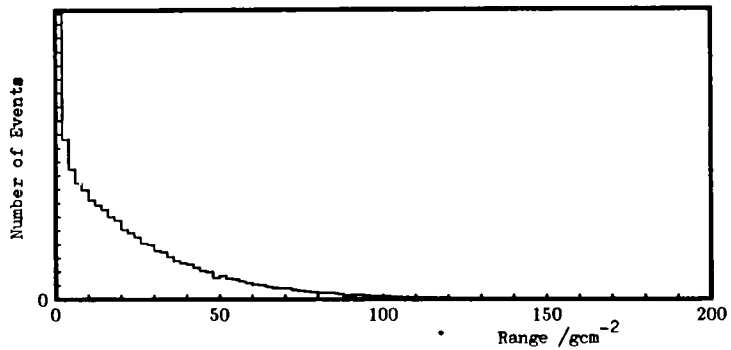

Fig 4.15(b) Maximum Photon Range from Entry Point in Iron

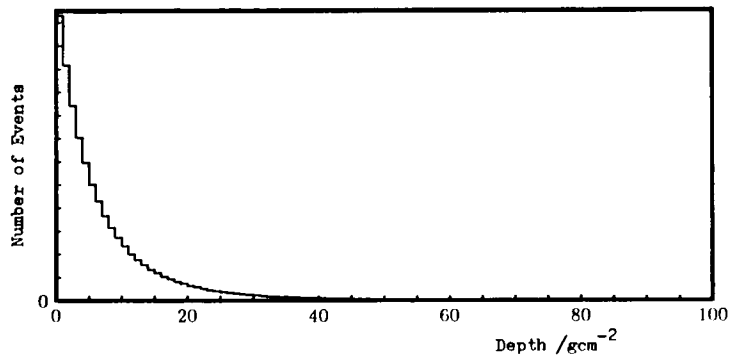

Fig 4.15(c) Maximum Distance Travelled Perpendicular to Detector Surface

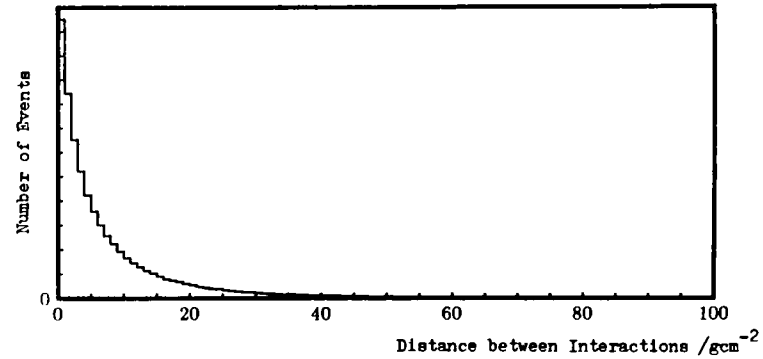

Fig 4.15(d) Distance between Interactions in Iron

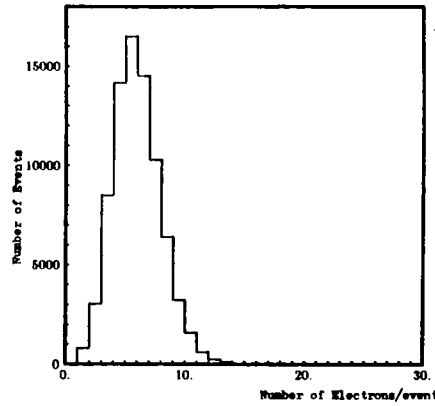

Fig 4.16(a) Number of Electrons Produced per Initial Photon in Iron - Monoenergetic 1.46MeV Source

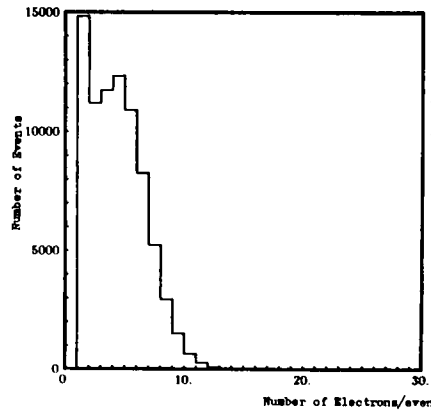

Fig 4.16(b) Number of Electrons Produced per Initial Photon in Iron - Spectrum as at rock surface.

The path length, range and penetration distances in iron (figs 4.15a-c) are correspondingly lower than in rock (figs 4.13a-c) for the same reasons. The path length and range distributions do not show identifiable peaks since the input spectrum contains many more low energy photons. The features of the rock and iron calculations are compared in table 4.3. Table 4.3 also shows the significance of each of the different photon interactions. Compton scattering and photoelectric absorbtion are the most important. The electron energy distribution is shown in fig 4.17. The two Compton edges corresponding to potassium-40 and thallium-208 (from the thorium series) computed from

$$E_e = E_\gamma \left(1 + \frac{M_e}{2E_\gamma}\right)^{-1}$$

are shown on the graph.

4.6 Electron Ranges

Having computed the distribution of electron production as a function of depth in the detector mass, we need to know the probability that any given electron finds its way to a gas region in the detector and produces a signal. To do this, we need to know the electron range as a function of electron energy.

This is a complex problem since (1) multiple scattering is very high, ref [2] says "Electrons which have energy less than 1.5 MeV in Copper are likely to deposit 10% of their energy behind their starting plane". (2) The bremsstrahlung cross section is appreciable, and (3) the projectile mass is equal to the mass of the target (orbital electron) so the fractional energy loss is large. Statistical fluctuations are high. The problem is described in terms of the electron practical range Rp which is tabulated or parameterised in several references [8,11].

The range of monoenergetic electrons varies as in the sketch of fig 4.18, ie a linear portion followed by a long tail. The practical

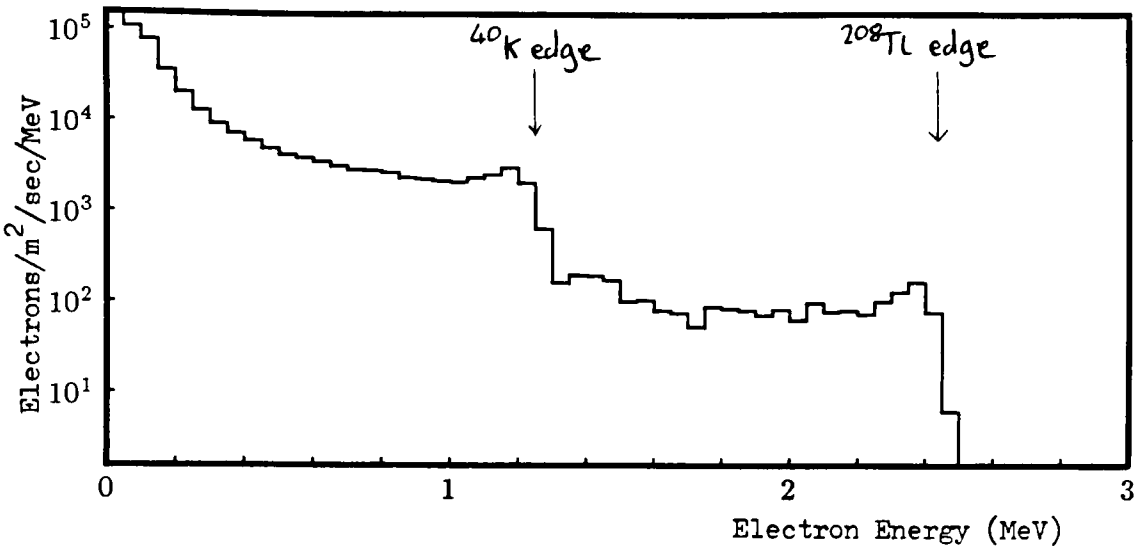

Fig 4.17 Spectrum of Electrons produced in the detector

		In Rock		In Iron	
		1.46MeV	Rock Spot.	1.46MeV	Wall Spot.
Mean # electrons produced		10.4	9.9	5.5	3.9
Mean Total path len (13a,15a)		87.2	80.3	58.5	33.6 g/cm
Mean Max range (figs 13b,15b)		47.0	43.0	41.4	23.9 g/cm
Mean depth distr. (13c,15c)		22.7	20.6	24.1	13.9 g/cm
Mean dist. between interactns		8.1	7.7	10.1	8.1 g/cm
% of interactions selected for all collisions	Compton	86.1%	85.5%	77.9%	70.0%
	P.E.	9.2%	9.5%	17.2%	24.2%
	Pair Prdn.	0.02%	0.03%	0.13%	0.08%
	Coherent	4.7%	4.9%	4.8%	5.8%
% of interactions selected for first enocunter of each photon	Compton	99.7%	98.8%	98.6%	79.2%
	P.E.	0.003%	0.6%	0.3%	16.8%
	Pair Prdn.	2.3%	0.3%	0.7%	0.3%
	Coherent	0.05%	0.3%	0.4%	3.7%

Table 4.3 Comparison of quantities from Monte-Carlo runs.

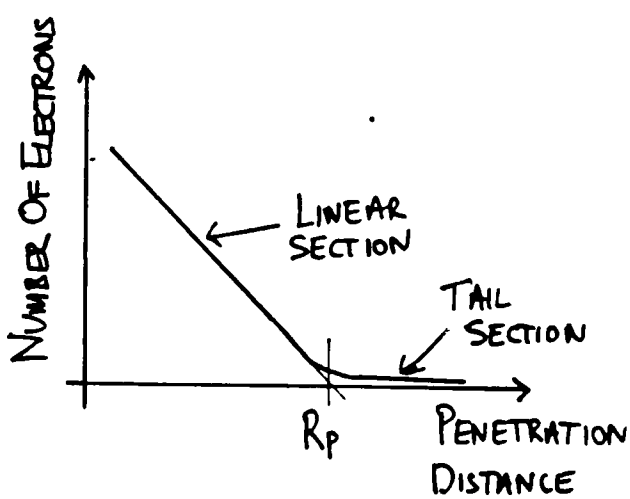

Fig 4.19 Sketch of definition of R_p

range is obtained by extrapolating the linear section to the axis. About 90 - 95% of incident electrons have stopped at this depth. The parameterisation used is from [11].

$$R_p = 0.55\,T\left[1 - \frac{0.9841}{1+0.0030T}\right] \quad (mg/cm^2)$$

for an electron of kinetic energy T (KeV). The values are quoted for aluminium. Data for other elements is sketchy but heavier elements such as iron should have similar practical ranges.

A useful quantity for desk calculations is the mean practical range for all the electrons produced by a photon of energy E_γ as shown in fig 4.19. This has been computed from the Monte Carlo program using the above parameterisation.

We may now compute the flux of electrons emitted from the cavern walls. All the electrons which interact in the rock within a distance R_p from the surface are assumed to escape from the surface

$$N_e = \frac{N_\gamma R_p}{R_\gamma} = \frac{6110 \times 0.11}{7.7} = 79 \text{ electrons}/m^2/\text{sec}$$

where N_γ is the surface γ flux, Rp the electron practical range and R_γ the interaction length of photons (the mean value of fig 4.13d). The same expression may also be used for the surface of any other material in the mine which has this flux of photons passing through it.

Fig 4.20 shows a plateau curve from a veto shield tube measured in the cavern by our Tufts collaborators [9]. Data taken at two separate locations in the mine are consistent. The rate is 450 Hz for 4 tubes. The total surface area of one tube is 7m x 0.027 x 2π = $1.13m^2$, so the rate from my calculation is 79 x 1.13 x 4 = 360 Hz which is in reasonable agreement with the measurement. More recent measurements by the Tufts group show that the singles rate has decreased to about 300Hz.

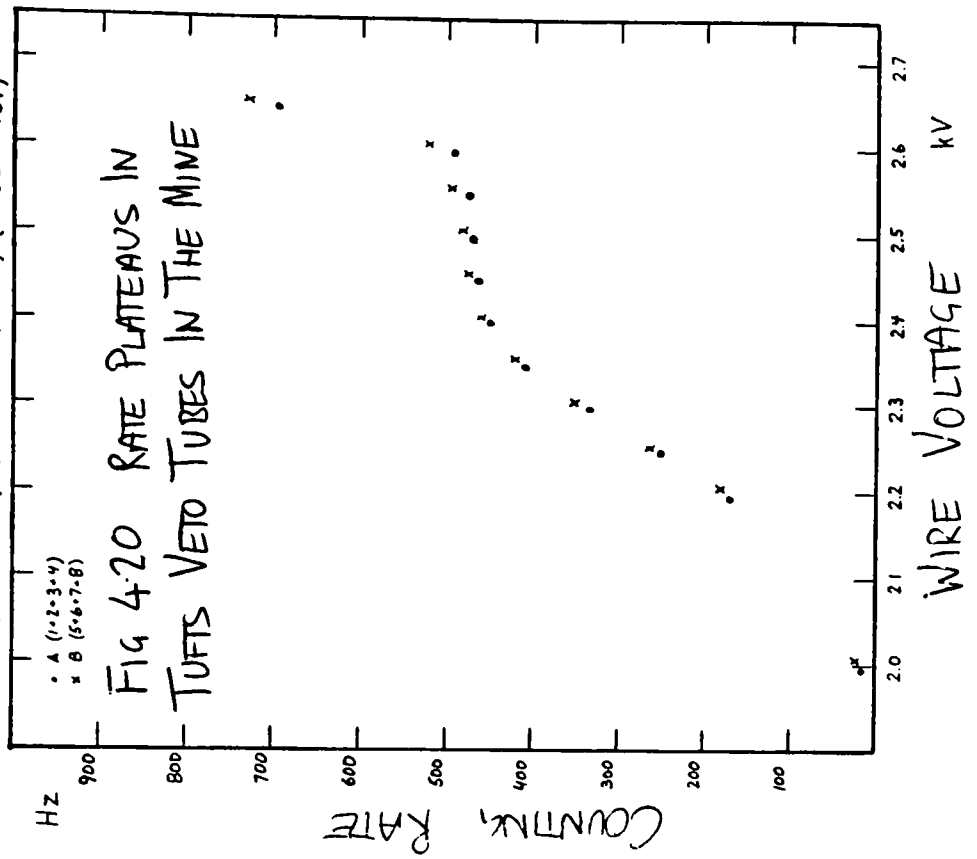

Fig 4.20 Rate Plateaus In Tufts Veto Tubes In The Mine

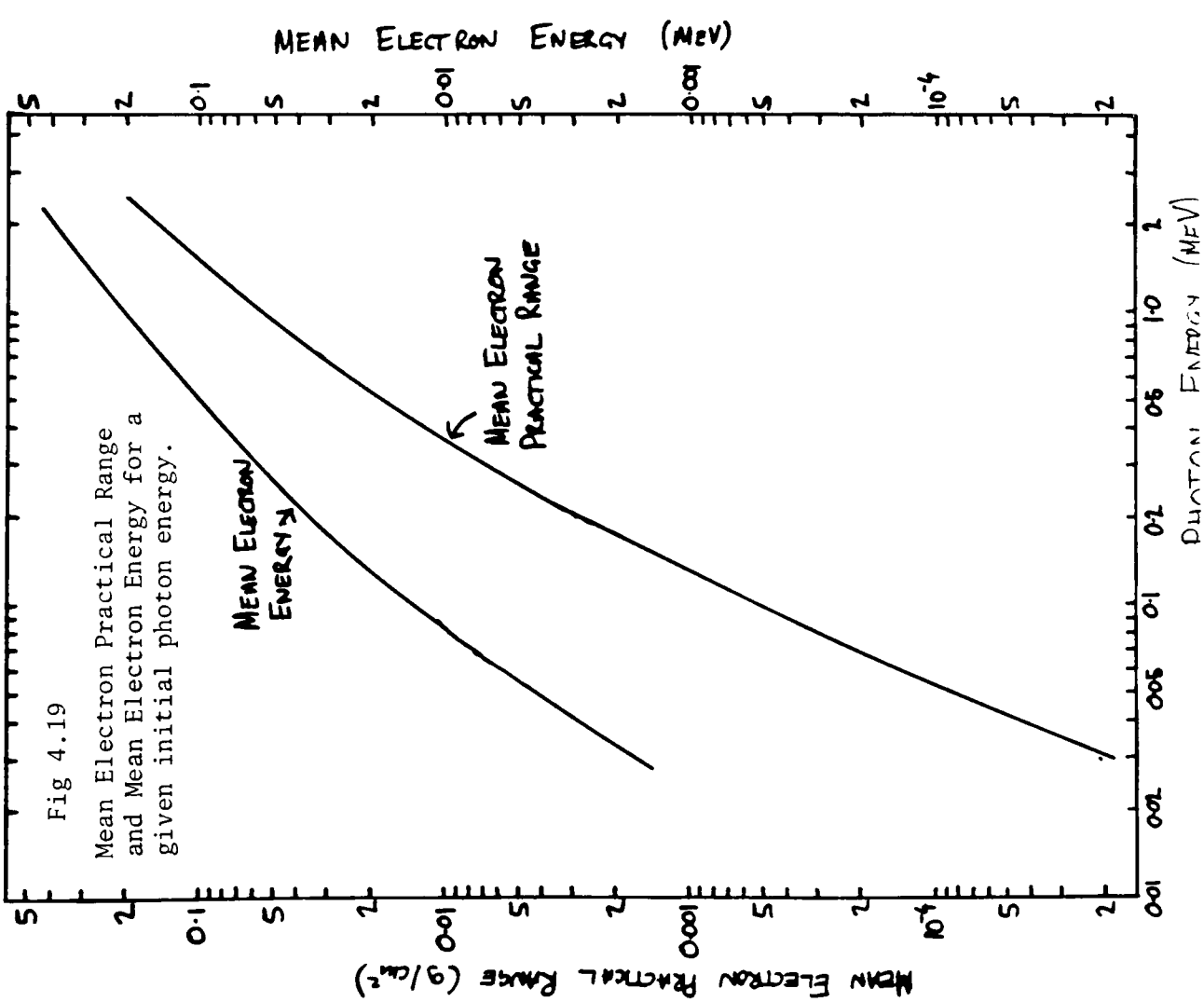

Fig 4.19

Mean Electron Practical Range and Mean Electron Energy for a given initial photon energy.

The early measurements were made before the ventilation system was operating and so radon gas may have been a problem. The rate from cosmic ray muons is negligible.

4.7 Expected Singles Rates in a Main Detector Module

The probability that an electron which is produced in the main detector reaches a region of active gas (ie in a tube) must now be computed. This is given by the total surface area perpendicular to the electron direction which is crossed by a 1 cm long track (per unit area) multiplied by the track length of the electron. For an electron which is travelling perpendicular to the tube axis, this is

$$P_{SEE} = \frac{\text{AREA OF TUBE } \perp r \text{ TO ELECTRON DIRECTION}}{\text{VOLUME OCCUPIED PER TUBE}} \times \frac{R_p}{\rho_{\text{DETECTOR}}}$$

This number is the same for all directions perpendicular to tube direction, since the tubes are circular. For other directions, the probability is less by a cosine factor, however, the electron direction changes due to multiple scattering as discussed above. To allow for this, the cosine factor is not applied and the above expression used for all directions. Using detector constants from Appendix B,

$$P_{SEE} = \frac{1.6}{2.0 \times 1.47} \times \frac{R_p}{1.59} = 0.34\, R_p \qquad (R_p \text{ in } g/cm^2)$$

A small contribution from photons which scatter in the gas itself is neglected ($< 10\%$).

The number of electrons seen per incident photon is 0.0544 from the Monte-Carlo. This means that the rates measured in the detector are 6110 x 0.0544 = 332 electrons/m^2 of exposed detector surface. A single free standing module has a surface area of about 12m^2. The predicted singles rate is 4 kHz. I measured a singles rate of 4.7 kHz for 110 active anode channels on the single test module in the mine. This

corresponds to a rate of 5.4 kHz for a fully active module. This is in agreement with the above prediction.

Fig 4.21 shows the distribution of electron production points in the detector mass. This has been weighted using the computed P_{SEE} for each electron entered. The distribution falls exponentially at 0.15 (anode channels)$^{-1}$ except that at low depths the fall is sharper, 0.23 (anode channels)$^{-1}$. Note that for photons which enter from the sides, only the tubes close to the edge of the outer module will be illuminated. This will induce signals as in fig 4.21 on the anodes. The signals will also be distributed over all the cathodes. Photons which enter from the top will evenly illuminate the anodes, but only affect the topmost cathode pads.

4.8 Singles Rates in the Complete Detector

The rates in the planes of the full detector depend on whether or not the plane is shielded by other modules. Four types of plane can be defined (fig 4.22) according to the amount of shielding.

The expected rates for each plane type are summarised in table 4.4. Note that the exposed planes on the two ends of the detector contribute more than 20% to the total detector rate. Table 4.5 shows the rates on the 8 anode and 16 cathode crates taking account of the multiplexing scheme discussed in chapter 3. Half of the crates experience a higher rate because they are connected to exposed end planes (types α and β). The exposed planes contribute more than 20% of the total detector singles rate. Table 4.5 shows also the rates on the crates if the end planes were removed from the general multiplexing scheme and read out elsewhere (connection scheme B). In the next chapter on triggering, connection scheme B will be used.

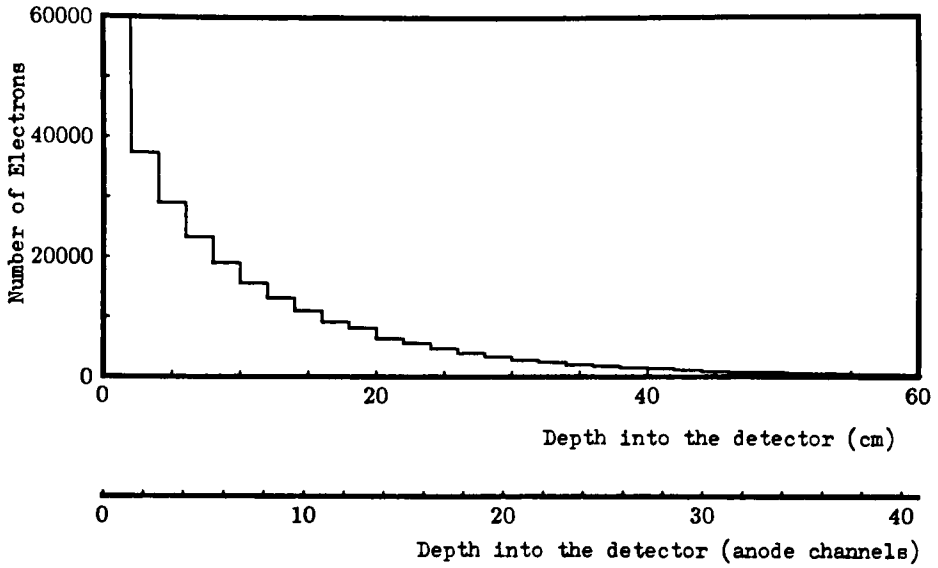

Fig 4.21 Electron production location distribution (from side)

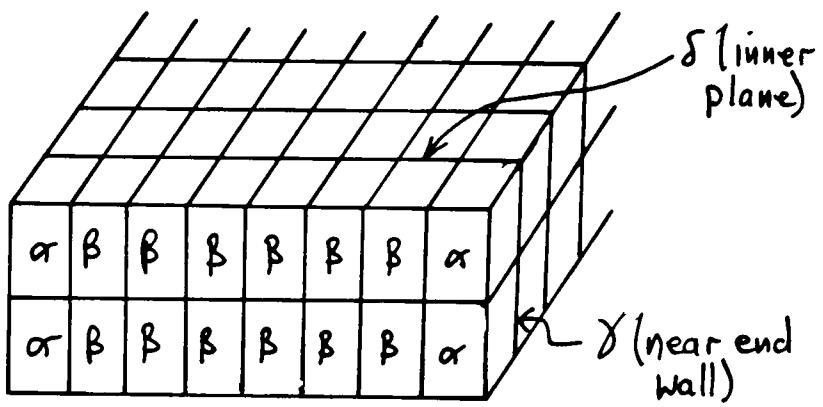

FIG 4·22 PLANE CLASSIFICATION FOR RADIOACTIVE RATES

Type	# planes	illuminated	exposed/plane	rate per plane (Hz)	av./wire
δ	360	top(or bottom)	0.5 m^2	166 - 166	5.3Hz
γ	120	top/side	1.75 m^2	166+415 - 581	18Hz
β	24	top/front	3.0 m^2	166+830 - 996	32Hz
α	8	top/side/front	4.25 m^2	166+415+830 - 1411	45Hz
Total	512			164672	
Ends	32			35192	

Table 4.4 Predicted singles rates.

The effects of extra "dead" steel located around the modules (base plates, support structure etc) shielding the detector has not been considered.

It is possible that many hits may appear in the detector at the same time. This will normally occur due to accidental coincidence which will be discussed in the next chapter on triggering. It is also possible for more than one of the electrons from a single photon to be seen. The probability of this occurring can be computed in the Monte-Carlo by combining the individual P_{se} values for each electron. For example, if there are 4 electrons, the probability of the first two being seen is

$$P_1 \times P_2 \times (1-P_3) \times (1-P_4)$$

The Monte-Carlo computes the total probability of obtaining double, triple, quadruple ... Compton scatters for each event by summing appropriate combinations of the individual probabilities. This is done in a four line recursive routine written in the C programming language. Table 4.6 summarises the overall rate per square metre of exposed detector of multiple Compton hits. The distribution of double Compton probabilities per event are shown in fig 4.23.

The hits from a given multiple scatter will be localised to the same order as the distances associated with fig 4.21, ie all the hits will be within about 20 anode channels. The events will be concentrated near the sides of the detector. The chance of seeing multiple hits within a group further into the detector are reduced for two reasons, firstly, few of the photons penetrate far into the detector and secondly, the ones which do are of low energy and less likely to scatter many times. This is indicated in fig 4.24 which shows the probability of two electrons from a single photon appearing within a group of 16 as a function of depth into the detector.

Scheme	Type	#crates	Rate/crate	Int. 16	Ext. 16
A	Anode 7int+1end	4	23904 Hz	1106 Hz	1709 Hz
	Anode 8internal	4	17264 Hz	678 Hz	1281 Hz
	Cathode 7int+1end	8	11952 Hz	553 Hz	821 Hz
	Cathode 8internal	8	8632 Hz	339 Hz	607 Hz
B	Anode 7internal	4	15106 Hz	594 Hz	1123 Hz
	Anode 8internal	4	17264 Hz	678 Hz	1281 Hz
	Cathode 7internal	8	7553 Hz	297 Hz	532 Hz
	Cathode 8internal	8	8632 Hz	339 Hz	607 Hz

Table 4.5 Rates per crate for two connection schemes. In scheme A, half of the crates serve only γ and δ type planes while the others have two α and six β planes. Connection scheme B assumes all the α and β planes are read out separately. Rates are also given for groups of 16 internal (external) planes which are far (close) from (to) the sides of the detector

Number of hits	Number of interactions/sec Per m^2 exposed	in complete detector
1	332	164,672
2	6.19	3070
3	0.058	28.8
4	3.1×10^{-4}	0.15
5	1.0×10^{-6}	$5.\times10^{-4}$

Table 4.6 Overall detector rate from multiple Compton scattering

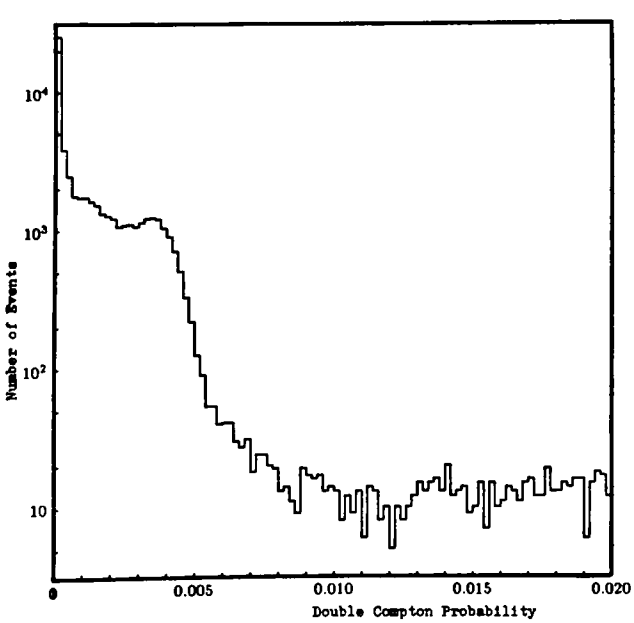

Fig 4.23 Double Compton Probability Distribution

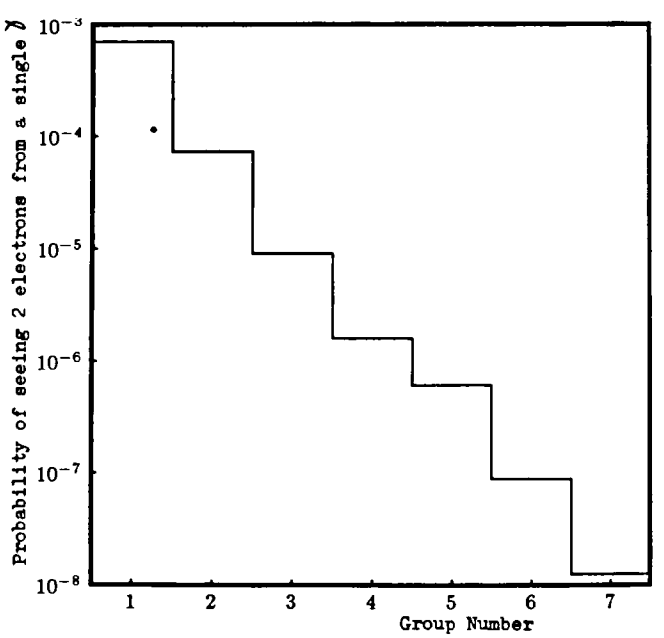

Fig 4.24 Probability per incident photon of two (exactly) electrons being detected in a group of 16 channels. Group number 1 is next to the exposed detector face.

4.9 Compton Electrons In The Wireplane Regions

So far, only the electron interactions in tubes have been discussed. The rates of events induced in the wireplanes have been computed. Internal wireplanes are situated in gaps in the detector bulk. Photons can reach the wireplanes either by emerging from the steel or by entering the detector along the gap. The events from the Monte Carlo were retracked in a detector geometry which contained a gap. For the calculation, the photons were assumed not to interact in the gap but were transported in vacuum until they reached the boundary of the module.

Fig 4.25 shows the construction of the modules close to the wireplanes and also shows the components which limit the size of the gap. Note that the wireplane boards are constructed out of two thin skins of fibreglass sandwiching an aluminium foil 'Hexel' structure. The planes represent little mass. The gap from stack to stack is about 13cm.

Figs 4.26 and 4.27 show some features of the calculation. Fig 4.26a shows the photon wireplane crossings as a function of depth into the gap. All the photons which enter through the gap (6110 photons/second/m^2) will cross a wireplane and may induce a signal. About half as many photons again emerge from the steel on one side and cross to the other side. These photons cross two wireplanes.

Fig 4.26a also shows the contribution from photons which cross the gap more than once. Fig 4.26b shows the number of crossings made per photon. A photon originating in the gap will make an odd number of crossings and a photon from the steel, an even number. Fig 4.26c shows the variation of the mean crossing depth as a function of gap size. As the gaps are widened the photons can penetrate further. The angular distribution (fig 4.27) of wireplane crossing angles is approximately isotropic.

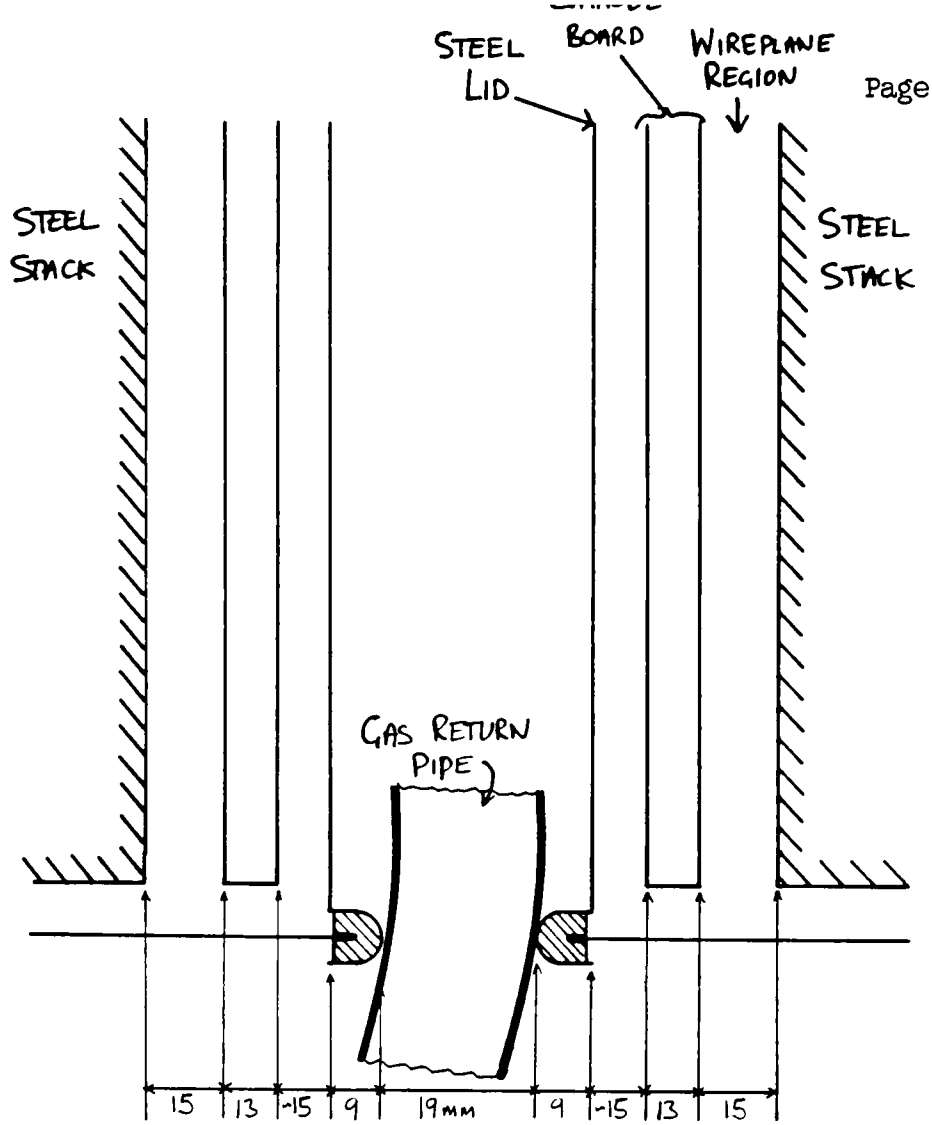

FIG 4.25 DIAGRAM OF GAP BETWEEN MODULES

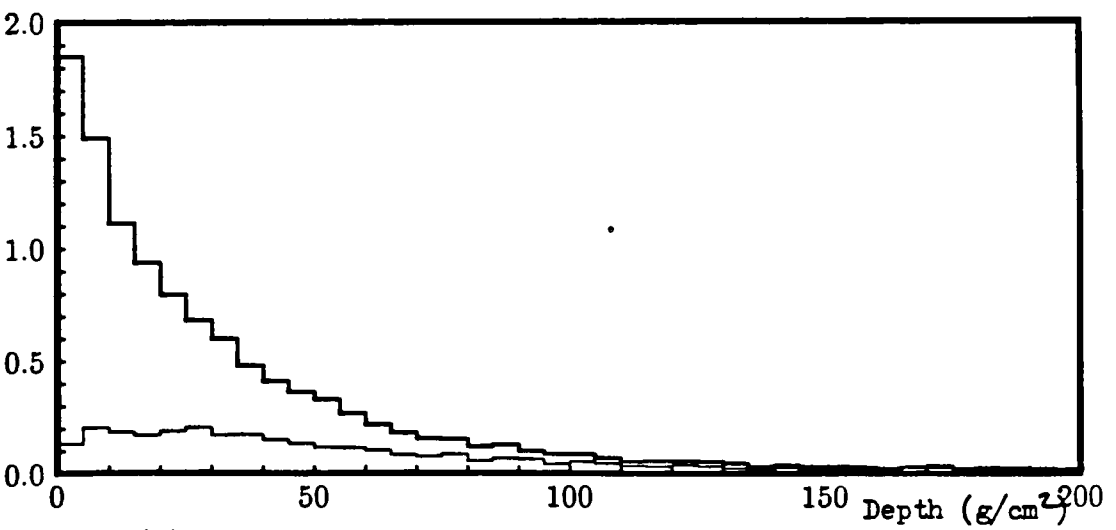

Fig 4.26(a) Photons crossing the gap as a function of depth into the gap. Most of the blobs will be produced near the outsides of the detector. The thin line is for photons which cross the gap more than once (2nd+ crossing only).

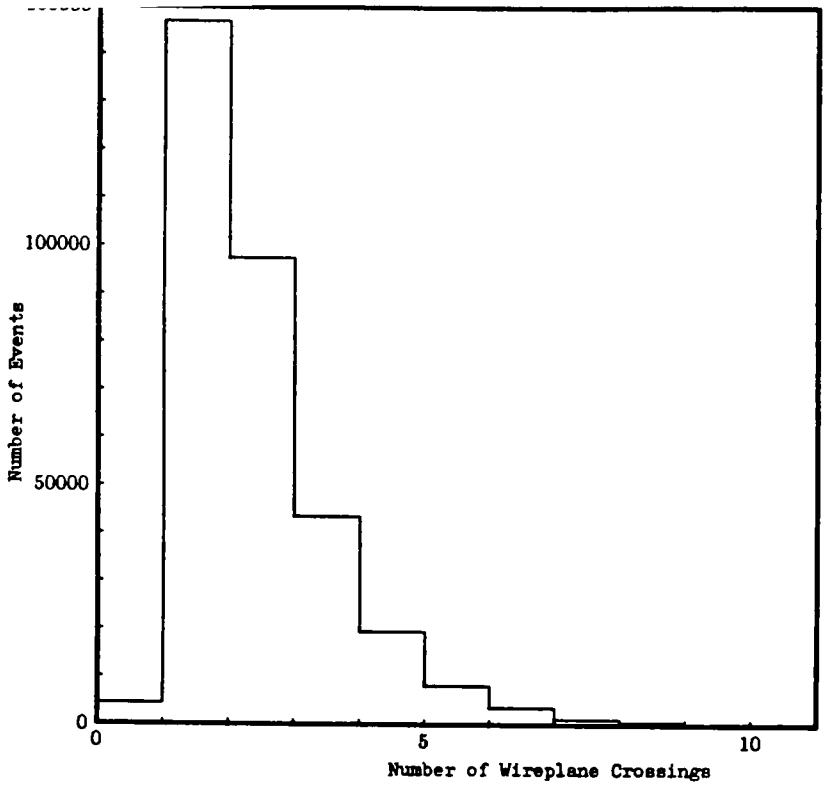

Fig 4.26(b) Distribution of the number of times a photon crosses a wireplane. Photons which start in the detector bulk will cross two wireplanes each time they cross a gap. Photons which start in the bulk will make an even number of crossings, those which start in the gap, an odd number.

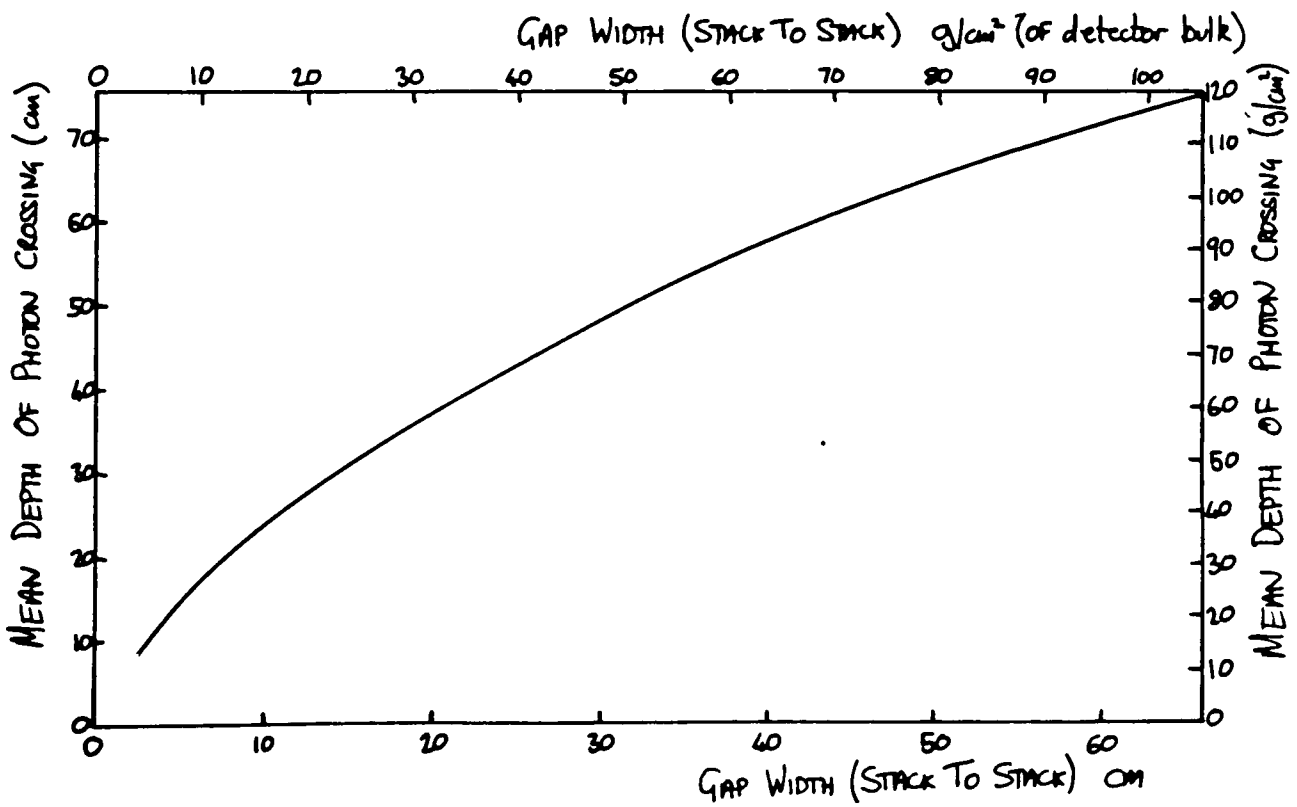

FIG 4.26(c) MEAN PENETRATION OF PHOTONS INTO GAP AS FUNCTION OF THE WIDTH OF THE GAP.

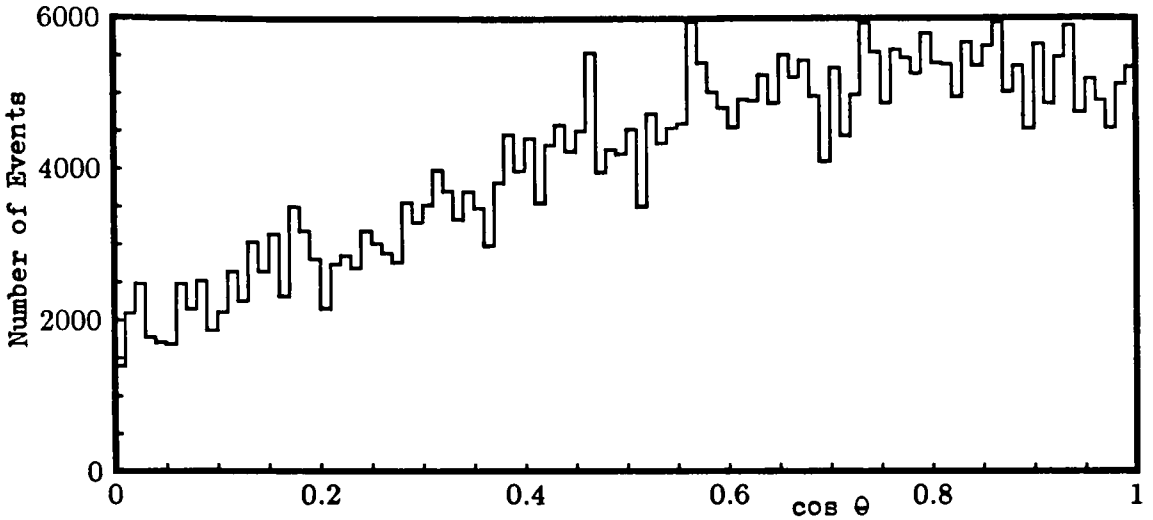

Fig 4.27 Distribution of angles of photons crossing the gap
Cosθ = +1 corresponds to photons crossing perpendicular
to the wireplane.

The Monte-Carlo predicts that the total rate of wireplane electrons may be parameterised as

$$1 \; (\; 3.07 + 0.257 \; w \;)$$

where l (m) is the total length of gap (390 m in the complete detector) and w (cm) is the width of the gap from one stack face to the other. This expression includes both the photons which enter from the steel and from the gap. For the complete detector, assuming w = 13 cm, the rate is 2500 Hz. It does not include the end wireplanes which will contribute a further 3200 Hz to the rate.

Wireplane events have important trigger implications, as they fire many channels at once. This prevents the use of a simple multiplicity trigger scheme. The scheme chosen in chapter 5 must reject these events. The events are characterised by the energy deposited by a single electron in the gas. The range of the electron in gas is ~20 cm. It will cause a large hit on every channel which it passes. These hits all appear at one time.

4.10 Properties Of Photon Induced Electron Events In The Wireplanes

The appearance of Compton Electrons in the wireplanes (nicknamed 'Blobs') has been studied in data from the mine. In order to verify that the data is produced by Compton scattering of photons, a test module at the Rutherford Appleton Laboratory has been exposed to a cobalt-60 source (fig 4.28). Cobalt-60 emits two photon lines at 1.173 and 1.332 MeV which are of similar energy to the photons in the Soudan cavity. The source was contained in a lead pot with 27mm thick sides.

The module, electronics and readout were very similar to the production system in the mine. The system was triggered on a single anode and single cathode signal coincidence with a 2.5 μs gate. The anode/cathode crossing was adjacent to the source. The module was operated with no drift voltage to exclude cosmic rays.

Data runs were taken for a variety of wireplane voltages and also for the system with the source removed. Events were scanned both on line and off line to check the quality of the data. A typical event is shown in fig 4.29. This event is very similar to those seen in the mine (fig 4.1). The primary trigger rates for source on and source off are shown in fig 4.30. When the rates are plotted against gas gain ($\propto e^{V_A}$) (see inset of fig 4.30), a change of slope indicating the appearance of the blobs is seen at around 2000 volts.

The detector is designed to operate at about 2200V. at which point it is sensitive to ionisation which has been produced in a tube and drifted. Compton electrons in the wireplane produce much larger signals. The optimum wireplane voltage to readout blobs is about 200V less than to study signals in the tubes. This agrees with a rough calculation which indicates that a blob has approximately four times as much pulse height as a tube hit. When the detector is run at an appropriate voltage to readout signals from the tubes, blobs appear as large signals which saturate and promote pathological behaviour in the

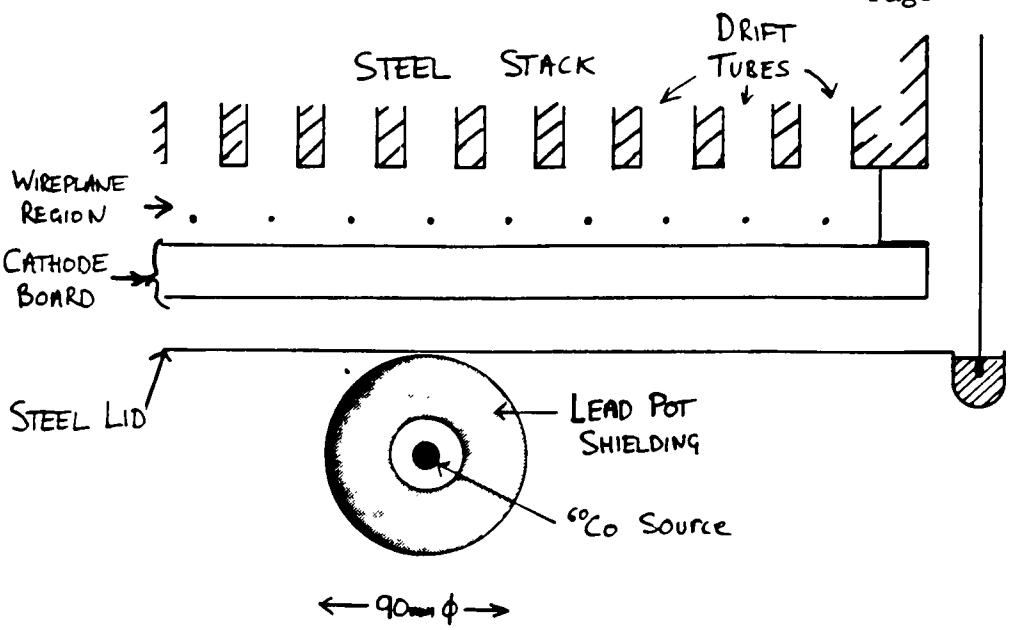

Fig 4.28 Detail of RAL Test Setup

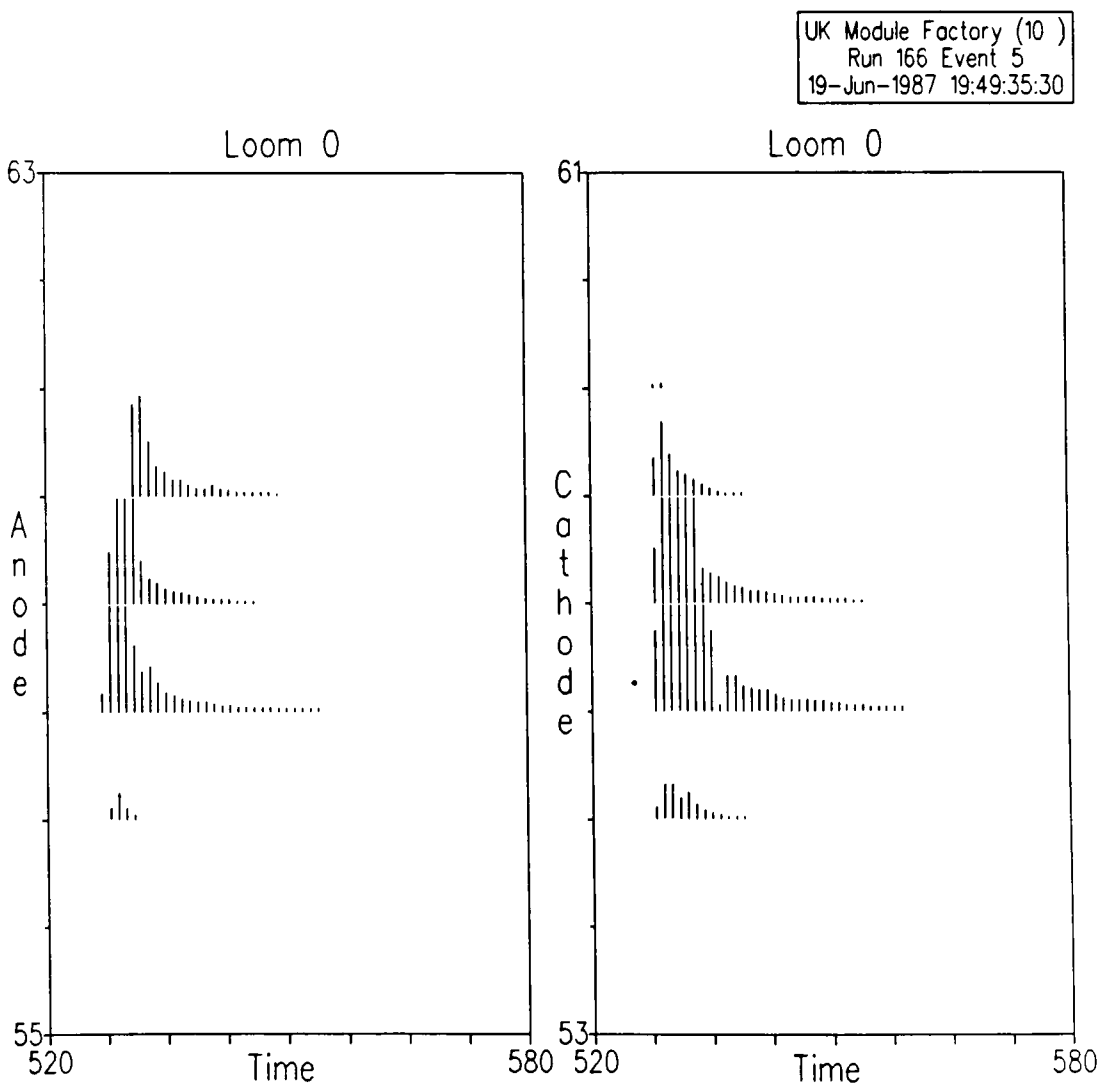

Fig 4.29 "Blob Event" produced at the Rutherford Laboratory in a test module with a Cobalt-60 source.

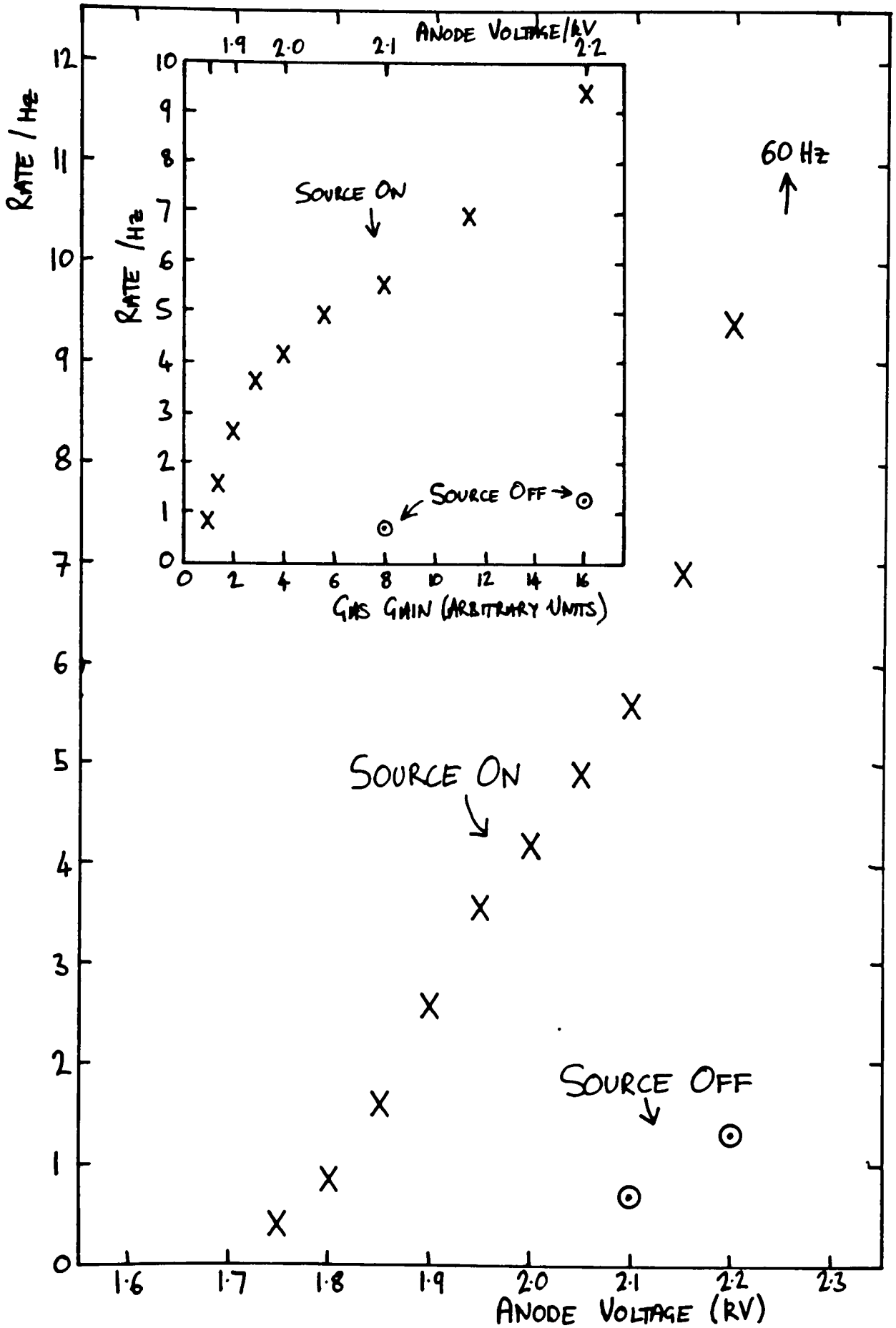

FIG 4.30 PRIMARY RATES ON TEST STAND

electronics. The problems encountered with blob signals which are of concern for the trigger design are

(1) Pulses are much longer than those which have drifted.

(2) Large pulses cause crosstalk on neighbouring channels.

(3) Some of the saturating pulses cause an electronic 'bounce' which appears as two separate pulses at the trigger logic and in the data (see fig 4.31).

Figs 4.32 and 4.33 show total and individual pulse height distributions. It may be possible to use blobs to calibrate wireplane gain in different regions of the detector from these distributions.

4.11 Summary

The different types of event expected in the Soudan experiment have been described. A detailed study of radioactive events has been conducted. The events are produced from gamma emissions of potassium-40 and members of the natural decay chains. These then enter the detector and produce Compton electrons in the tubes or wireplane regions. The expected rates of these two types of signals have been computed. Singles (wireplane events) are expected at a rate of 164 (2.5) kHz in the full detector. The features of the wireplane events have been studied by using a Cobalt-60 source on a single module at RAL. The events are found to have the same appearance as those in the mine. The pulses are very large compared to those which have drifted from the tubes.

References for Chapter 4

[1] See for example M. L. Marshak et al. Phys Rev Lett 54 (1985) 2079 and Phys Rev Lett 55 (1985) 1965

[2] Particle Data Book, Phys Lett 170B (1986)

[3] A. Heydemann "Handbook of Geochemistry" 1 385 (Springer-Verlag)

[4] K. Ruddick Soudan Collaboration Internal PDK notes 114 and 194

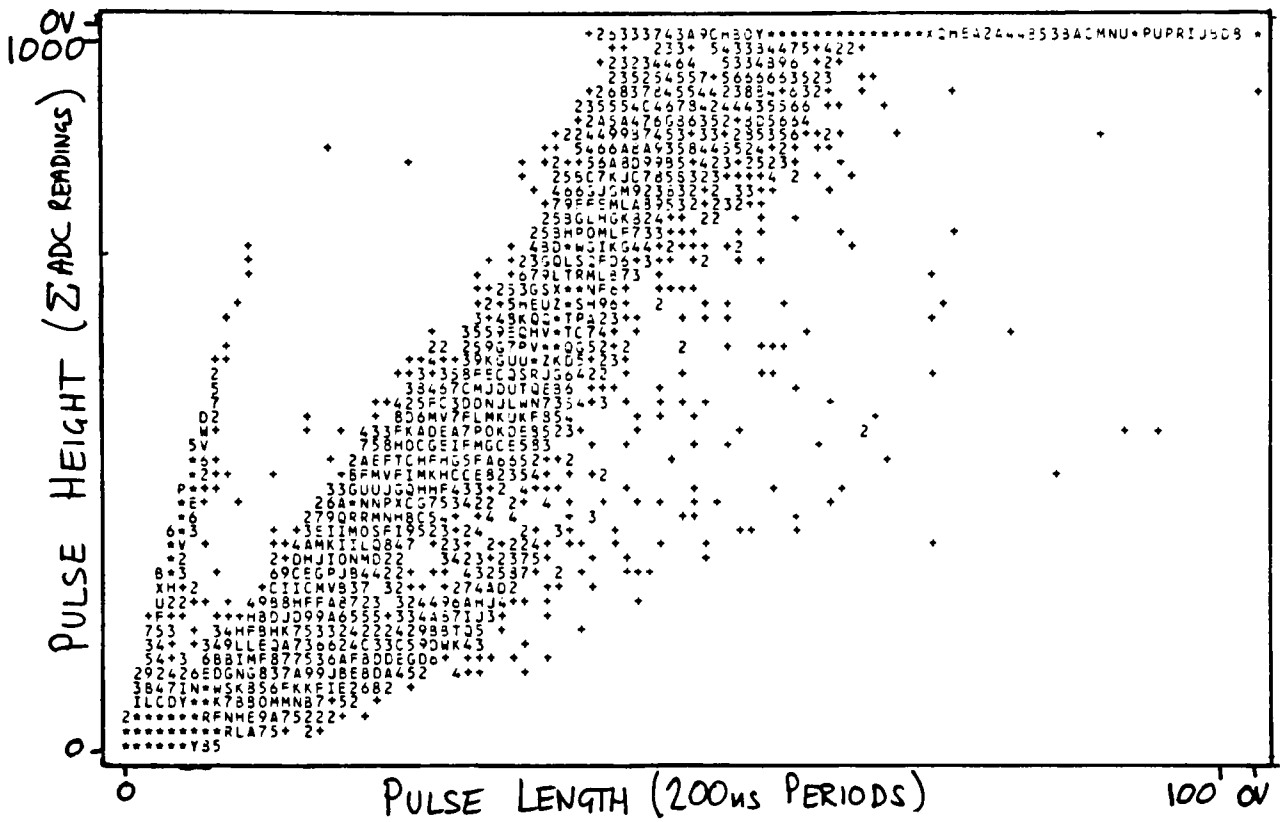

Fig 4.31(a) Pulse Height vs Pulse Lengthplot for a blob sample at 2200V anode voltage.
Scale : .+23456789ABCDEFGHIJKLMNOPQRSTUVWXYZ*

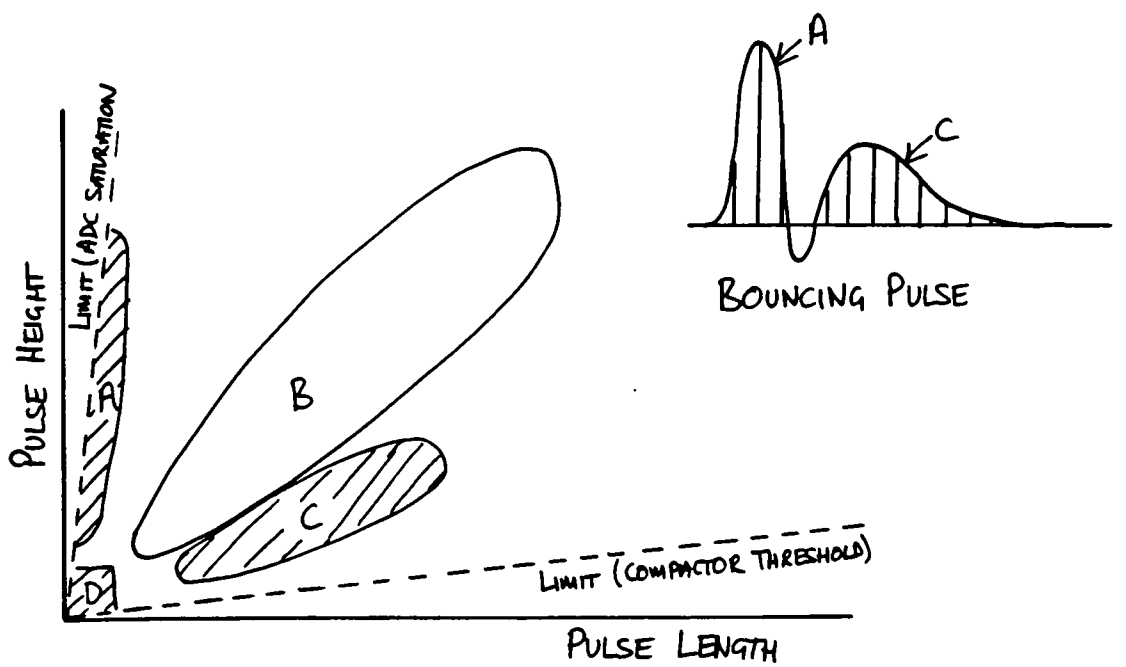

Fig 4.31(b) Anatomy of a Pulse Height vs Pulse Length Plot.
Region A: 1st part of a bouncing double-pulse
B: Normal Pulse
C: Tail part of a bouncing double-pulse
D: Crosstalk

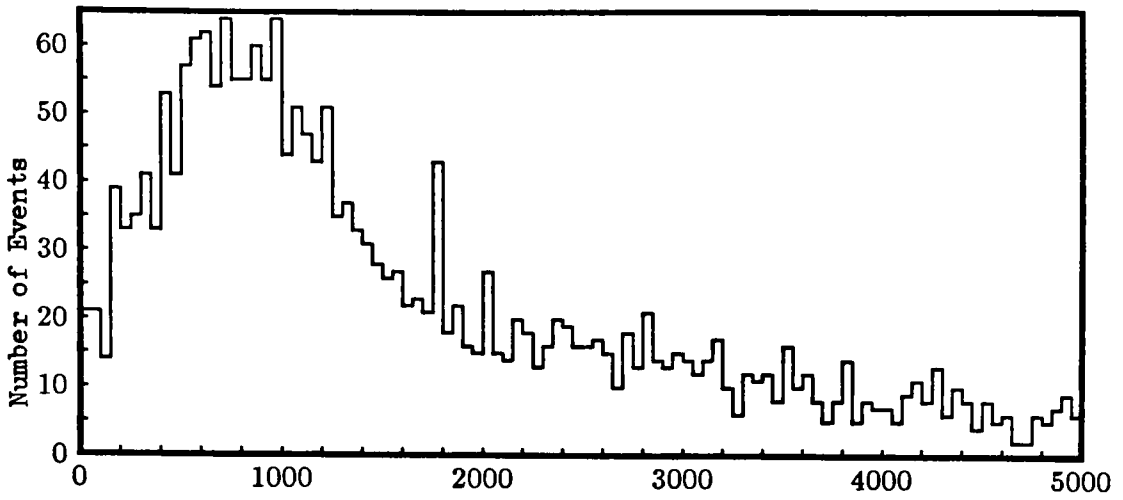

Fig 4.32 Total pulse height in blob distribution.

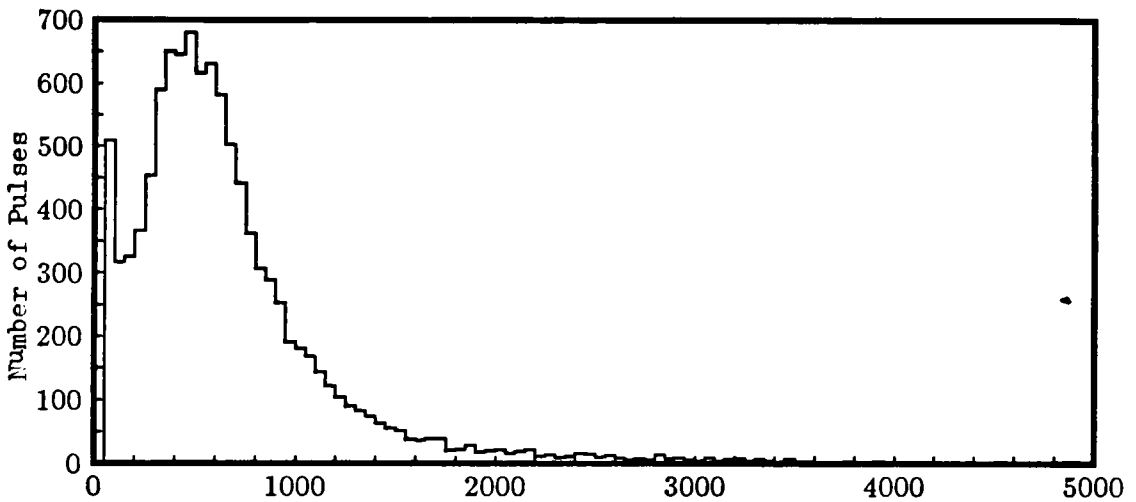

Fig 4.33 Pulse height of individual pulses in event.

[5] N. G. Gusev and P. P. Dmitriev "Quantum Radiation of Radioactive Nucleides" (1976) English Trans. (1979) Pergammon
E. Browne and R Firestone "Table of Radioactive Isotopes" (1986) Wiley

[6] E. Storm and H. I. Israel Nucl. Data Tables 7 (1970) 565

[7] Hubbel, Gimm and Overbro J. Phys. Chem. Ref. Data 9 (1980) 1023
EGS4 Manual Chapter 2 SLAC red report 286

[8] G. W. Kaye and T. H. Laby "Tables of Physical and Chemical Constants" Longman 14th ed. (1973)
F. Sauli CERN report 77-09

[9] Soudan Collaboration Internal PDK note 247

[10] Hubbel and Overbro J. Phys. Chem. Ref. Data 8 (1979) 69

[11] K. H. Weber Nucl. Instr. Meth. 25 (1964) 261

Chapter 5

TRIGGERING

This chapter discusses a comprehensive study I have made on the Soudan 2 main detector triggering system. I have designed an upgrade to the system which achieves the required rejection of both types of radioactive induced events (chapter 4) while preserving a high trigger efficiency for even the hardest modes of proton decay. The scope of the upgrade has been limited since it has been done in the context of electronic circuit boards designed to hold an entirely different set of circuitry. I believe that the design which has been achieved extracts the full potential of the decision making principle despite this limitation. The principle is the best which has been devised up to now.

5.1 Introduction

The Soudan 2 detector will emit some 180 Gigabits of information each second. Quite clearly it will not be possible for a physicist to sort through all this data. In most cases the data will contain zeros indicating that nothing is happening. A small portion of the data will contain pulses. A very tiny fraction of the information will be useful physics. Fig 5.1 shows on a logarithmic scale the expected rates at which these processes will occur. Seven orders of magnitude of automated data reduction are required before the data can be looked at manually.

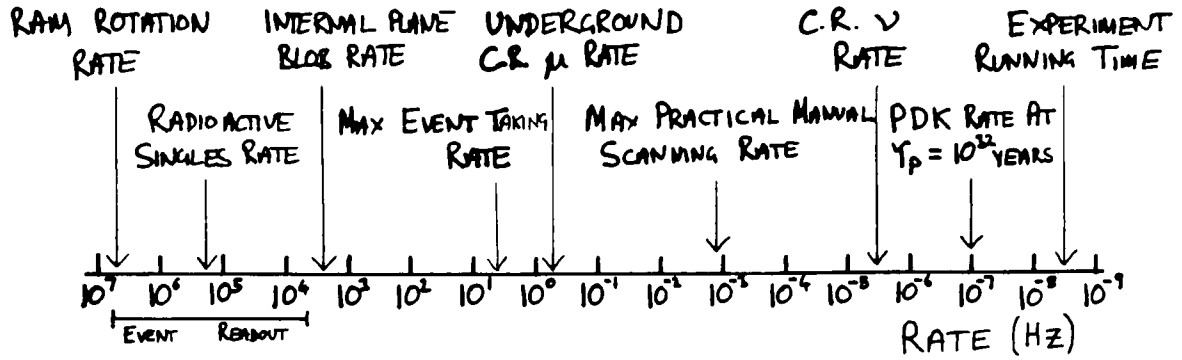

Fig 5.1 Time Scale of processes in the Soudan Experiment.

This data reduction is made in two distinct steps.

(1) Triggering : Hardware electronic circuitry monitors the signals from the detector and indicates by issuing a 'trigger' when it sees something interesting appearing on the signal lines. The data around the time of the trigger is issued is stored on the computer. Data when there is no trigger will be discarded.

(2) Filtering : The data on the computer is read from file and interpreted by a program. The program decides whether the event is 'interesting' or not.

The key in both of these steps is to design the correct decision making algorithms which achieve the required data reduction level while not removing real events. The baby must not be thrown out with the bathwater.

In the filtering step, the original data which was collected will be stored and may be re-filtered should a different algorithm be found. There is no such backup for the trigger step. If the circuitry fails to decide to read out a particular event, the event is forever lost. The triggering policy of the Soudan 2 experiment is to collect data on muons and contained events, but to reject radioactive events, which occur at too high a rate to store.

5.2 Desirable Triggering Properties

Although any triggering algorithm which selects real events and removes background is desirable, there are some general properties which quickly distinguish 'good' triggers from 'bad' ones. In some experiments, the signal events are so prolific that the trigger can be designed to throw out all but say 20% of real events in order to achieve a low background rate. In a proton decay experiment, the events are so rare that very few can be lost. A 10% loss in triggering efficiency is equivalent to a 10% detector dead time, a 10% detector downtime or a detector with 10% less modules. The following are desirable general properties of a trigger decision algorithm.

(1) The algorithm must be simple in order that it be fully understood by all who use or interpret data from the experiment.

(2) If a given arrangement of pulses produce a trigger, the addition of more pulses must still produce a successful trigger. This means that no component in the trigger should have power of veto. A problem which arises if the trigger does have a veto component is that spurious hits can activate the veto and disable triggering. It is very hard to enumerate how often this will happen without a clear understanding of the noise events (throughout the entire running time of the experiment), since the noise which is causing the vetoing will not appear on the data which is read in.

(3) The trigger should have some resilience to detector malfunction and it must be possible to disable the components of the trigger which service a malfunctioning part of the experiment in order to minimise the time the whole detector is down.

5.3 The Edges Trigger

The problem in the trigger design is working out how to reject blobs, since they each produce a comparable number of hits to a small proton decay event. Fig 5.2a shows (a) the signals received from a blob and from a track segment on a local group of wires. The picture may be simplified by considering only the start of each pulse (b). The feature which distinguishes blobs from other events is that the pulses

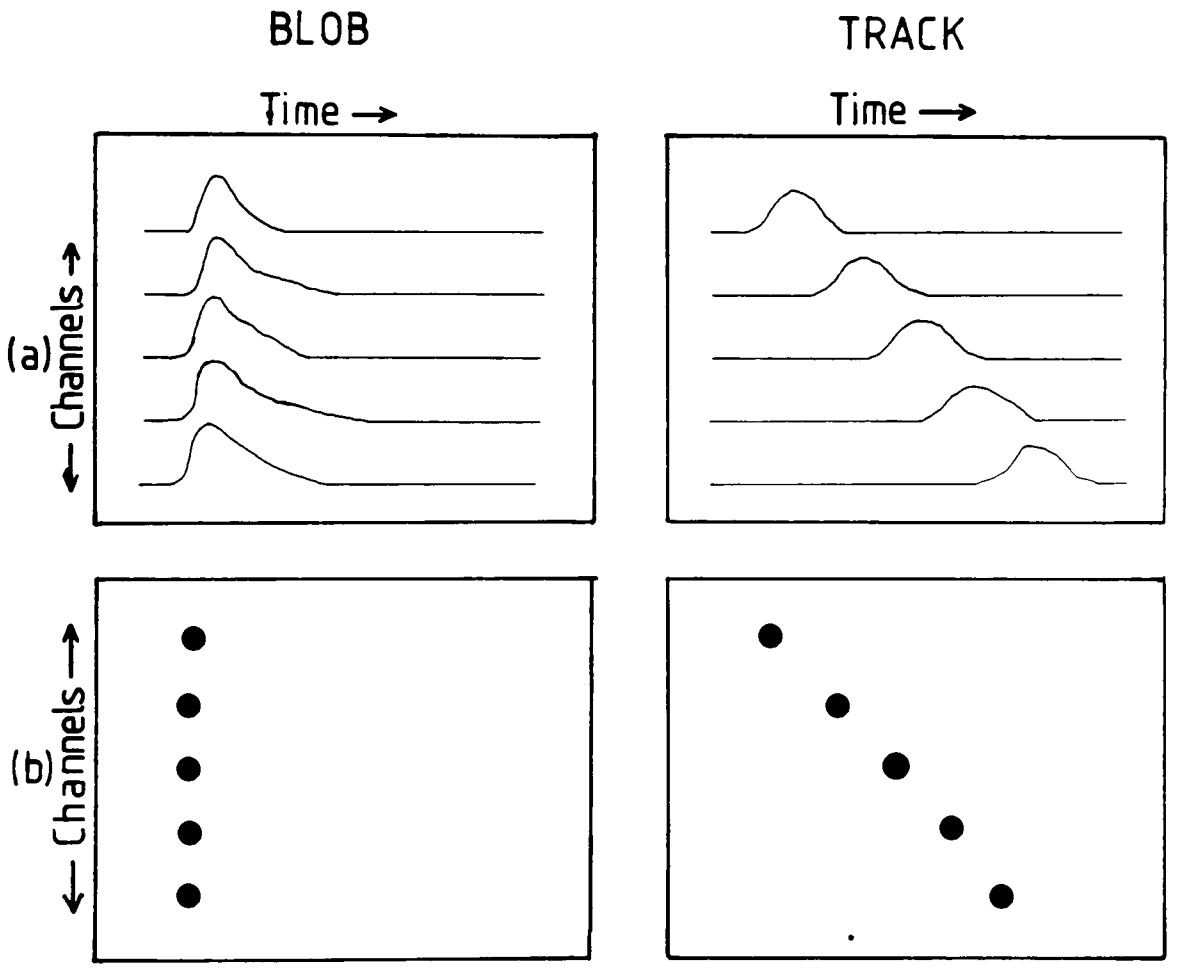

FIG 5.2a

all start at the same time whereas, in general, a track produces hits which start at different times.

If the data from an event were presented all at once (on a two

dimensional grid as in the pictures of fig 5.2a), the logic required to distinguish tracks and blobs would be complex. However, the data is presented in one dimension as a function of time as the event drifts in. The data may be processed in a pipeline fashion which makes the logic very much simpler.

The principle of the trigger is to detect when each channel goes above threshold (an edge) and to trigger if enough edges are seen in a local group of channels. The edges are counted over the time taken for pulses to drift the full length of a tube. The trigger logic is clocked (at 600ns) and a maximum of one edge is counted for each clock period.

The feature of allowing only a maximum of one edge per clock period effectively prevents blobs from producing a large number of edges. As is seen on the pictures at the start of chapter 4, the blob hits all arrive at once, the pulses have fast risetimes which ensure that they all reach the threshold immediately, the edges all appear within one or two clock periods and contribute little to the total count.

The pulses from a track are generated in different tubes. Particle tracks normally travel at some angle to the tubes and scattering in the iron cause the direction to change. The pulses diffuse as they drift to the wireplane. The pulses mainly appear at the wireplane at different times and generate separate edge pulses.

If two pulses appear on the same wire from two tracks, both pulses generate edges which increment the trigger count, provided the channel has gone below threshold between the pulses. A sample arrangment of pulses and the edges produced are shown in fig 5.2b.

In practice, the edges are totalled into a rolling accumulator, ie each edge increments the counter. After one drift time, the pulse 'expires' and the edge is removed from the total. Each clock period, the total is tested to see if enough edges are present to trigger

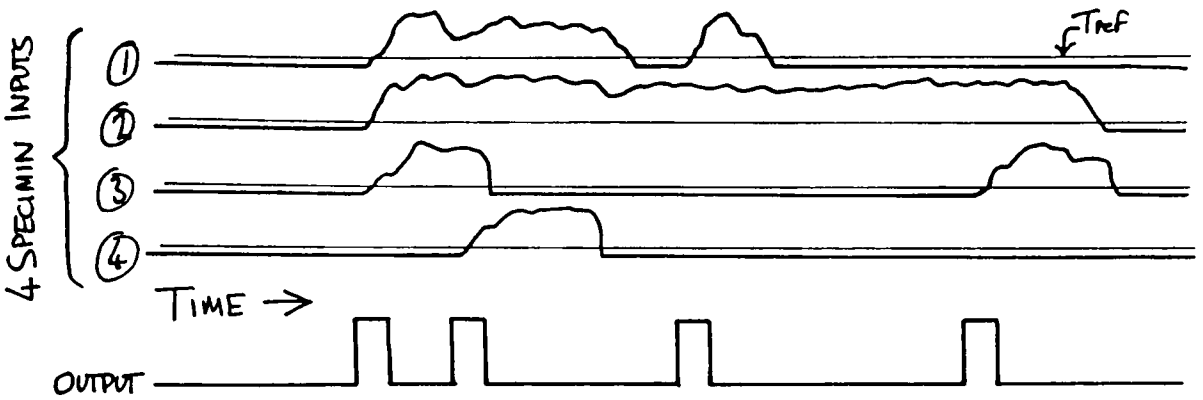

Fig 5.2b Principle of operation of 'edge' trigger.

5.4 Details of Implementation

In this section, I will give details of how the edges trigger is implemented in practice. The circuitry is duplicated for each group of channels on which the trigger decision is made. There are two different methods of implementation depending on whether the trigger acts on all the channels in each crate as one group or whether the implementation is at a more local level (16 or 32 channels per group). Both methods will be described.

As a background to understanding the edges trigger circuitry, I will first describe the architecture of the trigger sections of the multibus crates. The principle concern here is how the signals from local sections of the detector are combined to make a single decision and the conditioning of the signals at each stage.

The signals on the input to the flash ADC (see fig 3.7) are compared with a preset voltage Tref (Fig 5.3a). The discriminator output is conditioned in a PDK1000 gate array.

(1) A live channel register is used to disable oscillating, or noisy

channels from the trigger.

(2) An active channel latch records any activity on the channel. During compaction, only channels which have their active channel latches set are read out. The latch is used to reduce the dead time associated with reading out all the channels.

(3) A pulse stretcher (CAT latch). The output remains active for a preset countdown period after the input goes inactive. The countdown is retriggerable by a second pulse.

The stretched outputs from all 16 channels on a card are fed into both a PDK2000 and a PDK3000 gate array. The gate arrays have control lines from the microprocessor so that internal registers can be programmed. The PDK2000 has three output lines (TRA - TRC). The PDK3000 has four output lines (TRD - TRG). The PDK2000 also has a group of four lines which communicate with the PDK2000 in the nearest neighbour card in the multibus crate. The seven lines TRA through TRG are wire ORed on the backplane over all the cards in the crate. The circuitry in each gate array generates trigger requests on these lines when it detects the correct pattern of pulses on its input lines. The PDK2000 is used to house part of the edge trigger circuitry as described later.

The seven wire-OR lines on the crate backplane are read by a driver card and sent along a trigger bus to the trigger crate (fig 5.3b). One trigger crate controls the entire experiment. It ORs the signals from all the data crates in the experiment into two bundles of request lines, one bundle for anodes, the other for cathodes (fig 5.3c). The seven lines in each bundle are used to form a 14-bit memory address. Each location in the memory is programmed from the microprocessor in the trigger crate. If a '1' is programmed in the address corresponding to the 14 trigger lines, an experiment wide trigger is generated and the readout sequence described in chapter 3 starts. By programming the appropriate bits in the RAM, any combination of AND/OR logic functions of the anode and cathode lines may be selected.

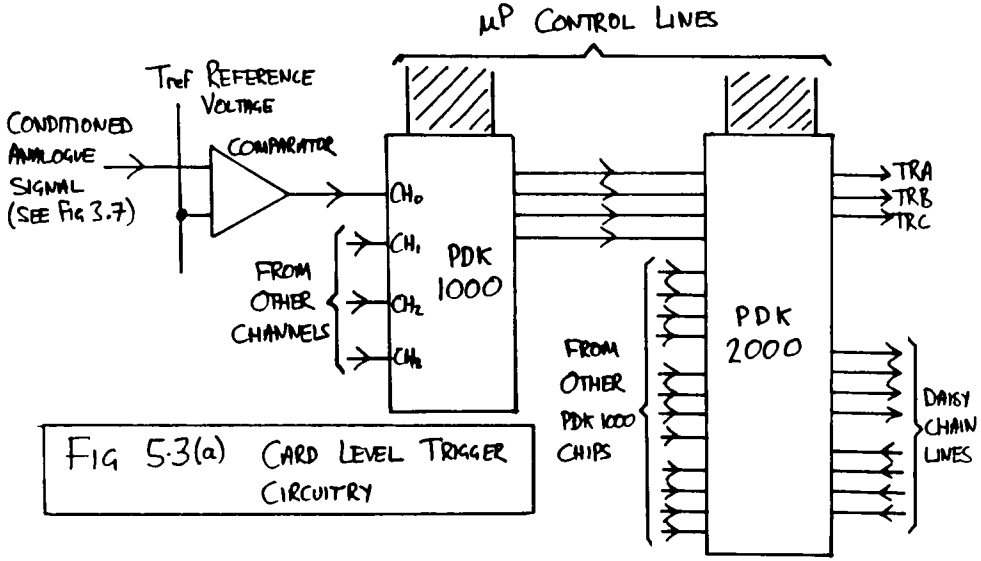

FIG 5·3(a) CARD LEVEL TRIGGER CIRCUITRY

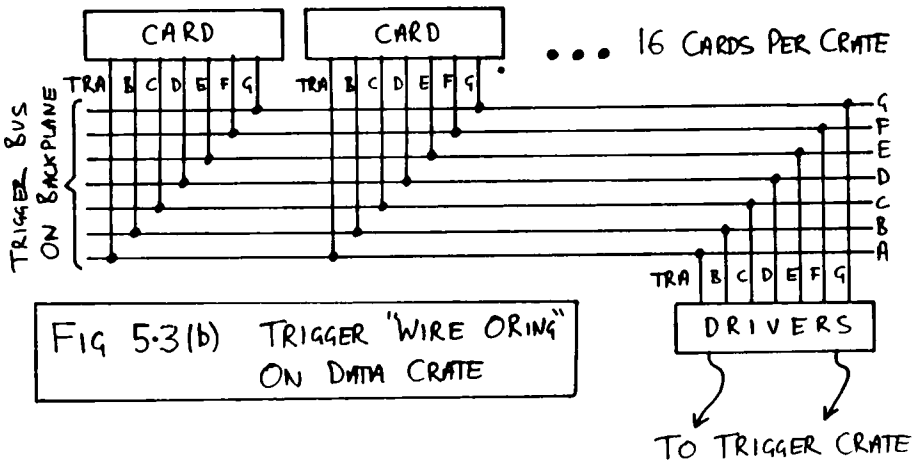

FIG 5·3(b) TRIGGER "WIRE ORING" ON DATA CRATE

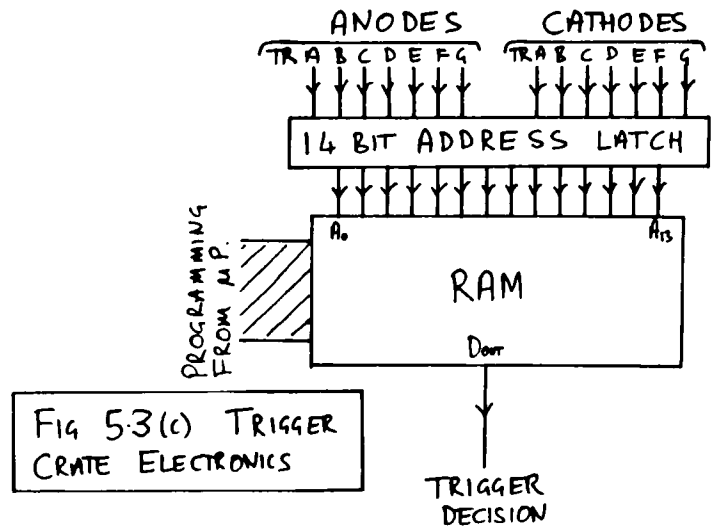

FIG 5·3(c) TRIGGER CRATE ELECTRONICS

Provision has been made for a second level trigger in the early stages of the readout sequence. The microprocessors have access to the active channel latches from the PDK1000s. If the 8086 software so decides, the second level trigger can issue a global abort signal which will stop the readout sequence and restart data taking.

The circuitry required for the edges trigger is housed in the PDK2000 gate array. Fig 5.4 shows the circuitry required to generate the edges and count the edges. At each clock period, each channel is compared with its state in the previous clock period (fig 5.4a). If a rising edge is seen, an output is asserted for the duration of the clock period. The outputs from all the circuits in the group are ORed together onto a single line (A). Whenever line A is high, an edge has been detected on one or more channels in the group. The pulses on line A are now counted using the circuit in fig 5.4b. The circuit contains a clocked FIFO (shift register) which stores the most recent values of line A. The FIFO is deep enough to cover the full drift time. A counter keeps track of the number of '1's in the FIFO. The counter is incremented whenever an edge signal goes into the FIFO and decremented when one comes out of the other end. The circuit must be initialised so that the FIFO is all clear and the counter reads zero after each trigger. The timing diagrams for this circuitry is shown in fig 5.5.

In most of the grouping schemes, all this circuitry is housed in the PDK2000 gate array. The lines which communicate with the neighbouring chips are used to overlap the groups. The particular grouping schemes under consideration will be studied later. If the trigger is implemented on a crate basis, the circuit on each card need only provide the function of fig 5.4a. The line A signal is fed out through one of the trigger lines (which will not be used for triggering) where it is wire ORed with the signals from the other cards in the crate. A new card in the crate contains the circuit of fig 5.4b and generates the trigger request. This scheme is now being implemented.

FIG 5·4 EDGE TRIGGER CIRCUITRY

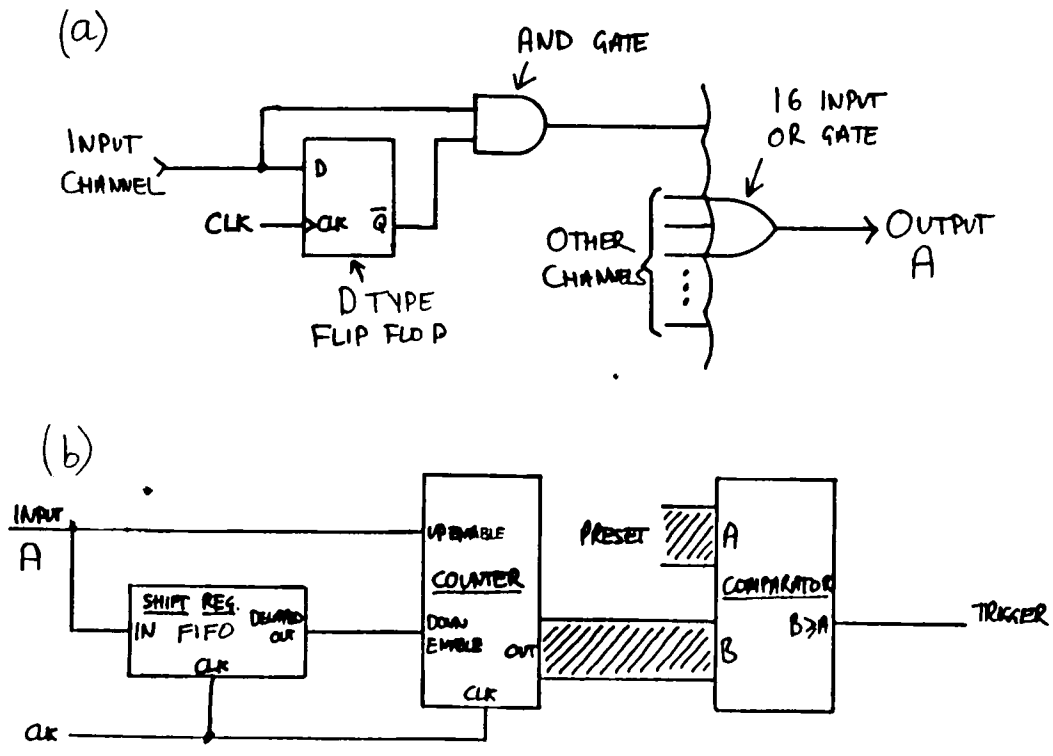

(a) TIMING DIAGRAM FOR FIG 5·4 a

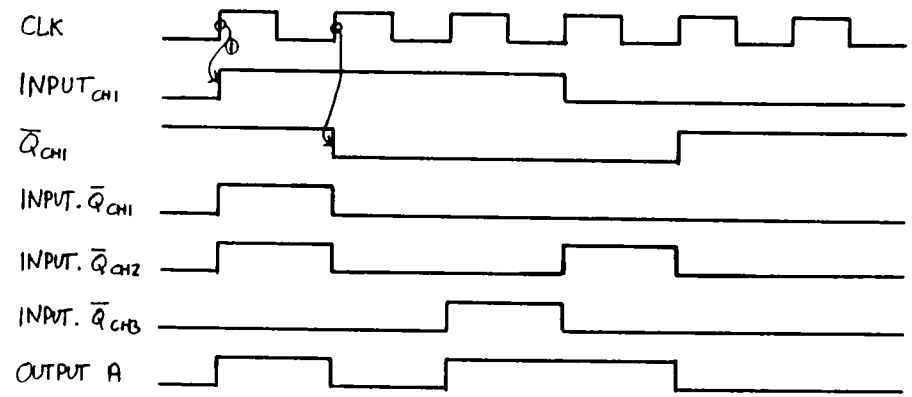

① SYNCHRONISED WITH CLK IN PDK 1000.

(b) TIMING DIAGRAM FOR FIG 5·4 b

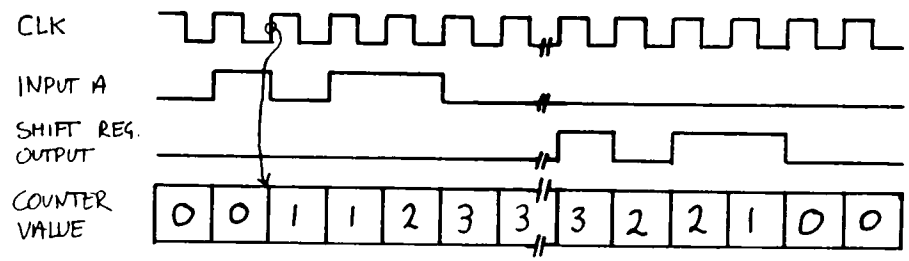

FIG 5·5 TIMING DIAGRAMS

5.5 Trigger Response to Radioactive and Noise Events

There are several parameters which may be changed on the trigger system to tune for maximum proton decay efficiency for a given maximum noise trigger rate. The effects of these parameters on noise and on monte-carlo proton decay events have been studied.

The method chosen for studying radioactive events was to use a file of blob events from the mine. The best sample avaliable is a tape which I took on a single test module. The module was not shielded. The measured rates have been compared with my calculation in chapter 4 and are in good agreement. The advantages of this method are that the single exposed module counts at a higher rate than a card level implemented group in the full detector (table 5.1). The events on the

	Singles Rate	Blob Rate
Plane on test module	2.4 kHz	100 Hz
Crate in full detector *	17 kHz	310 Hz
Card in full detector (16)*	680 Hz	12 Hz
Card in full detector (32)*	1.3kHz	24 Hz

* Ends excluded from multiplexing

Table 5.1 Predicted and measured rates for different connection schemes

tape contain about the same amount of (or perhaps slightly more) multiple coincidence events than will be seen in the full detector.

The data on the tape was taken with a PDK2000 circuit which generated a trigger if four or more anode channels appear within a 20 μs gate. The first 100 events from the tape were scanned to verify that the sample consisted of blobs. Of the 100 triggers, 98 were blobs, 1 was an event in which all the channels fired in time (electronic pickup). The other event contained electronic noise which can be fixed (there are a

large number of electronics channels and debugging is a major but convergent operation). During the scanning, the number of single hits within a 50μs window after the trigger were counted. The probability of an event containing an extra hit is 0.3/event. There were 5218 events on the tape.

A program was developed which read the data from the tape and simulated the hardware as described. It computed the maximum number of edges produced in the event for a given set of trigger parameters. The reduction factor of blob events as a function of number of edges is shown in fig 5.6. In order to achieve an overall trigger rate of less than 3 Hz, the 2500 Hz blob rate in the complete detector (for disconnected ends - see chapter 4) must be reduced by three orders of magnitude. With the CAT latches disabled (CAT=0) the trigger will provide the required reduction factor at #edges=12.

This operation can be improved by increasing the CAT time. The effect of this is that if there are two pulses on one channel, the second will only register a new edge if the gap between the two pulses is bigger than CAT. It was shown in the last chapter that if the detector gas gain is set to record pulses from the tubes, blobs produce very large pulses in the wireplane region. When these pulses saturate the electronics, they occasionally cause bounces in the signals. The CAT time can be set to smooth out these bounces. In practice, CAT can only be set in increments of 2μs. With CAT=2μs, the three orders of magnitude reduction is achieved at #edges=7 (fig 5.6). The 44 events which had 5 or more edges at CAT=2μs were scanned and classified according to whether they were caused by a correctable pathology in the electronics or a multiple coincidence of scatters and hits associated with the blob.

Pickup (all channels fire at once)			6
Noisy electronics channel			18
Blobs/RA coincs.	# edges = 5	19	20
	# edges = 6	1	
	# edges = 7+	0	

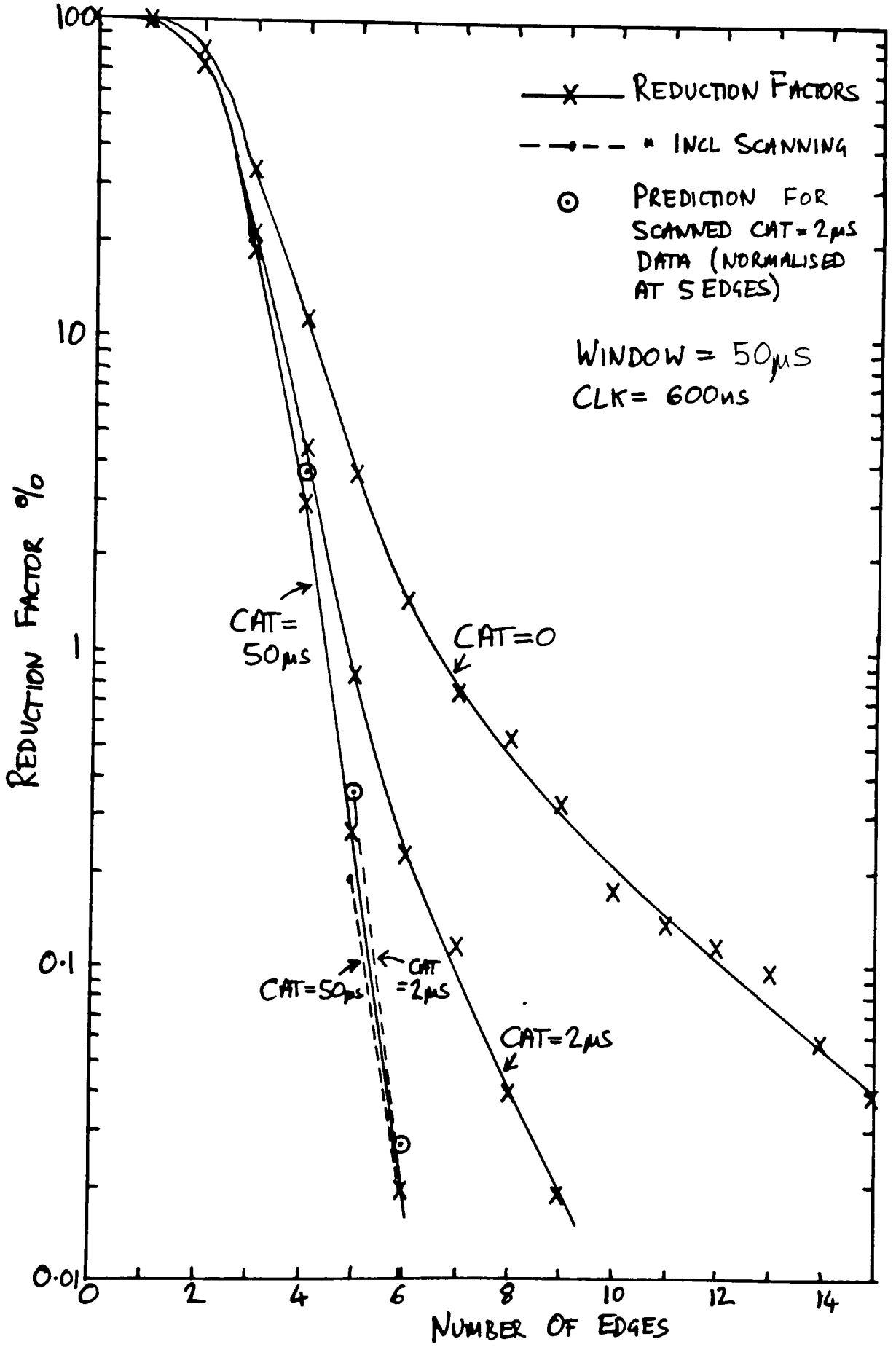

Fig 5.6 Edge Trigger performance on blob data from the tape.

The dashed line on the plot shows the curve for CAT=2μs assuming that the above 24 pathological events can be prevented. In this case #edges=6 will easily achieve the desired reduction factor. Lines for CAT = 50μs are included with and without scanning. Little further reduction is gained at this setting.

A prediction of the slope of the curve in fig 5.6 may be made by assuming that each event consists of a blob which contributed 2 edges and that the rest of the edges are generated from hits at the rate 0.3/event. The curve was normalised to the data at #edges=5. The predicted curve is consistent with the corrected reduction factors when the noise events are removed from the sample.

In summary, the full detector may be run with this trigger with #edges=6, CAT=2μs. The events which limit this setting are consistent with random coincidences and blob associated hits (at 0.3/event) in the single module. It may be possible to reduce the threshold to #edges=5 by segmenting the channels into smaller groups, but this will depend on the final noise level in the detector.

5.6 Trigger Response to Monte Carlo Proton Decay Events

The Soudan 2 detector Monte-Carlo has been used to generate events of the decay modes $p \rightarrow e^+\pi^o$, $p \rightarrow K^+\nu$ and $p \rightarrow K^o\mu^+$. The Monte Carlo generates the decay from a Fermi momentum smeared nucleon in an iron nucleus and tracks the products through the detector geometry as described in chapter 3. K^o particles are not tracked in the current version of the Monte Carlo, so the simulation of $p \rightarrow K^o\mu^+$ contains only hits from the muon. The ionisation from each tube crossing is drifted to the end of the tube and digitised at the appropriate rate. Diffusion and oxygen loss are included.

When the events are processed by the trigger simulation program, the efficiency curves shown in fig 5.7 are obtained. Fig 5.7a

corresponds to CAT=0 and Fig 5.7b to CAT=2μs. There is little difference in the change in CAT although increasing CAT decreases the efficiency, since it removes some of the pulses which appear close together on one channel. The efficiency corresponding to #edges=6, CAT=2μs is 81% for $p \rightarrow K^+\nu$ which represents the most difficult modes to trigger on. The efficiency for the other two modes is greater than 99%.

The consequences of increasing CAT are slight, for proton decay, most pulses appear on separate channels. However there is one problem with large CAT times. If a track crosses a wireplane, the ionisation in the wireplane region will be large (like a blob) and may cause crosstalk along several neighbouring channels. This effect has been seen in through going muon data on the surface. The crosstalk is in time with the main hits and does not generate extra edges. However, if CAT is set long, it prevents other real pulses which appear later on the channel from producing edges. The study of the file from the mine indicates that CAT can be set to its smallest non-zero value to remove electronic pathologies and that higher values are not necessary. Note that with a long CAT time, the trigger has the vetoing property (see section 5.2) which is to be avoided.

The effects of modifying other parameters have been explored. The other parameters have obvious settings which have been used in the above discussion. The changes to the parameters are predictable.

(1) Width of window. The effects of changing the time over which the edges are counted are shown in figure 5.8. $p \rightarrow e^+\pi^0$ and $p \rightarrow K^0\mu^+$ are most efficient when the full drift distance is used. $p \rightarrow K^+\nu$ reaches the maximum efficiency at about 80% of the total drift distance. Increasing the window width will increase the rate of coincident noise (randoms) in proportion to the width of the window. The window width should be set to correspond to the maximum drift distance. The hardware must accommodate different widths to allow for possible changes in drift velocity.

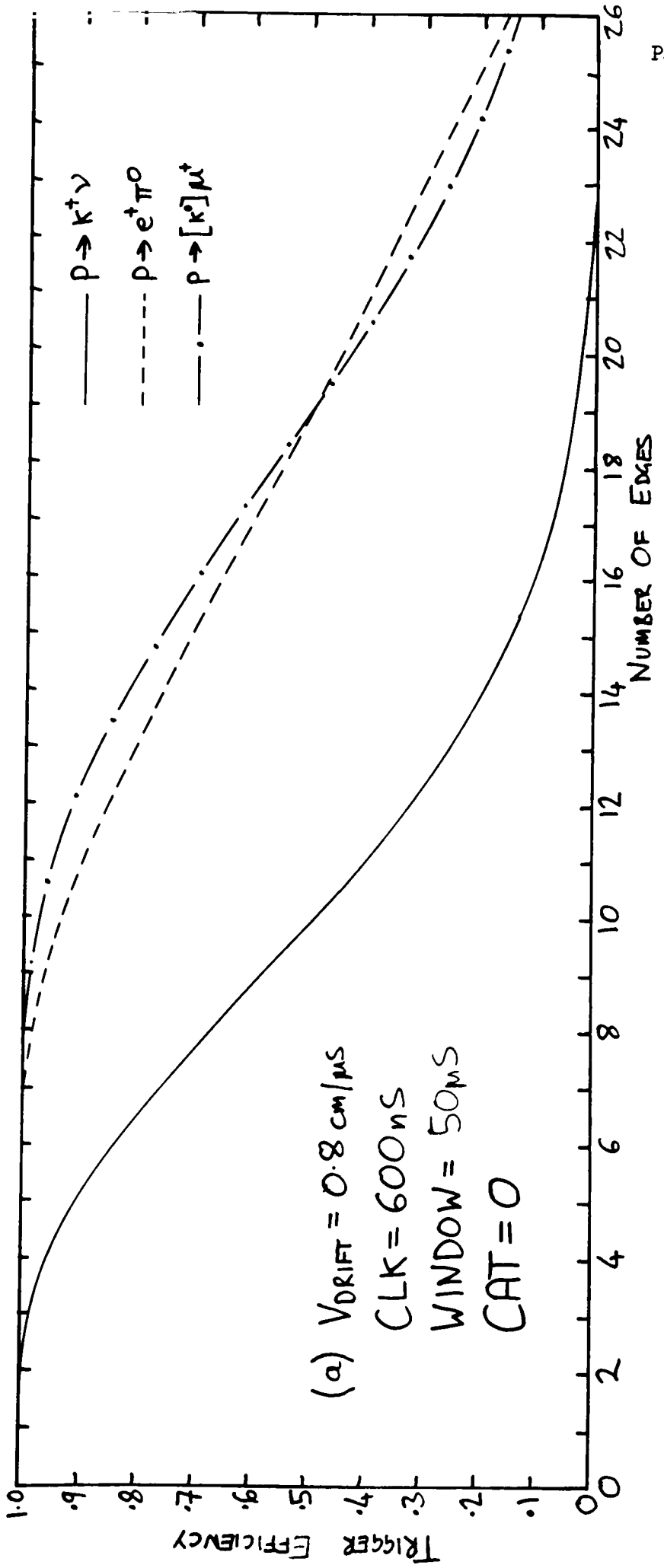

Fig 5.7(a) Trigger efficiencies for proton decay events

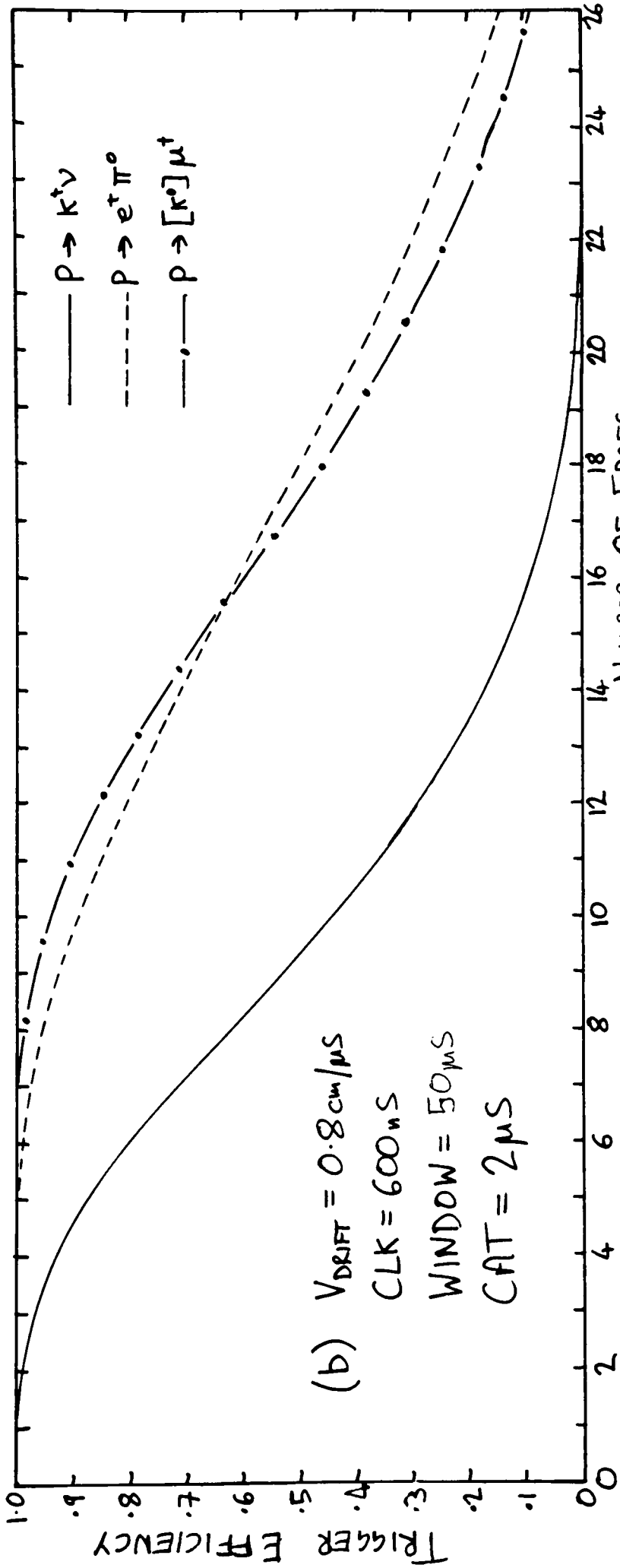

Fig 5.7(b) Trigger efficiencies for proton decay events

(2) Clock. The clock speed in the gate arrays is set to 600ns, pulses arriving on different channels will be counted as a single edge if they arrive within one clock period. Fig 5.9a shows the effect of changing this for the blob data. The change in slope at 600ns is caused by the characteristic spread of pulses from blobs. This was seen in the scanning. Fig 5.9b shows the effect of changing the clock period on the proton decay events. There is little detrimental effect in choosing 600ns.

(3) Channel grouping. The locality of summing of the edges may be chosen as discussed earlier. The only practical arrangements to consider are the following.

1. Crate level - 256 channels
2. Card level - 16 channels (16)
3. Card level, rolling - Each card contains two sets of circuitry, one for the 16 channels on the card, the other for 8 channels on the card and 8 from the neighbouring card (see inset of fig 5.10) (16R).
4. Card level 32 channels rolling. Each card contains one set of circuitry which counts on the 16 channels on the card and the 16 channels on the neighbouring card (32R).

Software simulation of these possibilities and also intermediate values are shown in fig 5.10 for the mode $p \rightarrow K^{+}\nu$. Rolling increases the efficiency, since it is unlikely that an event will be split between groups. The efficiency only falls off below groups of 16, so either 16R or 32R are good for proton decay. 16R will be less likely to contain random coincidences than 32R or crate level, so it will be possible to lower the number of edges threshold. Scanning the 20 events with five or more edges at CAT=2μs which were seen to be non-pathological electronics, only 5 of the events would have generated #edges=5 at 16R and 16 at 32R. Better statistics are needed to accurately survey this refinement.

The above analysis takes into account all the different types of coincidences between radioactive events except coincidences of singles which include no blobs. These are studied separately. It was shown in

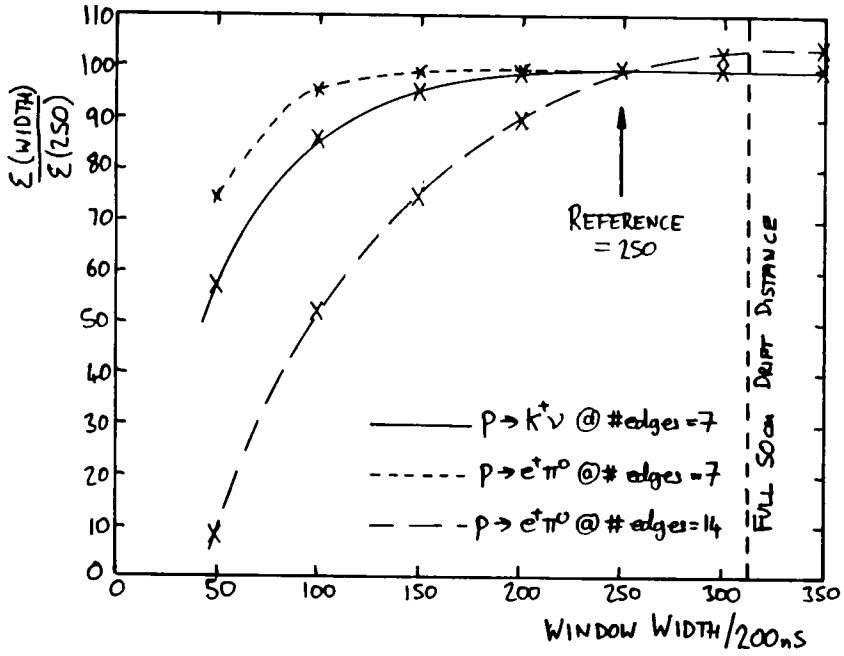

FIG 5·8 COMPARISON OF WINDOW WIDTH SETTINGS

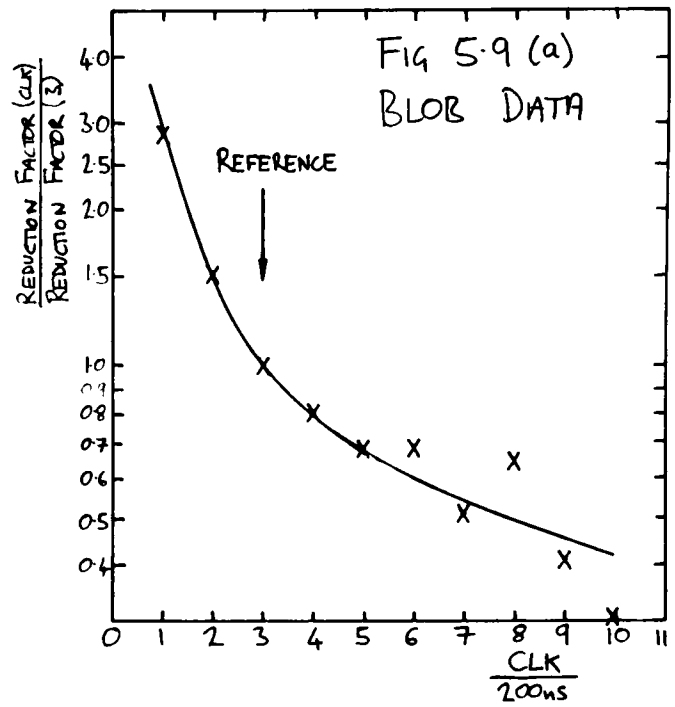

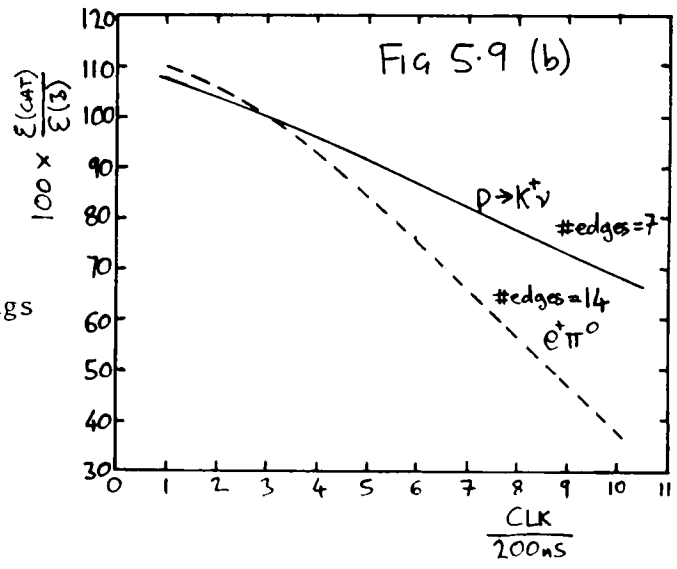

Fig 5.9 Comparison of clock period settings
(a) Blob data
(b) PDK simulation

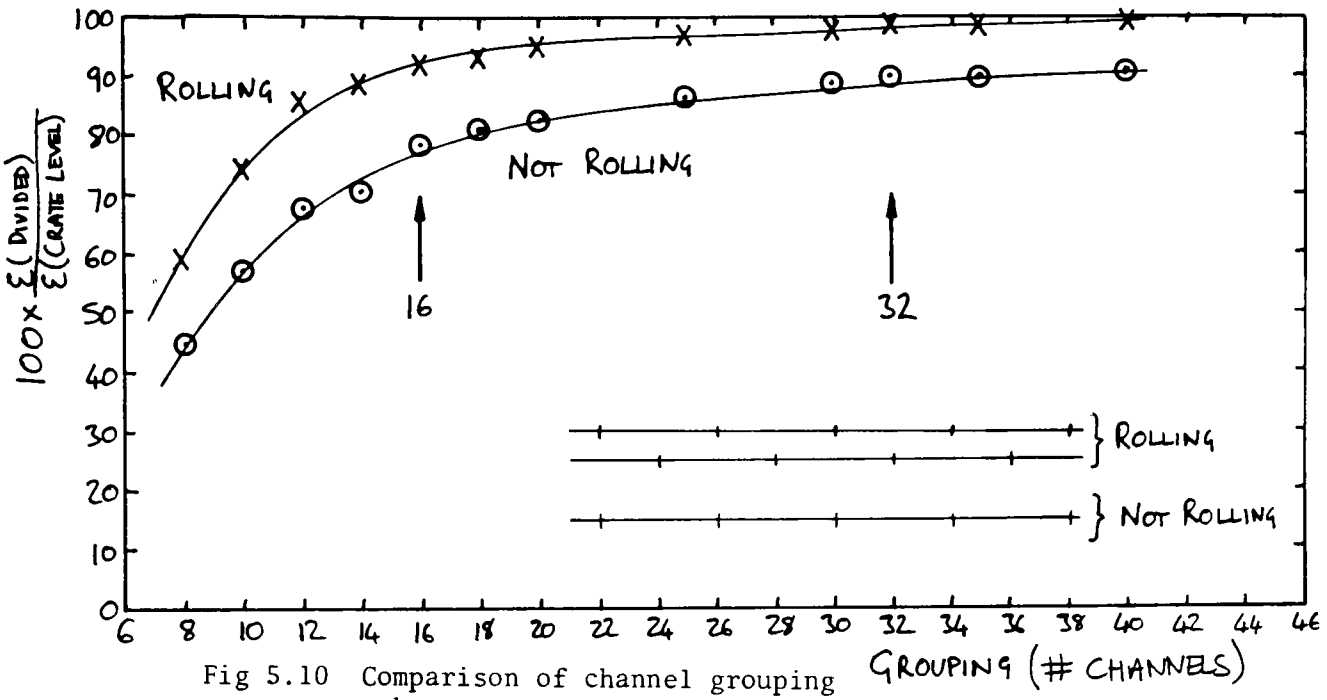

Fig 5.10 Comparison of channel grouping schemes.

chapter 4 that the number of quadruple comptons in an event is negligible, so with a trigger threshold of 5 edges or more, they can be neglected. The rates due to random coincidences may be computed. The probability of obtaining r edges in a window of N clock samples must be found. The probability of a sample being occupied is a = Rt where R is the singles rate and t is the time duration of one clock period. The calculation is not entirely straightforward, since the window over which the samples are tested rotates. The method chosen is to consider the N-1 clock ticks immediately beyond an occupied tick and find the binomial probability of r-1 clock periods being occupied.

$$\text{RATE}(r, N, a, R) = R \times {}^{N-1}C_{r-1}\, a^{r-1}(1-a)^{N-r}$$

This is then summed to find the probability of r-1 or more occupied clock ticks. The calculation has been done for the crate level and 16, 16R, 32 and 32R connection schemes including multiplexing, the results are summarised in table 5.2. At 5 edges, the trigger rate will be less than that from events containing blobs for the arrangements 16R and 16.

r	Crate	32R	32	16R	16
4	14000	30	14.4	4.0	1.9
5	3400	0.70	0.35	0.05	0.023
6	680	0.014	0.007	0.0004	0.0002
7	120	-	-	-	-
8	17	-	-	-	-

Table 5.2 Random singles coincidence rates in the full detector using rates from chapter 4 (connection scheme A)

5.7 Refinements

(1) The trigger scheme using edges will achieve the required rate reduction, the analysis has been based on a tape of events taken with a primary multiplicity requirement of 4. A small multiplicity requirement may be necessary in the final trigger scheme in order to remove events caused by electronic noise on one channel (normally caused by malfunctioning circuitry). The level of this will depend on the final noisiness of the experiment.

(2) The trigger has so far only been considered on the anodes, the circuitry could also monitor the cathodes and an anode .OR. cathodes trigger made. This would pick out events which are vertical which appear on few anodes.

(3) This trigger will also trigger on cosmic ray muons for muon astronomy. The trigger will be efficient to all muons except those travelling parallel to the wireplanes which will produce many pulses close together in time and not generate sufficient edges to trigger. A separate trigger will be necessary to fill in the bald patch. The particular muons we need to trigger on will travel through both top and bottom modules and produce multiplicities in excess of 100 in upper and lower cathode crates. The extra trigger could simply require a large multiplicity in both top and bottom cathode crates.

5.8 Earlier Triggering Schemes

Although it is firmly established that the edges trigger out performs earlier trigger designs, it is interesting to discuss the other schemes and the reasons why the edges trigger is better. There have been two previous schemes, both of which were designed by me, the FastOR trigger and the 'deblobber' trigger. Both of these triggers were designed more closely around the existing electronics and were both tested in hardware at the crate level.

The first idea, the 'deblobber' trigger, operates by generating two multiplicity signals from the existing electronics, for example a multiplicity of N=2 and M=6. A trigger is generated provided a preset amount of time t elapses between the N=2 appearing and the M=6 appearing. All the signals associated with a blob appear at once, so both N and M multiplicities appear together and no trigger is produced, whereas, in a real event the multiplicity increases as the ionisation drifts in and a trigger is produced. It was found that the trigger suppresses the blob rate by two orders of magnitude with t set to 1200 ns (min step 600 ns). The problem encountered with the scheme is that it contains a veto component, if a track crosses a wireplane it produces ionisation which initially appears as a blob (since a blob is just ionisation in the gas region). If the M=6 appears, and the veto operates, the trigger shuts off and does not change its mind when more track pulses drift in later. The edge trigger will not accumulate many edges from the wireplane crossing, but will count all the later pulses and so trigger. The circuitry for this trigger has been used extensively to operate the parts of the detector which have been installed at the mine since January 1987.

The second scheme, the FastOR trigger monitors a line which is true whenever any of the channels in a crate is above threshold. If the fraction of the time that this line is true within a rolling window

exceeds a preset value, a trigger is generated. The circuitry used to monitor the line is exactly the same as the one shown in fig 5.5b which is used for the edges trigger. This trigger is especially efficient for events which are spread in drift time, which are also particularly easy to pulse match. The problem is that a blob produces large signals which, take a long time to fall back below threshold, so the setting required for removing blobs is not efficient to proton decay. This trigger was used to take the events shown in figs 4.2a and b.

5.9 Summary

The edges trigger scheme has been described. Although the installation of the hardware for the trigger has not been completed at the mine, the algorithm has been tested offline on mine data taken with a multiplicity trigger. The rate of blobs is reduced by nearly an order of magnitude for each extra edge required (fig 5.6). This is as expected from random coincidence hits with the blob. At #edges=6, three orders of magnitude reduction is achieved, which is sufficient to take data at less than 3 Hz. This setting of the trigger is sensitive to over 70% of the $p \rightarrow \nu K^+$ proton decay events in the detector. The rates of triggers from electronic noise and from coincidences of radioactive singles are found to be small.

Chapter 6

THE FLUX OF ATMOSPHERIC NEUTRINOS AT UNDERGROUND DETECTORS

6.1 Introduction

A proton decay candidate will be produced by the appearance of a group of tracks originating in the detector which are kinematically consistent with the decay of a proton. The events will be identified as having originated in the detector by being contained, ie no tracks are seen to leave or enter the detector. The largest background source of contained events, as discussed at the start of chapter 4, are caused by neutrino interactions with the nucleons in the detector bulk.

The dominant source of such neutrinos is from the decay of secondary particles which are produced by interaction of cosmic ray particles in the top of the atmosphere. The flux of each type of neutrino and antineutrino has been calculated and will be described in this chapter.

The calculation is in three steps. (1) The flux of primary particles incident on the top of the atmosphere is obtained from experimental data. The primary cosmic rays are mainly protons and heavier nuclei. (2) A Monte-Carlo simulates the cascade process for incident protons and records the number of neutrinos produced per cascade (yields). The nuclei are treated as independent nucleons and the neutron yields are obtained from the proton yields by isospin symmetry. (3) The effects of the earth's magnetic field are included.

These steps are discussed in detail in the next sections. The calculation described was done in collaboration with T.K. Gaisser and Todor Stanev of the Bartol Research Institute, Newark, DE, USA.

6.2 The Flux of Primary and Secondary Cosmic Rays at the Top of the Atmosphere

Of the nucleons incident on the earth, about 75% arrive as single protons, 17% as alpha particles, and the rest in more complex nuclei (at the appropriate energies). I have collected together a comprehensive set of proton flux measurements which were carried out in the 60's and 70's, and a collection of helium flux measurements. Much recent work has been done on the measurement of elemental cosmic ray abundances, in order to try and work out their source, which is still unknown. The abundances are significantly different to those of terrestrial matter. These abundances will be used to calculate the contribution of $Z > 3$ nuclei to the overall nucleon flux by normalising it with absolute flux measurements of carbon.

For the calculation, the nucleons in a nucleus are assumed to interact independently, the composition will be compared at the same energy per nucleon. It will also be useful to compare the fluxes at the same rigidity for calculations involving magnetic fields. Rigidity is defined as

$$\text{RIGIDITY} = \frac{pc}{Ze} = \frac{A}{Ze}\left(E_n^2 - m_n^2c^4\right)^{1/2}$$

where p is the total momentum of the nucleus, E_n is the energy per nucleon, and Ze the charge. For all nuclei except hydrogen, A/Z = 2 has been assumed. Calculations involving magnetic fields for the nucleons of a given energy involve splitting the flux into hydrogen (A/Z=1) and all other particles (A/Z=2) and doing the computation for each group separately.

6.3 Solar Modulation

The cosmic ray protons and other nuclei are known to propagate through the galaxy. As they enter the region close to the solar system, the heliosphere, they encounter the solar wind. The solar wind is a magnetic field trapped in expanding solar plasma. This field produces a barrier which protons travelling to the earth must climb. The solar wind changes as the solar activity changes. Two good methods of monitoring solar modulation are sunspot counts (fig 6.1) and neutron monitors (fig 6.2). Neutron monitors measure the flux of hadrons which are produced in the cascades in the atmosphere by the incident protons and nuclei.

A period when there are few sunspots (eg 1965, 1977) is referred to as a solar minimum, and at these times, the solar wind is less, the potential barrier is lower, and most cosmic rays are seen. Similarly, times of high sunspot activity is called a solar maximum. Solar activity varies in cycles of 11 years, although features within a period are not the same on each cycle. For a more detailed description of the solar wind, see Longair [2].

For the neutrino flux calculations, we require the flux in the range 2 to 500 GeV per nucleon. The most important region is around 20 GeV/nucleon. The potential barrier of the solar wind affects the low rigidity particles most, and these particles are the most heavily modulated. There is little modulation above a rigidity of 10 GV (about 10 GeV for protons, 5 GeV/nucleon for other nuclei). Modulation above this rigidity is neglected. The fluxes at solar minimum will be surveyed first, since these are the most extensively measured. Changes at solar maximum will be discussed later.

Fig 6.1 MONTHLY MEAN SUNSPOT NUMBERS

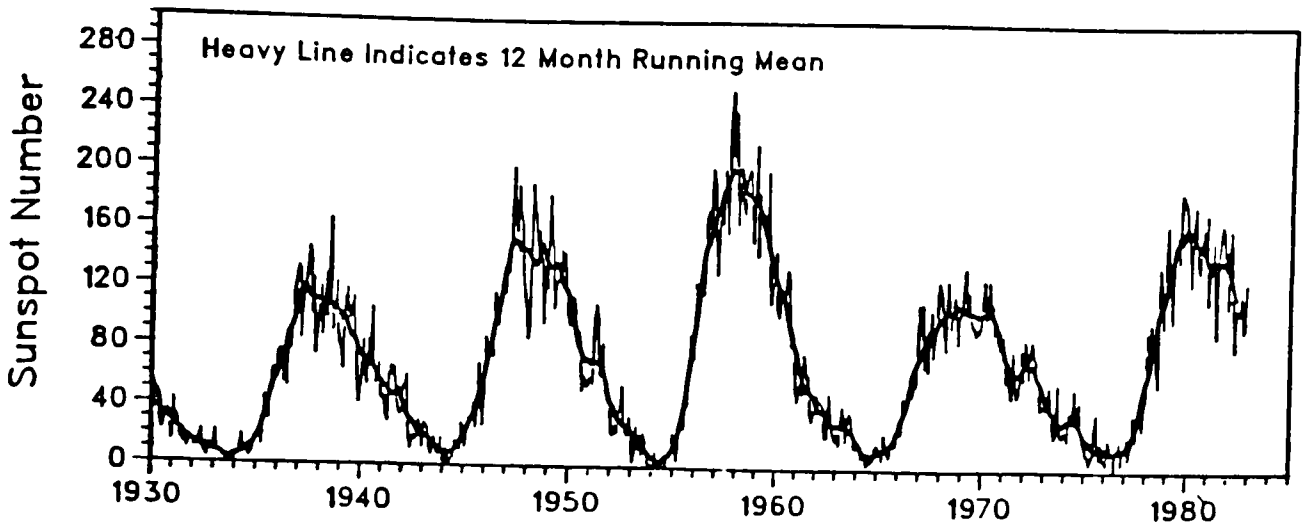

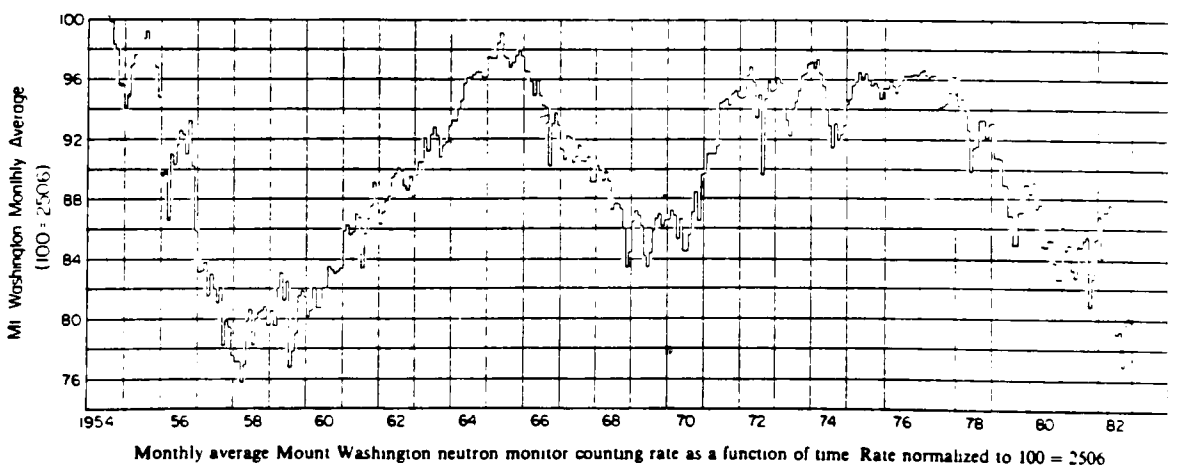

Monthly average Mount Washington neutron monitor counting rate as a function of time Rate normalized to 100 = 2506

Fig 6.2 From Lockwood and Webber(1984)

6.4 The Hydrogen Spectrum at Solar Minimum

The hydrogen spectrum at the top of the atmosphere was extensively measured at low energies around 1965, at a solar minimum, in order to investigate the solar modulation. In the early seventies, the higher energies were measured. The work was done on balloon borne multielement experiments which separated different charges, and also determined the energy or momentum of the particles. Several techniques were used, including Cerenkov detectors, photographic emulsion/absorber sandwiches and magnetic spectrometers. Many of the flights measured both hydrogen and helium fluxes. More recent work has been done on satellite borne experiments.

One of the problems with balloon borne experiments is that there is still about 3 to 6 g/cm^2 of atmosphere above the highest point the balloon can be flown. Corrections for this are usually made by the authors using Monte-Carlo calculations, although not all nuclear cross sections and spallation cross sections are known precisely. A further correction is also made for interactions in the top part of the detector. This second correction is also made for satellite experiments.

The compilation of hydrogen data is plotted with quoted errors on fig 6.3(a). To make it easier to see the discrepancies, the points are plotted on fig 6.3(b), with the vertical scale multiplied by $E^{2.5}$. Many of the points were read from graphs. Where no error bars had been drawn, errors the size of the plotting symbol were assumed. Regardless of the asymmetry of the errors around the data point, the points were assumed to have a symmetrical percentage error. Any errors in the energy introduced by finite bin widths have also been neglected. The references are shown in the caption to fig 6.3(a).

As is common in the field of cosmic ray physics, the spectrum was fitted to a $j = NE^{-\gamma}$ curve. It is seen on fig 6.3(b) that it is most appropriate to do this in two separate regions, since the slope changes at about 4.5GeV due to the solar wind. The fits have included all points

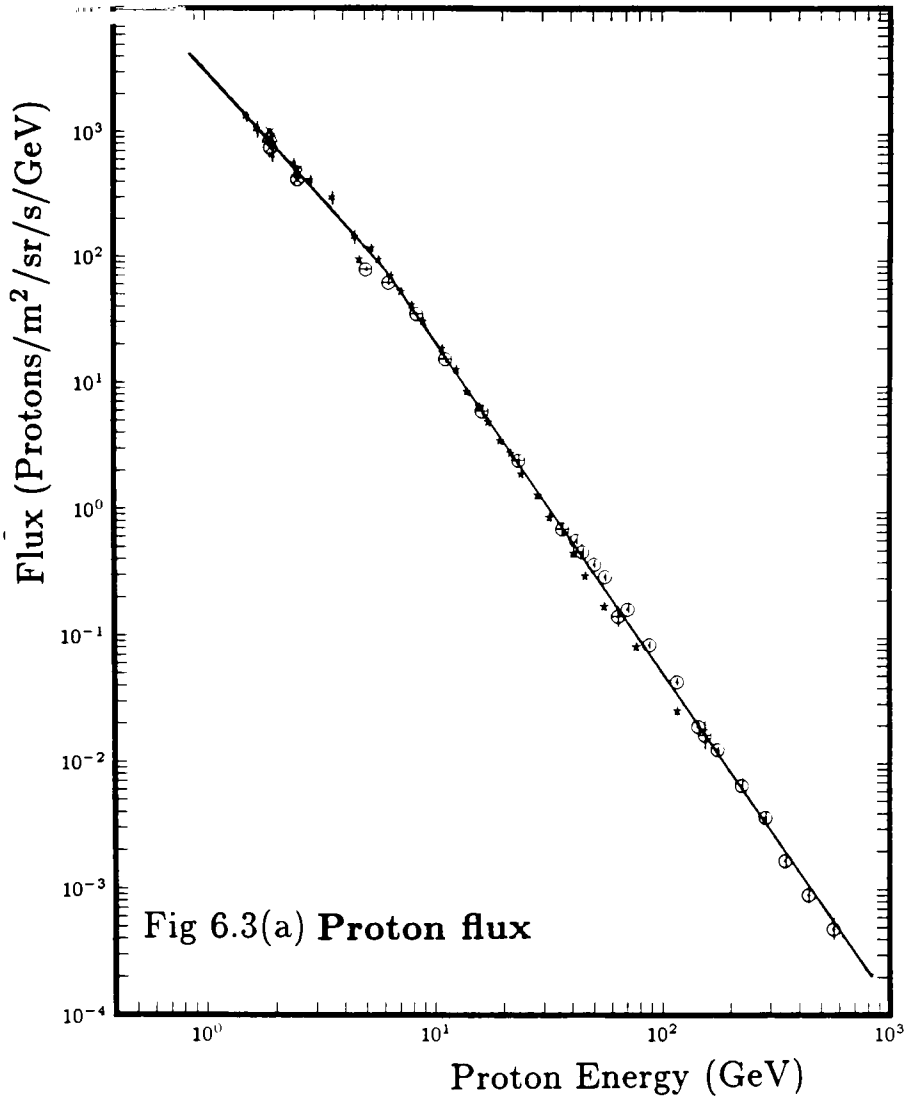

Fig 6.3(a) **Proton flux**

⋆ Badhwar et al. ICRC Ploudiv (1977) 1 203 Points from Simpson. Data in 1975
× Ormes and Webber JGR (1968) 73 4231 Flight 65-1
◇ Ormes and Webber JGR (1968) 73 4231 Flight 65-2
○ Ormes and Webber JGR (1968) 73 4231 Filght 66-2
• Ormes and Webber JGR (1968) 73 4231 Flight 66-1
⊗ Ormes and Webber JGR (1968) 73 4231 Flight in 1963
⊙ Ramaty, Ormes and Balasubrahmanyan Science 180 731 (1973) Flight Nov 1970
△ Webber and Yusak (1979) 16th ICRC (Kyoto) 1 383 Flight in 1977
÷ Freier and Waddington JGR (1968) 73 4261 Data of 3 flights in July 63,4,5
⊖ Smith et al Ap J (1973) 180 987 Balloon expt, flights in 1970,71
Low energy parameters to $j = NE^{-\gamma}$ fit: $N = 3228.8$, $\gamma = 2.01$
High energy parameters to $j = NE^{-\gamma}$ fit: $N = 10251.6$, $\gamma = 2.64$

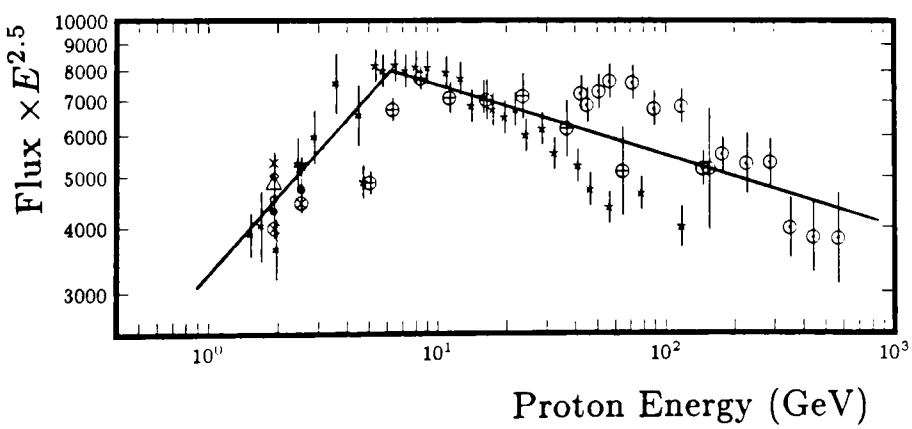

Low energy parameters to $j = NE^{-\gamma}$ fit: $N = 3228.8$, $\gamma = 2.01$
High energy parameters to $j = NE^{-\gamma}$ fit: $N = 10251.6$, $\gamma = 2.64$

Fig 6.3(b) **Proton flux**

except the lowest two of Smith et al. and the lowest one from Badhwar et al., as they are taken during a solar maximum period (these points are included on the two graphs). The fitted lines, and the parameters are shown in both figs 6.3(a) and (b).

It can be seen that agreement is adequate, except in the important 30 - 120GeV region, where the experiments disagree by a factor of up to 1.7. Apart from this, the points are all consistent to within 20%. It should be noted that the low energy points were taken 'around' the solar minimum, so the spread is not experimental discrepancy. The values from the fit are summarised in table 6.1.

6.5 The Helium Spectrum

The same procedure for helium as for hydrogen has been followed, although it was not possible to locate some of the original references from the compilation of Simpson [3]. The data are plotted on figs 6.4(a) and 6.4(b). Since helium at a given energy/nucleon has a higher rigidity than hydrogen, the effects of the solar wind are less and it is sufficient to fit the points to a single curve in the whole energy range. This has been shown on figs 6.4(a) and 6.4(b). The lowest of the Smith et al. points is not included in the fit, since it was taken around the solar maximum. The scatter on the points is similar to that for hydrogen, except that there is better agreement in the 30 to 120 GeV energy range. The data above 200 GeV are not known well, but this is not important for a neutrino background calculation. The points are consistent to within about 20%. The values of the fit are shown in table 6.1.

6.6 The flux of nucleons bound in nuclei of $Z \geqslant 3$

As described in the introduction, the contribution from heavy nuclei will be computed by summing the relative abundances for nuclei of

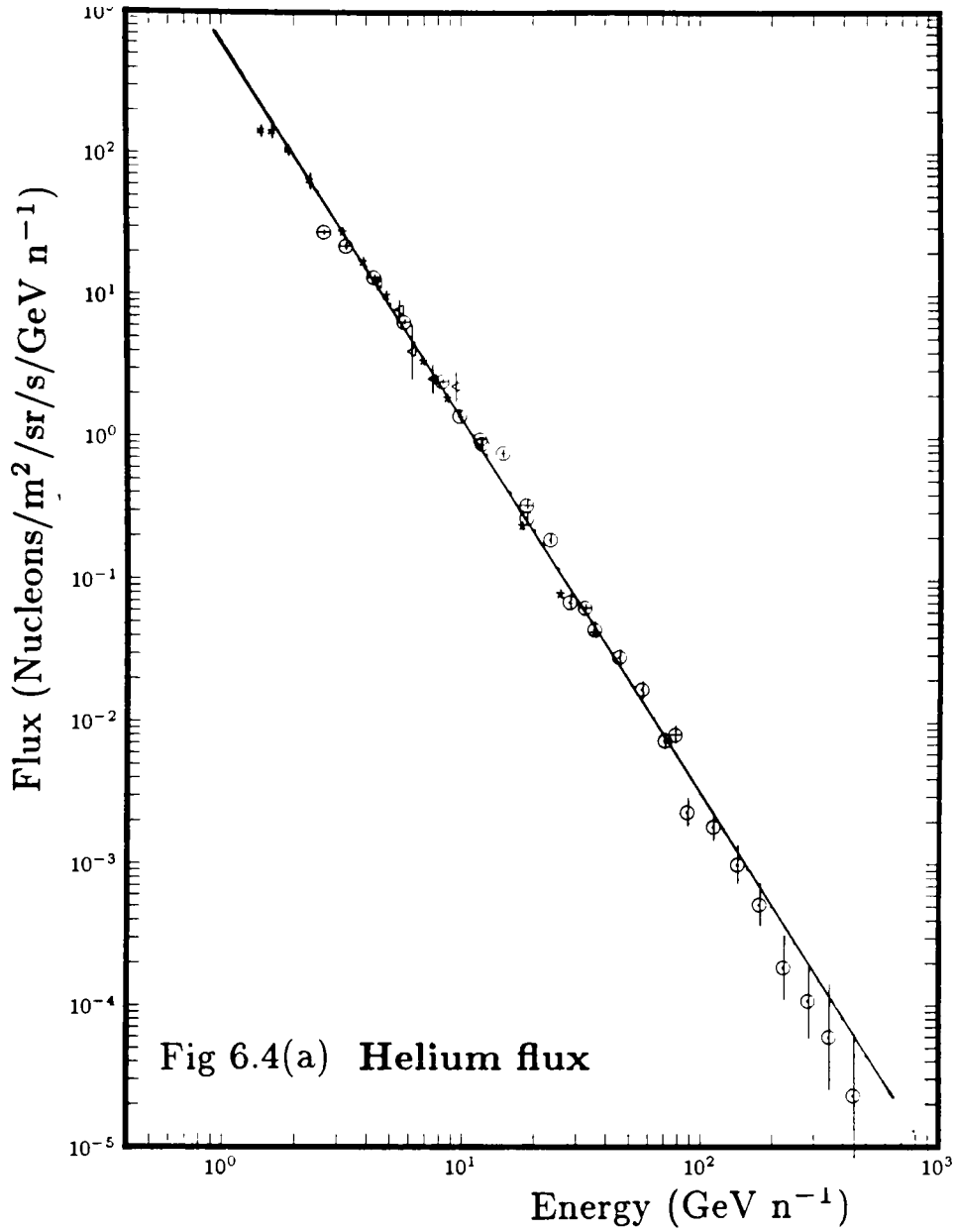

◁ Foster and Schrautemeier (1967), taken from Freier and Waddington JGR (1968) 73 4261
÷ Freier and Waddington JGR (1968) 73 4261
∴ Badhwar et al ICRC Ploudiv (1977) 1 203, Points read from Simpson (1983)
⊖ Smith et al Ap J (1973) 180 987
⊙ Ramaty, Ormes and Balasubrahmanyan, science (1973) 180 731
Parameters to $j = NE^{-\gamma}$ fit: $N = 619.4$, $\gamma = 2.65$

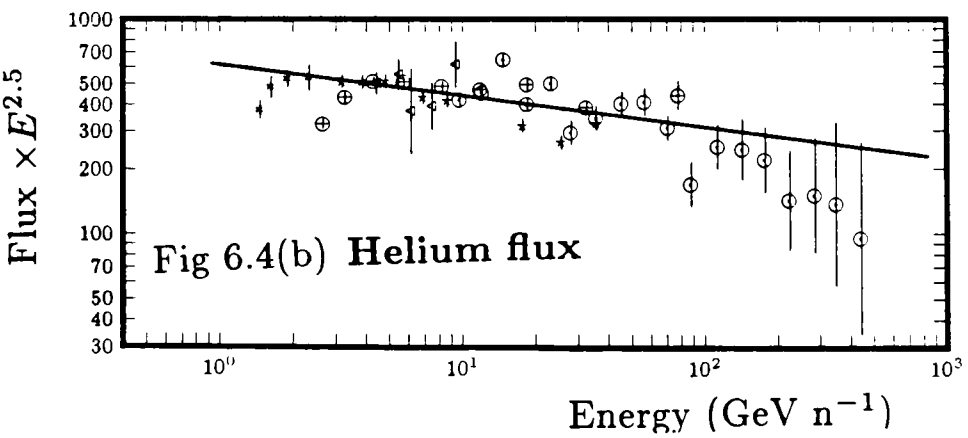

Parameters to $j = NE^{-\gamma}$ fit: $N = 619.4$, $\gamma = 2.65$

$Z \geqslant 3$ (Li+) and normalising with the flux measurements of carbon.

Recent cosmic ray work has been concerned with measuring the elemental abundances of galactic cosmic rays, and comparing them with abundances of other sources (the sun, the earth, meteorites, etc.). Experimental techniques are similar to those for hydrogen and helium. Improved charge/energy resolution has been obtained since 1977 by making the detectors curved so that the path length distribution through the detector has been made narrower. Both balloon and satellite borne experiments have been used. Balloon experiments are corrected for the overlying atmosphere. Fig 6.5 shows a plot of the measured abundances.

The relative abundance of nucleons incident in carbon, to all incident nucleons (except hydrogen and helium) has been computed. Abundances $\alpha(Z)$ are quoted as a ratio of particles, compared at a given energy per nucleon, relative to silicon (=100). The quantity

$$\frac{Li+}{C} = \sum_{Z \geqslant 3} \alpha(Z) A(Z) \Big/ \alpha(Z=6) A(Z=6)$$

has been computed. Elements with Z > 30 which contribute less than 10^{-5} % to the total flux (computed from the data of Letaw, Silberg and Tsao [4]) have been neglected. Using the compilation of Simpson [3], in the 1 - 2 GeV/nucleon range (600 - 1000 MeV/nucleon for lithium) Li+/C = 4.98. There is some evidence that this fraction is energy dependent, but experimental data on the spectra is no better than hydrogen, and, within experimental error, this ratio may be assumed constant with energy [5].

The spectrum of carbon has been taken from the review by Simpson [3] to normalise the relative abundances. Once again, experimental discrepancies indicate an uncertainty of around 20%. The fluxes are shown in table 6.1.

The total contribution from hydrogen, helium and other nuclei are shown in table 6.1. The uncertainty is 20%, except in the 30-120 GeV/n range, where larger discrepancies exist in the hydrogen data.

Solar Minimum Fluxes in Nucleons/m²/sr/sec/(GeV/nucleon)

Table 6.1

Energy	He Flux	Li+ flux	He & Li+ Flux	H Flux	Total	%H	%He	%Li+	R(H)	R(He)
2.00	141.6000	394.7314	536.3314	801.6243	1337.956	59.9	29.5	10.6	1.77	3.53
3.17	47.20000	116.4727	163.6727	317.6230	481.2957	66.0	24.2	9.8	3.03	6.06
5.03	16.70000	34.26699	50.96699	125.5710	176.5380	71.1	19.4	9.5	4.94	9.88
7.96	5.260000	10.15340	15.41340	42.89247	58.30587	73.6	17.4	9.0	7.90	15.81
12.60	1.550000	3.006416	4.556417	12.75890	17.31532	73.7	17.4	9.0	12.57	25.13
20.00	0.4500000	0.8836933	1.333693	3.767665	5.101358	73.9	17.3	8.8	19.98	39.96
31.70	0.1370000	0.2607498	0.3977498	1.116850	1.514600	73.7	17.2	9.0	31.69	63.37
50.30	0.3900000E-01	0.7671423E-01	0.1157142	0.3301049	0.4458191	74.0	17.2	8.7	50.29	100.58
79.60	0.1170000E-01	0.2273063E-01	0.3443063E-01	0.9826095E-01	0.1326916	74.1	17.1	8.8	79.59	159.19
126.00	0.3100000E-02	0.6730527E-02	0.9830527E-02	0.2922895E-01	0.3905948E-01	74.8	17.2	7.9	126.00	251.99
200.00	0.7900000E-03	0.1978343E-02	0.2768343E-02	0.8631221E-02	0.1139956E-01	75.7	17.4	6.9	200.00	400.00
317.00	0.1790000E-03	0.5837460E-03	0.7627460E-03	0.2558556E-02	0.3321302E-02	77.0	17.6	5.4	317.00	634.00
503.00	0.5400000E-04	0.1717417E-03	0.2257417E-03	0.7562264E-03	0.9819681E-03	77.0	17.5	5.5	503.00	1006.00

Solar Maximum Fluxes in Nucleons/m²/sr/sec/(GeV/nucleon)

Table 6.2

Energy	He Flux	Li+ flux	He & Li+ Flux	H Flux	Total	%H	%He	%Li+	F(H)	F(He)
2.00	62.93333	175.4362	238.3695	133.6040	371.9736	35.9	47.2	16.9	6.00	2.25
3.17	25.51351	62.95821	88.47173	133.4551	221.9268	60.1	28.4	11.5	2.38	1.85
5.03	12.84616	26.35922	39.20538	61.25416	100.4595	61.0	26.2	12.8	2.05	1.30
7.96	5.260000	10.15340	15.41340	27.67256	43.08597	64.2	23.6	12.2	1.55	1.00
12.60	1.550000	3.006416	4.556417	12.75890	17.31532	73.7	17.4	9.0	1.00	1.00
20.00	0.4500000	0.8836933	1.333693	3.767665	5.101358	73.9	17.3	8.8	1.00	1.00
31.70	0.1370000	0.2607498	0.3977498	1.116850	1.514600	73.7	17.2	9.0	1.00	1.00
50.30	0.3900000E-01	0.7671423E-01	0.1157142	0.3301049	0.4458191	74.0	17.2	8.7	1.00	1.00
79.60	0.1170000E-01	0.2273063E-01	0.3443063E-01	0.9826095E-01	0.1326916	74.1	17.1	8.8	1.00	1.00
126.00	0.3100000E-02	0.6730527E-02	0.9830527E-02	0.2922895E-01	0.3905948E-01	74.8	17.2	7.9	1.00	1.00
200.00	0.7900000E-03	0.1978343E-02	0.2768343E-02	0.8631221E-02	0.1139956E-01	75.7	17.4	6.9	1.00	1.00
317.00	0.1790000E-03	0.5837460E-03	0.7627460E-03	0.2558556E-02	0.3321302E-02	77.0	17.6	5.4	1.00	1.00
503.00	0.5400000E-04	0.1717417E-03	0.2257417E-03	0.7562264E-03	0.9819681E-03	77.0	17.5	5.5	1.00	1.00

6.7 The Low Energy Flux at Solar Maximum

Most of the work on differential fluxes has been presented in the previous sections. There is little work on the flux below 10 GeV in periods of solar maximum, all that has been found is from the 1954 - 1965 solar cycle in a compilation by Nerurkar [6] (fig 6.6). Most cosmic ray modulation is studied using either neutron monitors, sunspots, or low energy integral spectra, where the effects are larger. It is not known how to extract the data required for the neutrino calculation from these studies.

The data of fig 6.6 has been used to calculate the change in flux of the A/Z = 1 (hydrogen) and A/Z = 2 (helium and Li+) particles given in table 6.1. The results are shown in table 6.2. The last two columns of table 6.2 show the factors used to adjust the fluxes. There is insufficient data to judge how accurate these figures are. The solar wind is not understood well enough to provide a calculation of this effect.

6.8 Proton Yields

The second step in the calculation is to compute the number of neutrinos produced by each proton or neutron as its cascade develops. At the time this calculation was started, Tom Gaisser and Todor Stanev had developed a cascade Monte-Carlo for incident protons [7] and few changes were necessary for the work which I did in collaboration with them.

The simulation consists of generating hadronic interaction secondaries according to the parameterisation of the form originally suggested by Stenlund and Otterlund until all the energy of the primaries is used. Details of the charge ratio, K/π ratio, transverse momentum distributions etc. were included in the parameterisation. The parameterisation was normalised in the 20 GeV energy region, which is

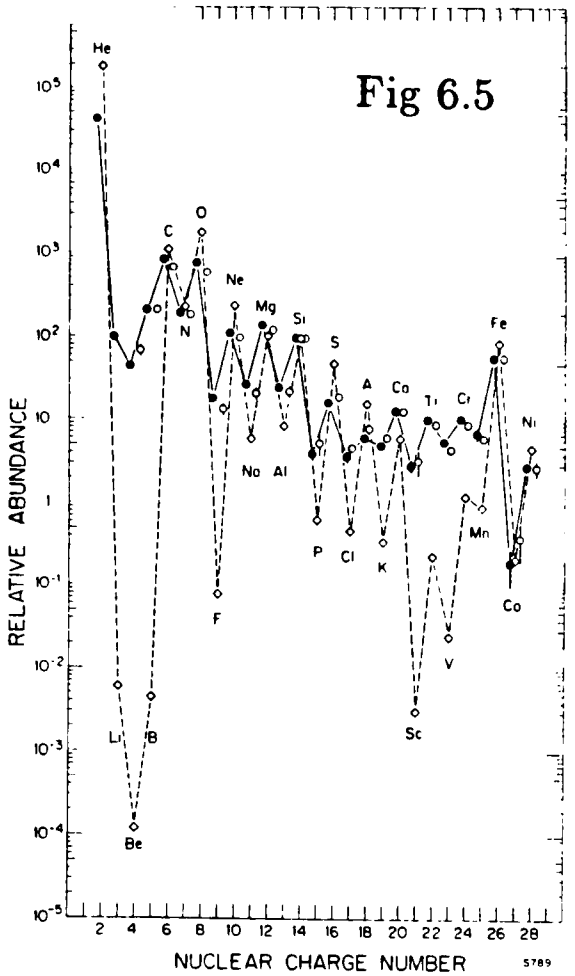

From Simpson(1983)

Cosmic Ray Abundances Relative to Silicon (solid circles 70-280MeVA^{-1}, open circles 1-2GeV/nucleon) Also shows solar system abundances (diamonds)

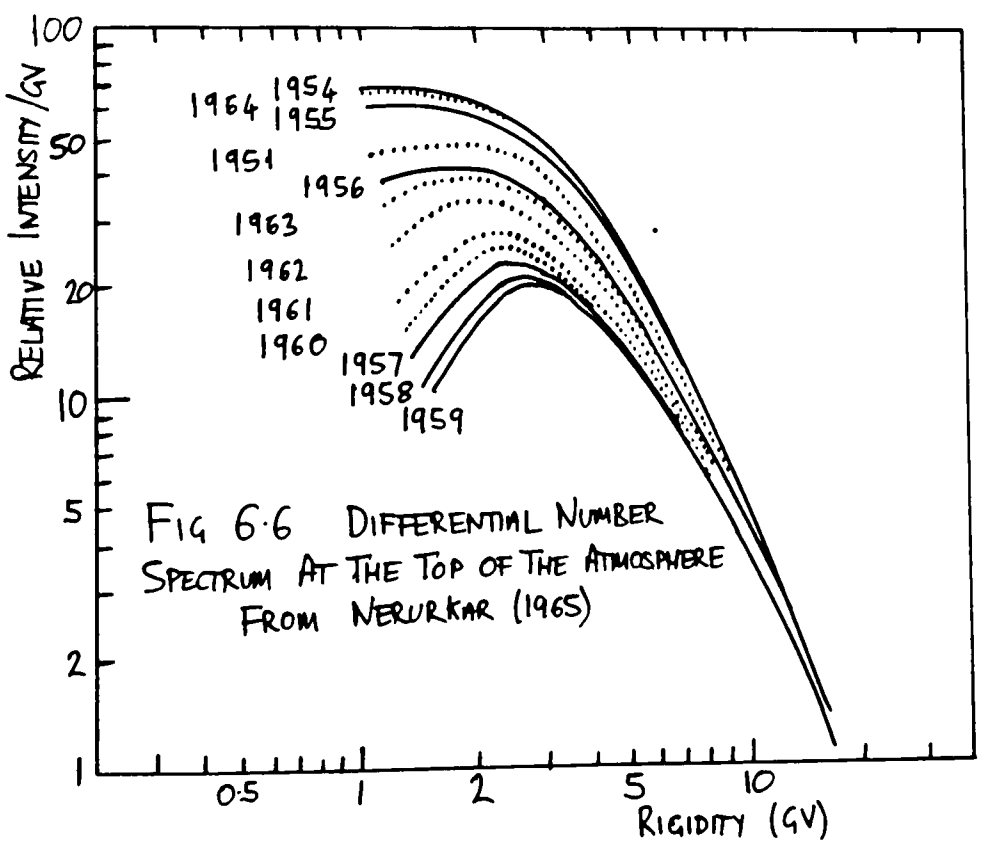

FIG 6·6 DIFFERENTIAL NUMBER SPECTRUM AT THE TOP OF THE ATMOSPHERE FROM NERURKAR (1965)

the most important for the production of neutrinos in the energy range 0.2 to 3 GeV. The model was tested and adjusted to reproduce data at both ends of the proton energy region of concern, (from a few GeV to a TeV). The calculation then simulates all secondary decays in the atmosphere. Reactions with branching ratios greater than 1% (also $\pi^{\pm} \rightarrow e^{\pm} \nu_e$) are included. The one limitation in the calculation is that the kinematics are done in one dimension, i.e. all secondary particles are assumed to travel in the same direction as the initial proton. Details of energy loss by charged particles as they are tracked in the atmosphere are also included.

The calculation was carried out for ten separate proton energies (2, 3, 5, 7, 10, 20, 50, 100, 200 and 500 GeV total energy), and repeated for six separate proton zenith angles (cos = 1.0, 0.75, 0.5, 0.25, 0.15, and 0.05). In the cases of the last three angles, the effects of the curvature of the earth and the atmosphere were included. A simple geometrical argument shows that for upward angles at the detector, the angle to the vertical is the same as the angle to the local vertical at the point where the cascade took place, so the same calculated yields may be used for upward going neutrinos.

Since the cascades of protons with high energies are larger than those with low energies, more neutrinos are produced per proton, so less protons need to be fed through the Monte Carlo to obtain acceptable statistics on the yields.

By folding the yields Y_p obtained with the cosmic ray proton flux ϕ_p (as will be described in more detail later), the response curves shown in fig 6.7 are obtained. These show the range of proton energies responsible for producing neutrinos in three separate neutrino energy ranges. Similar curves are also obtained for electron type neutrinos and for muons at various atmospheric depths.

6.9 Neutron Yields

It is not possible to calculate the yields from neutron cascades (pn and nn) in the same way as for protons, since there is little accelerator data with neutron beams. The procedure adopted is to assume that the neutron induced neutrino yield is equal to the proton induced antineutrino yield and vice versa. (also for muon yields). This is discussed in this section.

The proton induced initial state (pp or pn) may be transformed into the neutron initial state (nn or np) by an isospin rotation of π about the I_2 axis (ie replacing I_3 by $-I_3$). Since isospin is conserved in the strong interaction, the reaction (before any weak decay) of a proton induced interaction can be transformed into an equivalent neutron induced interaction by the same transformation ($I_3 \rightarrow -I_3$) on each of the products. It is convenient to show this schematically as

$$p \rightarrow \begin{pmatrix} p \\ n \end{pmatrix}, \begin{pmatrix} \pi^+ \\ \pi^0 \\ \pi^- \end{pmatrix}, \begin{pmatrix} K^+ \\ K^0 \end{pmatrix}, \begin{pmatrix} \bar{K}^0 \\ K^- \end{pmatrix}, (\Lambda^0), \begin{pmatrix} \Sigma^+ \\ \Sigma^0 \\ \Sigma^- \end{pmatrix}, \quad \text{etc}$$

$$n \rightarrow \begin{pmatrix} n \\ p \end{pmatrix}, \begin{pmatrix} \pi^- \\ \pi^0 \\ \pi^+ \end{pmatrix}, \begin{pmatrix} K^0 \\ K^+ \end{pmatrix}, \begin{pmatrix} K^- \\ \bar{K}^0 \end{pmatrix}, (\Lambda^0), \begin{pmatrix} \Sigma^- \\ \Sigma^0 \\ \Sigma^+ \end{pmatrix}, \quad \text{etc}$$

We must now consider how each of the multiplets decay to produce muons and neutrinos. Take for example the pion triplet.

$$\begin{pmatrix} \pi^+ \\ \pi^0 \\ \pi^- \end{pmatrix} \rightarrow \begin{pmatrix} \mu^+ \nu \\ \text{No } \nu \text{ or } \mu \\ \mu^- \bar{\nu} \end{pmatrix}$$

In this case, an $I_2 \rightarrow -I_3$ transformation exchanges pion particle and antiparticle and the lepton particle/antiparticle labels are interchanged. This is consistent with the procedure adopted.

Strange particles are always generated in pairs, since strangeness is conserved in the strong interaction. There are four possibilities:

(1) Meson - Antimeson : For example $K\bar{K}$.

a. The $I_3 \rightarrow -I_3$ transformation, when applied to either $K^+\bar{K}^o$ or $K^o K^-$ is equivalent (for the two particles together) to a particle antiparticle exchange, so these reactions will be calculated correctly by the procedure.

b. When the two kaons are in a $|I,I_3\rangle$ state of $|\frac{1}{2},+\frac{1}{2}\rangle_a|\frac{1}{2},-\frac{1}{2}\rangle_b$, the amplitude will be independent of whether particle a is chosen from $(\bar{K}^o,K^-)$ and particle b from (K^+,K^o) or vice versa. For proton interactions, as many K^+K^- pairs will appear as K^oK^{-o}. The isospin transformation $I_3 \rightarrow -I_3$ maps $K^+K^- \leftrightarrow K^oK^{-o}$, so the two states will also have equal amplitudes in neutron interactions. This is correctly accounted for by the procedure.

(2) Baryon - Antibaryon : The same manipulations as in (1) are also valid here, and one can see that this type of interaction is also handled correctly by the procedure.

(3) Baryon - Meson : Neither a single meson multiplet or a single baryon multiplet possess the property that a transformation $I_3 \rightarrow -I_3$ is equivalent to particle antiparticle interchange, so this type of interaction is not properly described by the procedure.

(4) Antibaryon - Antimeson. As for (3).

In summary, the procedure for computing the neutron yields will be good since (1) The neutron component of the total incident nucleon flux is small <20%. (2) The procedure describes all the interactions fully. except where a strange baryon - meson pair are produced, this type of process is responsible for only a very small proportion of the recorded muons and neutrinos (most are from pions).

6.10 The Earth's Magnetic Field - Penetration probabilities

The proton fluxes must be corrected for the earth's magnetic field. This will bend low rigidity particles away from the earth. In

the calculation, the particles below a cutoff rigidity will be discarded and those above assumed to be unaffected by the field. The cutoff is taken from Stromer [8] For any given neutrino direction, the point of production is calculated (assumed to be 20km above sea level). This point is then translated into geomagnetic coordinates (An inclined offset magnetic dipole approximating the field in 1980 is used) and inserted into the Stormer cutoff expression. This part of the calculation has been taken from Cooke [9].

The total field of view at the detector is divided into annular zones of equal solid angle Θ_i. The effect of the cutoffs is averaged over the solid angle of each zone, and the results given in the form of penetration probabilities, the proportion of the solid angle of the zone for which the cutoff is below the rigidity considered. The cutoffs for eight zones are shown in fig 6.8 for Soudan (48.0N, 268.0E). Cooke has also computed the penetration probabilities for the other detector sites. These may be fed into the calculation to compute the fluxes at any of the sites. The Soudan site is at the highest geomagnetic latitude and so has the lowest cutoffs.

6.11 The neutrino flux at each detector site

The Monte Carlo outputs are interpolated to produce yields at the centre of each angular zone. Interpolation is also used to provide the yields at the energies for which the flux has been computed in table 6.1. The yields Y, penetration probabilities P and primary fluxes ϕ are combined to calculate the neutrino flux.

$$\nu \text{ FLUX}(E_\nu, \Theta_i) = \int Y_p P_p \phi_p + \left(\frac{1}{2} Y_p + \frac{1}{2} Y_n\right) P_N \phi_N \, dE_N$$

Note that the energy E_N corresponds to a single energy per nucleon for which Y has been calculated, whereas E_ν corresponds to an energy bin. The integral is evaluated using the substitution $dE_N \rightarrow E_N \, d \ln(E_N)$ using Simpson's rule.

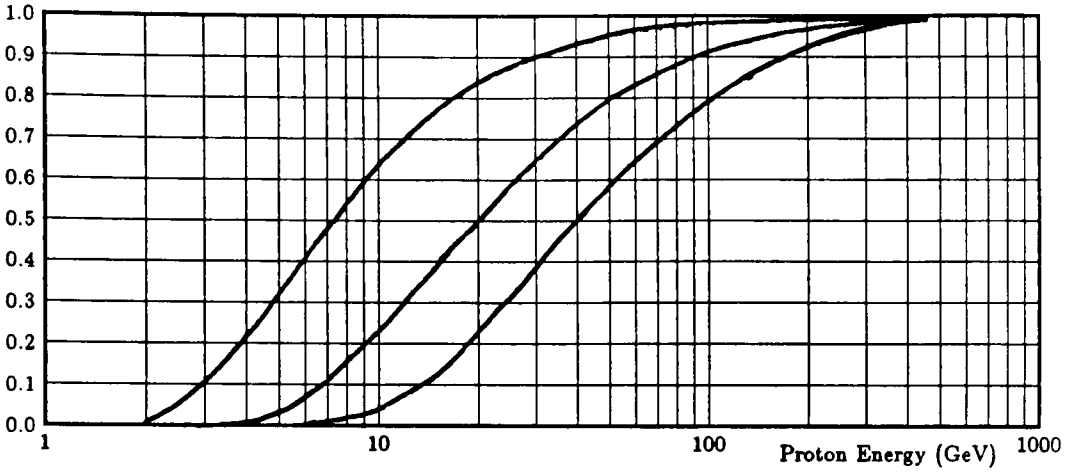

Muon type neutrino

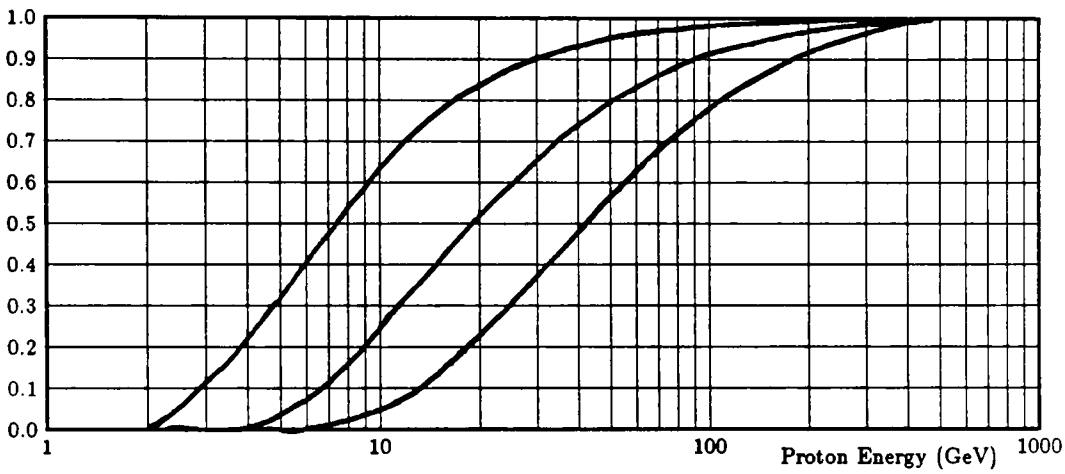

Muon type antineutrino

Fig 6.7 **Cumulative yield graphs. The quantity plotted is**

$$CY(E_p) = \frac{\int_{2\ \mathrm{GeV}}^{E_p} Y(E'_p)\phi(E'_p)dE'_p}{\int_{2\ \mathrm{GeV}}^{502\ \mathrm{GeV}} Y(E'_p)\phi(E'_p)dE'_p}$$

The figure shows the fraction of the flux which is produced by protons of energy E_p or less at the top of the atmosphere. The three curves shown are (from left to right) the flux in the ranges 0.3 to 0.4 GeV, 1.0 to 1.1 GeV and 2.0 to 3.0 GeV respectivly. The curves are calculated at solar minimum, at senith angle $\lambda = 0.$ at Soudan (where the geomagnetic cutoff is below 2 GeV).

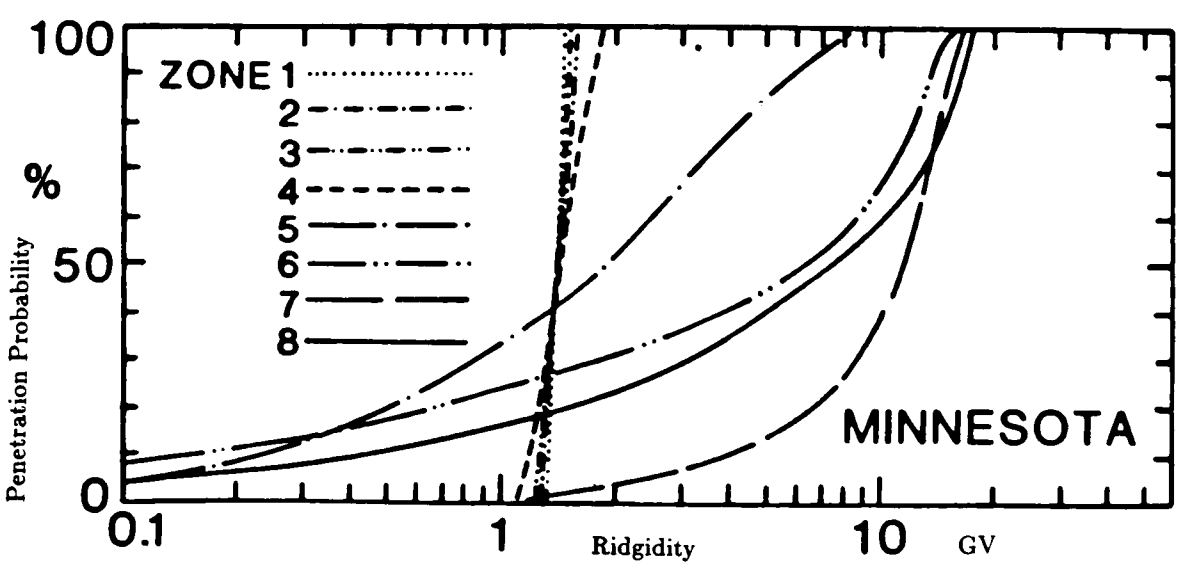

Fig 6.8 Cutoffs at Soudan (48.0N, 268.0E)

The neutrino flux, averaged over the angular zones $\bar{\phi}_\nu$ is shown in fig 6.9(a) for each neutrino type for Soudan and in fig 6.9(b) for several different sites. The angular differences $\left(\phi(\theta) - \bar{\phi}_\nu\right)/\bar{\phi}_\nu$ are shown in fig 6.10 for several energy bins at each site. The sites of NUSEX and Frejus and of IMB and Soudan are close together and no difference is seen in the fluxes at these pairs of sites. The fluxes are tabulated for Soudan in ref [10].

6.12 Comparison of Calculated Muon Fluxes with Experimental Data

The muon fluxes at sea level were also computed in the same way, using the muon yields. These can be used to compare the results of the calculation with experimental data. Fig 6.11 shows the sea level horizontal and vertical muon spectra at high geomagnetic latitudes. The calculation has been corrected to atmospheric depth 1033 g/cm^2 from the data at 1000 g/cm^2 at solar maximum at the Soudan site. The calculation and experimental data agree well.

Fig 6.12 shows the depth dependence of low energy muon fluxes which were computed from the $\theta_i = 0$ Monte-Carlo run. Agreement with data is good except for the highest altitude data point. It is possible that the experimental flux was contaminated by pions which would have caused an overestimate in the flux at high altitude. The calculation agrees with those of Perkins [11] who used two methods to calculate the neutrino fluxes. The 'Olbert' method infers the neutrino fluxes from the measured muon fluxes as a function of latitude and the 'Monte Carlo' method is similar to the calculation described here, although a different interaction parameterisation is used. The μ^+/μ^- ratio of all muons E > 2 GeV was found to be 1.25, which compares well with the observed ratio (1.25 to 1.3). This topic is discussed further in [12].

The vertical and total neutrino fluxes (figs 6.13 and 6.14) compare well with other calculations of neutrino flux at solar minimum.

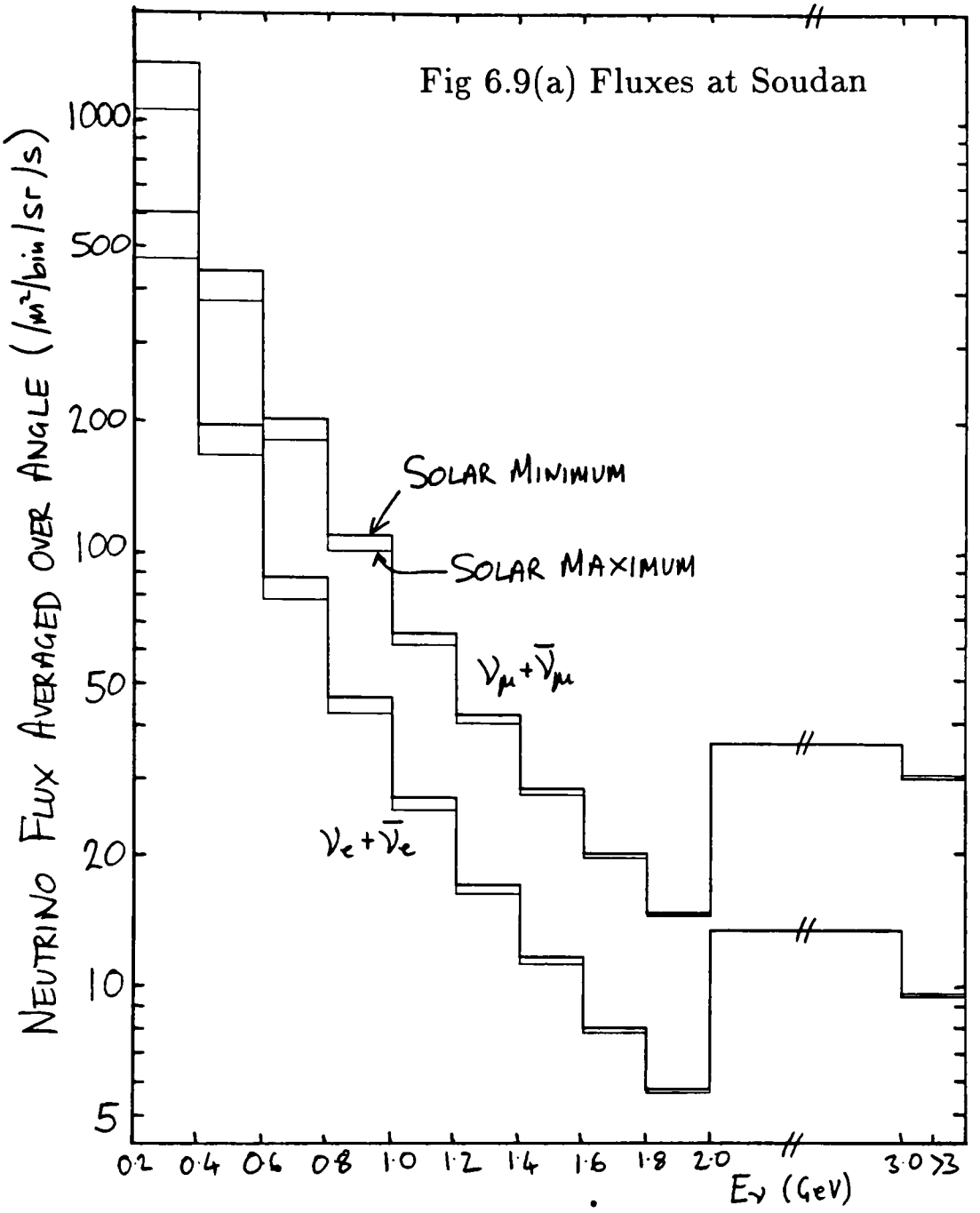

Fig 6.9(a) Fluxes at Soudan

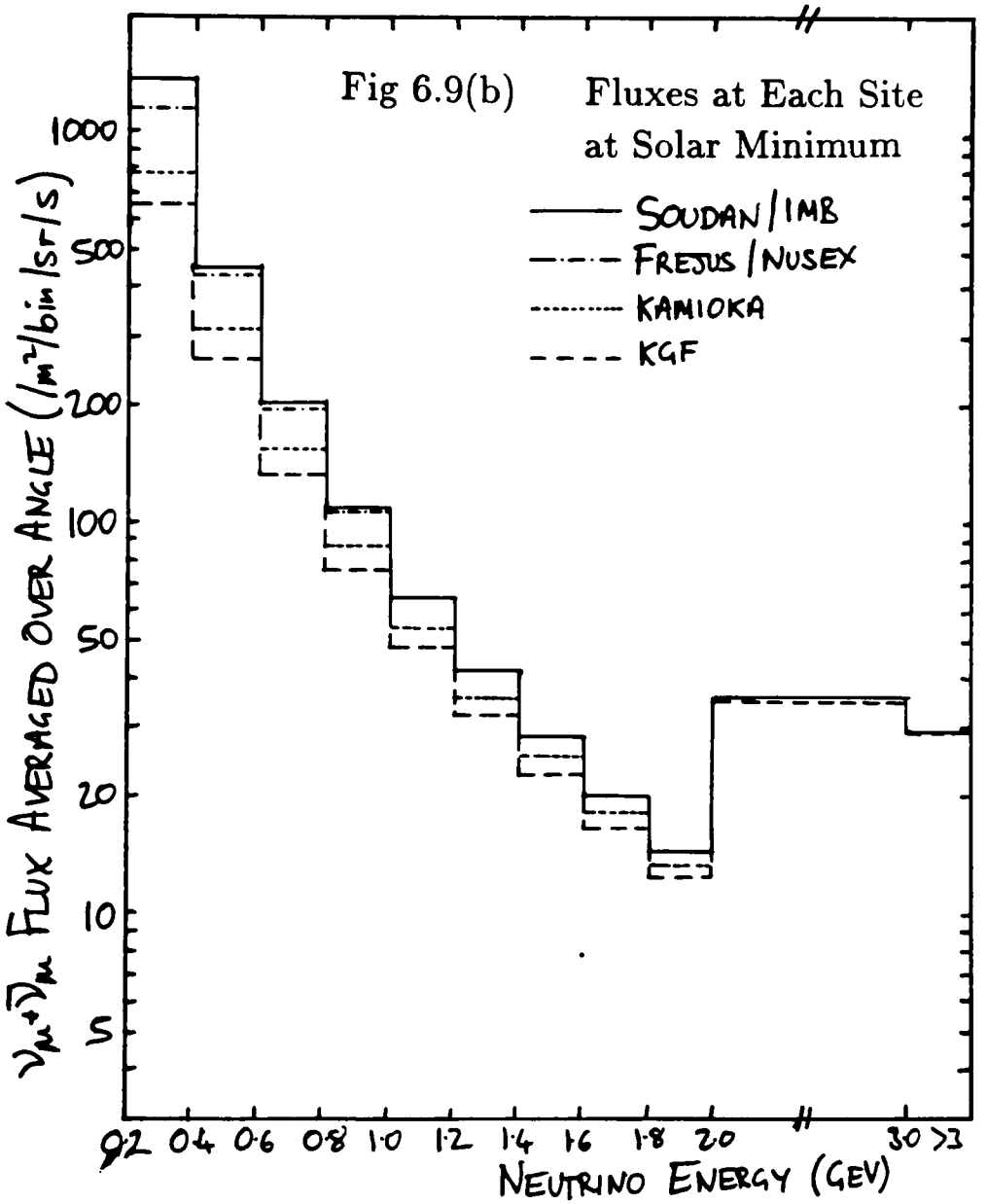
Fig 6.9(b) Fluxes at Each Site at Solar Minimum
SOUDAN/IMB
FREJUS/NUSEX
KAMIOKA
KGF
$\nu_\mu + \bar{\nu}_\mu$ FLUX AVERAGED OVER ANGLE ($/m^2$/bin/sr/s)
1000
500
200
100
50
20
10
5
0·2 0·4 0·6 0·8 1·0 1·2 1·4 1·6 1·8 2·0 3·0 >3
NEUTRINO ENERGY (GEV)

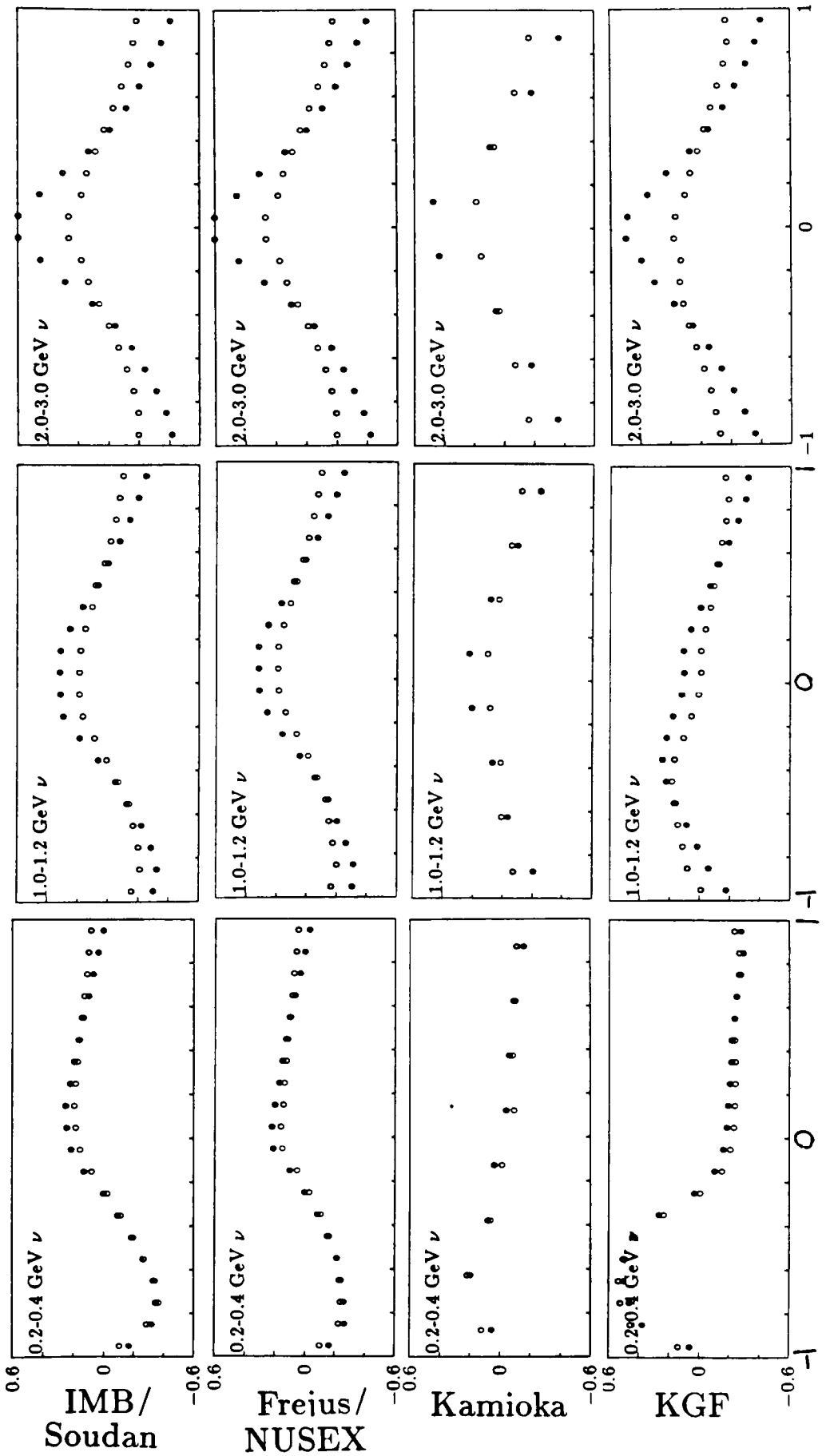

Fig 6.10 Flux variation with zenith angle
(see text)

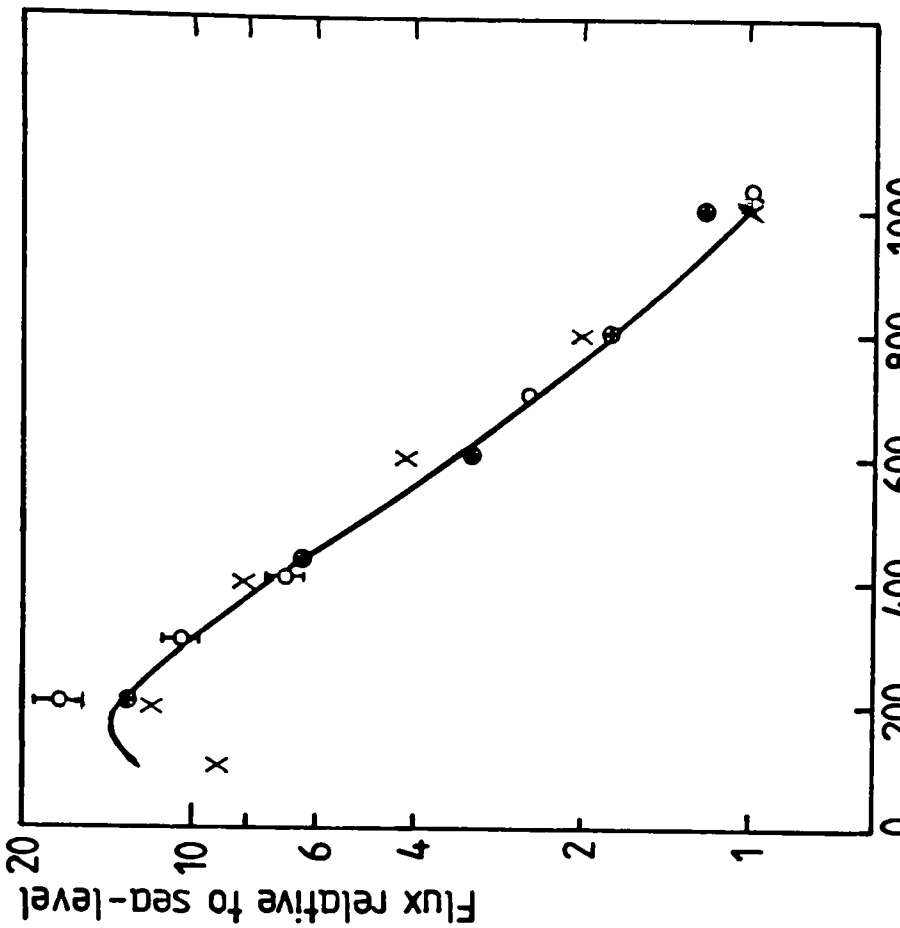

Fig 6.12 Depth Dependance of $\lambda = 50°$ muon fluxes
o Conversi ($p_\mu = 315 - 348$ MeV/c)
— Perkins (Olbert Method)
⊕ Perkins (MC method) ($p_\mu = 285 - 385$ MeV/c)
x This calculation ($p_\mu = 285 - 385$ MeV/c)

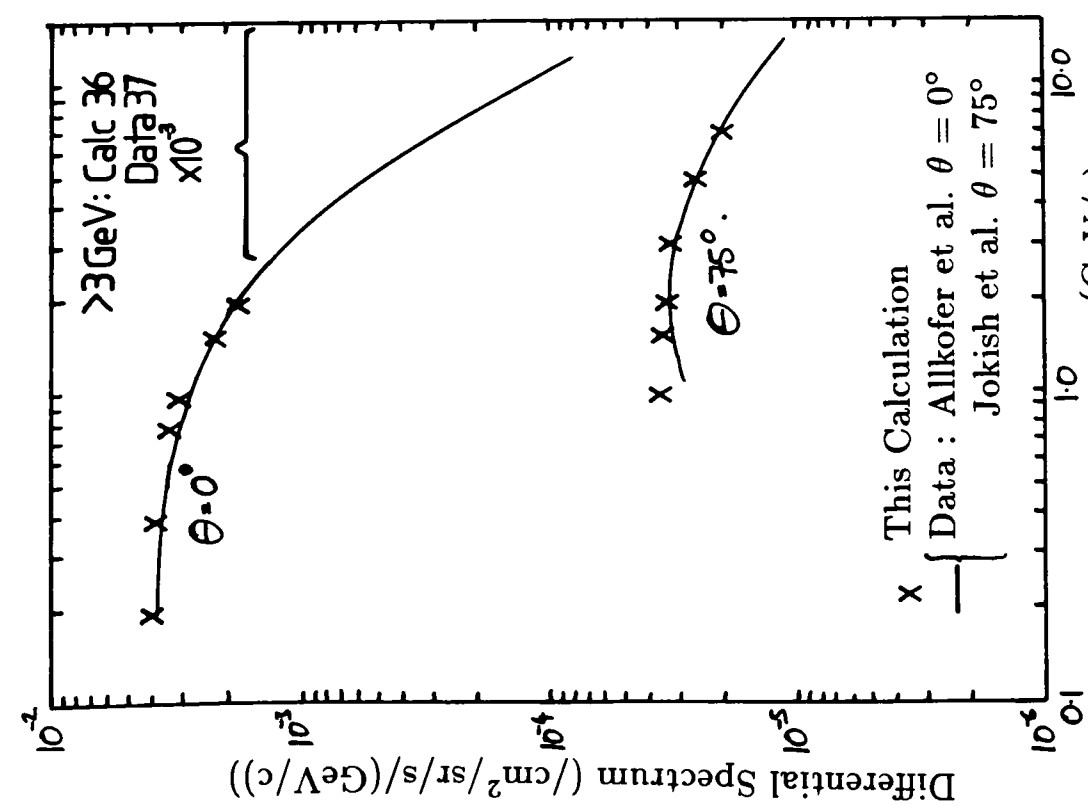

Fig 6.11 Vertical and Horizontal Muon Fluxes

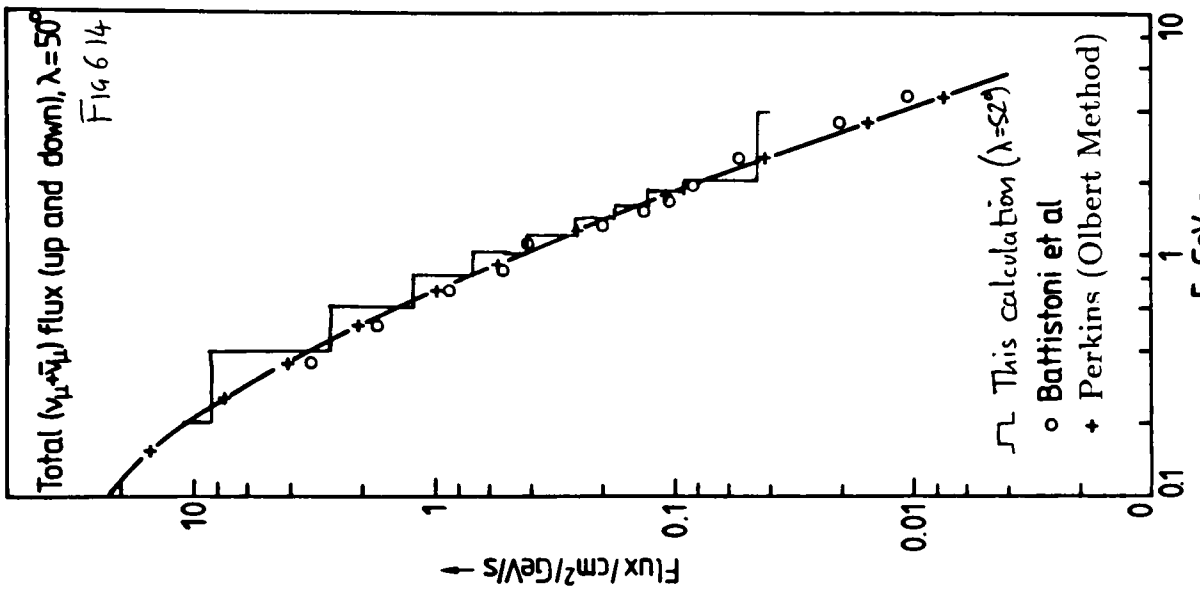
Total ($\nu_\mu+\bar{\nu}_\mu$) flux (up and down), $\lambda=50°$
Fig 6.14
Flux/cm²/GeV/s
E_ν GeV
This calculation ($\lambda=52°$)
Battistoni et al
Perkins (Olbert Method)

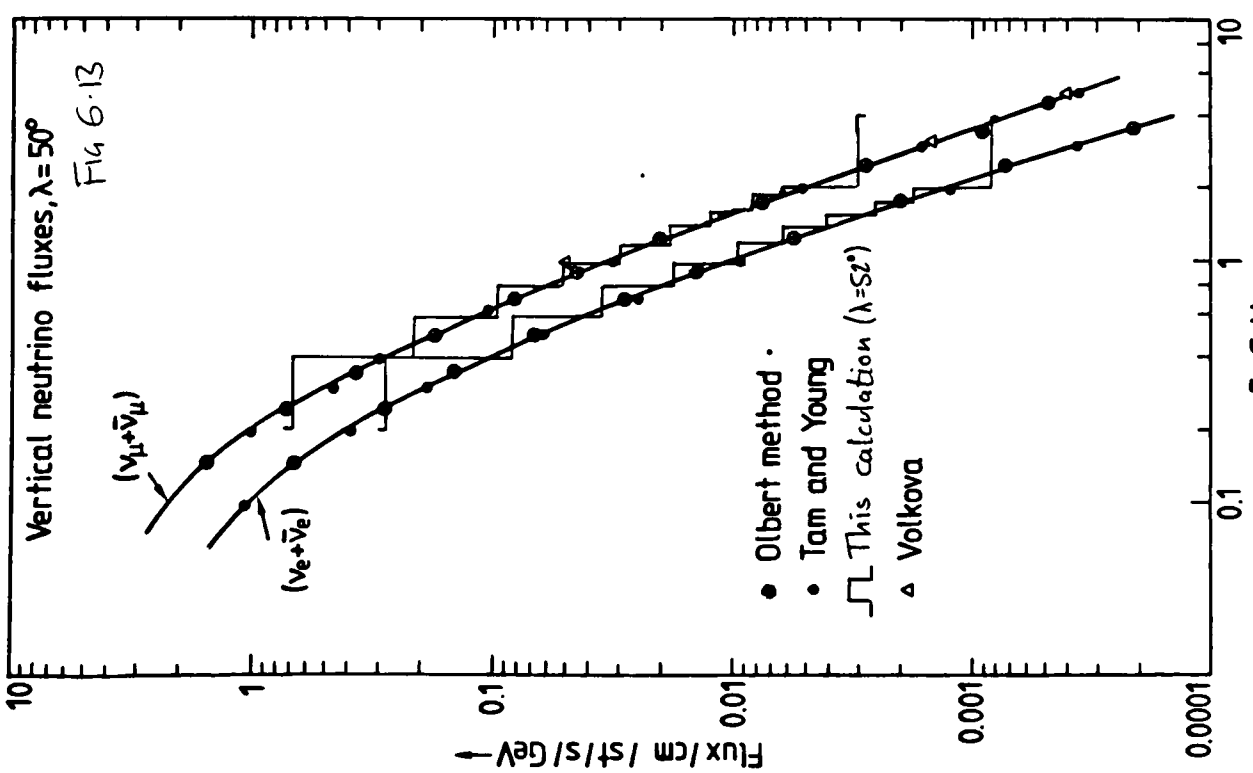
Vertical neutrino fluxes, $\lambda=50°$
Fig 6.13
($\nu_\mu+\bar{\nu}_\mu$)
($\nu_e+\bar{\nu}_e$)
Olbert method
Tam and Young
This calculation ($\lambda=52°$)
Volkova
Flux/cm²/st/s/GeV
E_ν GeV

6.13 Other Possible Sources of Neutrinos

In order to produce a noticeable signal in a proton decay detector, neutrinos must have energies of $>$ 100 MeV (for calorimeters) and $>$ 10 MeV (for Water Cerenkov detectors). Neutrinos from the sun are not energetic enough to produce a proton decay candidate event. The highest energy solar neutrinos are from boron-8 decay (end point ~14 MeV) and from the reaction $^3He + p \rightarrow ^4He + e^+ + \nu_e$ (18.8 MeV). Similarly neutrinos from terrestrial nuclear reactors are of too low an energy to be of concern.

Another possible source of neutrinos is as a remnant of the big bang. The 2.7K background radiation in the universe is mentioned in chapter 1. In addition, in the big bang model, there will be a background neutrino radiation which will also be left over. As the early universe cooled, the last particles to freeze out were the electron/positron. When this happened, the photons and neutrinos were essentially decoupled and have evolved independently since. Assuming massless left handed neutrinos, in terms of the photon number density N_γ [19] the number density of neutrinos of flavour i is given by

$$N_i = \frac{4}{11} \times \frac{3}{4} \times \frac{1}{2} \times N_\gamma$$

where the 4/11 is a temperature factor containing details of the decoupling from the photon radiation when the electrons froze out. 3/4 reflects the Fermi-Dirac statistics of the neutrinos as opposed to the Bose-Einstein statistics of the photons and the 1/2 is because the photon has two helicities wheres the left handed neutrino has only one. Assuming T_γ = 2.7K, a statistical mechanics calculation [19] yields $N_\gamma = 400/cm^3$, so N_i = 54 neutrinos per flavour per cubic centimetre (and about the same number of antineutrinos). These neutrinos have energy $E=kT_\nu$ where $T_\nu = (4/11)^{1/3} T_\gamma$ = 1.9K and $E_\nu \sim 10^{-4}$ eV. The cross section on nucleons at this energy is

$$\sigma \sim \frac{G^2 E^2}{\pi (\hbar c)^4} \simeq 10^{-64} cm^2$$

which gives an interaction rate in ordinary matter of about 10^{-11}/year/kTon. These neutrinos have a negligible contribution to the proton decay background.

Referenoes

[1] Lockwood J.A. and Webber W.R. Ap. J. 279 (1984) 151

[2] Longair M. S. "High Energy Astrophysics" CUP (1981)

[3] Simpson J.A. Ann. Rev. Nucl. Part. Sci 33 (1983) 325

[4] Letaw J.R., Silberberg R. and Tsao C.H. Ap. J. 279 (1984) 144

[5] Webber W.R. Ap. J. 255 (1982) 329

[6] Nerurkar N.W. Proc. Intl. Conf. Cosmic Rays (London) 1 (1965) 184

[7] Gaisser T. K. and Stanev T. "Cosmic Neutrinos" Proc. 6th Workshop on Grand Unification, Minneapolis, MN (1985).

[8] Stormer C. Ap. J. 1 (1930) 237

[9] Cooke D.J. Phys. Rev. Lett. 51 (1983) 320

[10] Barr G. D. and Gaisser T. K. Soudan 2 internal memo (not published)

[11] Perkins D. H. "Atmospheric Neutrino Fluxes" Oxford Nuclear Physics report 85/84 (1984).

[12] Gaisser T. K., Stanev T. and Barr G. D. "Muon Charge Ratio and Ratio of Neutrinos to Antineutrinos in Atmospheric Cosmic Rays" Proc. 20th Intl. Cosmic Ray Conf. Moscow (1987).

[13] Allkofer O. C. et. al. Phys Lett 36B (1971) 425

[14] Jokish A. et. al. Phys Rev D19 (1979) 1368

[15] Conversi M. Phys Rev 17 (1950) 749

[16] Tam A. C. and Young E. C. M. Acta Phys Acad. Sci Hung. 29 Suppl 4, (1970) 307

[17] Volkova L. V. Sov. J. Nucl. Phys. 31 (1980) 784

[18] Battistoni G. et. al. NIM 219 (1984) 310

[19] Bernstein J. "Neutrino Cosmology" Lectures given at the CERN academic training program 1983-4 CERN 84-06

Chapter 7

NEUTRINO INTERACTIONS ON FREE NUCLEONS

7.1 Introduction

In chapter 6, the flux of neutrinos passing through underground detectors has been described. In this chapter, the physics of neutrino interactions will be studied. In a proton decay background study, complete information about neutrino induced final states is required. There are three possible approaches to the problem.

(1) A small part of the detector can be exposed to a neutrino beam. The sample of events may then be compared to the events seen in the underground exposure to see if a particular proton decay candidate is compatible with the appearance of the neutrino interactions. The collaboration eventually proposes to adopt this approach.

(2) A collection of measurements from bubble chamber photographed events is run through a simulation program of the proton decay detector.

(3) A Monte-Carlo event generator program is written to generate neutrino events to run through the detector simulation. This method has been used in this thesis.

The three methods all suffer drawbacks. In methods (1) and (2), the neutrino flux from the accelerator will not be the same as the atmospheric neutrino flux, corrections to this will be difficult as the

neutrino energy must be estimated to apply a weight (difficult for neutral currents). In method (2), scanning inefficiencies must also be considered. Methods (2) and (3) must include a simulation of the effects of final state particles which reinteract with other nucleons in the parent nucleus. For method (3), no comprehensive generator is readily avaliable for such low energies, and one must be developed.

In methods (1) and (2), only muon type neutrino and antineutrino data are easily produced. Electron neutrino charged current data must be 'constructed' by replacing the muon with a suitably simulated electron track.

In this chapter, the physics involved in making a comprehensive low energy neutrino event generator for use in method (3) will be described. The generator must be able to produce all the possible types of events which may appear in the detector. Particular attention is paid to the neutrino energy region below 2 GeV. One of the problems of this study is simply keeping track of the large number of possible combinations of interactions. The cross sections to be described are dependent on the type of the incident neutrino (ν_e, $\bar{\nu}_e$, ν_μ or $\bar{\nu}_\mu$), on the type of the target nucleon (p or n) and on the type of the interaction (Charged Current (CC) or Neutral Current (NC). These 16 possibilities are considered separately in the generator.

Perturbative QCD cannot be applied to this problem, since $\alpha_s \sim 1$. Hadronic resonance production dominates the final state. The most prominent of these is the delta resonance $\Delta(1234)$. In the Monte-Carlo, contributions from the 16 most important nucleon and delta resonances are included. The resonant final state is allowed to decay and multiparticle final states may be produced (see fig 7.1). This will be discussed in detail in the next sections. It is found that summing the contributions from these modes of interaction reproduce the experimentally measured total cross sections for some final states, but underestimate the cross sections of others, in particular the higher multiplicity states. A non-resonant inelastic interaction is constructed

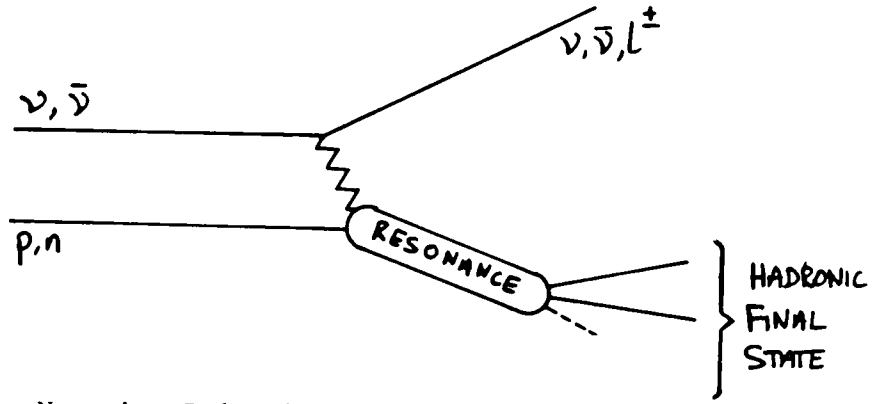

Fig 7.1 Neutrino Induced Resonance Production

to fill this gap. This interaction is based on the deep inelastic scattering formulation which is successful at higher energies.

7.2 The Kinematics of Neutrino Nucleon Interactions

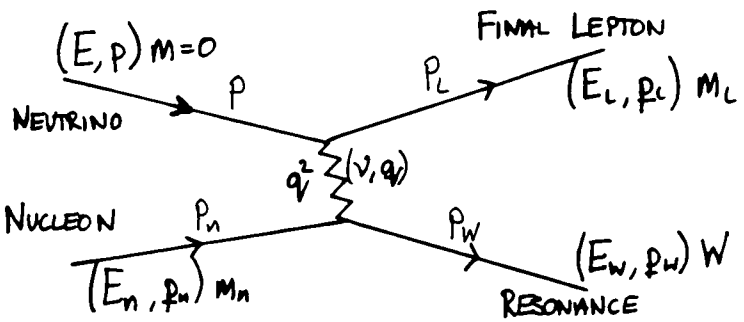

Fig 7.2

Consider an event as shown in fig 7.2 of known neutrino energy in the nucleon rest frame in which a lepton of mass m_l and hadronic final state of mass W are produced. The final state four vectors p_l and p_W must be determined. By using conservation of energy and momentum, and by equating $p_l \cdot p_l = m_l^2$, only two variables need to be chosen. For resonance work, it is common to choose the four momentum transfer squared q^2 and W as the two independent variables (some authors use q^2 and ν). Once these have been chosen, all other kinematic quantities are

fixed and may be computed using the formulae to be presented below.

Quasielastic and elastic scattering have the additional constraint that the final nucleon mass is fixed, so $W = m_n$, only q^2 may be selected, the other quantities become constrained.

The differential cross sections for resonance production are expressed most conveniently as $d\sigma/dq^2/dW$ and may be used to select values for q^2 and W for each event generated. This will be discussed for each type of interaction in the following sections.

Assuming that the incoming neutrino has its momentum along the z axis, ie $E = p_z$, $p_x = p_y = 0$ and the plane containing $\underline{p}_l$ and $\underline{p}_W$ is the x-z plane ($p_{yl} = p_{yW} = 0$) the following expressions define the kinematics of the event in the nucleon rest frame :

$$\nu = (E - E_l) = (W^2 - m_n^2 - q^2)/2m_n$$

$$q_4^2 = \nu^2 - q^2$$

$$p_{zl} = (E_l^2 + E^2 - q_4^2 - m_l^2)/2E$$

$$p_{xl}^2 = q_4^2 - (p - p_{zl})^2$$
$$= q_4^2 - (E - p_{zl})^2$$

$$p_{zW} = E - p_{zl}$$

$$p_{xW} = -p_{xl}$$

At a fixed value of E, the allowed kinematic region on the (q^2, W) plane may be derived. The Lorentz invariant quantity

$$S = (p + p_N)^2 = (E^* + E_N^*)^2 = (E_l^* + E_W^*)^2$$

is the total centre of mass energy of the system (asterisks denote centre of mass variables). The maximum value of W is such that

$$S = (W + m_l)^2 \Rightarrow W_{MAX} = \sqrt{S} - m_l$$

where s is computed using

$$S = m_n^2 + 2m_n E$$

and the minimum value is the smallest which still allows decay into nucleon and pion

$$W_{MIN} = m_n + m_\pi$$

The limits of q^2 are obtained by expressing q^2 in terms of the centre of mass angle θ^* (see fig 7.3).

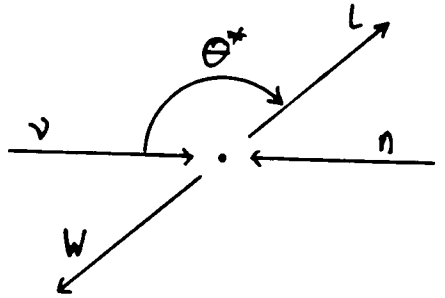

CENTRE OF MASS SYSTEM

FIG 7.3

$$q^2 = (p - p_l)^2 = m_l^2 - 2E^*(E_l^* - |p_l|^* \cos\theta^*)$$

$$q^2 = m_l^2 - \frac{(s-m_n^2)}{2s}\left[(s+m_l^2-W^2) - ((s+m_l^2-W^2)^2 - 4sm_l^2)^{1/2}\cos\theta^*\right]$$

Maximum and minimum values of q^2 are obtained by setting $\cos\theta = \pm 1$. The kinematically allowed region at E = 1 GeV is shown in fig 7.4. For neutral currents in which $m_l = 0$, the limits simplify to

$$-(s-m_n^2)(s-W^2)/s \leqslant q^2 \leqslant 0$$

Inelastic differential scattering cross sections are cast in terms of the independent variables x and y

$$x = \frac{-q^2}{2q\cdot p_n} = \frac{-q^2}{2m_n\nu} \qquad \text{and} \qquad y = \frac{q\cdot p_n}{p\cdot p_n} = \frac{\nu}{E} \text{ in the nucleon rest frame}$$

q^2 and W can then be computed using the following relations

$$q^2 = -2\, m_n\, x\, y\, E$$

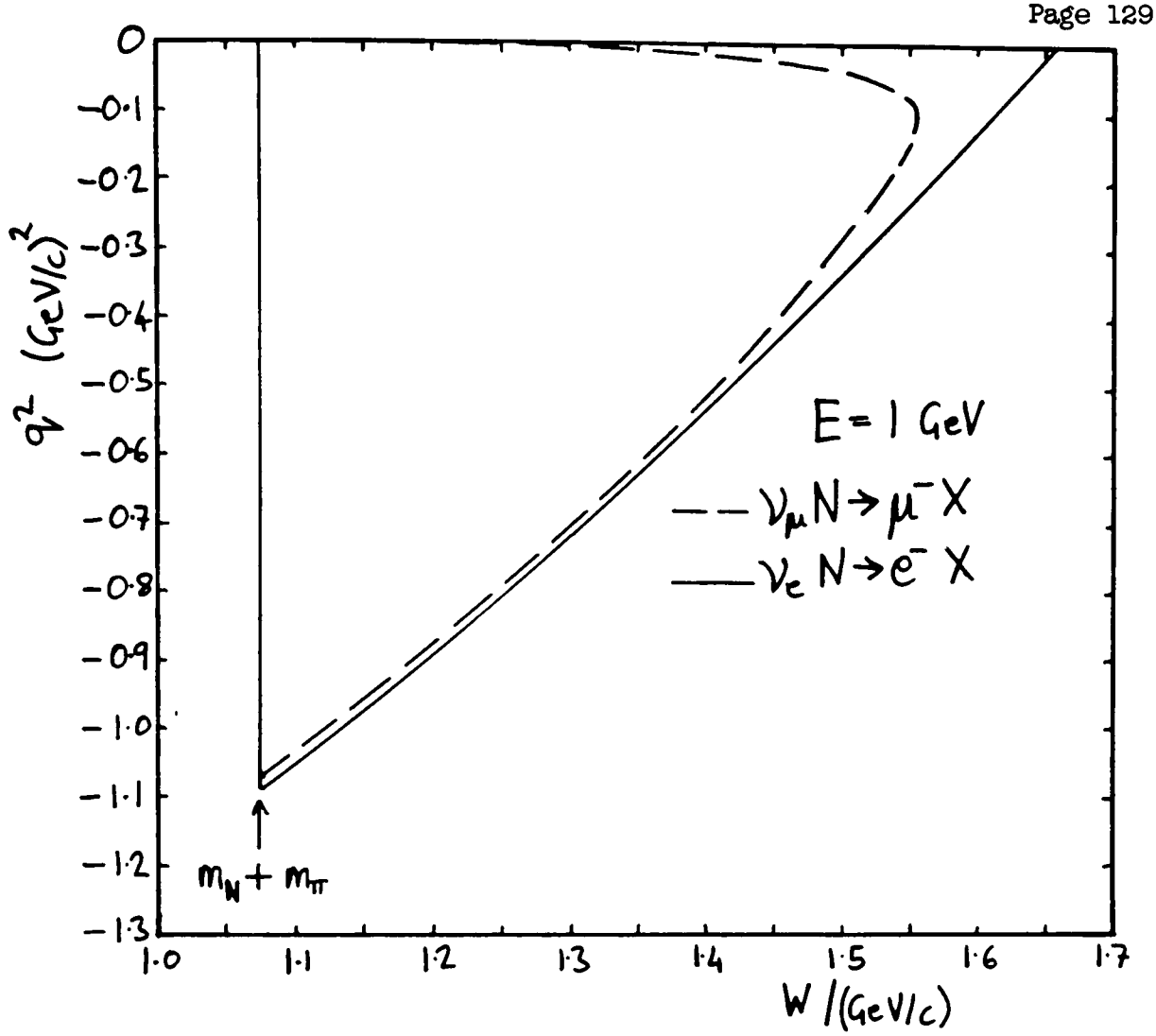

Fig 7.4 Kinematically allowed regions in (q^2,W) space for 1 GeV neutrino charged current interactions.

$$W = \left(m_n^2 + 2\, m_n\, y\, E + q^2 \right)^{1/2}$$

It is then straightforward to find the other kinematic variables using the expressions above.

7.3 Elastic and Quasielastic Neutrino Nucleon Scattering

The differential cross sections for elastic ($\nu N \to \nu N$) and quasielastic ($\nu N \to \mu N'$) scattering are taken from the book by Commins

and Bucksbaum [1]. It is expressed in terms of form factors f_1, f_2, and g_1. The form factors express the fraction of each interaction term on the nucleon as a whole. If the nucleon were a structureless spin 1/2 Dirac particle, the form factors would be $f_1 = g_1 = 1$ and $f_2 = 0$. To take account of the nucleon structure these values are allowed to be functions of q^2. Values for each form factor are given in [1]. f_1 and f_2 are determined from electron scattering experiments and are changed depending on whether the target is a proton or a neutron and the interaction CC or NC. g_1 is the axial vector form factor and is assumed to be of the form

$$g_1 = \frac{1.25}{\left(1 - q^2/m_A^2\right)^2}$$

The "1.25" is obtained from nuclear beta decay data and m_A is extracted from the q^2 dependence of the experimental neutrino scattering cross sections. The preferred value given in [1] of $m_A = 0.95$ GeV/c^2 has been used.

The total cross section as a function of E is compared with data in fig 7.5 for charged current interactions. Good agreement is seen. Note that charged current quasielastic interactions with initial state particles νp and $\bar{\nu} n$ do not occur. In fig 7.6 the differential cross sections are shown at E = 0.5 GeV and at E = 2 GeV. The conventional $1/q^2$ behaviour is only apparent at high energy. Interactions of low energy are almost uniform in q^2, a large fraction of the energy is transferred to the nucleon.

7.4 Neutrino Induced Resonance Production

The differential cross sections $d\sigma/dq^2/dW$ for the production of resonances are taken from Rein and Seghal [2]. The treatment follows similar lines to the quasielastic and elastic cross sections in the previous section. The form factors are constructed from quark model representations of the final state resonance. The axial form factors contain the factor

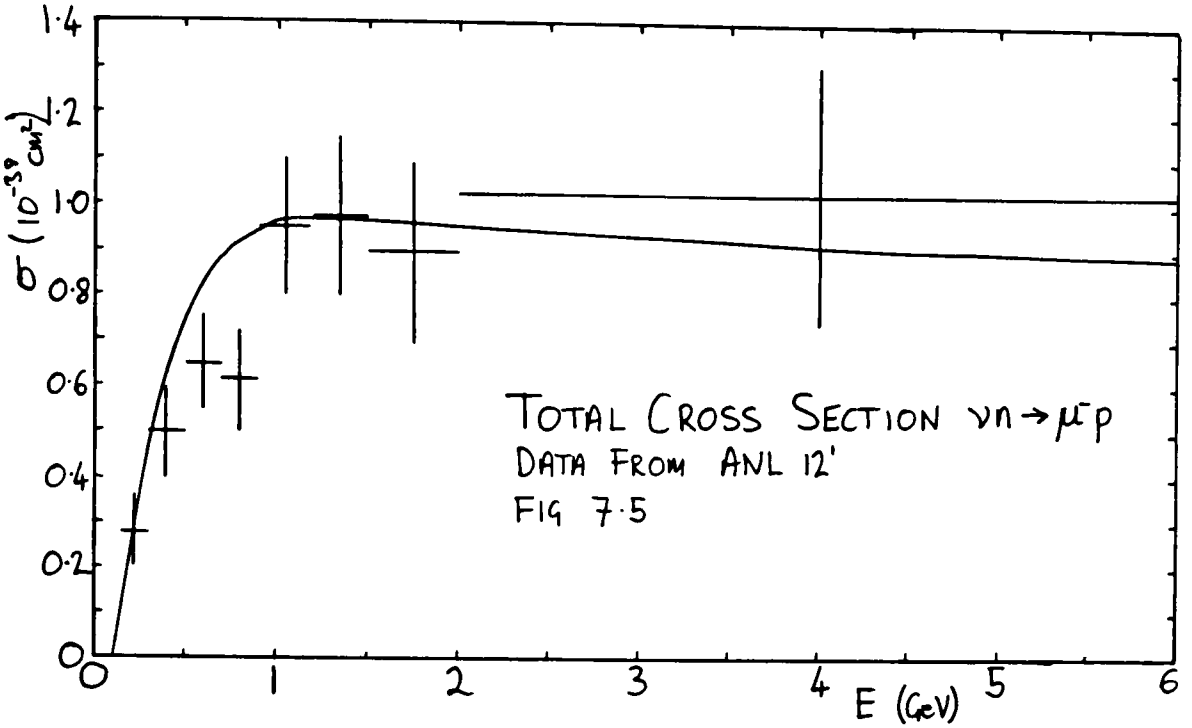

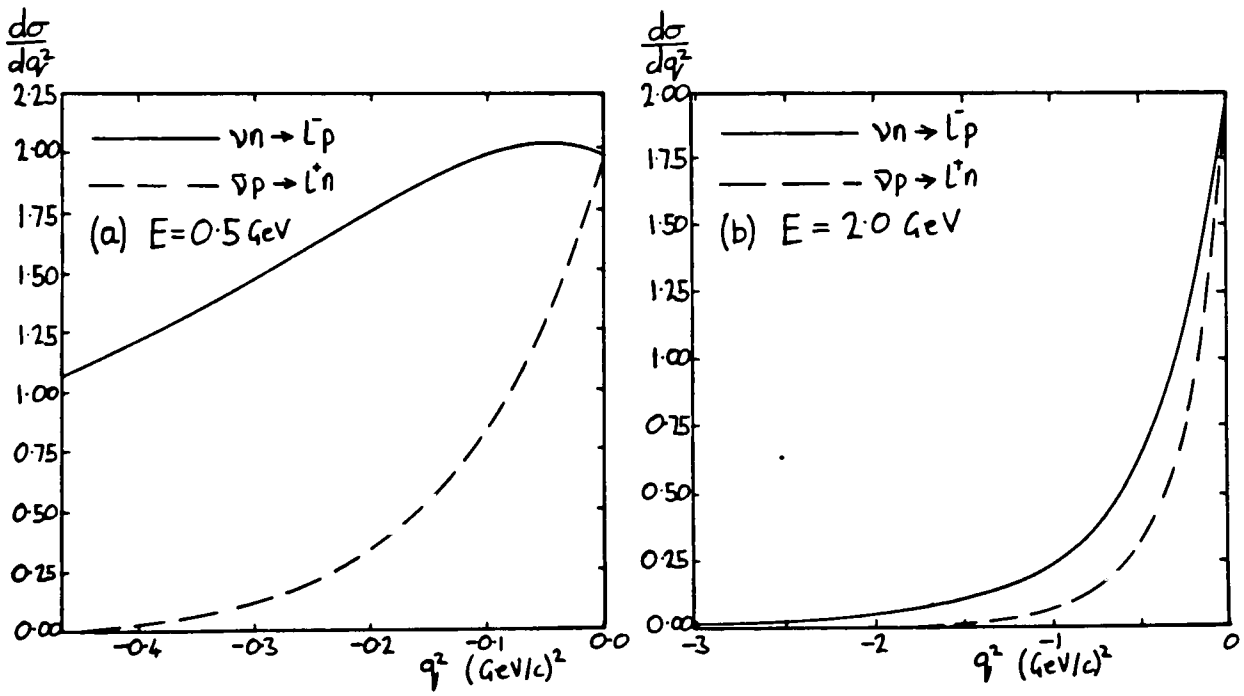

FIG 7·6 DIFFERENTIAL QUASIELASTIC CROSSSECTIONS

$$\frac{1}{\left(1 - q^2/M_A^2\right)^2}$$

which is familiar from the previous section. The value for m_A is also chosen to be 0.95 MeV/c^2 as used by Rein and Seghal. A total of 16 nucleon and delta resonances are used (see table 7.1). The oscillator

Code No.	Resonance (L 2I 2J (Mass))	PDB designation	Width (GeV)	Oscillator Quantum Number
1	P_{33} (1234)	Δ(1232)	0.124	0
2	P_{11} (1450)	N(1440)	0.370	2
3	D_{13} (1525)	N(1520)	0.125	1
4	S_{11} (1540)	N(1535)	0.270	1
5	S_{31} (1620)	Δ(1620)	0.140	1
6	S_{11} (1640)	N(1650)	0.140	1
8	D_{13} (1670)	N(1700)	0.080	1
9	D_{15} (1680)	N(1675)	0.180	1
10	F_{15} (1680)	N(1680)	0.120	2
11	P_{11} (1710)	N(1710)	0.100	2
12	D_{33} (1730)	Δ(1700)	0.300	1
13	P_{13} (1740)	N(1720)	0.210	2
14	P_{31} (1920)	Δ(1910)	0.300	2
15	P_{35} (1920)	Δ(1905)	0.340	2
16	F_{37} (1950)	Δ(1950)	0.340	2
17	P_{33} (1960)	Δ(1920)	0.300	2

Table 7.1 Resonances Included in the Neutrino Event Generator

quantum number shown in table 7.1 is a quantum number of each resonant state in the quark counting model used in [2] and appears in the form factors. The resonances included are listed in the particle data book (1984) [8] as 4 star "Good clear and unmistakable" or 3 star "Good but in need of clarification or not absolutely certain" resonances. The isospin I=3/2 channel is dominated by the $P_{33}(1234)$. In the I=1/2 channel, the $S_{11}(1540)$, $D_{13}(1525)$ and P_{11} (1450) also have large contributions. The other resonances contribute little, but have different decay modes which may be important for particular proton decay mode studies.

The total cross sections are obtained by numerically integrating over q^2 and then W. Fig 7.7 shows the integrand of the q^2 integral at fixed W for the $\Delta(1234)$ resonance. Note that the q^2 distribution has a

large contribution at high q^2 as for low energy quasielastic interactions. The W integrand is shown in fig 7.8. The shape is given predominantly by a spin dependent Breit-Wigner factor in the density of states part of the cross section. The total cross sections as a function of energy are given for a sample of resonances in fig 7.9. In general, the cross sections rise steeply from threshold and flatten off by E = 20 GeV. Antineutrino cross sections are less than neutrino cross sections and rise more slowly. Some of the more exotic resonances have cross sections which are still rising at E = 20 GeV.

The generator selects a value of q^2 and of W from the appropriate expression and the final state four vectors of each particle are determined from the expressions of section 7.2. The resonance is allowed to decay according to the branching ratios given in the particle data book. In all cases, the decays are two body, the angle of emission of the products is chosen isotropically in the centre of mass. The branching ratios used are shown in table 7.2. In some cases the branching ratios were adjusted slightly in order to make the total 100%. The final state charges are assigned using Clebsch Gordon coefficients by expressing the parent isospin I = 3/2 or I = 1/2 as a vector sum of the daughters.

The total exclusive cross sections may now be computed by summing the product of the cross sections and branching ratios over all the resonances. In the case of $\nu p \rightarrow \mu^- \Delta^{++} \rightarrow \mu^- p \pi^+$, the resulting cross section agrees well with bubble chamber measurements [6], see fig 7.10. This cross section is due almost entirely to the resonance $\Delta(1234)$. Other exclusive channels and the total cross section predictions fall below the data. Rein and Seghal overcome this problem by adding a non resonant I = 1/2 background. This method does not indicate how the non resonant state should decay. I have used a different approach.

The cross section expressions from Rein and Seghal neglect the mass of the final lepton which will not affect the background calculations from the generator, since the model correctly fits the

Fig 7.7 Differential cross section for Δ^{++} production

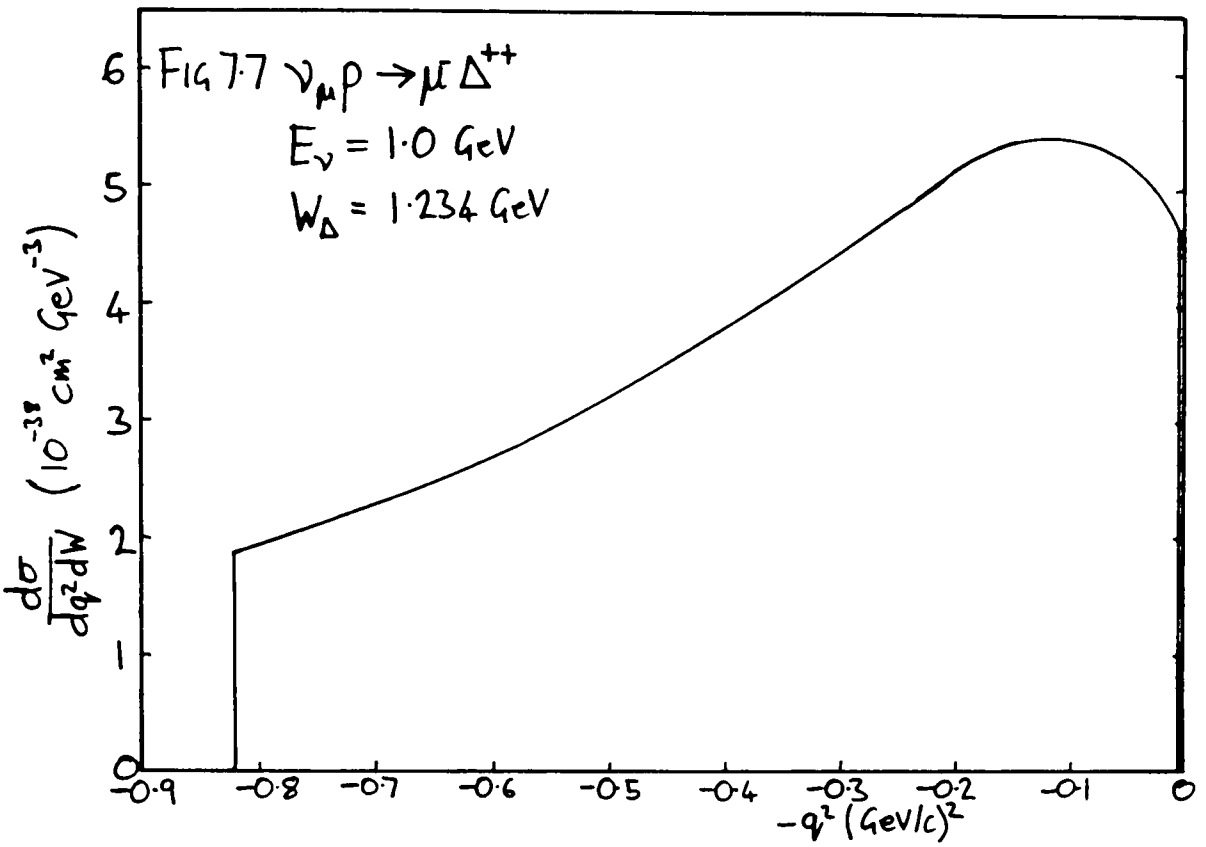

Fig 7.8 Differential cross section for Δ^{++} production

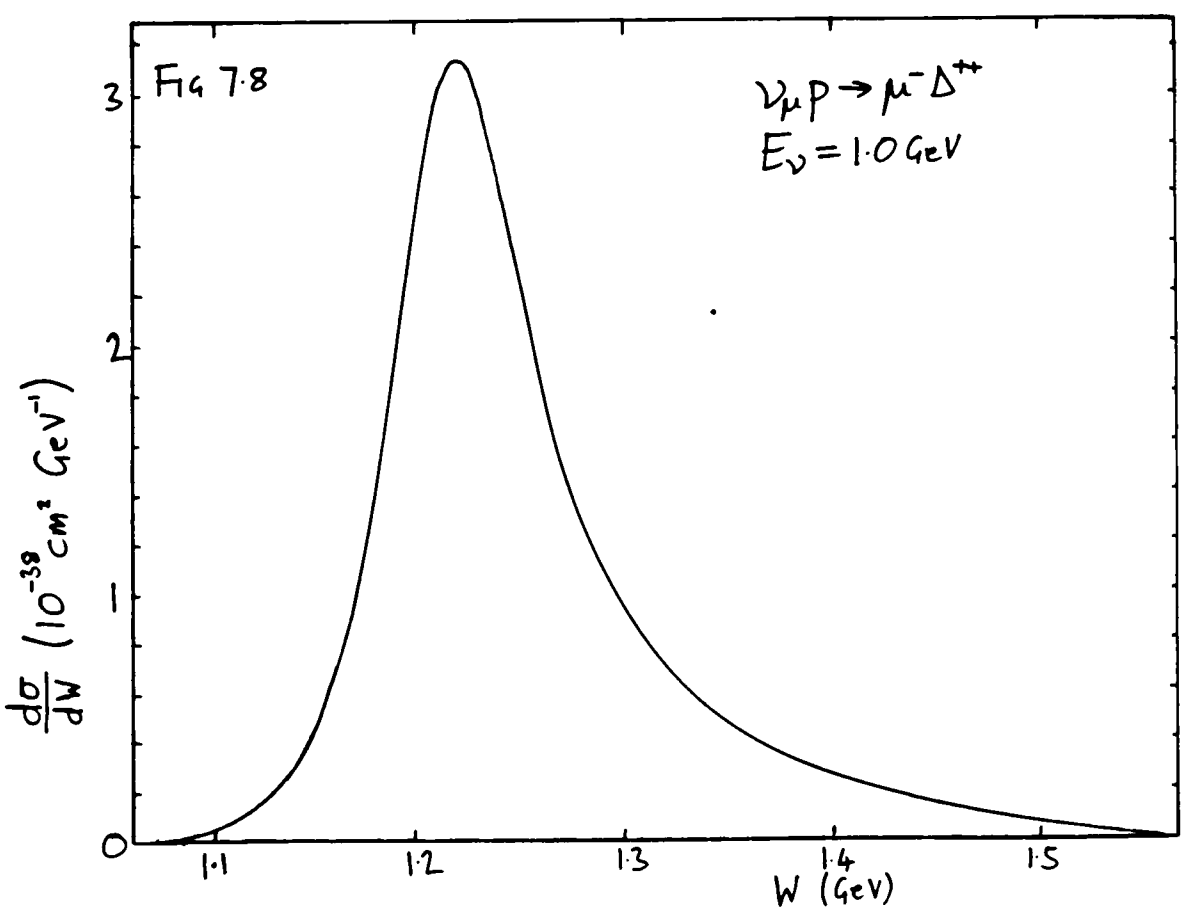

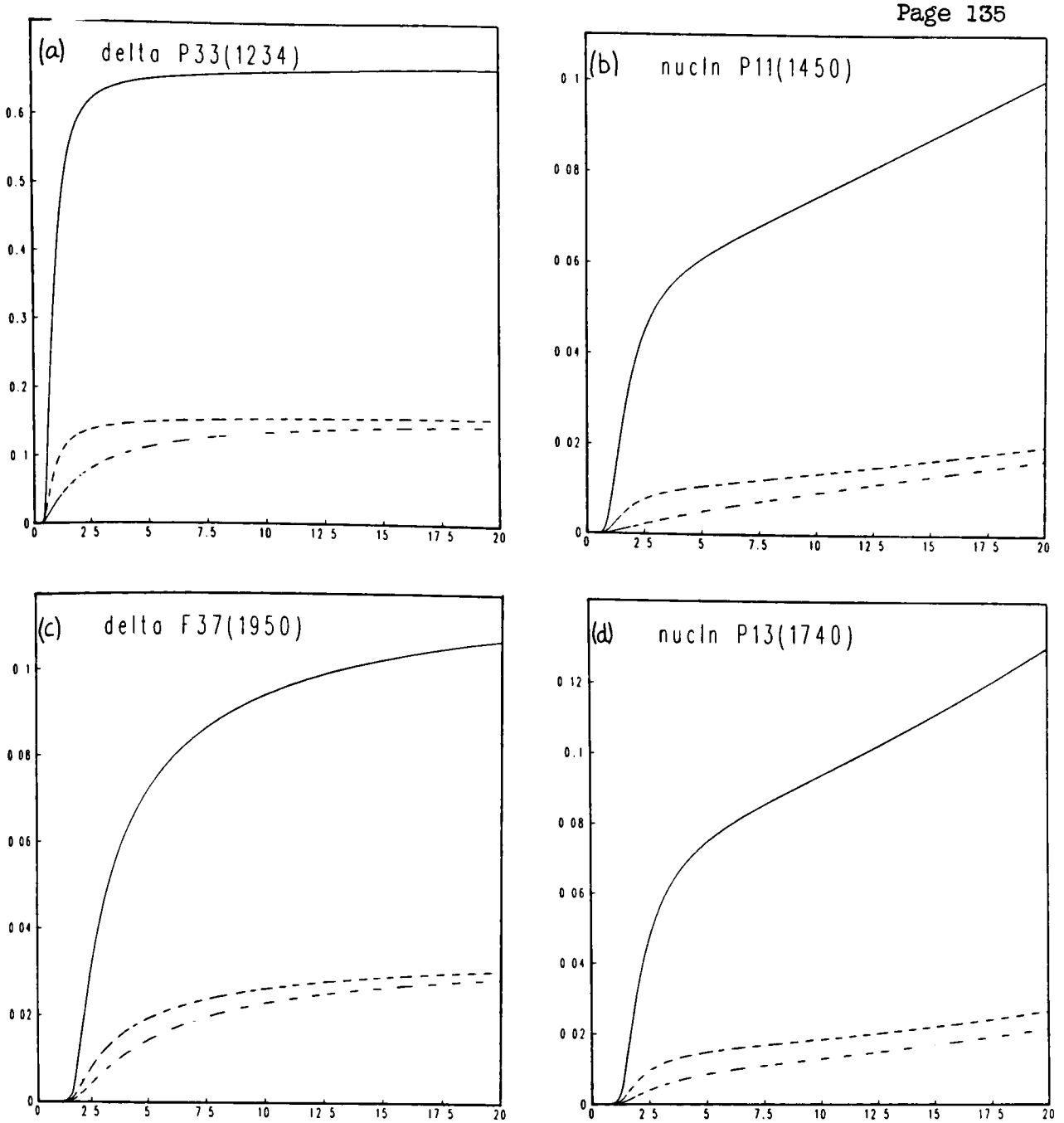

Fig 7.9 Total Cross sections for exitation of resonances

νp, $\bar{\nu} n$ } Charged Current

νp, $\bar{\nu} n$ } Neutral Current

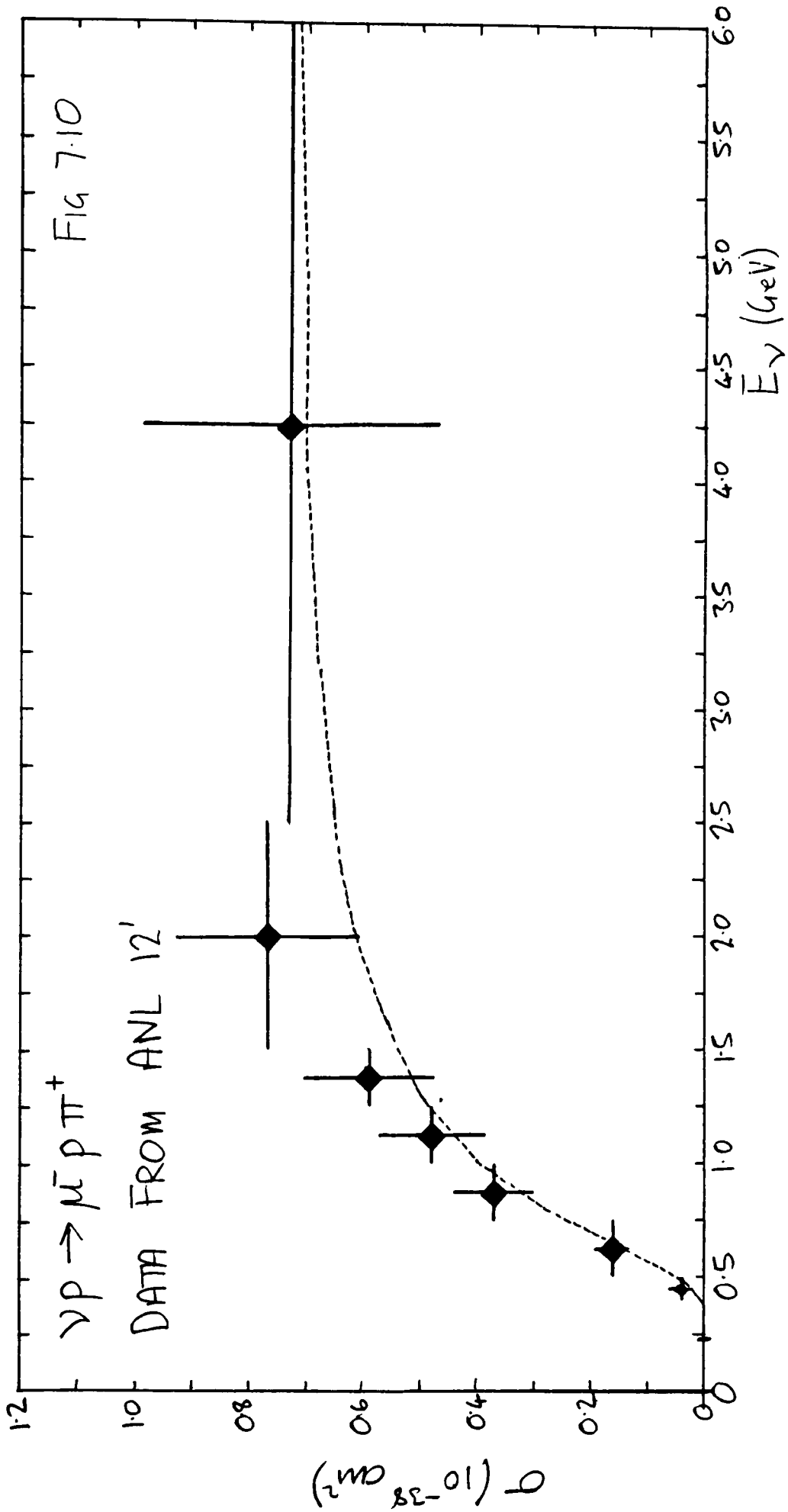
FIG 7.10
$\nu p \to \mu^- p \pi^+$
DATA FROM ANL 12'
σ (10^{-38} cm^2)
$\bar{E}_\nu$ (GeV)
0
0.2
0.4
0.6
0.8
1.0
1.2
0.5
1.5
2.0
2.5
3.0
3.5
4.0
4.5
5.0
5.5
6.0

Code Number	Resonance N	Decay Mode						
		$N\pi$	$N\eta$	$\Delta\pi$	$N\rho$	$N\varepsilon$	ΛK	ΣK
2	P_{11} (1450)	.580	.120	.180	.070	.050	.000	.000
3	D_{13} (1525)	.549	.001	.210	.210	.030	.000	.000
4	S_{11} (1540)	.500	.400	.020	.050	.030	.000	.000
6	S_{11} (1640)	.550	.015	.060	.200	.050	.075	.050
8	D_{13} (1670)	.108	.040	.400	.050	.400	.002	.000
9	D_{15} (1680)	.350	.010	.589	.050	.000	.001	.000
10	F_{15} (1680)	.595	.005	.110	.100	.190	.000	.000
11	P_{11} (1710)	.110	.220	.100	.250	.150	.130	.040
13	P_{13} (1740)	.180	.035	.200	.300	.200	.050	.035

Code Number	Resonance Δ	Decay Mode			
		$N\pi$	$\Delta\pi$	$N\rho$	ΣK
1	P_{33} (1234)	1.000	.000	.000	.000
5	S_{31} (1620)	.300	.400	.300	.000
12	D_{33} (1730)	.150	.450	.400	.000
14	P_{31} (1920)	.350	.005	.400	.250
15	P_{35} (1920)	.150	.220	.600	.030
16	F_{37} (1950)	.390	.400	.200	.010
17	P_{33} (1960)	.200	.375	.375	.050

Table 7.2 Primary Decay Modes for Resonances in the Neutrino Event Generator. (Seperate listings for nucleon and delta type Resonances)

data. Once q^2 and W have been selected, the kinematics which are used to compute the particle four vectors do take the lepton mass into account, so kinematically perfect events will be produced by the generator.

7.5 The Inelastic Contribution to the Neutrino Cross Section

The method adopted here is to use deep inelastic scattering theory which predicts the total inclusive cross section. From [8]

$$\frac{d^2\sigma^{\nu}_{\bar{\nu}}}{dxdy} = \frac{G_F^2 ME}{\pi}\left[\left(1-y-\frac{M}{2E}xy\right)F_2^{\nu}_{\bar{\nu}} + \frac{y^2}{2}2xF_1^{\nu}_{\bar{\nu}} \pm \left(y-\frac{y^2}{2}\right)xF_3^{\nu}_{\bar{\nu}}\right]$$

for the total neutrino-nucleon cross section where x and y are kinematic variables as described in section 7.2. At high energy, the cross

section is proportional to E which is in agreement with data [8]. Expressions for the structure functions F_1, F_2 and F_3 in terms of the quark density functions u(x), d(x), s(x) etc. are given in [8]. These play a similar role to the form factors in the resonant and elastic scattering expressions. Different functions are required for F_1, F_2 and F_3 for charged and neutral currents and for neutrino and antineutrino interactions.

The quark density functions have been taken from the parameterisations of Gluck, Hoffmann and Reya [3]

Valance Quarks (proton)
$$U_V(x) = 2 \times 1.23 x^{0.421} (1-x^2)^{3.37}$$
$$d_V(x) = 2 \times 0.541 x^{0.364} (1-x^2)^{5.09}$$

Sea Quark distributions
$$U_S(x) = d_S(x) = 2 \times 0.25 (1-x)^7$$
$$S_S(x) = 2 \times 0.0625 (1-x)^7$$

The neutron distributions are obtained by exchanging u and d distributions. In the final model, the s quark sea distribution is neglected, as it is a small contribution and hadronisation of the final state is difficult. The inclusive neutrino and antineutrino cross sections on a target composed of equal numbers of protons and neutrons is computed by numerical integration of $d\sigma/dx/dy$ over the kinematically allowed region of the x-y plane.

Once the values of x and y have been chosen for a particular event, the other kinematic parameters are defined. The hadronic final state is now allowed to 'decay' into the final hadronic particles. The multiplicity of the final (hadronic) state is found to be proportional to ln W [4]. The multiplicity of a given event is chosen by a method inspired by KNO (Koba, Nielsen, Olesen) scaling. It is experimentally observed [4] that for the multiplicity distribution P(n,W), the plot of $\langle n \rangle$ P(n,W) against $n/\langle n \rangle$ will be independent of W (see fig 7.11 from [4]) in the high energy scattering events, where $\langle n \rangle$ may be fitted to the form

$$\langle n \rangle = a + b \ln W$$

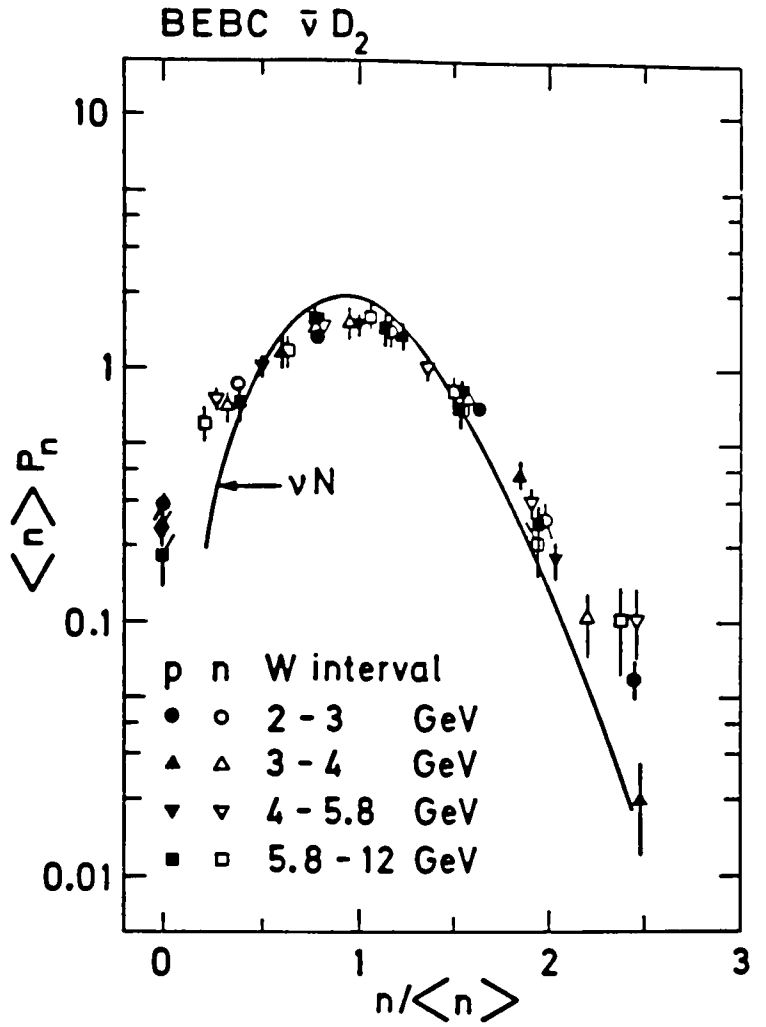

Fig 7.11 KNO multiplicity Distribution which has been used for the event generator. Data from a compilation by Schmitz [4]. Line is an 'eyeball' fit to neutrino data (from Schmitz).

For the low energy events in this study, the mean multiplicity is selected using the above parameterisation and then a multiplicity selected from the distribution of fig 7.11. The values used for a and b are summarised below

Reaction	a	b
p	0.5	1.3
n	0.0	1.3
p	0.2	1.3
n	0.2	1.3

These were estimated using the summary of data found in [4] for the charge multiplicity at higher energies. Note that ‹n› here is the total hadronic multiplicity. It will be seen later that a good overall fit to the data is obtained using these figures.

The above treatment is for inclusive cross sections. Since a complete description of quasielastics/elastics and resonance production has been included separately, a part of the inclusive cross section must be removed. The resonances can only produce a significant contribution for a multiplicity of 3 or less, so only the low multiplicity must be corrected. A constant fraction of the inclusive cross section for each multiplicity separately is subtracted, the fractions are chosen by requiring that the resonance contribution is exactly cancelled by the correction at E = 20 GeV.

The total cross section as a function energy for neutrinos and for antineutrinos are shown in figs 7.12 and 7.13. Also shown are the total resonance production and the total inclusive cross section (before low multiplicity removal). The corrected cross section fits the data extremely well, especially in the most important region around E = 1GeV.

The particle type assignment for the inclusive reactions is taken from Corrigan [5]. The meson type assignment is the same as the algorithm used in the cascade Monte-Carlo of Gaisser and Stanev as used in Chapter 6. Firstly the nucleon is selected. For an initial νp state, the probability of getting a proton (neutron) is 2/3 (1/3), for $\bar{\nu}n$, 1/3 (2/3) and for νn and $\bar{\nu}p$, 1/2 (1/2). Next, the final state is given the correct charge by assigning π^+ or π^- to the necessary number of particles. The remaining particles are assigned in pairs as $\pi^+\pi^-$(60%), $\pi^0\pi^0$(30%), K^+K^- (5%) and $K^0\bar{K}^0$ (5%). If there is a single odd particle left, it is assigned as π^0.

The final state four vectors of the hadronic part of the event are obtained by 'decaying' the hadronic system of mass W as given by phase space. This is done with code in the Soudan 2 Monte-Carlo which is also used for simulating multiparticle proton decay events.

Using the assignments described above, the cross sections of various exclusive processes have been computed and are shown compared with data [6,7] in figs 7.14-19. In all cases, agreement is good. The model will also be used to predict the cross sections for the modes for

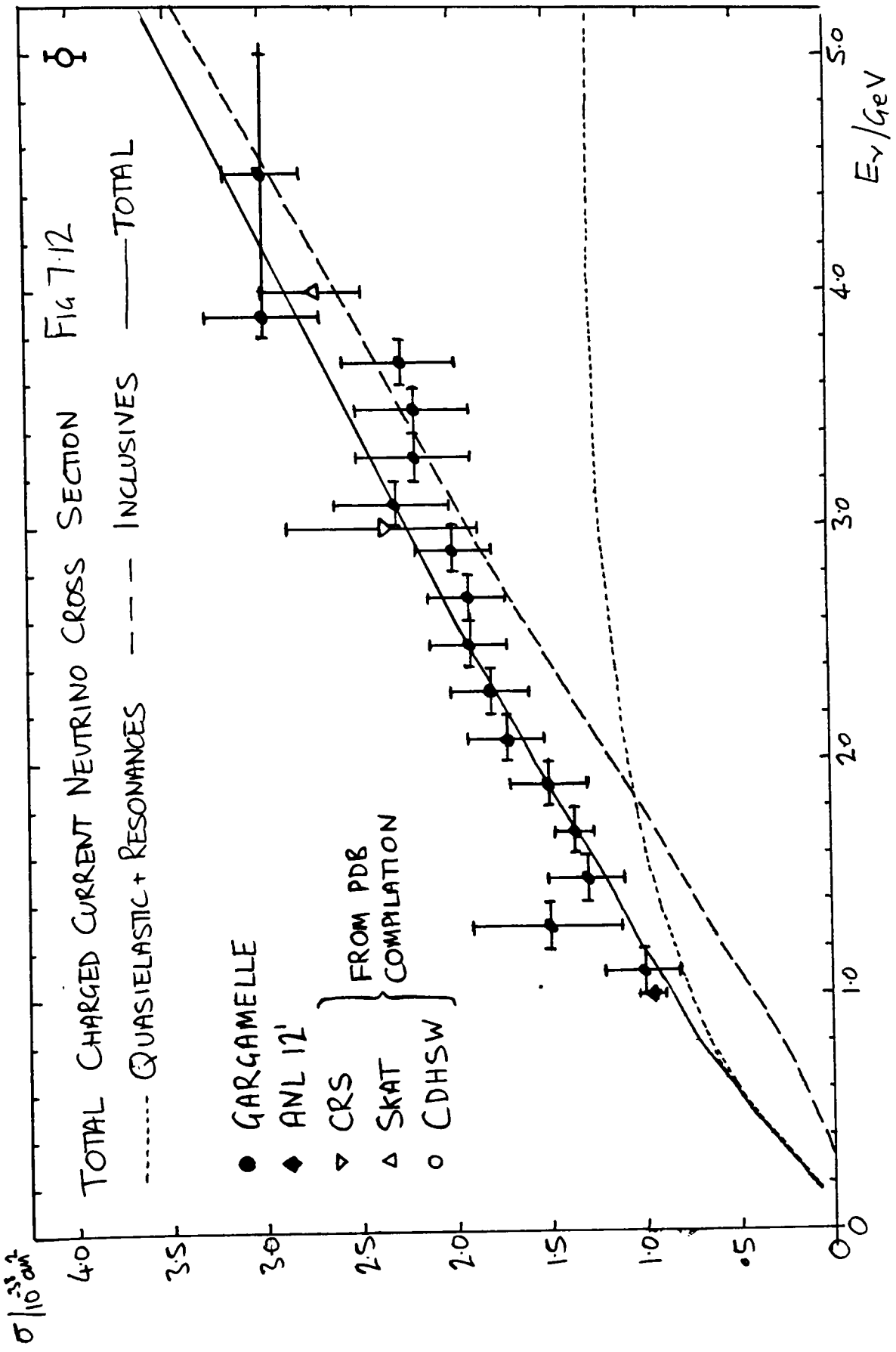
TOTAL CHARGED CURRENT NEUTRINO CROSS SECTION
FIG 7·12
------ QUASIELASTIC + RESONANCES - - - - INCLUSIVES ——— TOTAL
● GARGAMELLE
◆ ANL 12'
▽ CRS
△ SKAT
○ CDHSW
} FROM PDB COMPILATION
σ/10⁻³⁸ cm²
Eν/GeV
4·0
3·5
3·0
2·5
2·0
1·5
1·0
·5
0
1·0
2·0
3·0
4·0
5·0

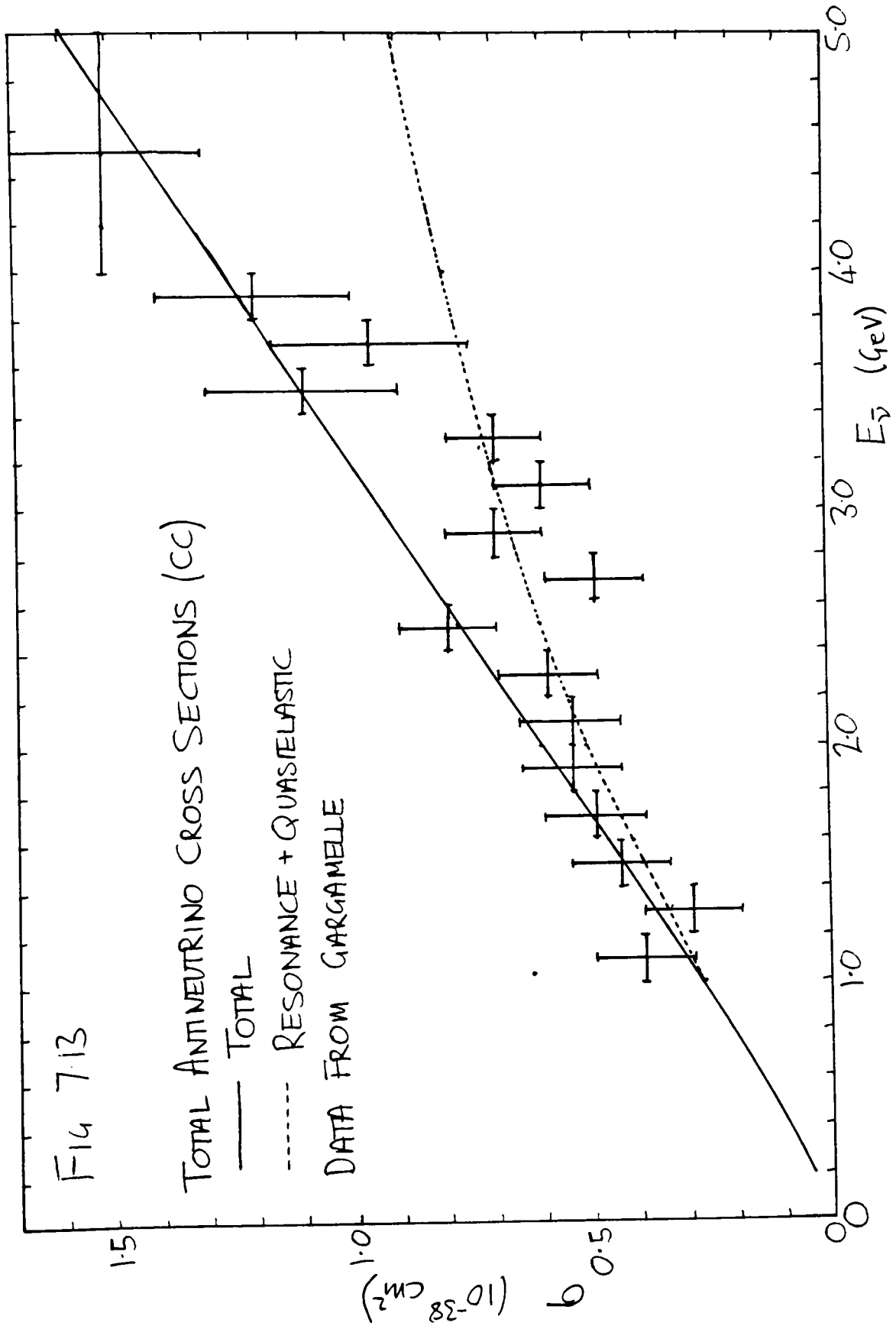
FIG 7.13
TOTAL ANTINEUTRINO CROSS SECTIONS (CC)
TOTAL
RESONANCE + QUASIELASTIC
DATA FROM GARGAMELLE
σ (10⁻³⁸ cm²)
Eν̄ (GeV)
0
0.5
1.0
1.5
2.0
3.0
4.0
5.0

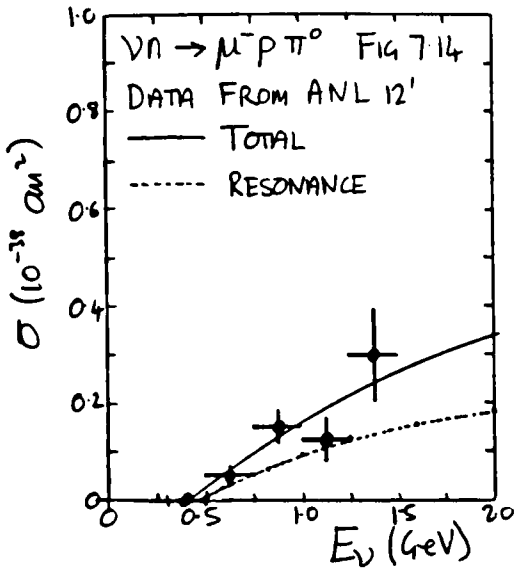

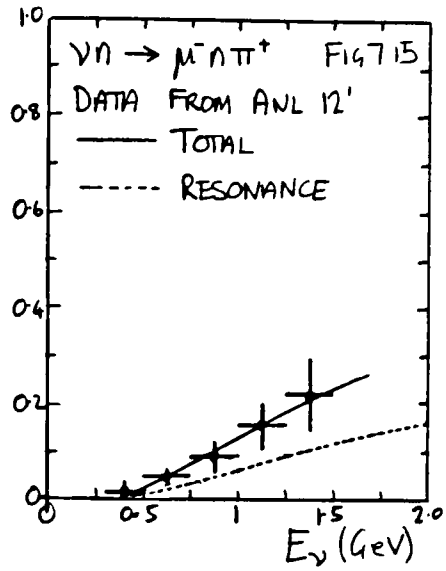

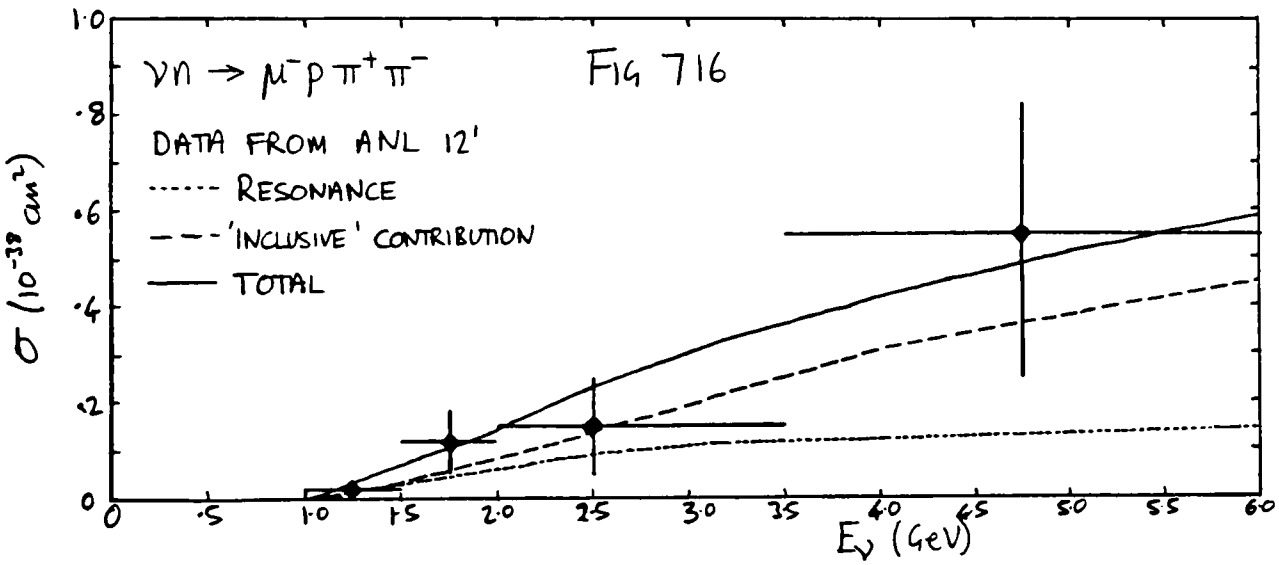

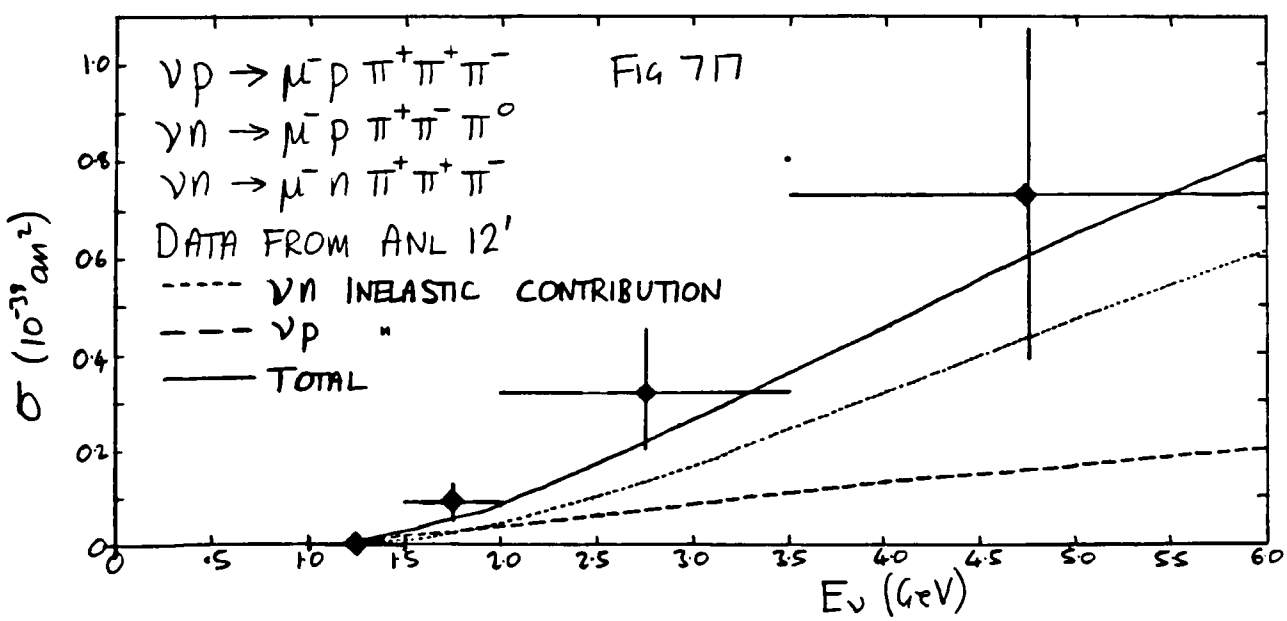

Figs 7.14-7.17 Comparison of exclusive total cross sections

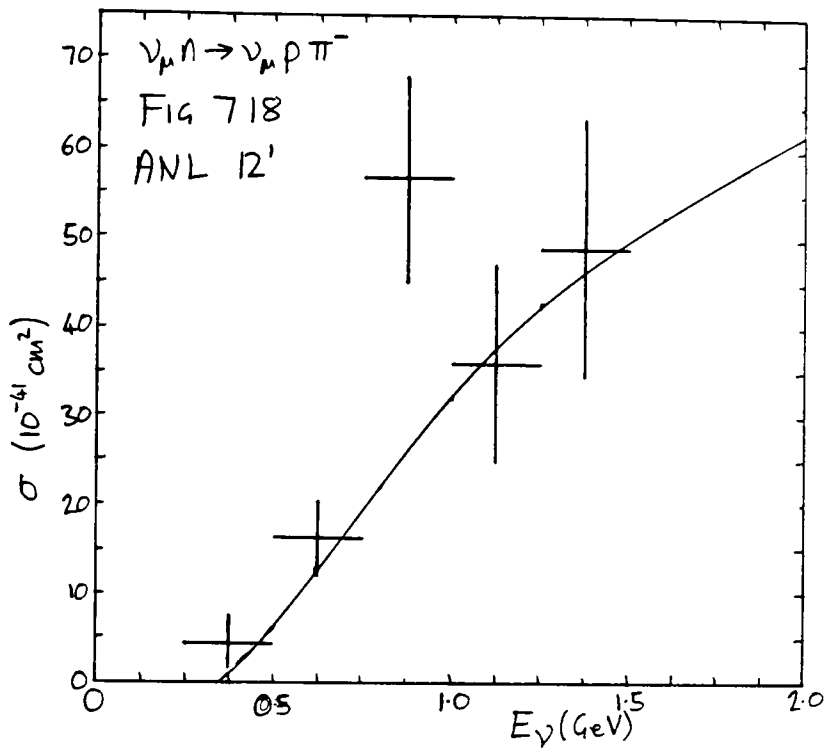

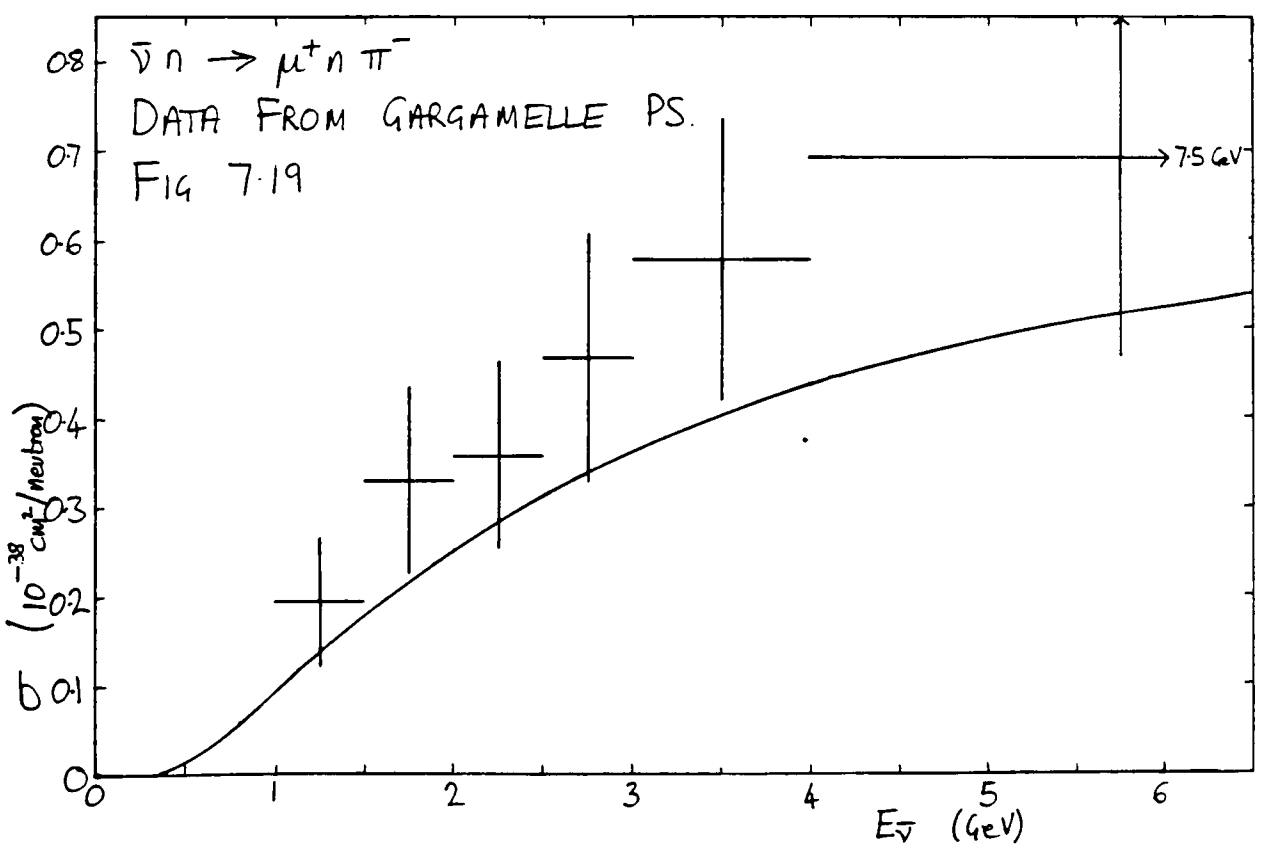

Fig 7.18-7.19 Comparison of exclusive channel cross sections.

which there is no data (mainly neutral currents). The authors of [2] have compared the differential cross sections with data for the resonance model. The data fits the predicted W and q^2 distributions well.

Figs 7.20 and 7.21 show the total distributions of W and q^2 for neutrino interactions expected in the mine using the flux prediction from chapter 6 at solar minimum. The contribution from the inelastic interactions has been shown separately. In both W and q^2 distributions, the inelastic contribution occupies a large portion of the high end of the distribution, which is to be expected, since the inelastic interactions are mainly generated by high energy neutrinos.

In the later stages of the development of this model, it was discovered that the IMB background Monte-Carlo has also been based of the work of Rein and Seghal [2]. The generation of inelastic events in the IMB Monte Carlo also appeals to deep inelastic scattering theory, however the multiplicity and charge assignments have been done in a different way in the two codes.

7.6 Predicted Neutrino Event Rates in Underground Detectors

The cross sections described above may now be combined with the fluxes from chapter 6 to predict the overall neutrino event rates. The fraction of the detector which is composed of protons or neutrons is computed from appendix B, 47.3% of the detector is protons.

The predicted rates for each of the different generation methods is given in table 7.3. These rates correspond to all events in the range 0.2 to 20 GeV. The majority of events will be elastic or quasielastic. Low energy elastic events will not deposit any energy in the detector. The total number of events per kiloton year (excluding elastics) will be 255. This includes many events which will be below trigger threshold. Table 7.4 shows the breakdown of these numbers by final state. Fig 7.22 indicates the neutrino energy spectrum for

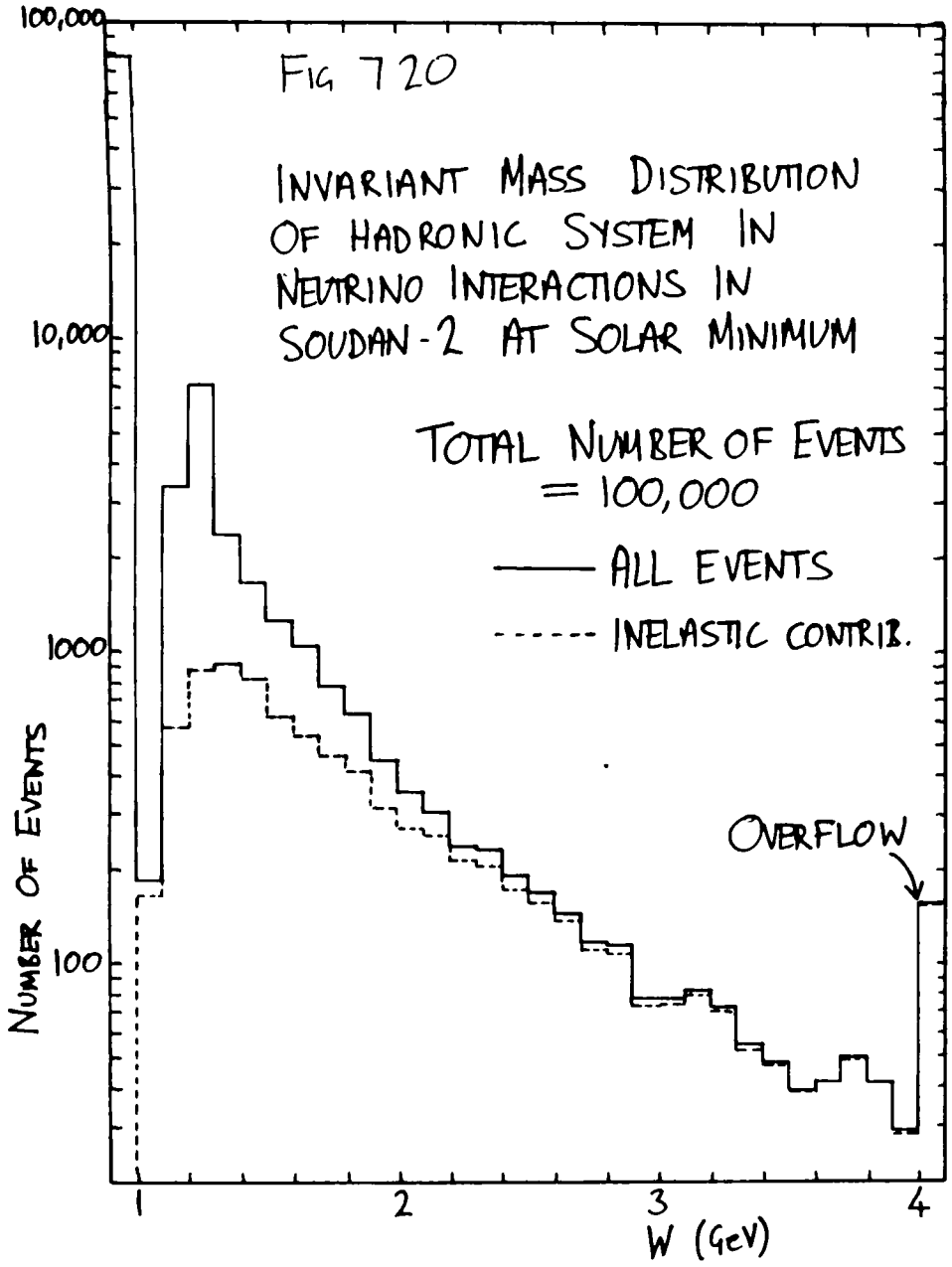
FIG 7.20
INVARIANT MASS DISTRIBUTION OF HADRONIC SYSTEM IN NEUTRINO INTERACTIONS IN SOUDAN-2 AT SOLAR MINIMUM
TOTAL NUMBER OF EVENTS = 100,000
ALL EVENTS
INELASTIC CONTRIB.
OVERFLOW
NUMBER OF EVENTS
100,000
10,000
1000
100
1
2
3
4
W (GeV)

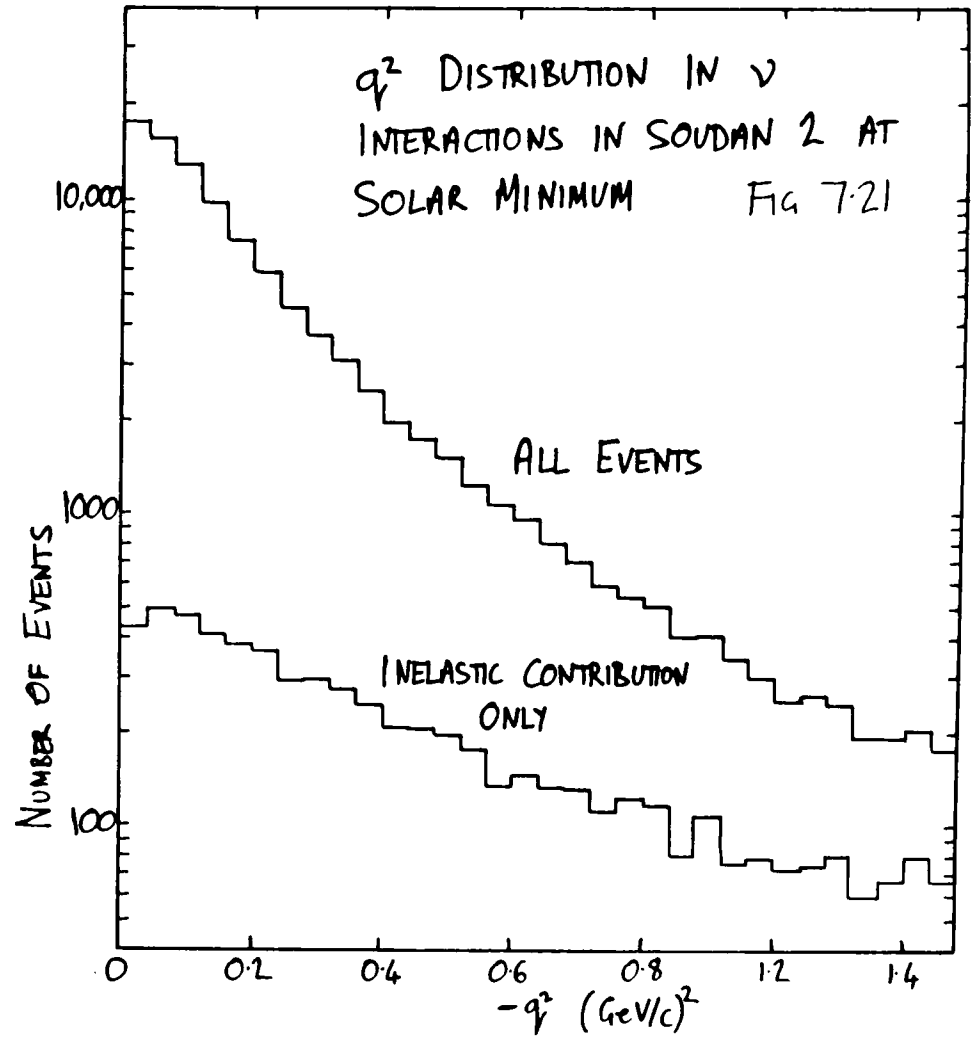
q^2 DISTRIBUTION IN ν INTERACTIONS IN SOUDAN 2 AT SOLAR MINIMUM
FIG 7.21
ALL EVENTS
INELASTIC CONTRIBUTION ONLY
NUMBER OF EVENTS
10,000
1000
100
0
0.2
0.4
0.6
0.8
1.2
1.4
$-q^2$ (GeV/c)^2

State	I-3/2 Res	I-1/2 Res	Q.Elas.(E.)	Inelastic
$\nu_\mu p$ CC	13.35	-	-	5.49
$\nu_\mu p$ NC	3.25	0.47	(60.48)	1.71
$\nu_\mu n$ CC	4.94	3.35	85.71	13.84
$\nu_\mu n$ NC	3.61	0.63	(47.45)	1.13
$\bar{\nu}_\mu p$ CC	1.39	1.24	27.08	2.59
$\bar{\nu}_\mu p$ NC	1.44	0.26	(29.14)	0.55
$\bar{\nu}_\mu n$ CC	4.58	-	-	1.72
$\bar{\nu}_\mu n$ NC	1.59	0.29	(23.47)	0.57
$\nu_e p$ CC	6.54	-	-	2.10
$\nu_e p$ NC	1.46	0.20	(28.86)	0.63
$\nu_e n$ CC	1.96	1.19	34.93	4.63
$\nu_e n$ NC	1.31	0.21	(18.53)	0.35
$\bar{\nu}_e p$ CC	0.65	0.52	12.95	0.90
$\bar{\nu}_e p$ NC	0.63	0.10	(13.81)	0.19
$\bar{\nu}_e n$ CC	1.75	-	-	0.54
$\bar{\nu}_e n$ NC	0.57	0.10	(9.12)	0.18
Total	49.02	8.56	160.67 (230.86)	37.12

Totals (excl elastics)	
ν_μ	137.48
$\bar{\nu}_\mu$	43.30
ν_e	55.51
$\bar{\nu}_e$	19.08
Totals	255.37

Table 7.3 Expected Event rates in One Kiloton Year Exposure of Soudan 2 at Solar Minimum for Each Type of Event Generated.

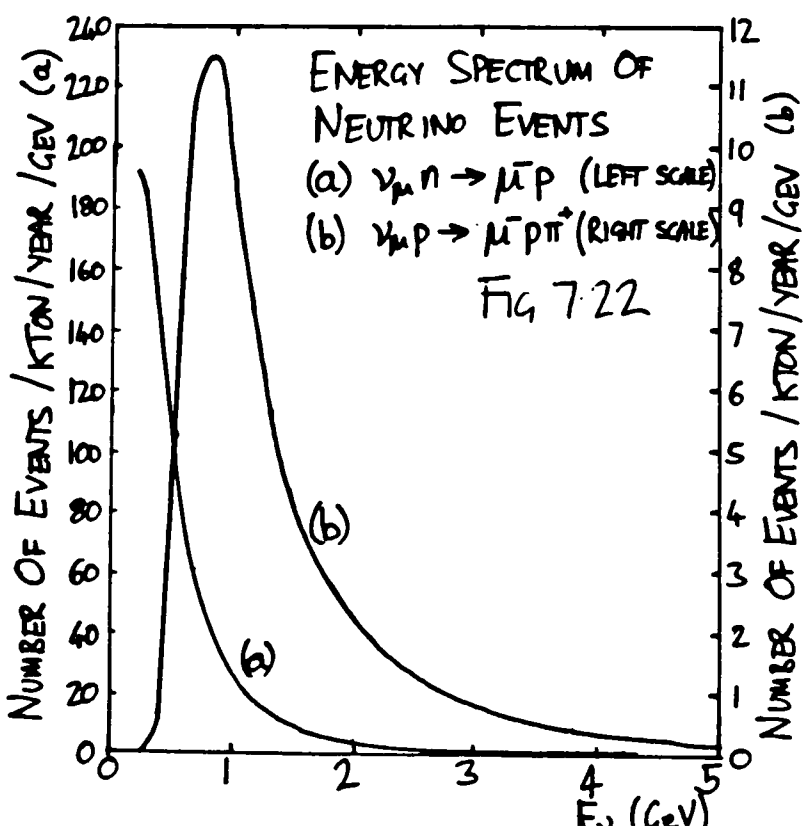

	ν_μ	ν_e
$\nu p \to \nu p$	60.48	(28.86)
$\nu n \to \nu n$	47.45	(18.53)
$\bar{\nu} p \to \bar{\nu} p$	29.14	(13.81)
$\bar{\nu} n \to \bar{\nu} n$	23.47	(9.12)
Total Elastics	160.54	(70.32)
$\nu n \to l^- p$	85.71	(34.93)
$\bar{\nu} p \to l^+ n$	27.08	(12.95)
Total Quasielastics	112.79	(47.88)
$\nu p \to l^- p \pi^+$	12.74	(6.30)
$\nu n \to l^- p \pi^0$	6.98	(2.63)
$\nu n \to l^- n \pi^+$	5.94	(2.19)
$\bar{\nu} p \to l^+ n \pi^0$	1.07	(0.49)
$\bar{\nu} p \to l^+ p \pi^-$	0.83	(0.37)
$\bar{\nu} n \to l^+ n \pi^-$	4.28	(1.65)
Single Pion CC Total	31.84	(13.63)
$\overset{(-)}{\nu} p \to \overset{(-)}{\nu} p \pi^0$	3.11	(1.39)
$\overset{(-)}{\nu} p \to \overset{(-)}{\nu} n \pi^+$	1.73	(0.76)
$\overset{(-)}{\nu} n \to \overset{(-)}{\nu} n \pi^0$	3.47	(1.25)
$\overset{(-)}{\nu} n \to \overset{(-)}{\nu} p \pi^-$	1.96	(0.70)
Single Pion NC Total	10.27	(4.10)

	ν_μ	ν_e
Two Meson Production		
$\overset{(-)}{\nu} N \to \overset{(-)}{\nu} N \rho$	0.43	(0.15)
$\overset{(-)}{\nu} N \xi$	0.12	(0.04)
$\overset{(-)}{\nu} \Delta \pi$	0.46	(0.70)
$\overset{(-)}{\nu}$ Inel	0.94	(0.35)
$\overset{(-)}{\nu}$ Strg	0.04	(0.01)
$\nu N \to l^- N \rho$	0.85	(0.32)
$l^- N \xi$	0.24	(0.08)
$l^- \Delta \pi$	0.89	(0.33)
l^- Inel	6.47	(2.32)
l^- Strg	0.07	(0.03)
$\bar{\nu} N \to l^+ N \rho$	0.36	(0.14)
$l^+ N \xi$	0.08	(0.03)
$l^+ \Delta \pi$	0.38	(0.15)
l^+ Inel	2.15	(0.76)
l^+ Strg	0.03	(0.01)
Total	13.51	(4.89)
High Multiplicity Interactions		
$\overset{(-)}{\nu} N \to \overset{(-)}{\nu} N \eta$	0.22	(0.08)
$\nu N \to l^- N \eta$	0.51	(0.19)
$\bar{\nu} N \to l^+ N \eta$	0.16	(0.07)
$\overset{(-)}{\nu} N \to \overset{(-)}{\nu} N\, 3\pi$	1.45	(0.50)
$\nu N \to l^- N\, 3\pi$	3.01	(1.02)
$\bar{\nu} N \to l^+ N\, 3\pi$	1.09	(0.36)
All CC+NC 4π or more	5.89	(1.85)
Total	12.33	(4.07)

Overall Total (excluding elastics) 180.74 (74.57) = 255.31

Table 7.4 Mode by Mode Neutrino and Antineutrino Interacton Rates in the Soudan 2 Detector at Solar Minimum. The unbracketed (bracketed) numbers are for muon (electron) type neutrinos. Strng means final states produced by the decay of resonances to strange particles ($K\Lambda$ or $K\Sigma$). Rates are in events per kiloton per year.

$\nu n \rightarrow \mu^- p$ events, ie most of the events are low energy. Fig 7.22 also shows the distribution for $\nu p \rightarrow \mu^- p \pi^+$ events (vertical scale on right hand side). The energy of these events is peaked at about 0.9 GeV, which is the most important region for detecting proton decay (where there is no final state neutrino). Fig 7.23 shows the visible energy distribution which is assumed to be the neutrino energy for charge current interactions and the initial minus the final neutrino energy for neutral currents. Fig 7.23a includes all events and is dominated by elastic and quasielastic scattering. Fig 7.23b and c show the contribution from CC and NC respectively where elastics and quasielastics have been excluded.

The combined model agrees well with low energy data and may be extended in a natural way to predict interactions where few or no measurements have been made. The generator reproduces the total cross sections for single, 2 and 3 pion data well. The production of strange particles has not been comprehensivly covered, no strange resonances are included and the production of strangeness final states from deep inelastic scattering off strange sea has not been treated. Resonances are allowed to decay into strange final states. There is little strangeness production data at low energy.

The numbers from the generator can be relied to be correct to the same degree of accuracy as the experimental data point errors on the figures. This approach is complimentary to the neutrino beam exposure which the collaboration plans to do on a small part of the detector. It will allow an understanding of the early years of underground exposure, will be used in understanding the neutrino beam data and may be used to correct the beam data for differences between the accelerator and atmospheric spectra.

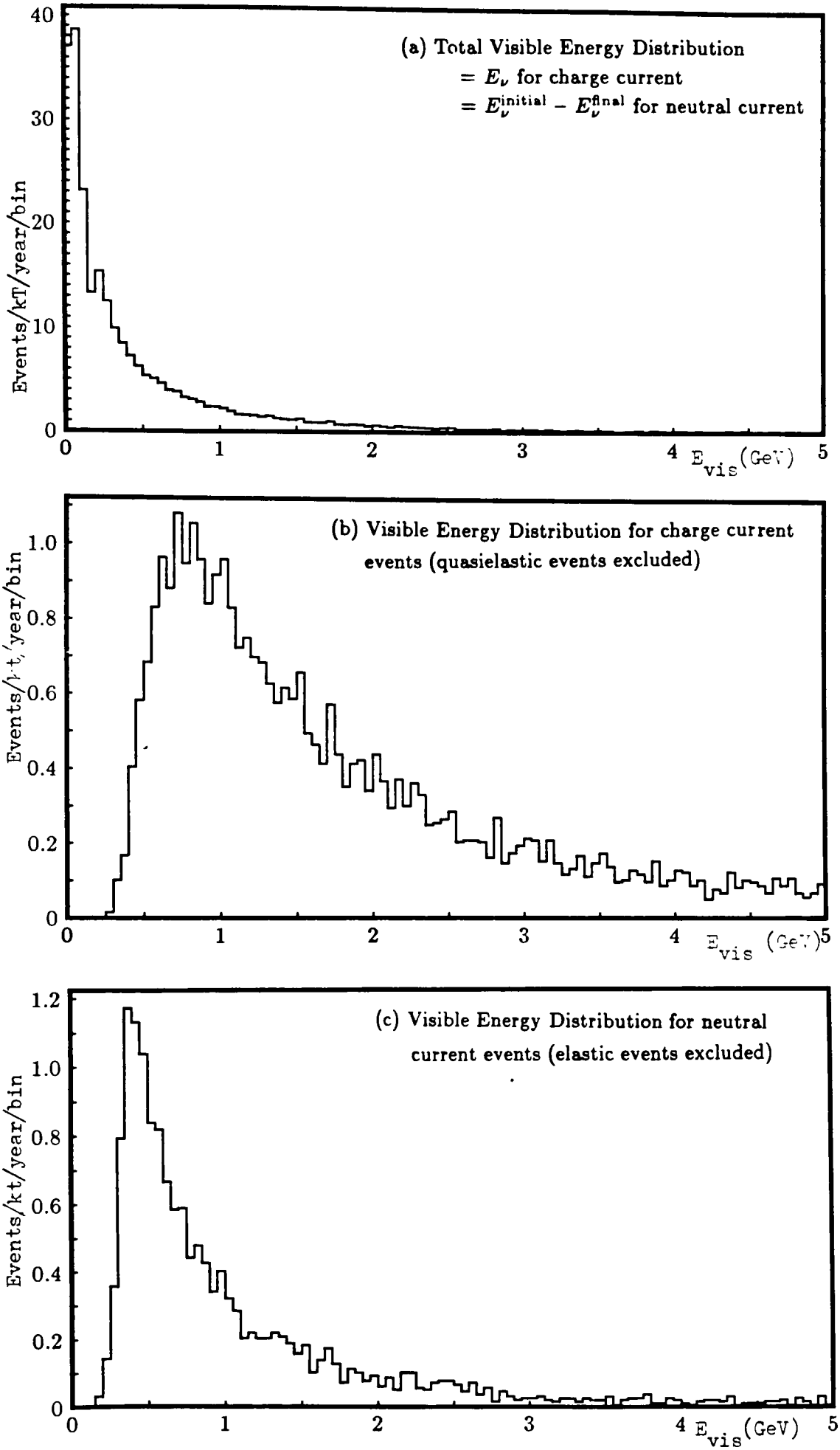
(a) Total Visible Energy Distribution
= E_ν for charge current
= $E_\nu^{initial} - E_\nu^{final}$ for neutral current
Events/kT/year/bin
E_{vis}(GeV)
(b) Visible Energy Distribution for charge current events (quasielastic events excluded)
Events/kt/year/bin
E_{vis} (GeV)
(c) Visible Energy Distribution for neutral current events (elastic events excluded)
Events/kt/year/bin
E_{vis}(GeV)

Fig 7.23

7.7 Summary

The results of a careful study of low energy neutrino interactions has been described. A Monte Carlo event generator program has been developed. The model treats elastic/quasielastic interactions and resonance production separately. The remainder of the cross section is described by a deep inelastic model, which has been built from high energy data. The contribution from inelastics below 1 GeV is a few percent. The model predicts the total cross section for all exclusive channels which compares well with accelerator data where avaliable. Elastic and quasielastic events are most common at low energy, single pion production is most probable at 0.9 GeV which is the region which will be searched for proton decay signals. Above 3 GeV, the neutrino flux falls as E^{-3} and the cross section rises as E, so the number of events expected will fall as E^{-2}.

References

[1] Commins and Bucksbaum "Weak Interactions of Leptons and Quarks" CUP (1983)

[2] Rein and Seghal Annals of Physics (NY) 133 (1981) 79

[3] Gluck, Hoffmann and Reya Z Phys C13 (1982) 119

[4] N. Schmitz Proc Intl Symp on Lepton and Photon Interactions at High Energies Bonn (1981) p527

[5] G. Corrigan D. Phil Thesis, Oxford (1983)

[6] ANL 12' data :
S. J. Barish et al. Phys Rev D 16 (1977) 3103
S. J. Barish et al. Phys Rev D 19 (1979) 2521
M. Derrick et al. Phys Lett B92 (1980) 363

[7] Gargamelle data :
T. Eichten et al. Phys Lett B46 (1973) 274
W. Lerche et al. Phys Lett B78 (1978) 510
T. Bolognese et al. Phys Lett B81 (1979) 393

[8] "Review of Particle Properties" Particle Data Group
Rev Mod Phys 56 (1984)
Phys Lett 170B (1986)

Chapter 8

NUCLEAR EFFECTS AND A BACKGROUND CALCULATION FOR THE PROTON DECAY MODE $p \rightarrow K^+\nu$

8.1 Interaction of Elementary Particles with Nuclear Matter

The signatures of both proton decay and neutrino events have so far been presented without regard to the fact that the nucleon which decays or the target nucleon is bound inside a nucleus. The nucleus will change the appearance of an event since (1) The initial state nucleons are not stationary, they move with a Fermi momentum which is associated with the confinement of the nucleon wavefunction within the nucleus. (2) The final state particles may reinteract with other nucleons within the same nucleus. Both of these effects must be taken into account in any calculation of the appearance of events in a nucleon decay detector. The problems involved are different for a water Cerenkov detector and for a tracking detector made from heavier elements (iron in the case of Soudan 2). In particular, if the parent nucleus breaks up, the protons which are emitted are below threshold in a water Cerenkov detector but may be detectable in a tracking calorimeter.

This chapter is in two parts, the first describes the intra-nuclear processes which affect the appearance of proton decay and background events. In the second part, a sample background calculation is discussed to show an example of the use of the results of these last three chapters.

The momentum distribution of nucleons inside a nucleus (Fermi Momentum) is described by Bodek and Ritchie [1] and has been coded into the Soudan 2 detector Monte Carlo [2]. The distribution is flat in momentum up to a cutoff K_ρ corresponding to a Fermi-Dirac distribution at zero temperature plus a small high momentum tail. The value of K_ρ is slightly different in a given nucleus, for protons and neutrons, to reflect the different number of each in a nucleus. For iron, K_ρ = 251 (263) MeV/c for protons (neutrons). In carbon, K_ρ = 229 (229) MeV/c. In a proton decay or neutrino interaction event which is generated in a Monte-Carlo, the nucleon which is generated is virtual ie its mass is less than that of a free nucleon. This is necessary in order to conserve momentum and allow both initial and final nuclei to be on mass shell. In practice, the nucleus may break up, and this situation may be more complicated.

Understanding the reinteraction of secondaries in the final state nucleus is a bigger problem, there are many possibilities. Several recent review papers have been written [3,4,5] on meson-nucleus interactions. Experimental studies of charged meson interactions on nuclei have been carried out within the last ten years at the "meson factories" at SIN in Switzerland, TRIUMF in Vancouver, LAMPF (New Mexico) and elsewhere. I will begin by discussing the interactions of pions with nuclear matter, and then extend the arguments to other hadrons. Section 8.4 will approach the subject of whether the final state nucleus will break up, and whether these fragments will be visible in the detector. Each of these effects must be considered for both proton decay events and neutrino background.

8.2 Interactions of Pions in Nuclear Matter

Compilations of pion cross sections on free nucleons are given in ref [6]. The cross sections at momenta below 800 MeV/c are dominated by the coupling of the pion-nucleon state to the $\Delta(1234)$ resonance, as in the neutrino interactions discussed in chapter 7. The π^+p (π^-p) cross

section is about 200 mb (70 mb) at the resonance peak. The $\pi^+ p$ cross section at this energy is all elastic scattering, whereas the $\pi^- p$ elastic cross section is only one third of the total cross section, since the resonance can decay into $\pi^- p$ ($\pi^0 n$) with probability 1/3 (2/3). The features of $\pi^+ n$ and $\pi^- n$ interactions are related to the ones above by an isospin rotation.

The cross sections of pions on nuclei have been measured or deduced by Ashery et. al. [3,4]. The cross sections on iron (from [3]) are shown in fig 8.1. The peak corresponding to the delta resonance has been washed out by the Fermi momentum of the constituent nucleons, the cross section only changes by a factor of 1.5 in the momentum range 173 to 429 MeV/c.

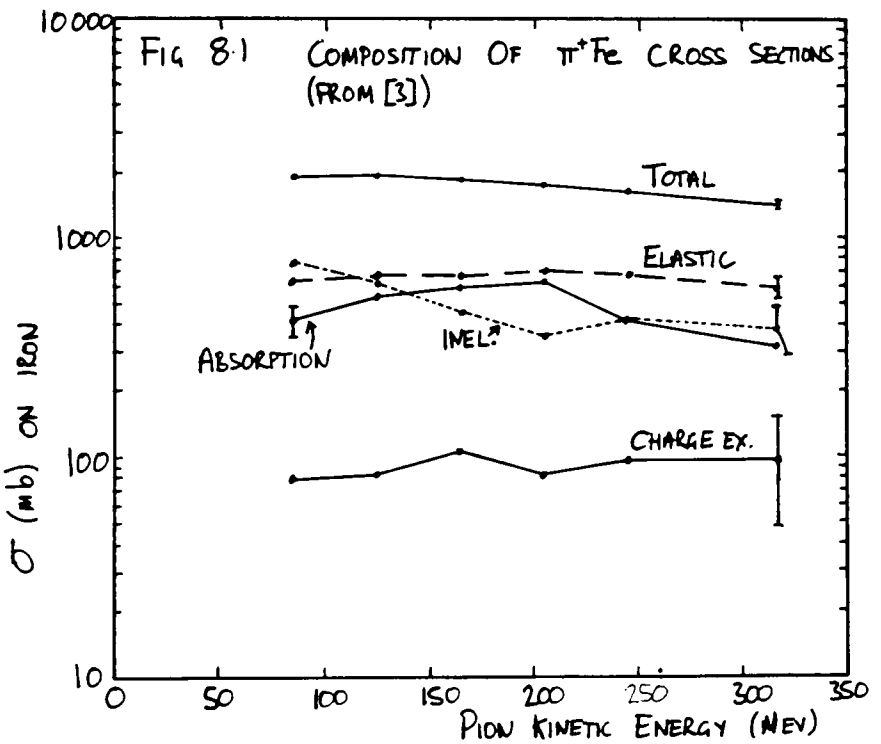

FIG 8.1 COMPOSITION OF π^+Fe CROSS SECTIONS (FROM [3])

These results may now be used to estimate the interactions of a pion which starts from within the nucleus at a proton decay or neutrino interaction vertex. The following properties of pion nucleus interactions must be taken into account.

(1) The de Broglie wavelength of a 300 MeV/c pion is 0.66 fm which is comparable with the size of the internucleon spacing in the nucleus (the radius of an iron nucleus is about 1.2 $A^{1/3}$ fm = 4.6 fm). This means that interactions inside the nucleus do not involve single nucleons but are coherent.

(2) Part of the pion nucleus total cross section is absorption. This means that no pion is seen in the final state. Ashery and Schiffer [4] review models which are under development to explain this in terms of the pion + nucleon producing a delta resonance which then interacts with other nucleons in the nucleus and de-excites without pion emission (see fig 8.2). This process competes with the decay of the delta.

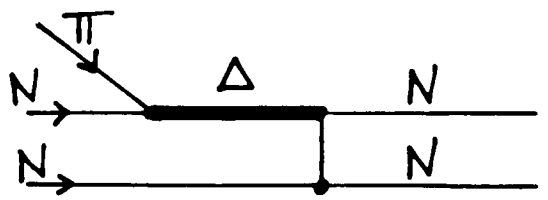

Fig 8.2 Mechanism for pion absorption in nuclei.

(3) The delta has a width of 115 MeV which corresponds to a path length of about 1.7 fm. In many cases, the delta will decay while still inside the nucleus. When the delta is produced, the nucleons do not affect the final density of states of the delta. However many of the states for the nucleon from the decay of the delta are occupied by the other nucleons in the nucleus, the final state phase space is restricted. The restriction of nucleon phase space is referred to as Pauli blocking and has been observed in accelerator neutrino experiments.

(4) The total cross section for positive pions on iron nuclei is about 1.8 b/nucleus in the energy range below 430 MeV/c (see fig 8.1). Using the average single nucleon cross sections in this energy range the cross section could be predicted to be

$$Z\sigma_p + N\sigma_n = 26 \times 0.13 + 30 \times 0.05 \text{ b} = 4.9 \text{ b/nucleus}$$

The reason for the difference between the measured (1.8b/nucleus) and computed (4.9b/nucleus) is that some of the nucleons in iron are screened by the ones on the beam side of the nucleon, ie most of the interactions are in the edge of the nucleus. This effect is known as shadowing.

The mean free path of pions in nuclear matter may be crudely estimated by assuming that the nucleons are contained in a sphere of radius 1.2 $A^{1/3}$ fm. This leads to a nucleon density of

$$n = \frac{A}{\frac{4}{3}\pi R_0^3} = \frac{A}{\frac{4}{3}\pi (1.2)^3 A} = 0.138 \text{ nucleons}/(\text{fm})^3$$

which may be used to compute the mean free path.

$$\lambda_{nn} = \frac{1}{n\sigma} = \left[n\left(\frac{Z}{A}\sigma_p + \frac{N}{A}\sigma_n\right)\right]^{-1} = 0.83 \text{ fm}$$

A simple Monte-Carlo calculation has been used to determine the escape probability (without interaction) averaged over all starting positions in the nucleus. The calculation was performed with various interaction lengths. The results are shown in fig 8.3. For pions with an interaction length of 0.83 fm, the probability of escape without interaction from iron (r = 4.6 fm) is 0.14. 86% of all pions will interact in the parent nucleus, (including those which elastic scatter).

A comprehensive intra nuclear cascade Monte Carlo has been developed by the IMB collaboration [7]. This tracks particles from their production points in the nucleus and generates single particle interactions with the Fermi smeared nucleons. Pauli blocking is included by suppressing any interaction which produces a nucleon below the Fermi cutoff momentum K_p. Pion absorption is included separately. The Monte Carlo is tuned to fit the data from Ashery et. al. [3] for oxygen by adjusting the strength of the absorption interactions. The model is currently being extended to include the effects of interactions in iron nuclei.

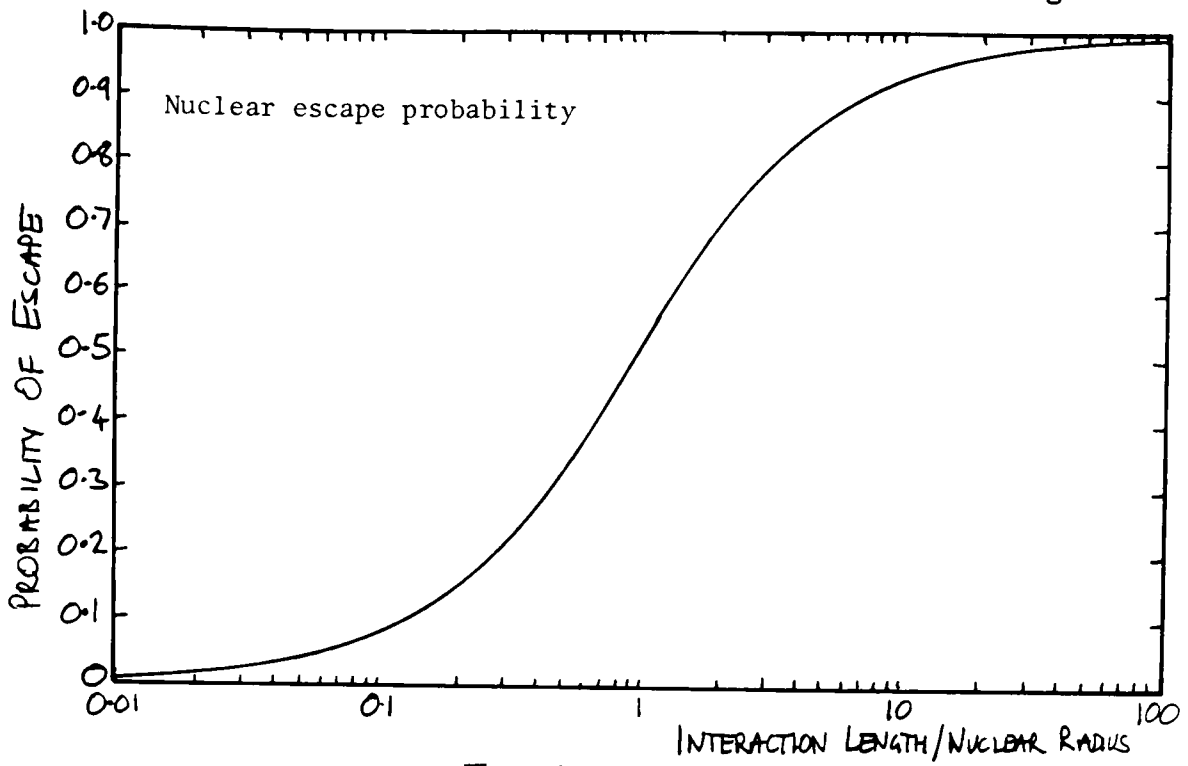

FIG 8·3

Gaisser Nowakowski and Paschos have done a complimentary calculation [8], considering π-nucleon encounters in the nucleus as delta resonance excitations. The calculation is for oxygen. The π may decay "forward" or "backward", since the πN cross section in the region dominated by the delta resonance is heavily peaked forward/backwards. This model is used to compute the background to $p \to e^+\pi^0$ in a water Cerenkov detector. The pion from an $e\pi^0(N)$ neutrino induced final state will be travelling in roughly the same direction as the electron. If it were scattered through 180 degrees, the particles would appear back to back and the event would be recognised as a proton decay candidate.

8.3 Interactions of Other Particles in Nuclear Matter

In the previous section, the cross sections for pions on nucleons was used to estimate the pion interaction length in nuclear matter. The same procedure has been used for other hadrons and is summarised in table 8.1.

Pions have larger cross sections than the other particles, since the reactions are dominated by the delta resonance as discussed above. Mesons which contain a strange antiquark (K^+,K^o) interact much more weakly in nuclear matter since they are unable to form a qqq resonant state (the nucleons do not have a strange quark which can annihilate with the meson's antiquark). The interactions are entirely elastic scattering. Assuming that the pion absorption model of delta production described above is correct, kaons will not be absorbed in nuclei. K^+ cross sections are almost a factor of ten lower than pion cross sections. K^o cross sections will be similar, since they are related by an isospin rotation.

Particle	Cross section	Interaction length	Probability of escape without any interaction
Pi+	4.9 b/nucleus	0.83 fm	0.14
Pi-	5.2 b/nucleus	0.78 fm	0.13
K+/K0	.67 b/nucleus	6.05 fm	0.60
K-/K0	3.9 b/nucleus	1.04 fm	0.17
nucleons	2.0 b/nucleus	2.07 fm	0.31

Table 8.1 Estimate of escape probability in iron of each type of hadron.

The angular distributions of kaon interactions (elastic) is given in the paper by Eisenstein [9]. From his plots of K^+ scattering in Calcium (A=40), it appears that more than 99% of the scatters are of less than 15 degrees in the centre of mass. I conclude that the nuclear rescattering effects on K^+ and K^o can be completely neglected for our purposes.

K^- and $\overline{K^o}$ contain an antiup or antidown quark, these can interact with nucleons to produce resonances, for example, the Λ(1520). The K^- N cross sections are a significant fraction of the pion cross sections. A good description of nucleus-kaon interactions may be found in [10].

8.4 Nuclear breakup

The kinetic energy released in a proton decay event is up to 938 MeV. This is several times larger than the nuclear binding energy (about 9 MeV per nucleon). It would seem likely that the nucleus is not left intact when a proton decay occurs. A breakup may be caused either by the reinteraction of a final state particle from the primary interaction (as discussed above), or in the deexitation of the residual nucleus. Nuclear fragments may be moving fast enough to be detected (a 250 MeV/c proton (kinetic energy 33 MeV) will travel about 1.5 cm in the detector). This effect will not be seen in water Cerenkov detectors since the Cerenkov threshold for detecting protons is too high (1.1 GeV/c).

In order to illustrate that events of total energy of approximately 1 GeV can produce nuclear breakup which will be visible, a data summary tape (DST) from a low energy neutrino experiment on a neon-hydrogen target has been studied.

The neutrino experiment was carried out at CERN in 1983 and 1984 by an collaboration from Athens, Padova, Pisa and Wisconsin [11,12]. The experiment was performed to search for evidence of the oscillation of $\nu_\mu \rightarrow \nu_e$. This was done by creating a low energy neutrino beam directly from the PS accelerator and directing it at the Big European Bubble Chamber (BEBC). The experimental arrangement and calculated neutrino beam energy spectrum are shown in figs 8.4 and 8.5. BEBC was filled with a mixture of 70% Ne and 30% H_2 for the experiment.

Almost 8×10^5 pictures were taken and scanned in the two runs. The details of scanning are given in [11,12]. Briefly, the pictures were searched for neutral induced events with two or more prongs (other events which are not of concern here were also accepted). All measured events (about 2000) were inspected by physicists. The DST was supplied containing identified charged current events (494), which were identified by the presence of a muon candidate track and a total

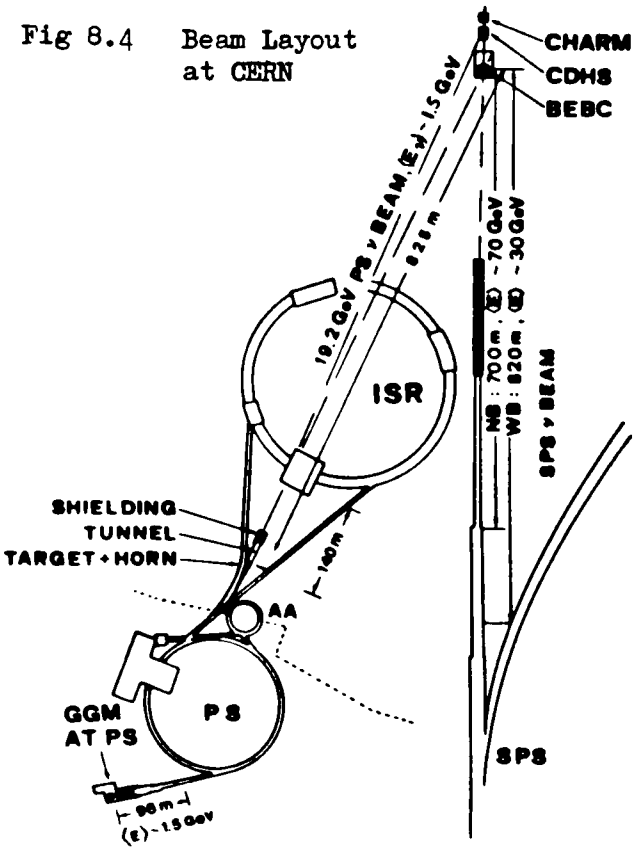

Fig 8.4 Beam Layout at CERN

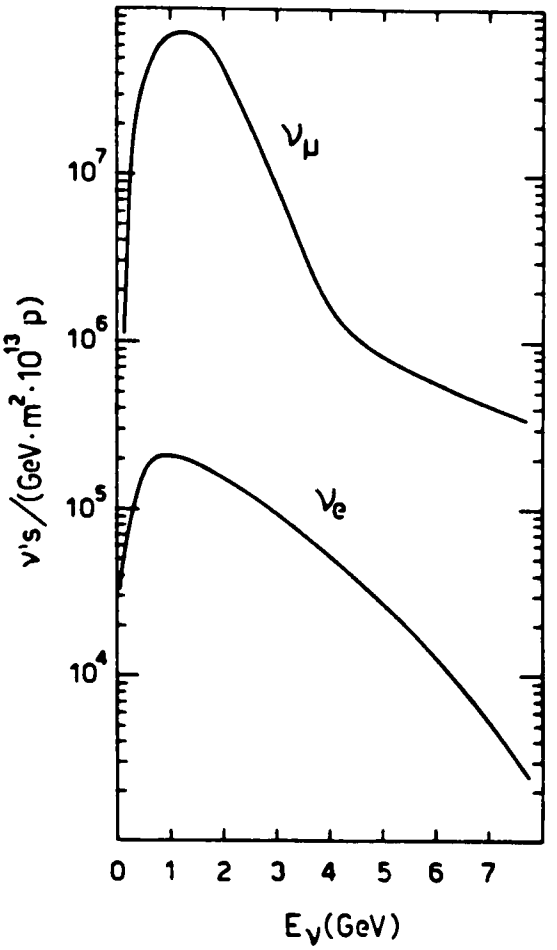

Fig 8.5 ν spectrum at BEBC

momentum direction such that the angle to the incoming beam satisfied $\cos\theta > 0.8$ [11,12].

Proton tracks were identified from the pictures by physicists. All tracks which were ambiguous were assigned as a pion. The missed protons were corrected for each event by minimising the quantity $\eta = E_\nu - p_L$. E_ν is the neutrino energy and p_L is the total momentum in the beam direction. For charged current interactions, $\eta = 0$. A positive value of η is obtained if there are protons which have been incorrectly assigned as pions. The pions in the event are optionally reassigned as protons to minimise the value of η. This technique is described in full in [12].

The results of my study are shown in figures 8.6-8.9 which were made from the DST. Fig 8.6 shows the kinetic energy distribution of the muon in each event. The number of protons emerging from the primary

vertex in each event is shown in fig 8.7. Some of the events in the zero and one proton bins correspond to interactions from the hydrogen part of the liquid. There are a significant number of events in which more than one proton is seen.

The collaboration did not try to look for neutrons in the events. Neutrons produce a 'neutron star' remote from the primary vertex. In the bubble chamber experiment, it was difficult to determine whether or not a given star came from the vertex. Since neon has 10 protons and 10 neutrons, about an equal number of energetic neutrons as protons will be emitted in this type of interaction.

The distribution of proton kinetic energies is shown in fig 8.8. The events will have one nucleon which originated from the neutrino interaction itself. In order to obtain a distribution which does not overestimate the high energy region, the histogram was also made with the most energetic proton in each event excluded (thin line on fig 8.8). Note that the thin line is a conservative estimate of the number of breakup protons, since in some cases, the leading nucleon is a neutron, and a breakup proton has been incorrectly removed from the event. In this sample, there are 223 protons which are above the T = 30 MeV threshold for being visible in Soudan 2 in the total 494 events. I conclude that there is a significant chance that tracks associated with the parent iron nucleus will be seen in neutrino interactions and proton decay events in Soudan 2.

Fig 8.9 shows the distribution of the angle between the proton and the muon. The thin line indicates the distribution for all protons except the one of highest energy which is consistent with an isotropic distribution. The most energetic proton is more closely along the line of the muon.

This effect is also seen in pion-^{61}Ni scattering, where the final state nucleus is identified by gamma spectrometry [4]. The distribution of atomic weight of the final state nucleus peaks at A=56, ie 6 nucleons are lost. Nuclei down to A=44 were identified.

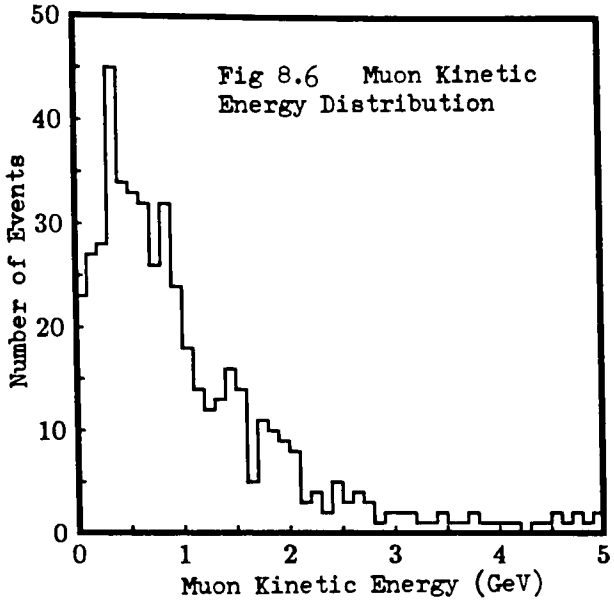

Fig 8.6 Muon Kinetic Energy Distribution

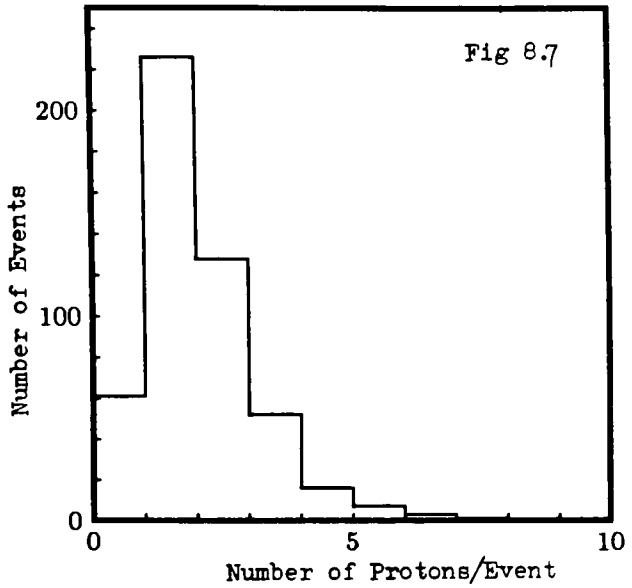

Fig 8.7

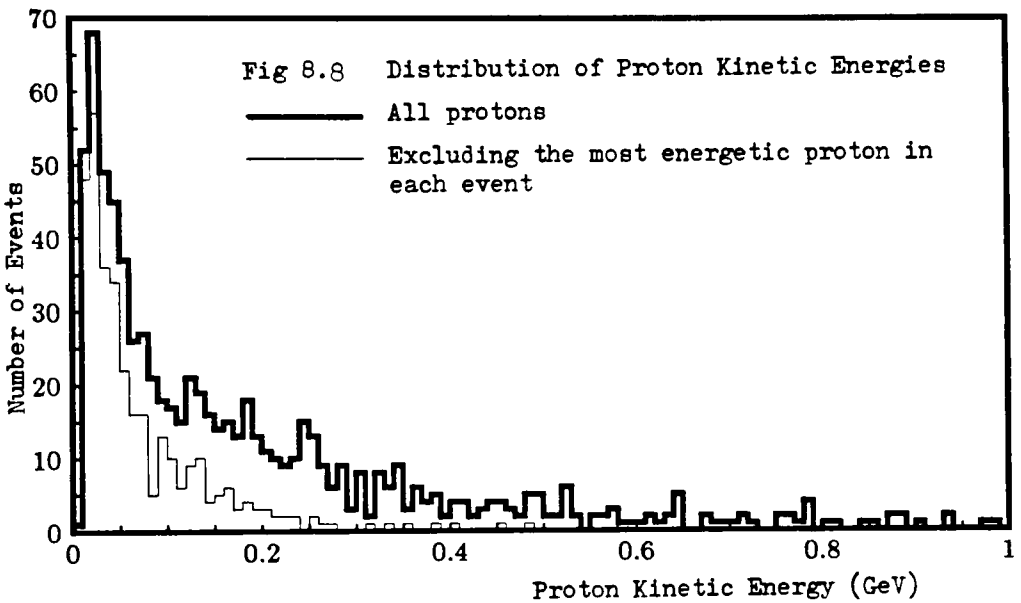

Fig 8.8 Distribution of Proton Kinetic Energies

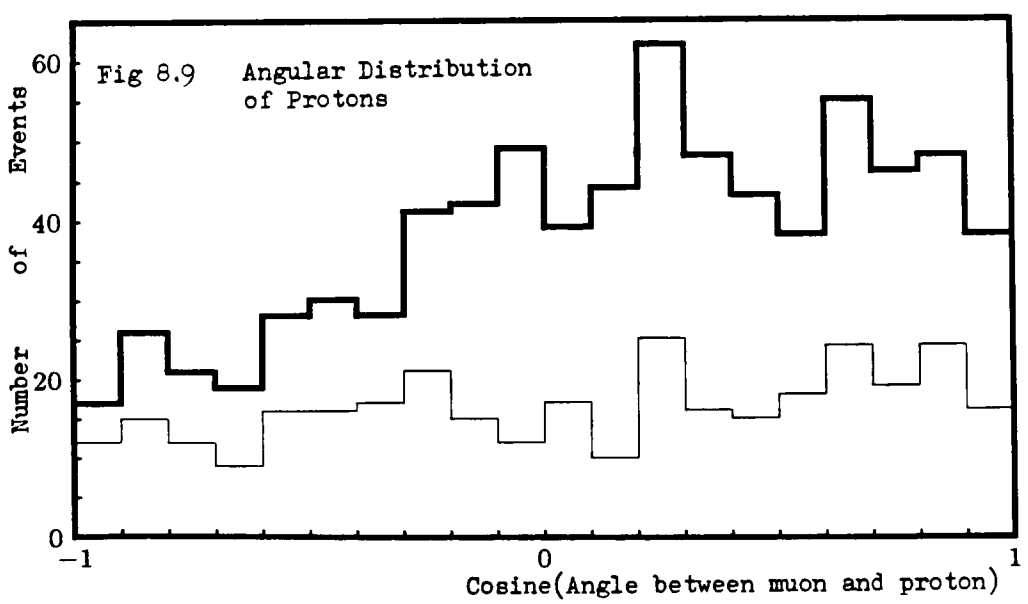

Fig 8.9 Angular Distribution of Protons

8.5 The Signature of the Proton Decay Mode $p \rightarrow K^+\nu$

In order to illustrate the use of the calculations of chapters 6 to 8, I will discuss the background to the proton decay mode $p \rightarrow K^+\nu$. Since the detector Monte-Carlo has not been fully calibrated and some of the pattern recognition capabilities of the detector have not been studied, this analysis must be regarded as preliminary. The detector provides a lot of information on each event and we will only learn how to use it best when there has been a substantial exposure.

The proton decay into a kaon and neutrino is a two body decay, the momenta and energies of the decay products are uniquely defined in the rest frame of the proton. The kaon (neutrino) has total energy 599 (339) MeV. As discussed in section 8.1, the proton is moving relative to the lab frame, due to the Fermi momentum. This smears the energy and momentum of each particle. Fig 8.10 shows the total energy distribution of the kaon in the lab frame using the Fermi momentum distribution described in section 8.1. As discussed in section 8.3, the kaon will rarely interact in the nuclear matter of the parent nucleus, the few which do will only be elastically scattered through small angles, which can be neglected.

The kaon slows down in the detector by dE/dx energy loss and ranges out in 10 cm in a small fraction of its mean lifetime (12 ns). The track will be seen in the detector and will heavily ionize in the gas crossings, ie large pulses will be seen. Fig 8.11 shows the track length distribution (from production to stopping).

Once the kaon has stopped, it will decay, the most likely modes of decay are to $\mu^+\nu$ (63.5%) or $\pi^+\pi^o$ (21.2%) [13]. In this example, the discussion will be limited to the $\mu^+\nu$ decay. The muon which is produced is also monochromatic (E = 257.7 MeV). The characteristics of the signals produced by such a muon were studied in chapter 3. The muon direction will be measured from the increase in ionisation and multiple scattering near the stopping point. An example of a Monte-Carlo generated event is shown in fig 4.4.

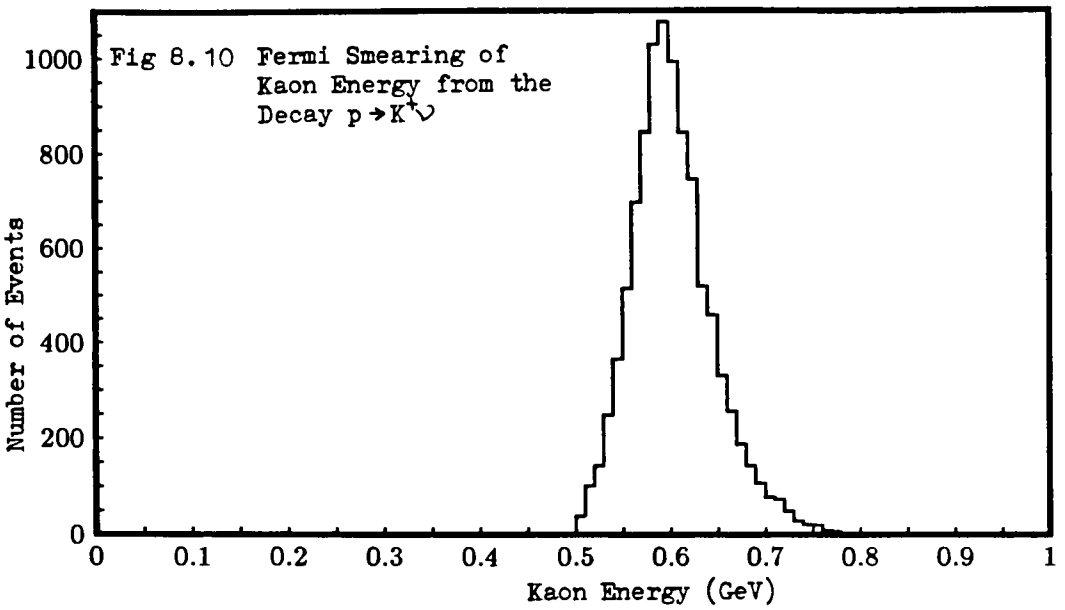

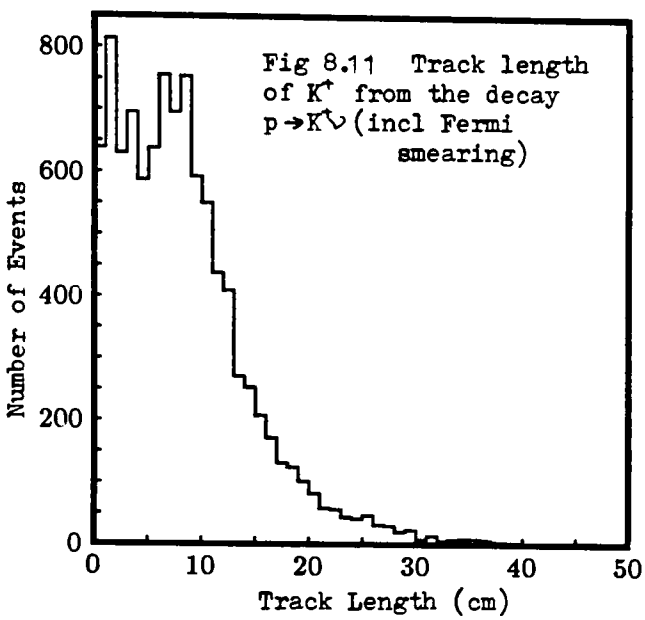

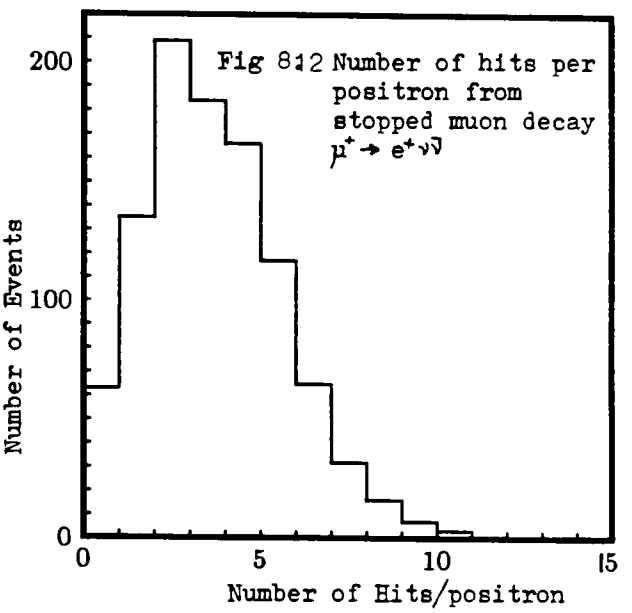

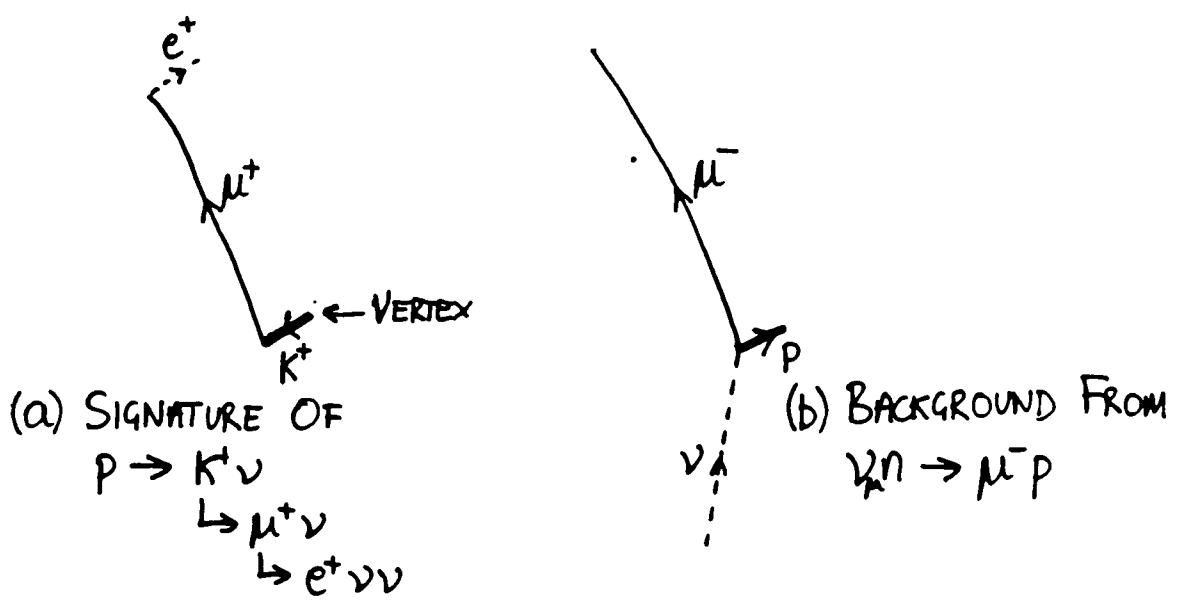

Fig 8.13 Signature of $p \rightarrow K^+\nu$ and layout of tracks of neutrino background event.

The muon will decay at rest to $e^+\nu\bar{\nu}$ which will produce hits in the proximity of the end of the muon track. The energy of the positron is not constrained (typically 30 MeV). A complete pattern recognition study of the efficiency with which the positron hits can be separated from the multiple scatter hits at the end of the muon has not yet been carried out. Fig 8.12 shows the number of tube hits in the positron shower per event. The efficiency is expected to be high.

8.6 The Neutrino Background to the Decay Mode $p \rightarrow K^+\nu$

The background to this decay mode may be produced by several different types of neutrino interaction. In order to generate signals which could produce the above signature, the event must contain a track which is compatible with the positive muon, a track which may be interpreted as the kaon and no other tracks. dE/dx measurements of the pulses may be used to exclude the possibility of the kaon track being produced by a light particle ($\mu^{\pm}$,$\pi^{\pm}$) or the muon track by a heavy particle (K, p). dE/dx measurements will not, however, be good enough to resolve the difference between the kaon and a proton of the same length, since the track length is short and the fluctuations are large.

The most common type of charged current neutrino interaction, quasielastic scattering, $\nu n \rightarrow \mu^- p$, can reproduce the signature (fig 8.13). A negative muon and a proton are produced at the interaction point and the proton is confused with a kaon moving in the opposite direction.

Other neutrino interactions could also produce the signature. Charge current events from electron type neutrinos contain an electron shower which will not be confused with the signature. In order for any other channel to fake the signature, either the dE/dx measurements described above must fail to identify the particle type, or one or more of the reaction products must be absorbed in the nucleus without visible nuclear breakup. The calculation which follows will be carried out only

for the quasielastic interaction $\nu n \rightarrow \mu^- p$.

From chapter 7, 85 quasielastic muon neutrino events per kiloton per year are expected. The number of events which are confused with proton decay may be reduced by applying geometrical cuts derived from event kinematics, since range is a unique function of momentum. By choosing a wide range for the cuts, the efficiency for accepting real proton decay events is high, whereas by using a narrow range, the signal to background ratio can be increased. There are four possible constraints which can be made on an event before it is accepted as a candidate. The cuts have been chosen after a study of Monte Carlo generated events.

(1) The muon track length must be compatible with that of a 257.7 MeV muon as studied in chapter 3. Two separate sets of cuts are studied in order to show the effects of a wide and a narrow cut. The track length distribution from quasielastic events is shown in fig 8.14a and for proton decay events in fig 8.15a. The total 85 events/kT/year are reduced as follows

	Cut (cm)	PDK Efficiency	Neutrino Events/kT/year
(a)	22.0 to 40.0	89.0 %	13.4
(b)	26.0 to 36.0	69.3 %	7.6

(2) The kaon track length must be large enough to be visible and be consistent with the track length distribution of fig 8.11. The proton track length distribution from all quasielastic events is shown in fig 8.14b. The muon and kaon track lengths are independent in the proton decay signature, so the efficiencies may be combined by multiplying. A scatter plot of muon versus proton track length is shown (fig 8.14c) for neutrino events. The same plots for proton decays are shown in fig 8.15. The effects of the combined cuts on both samples are shown :

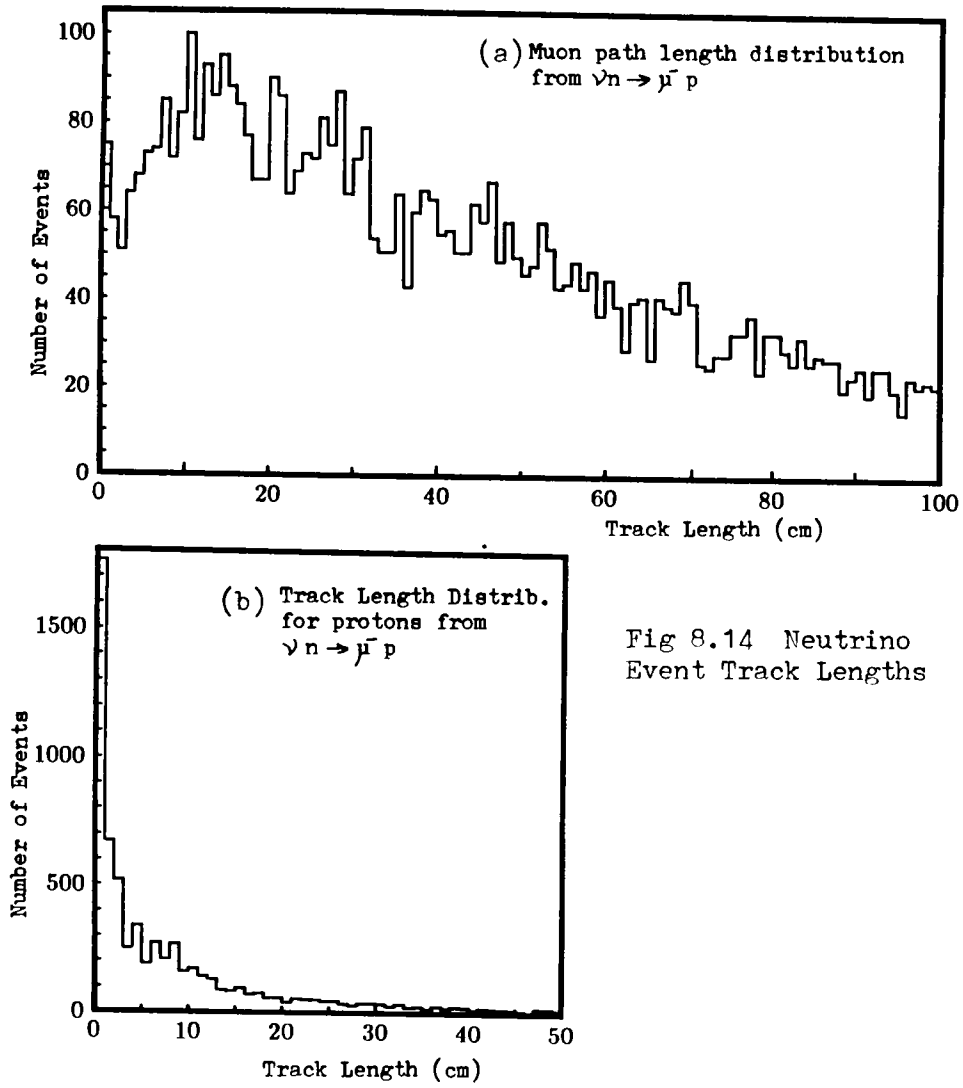

Fig 8.14 Neutrino Event Track Lengths

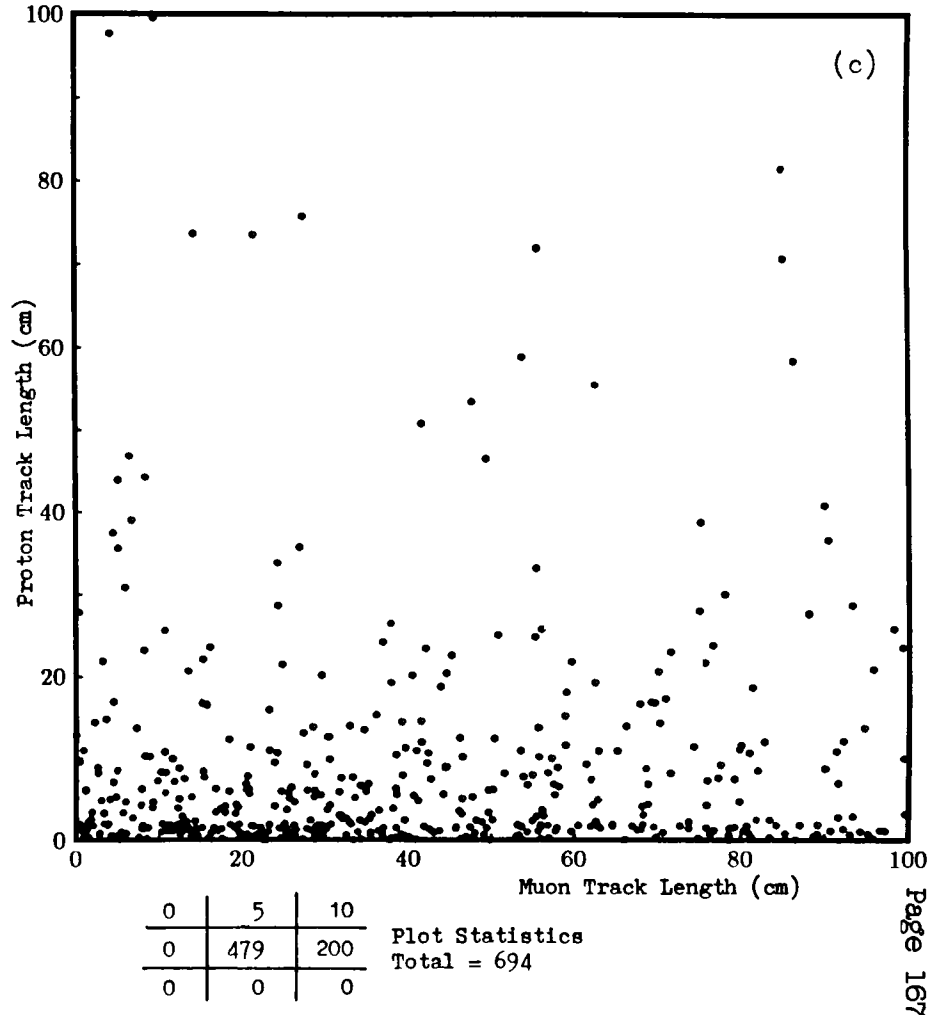

Scatter Plot of fig 8.14(a) vs fig 8.14(b)

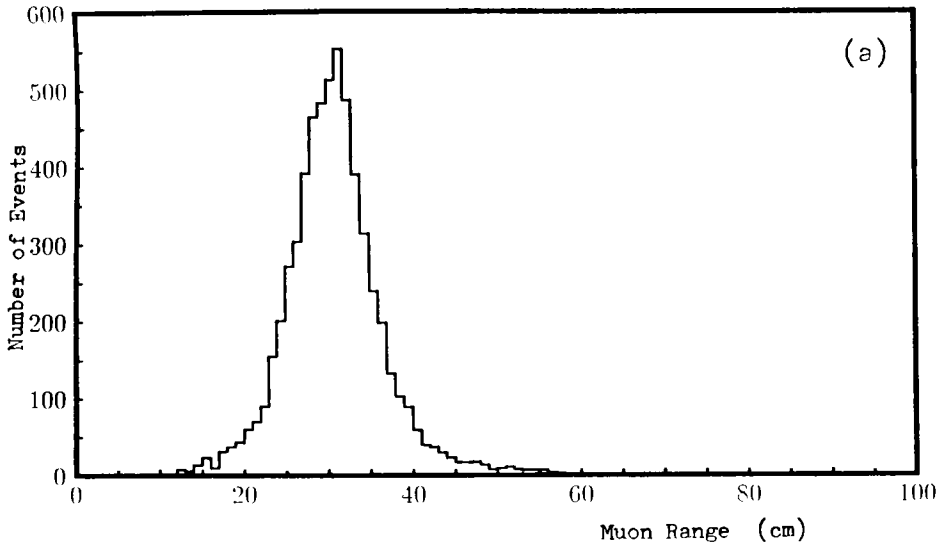

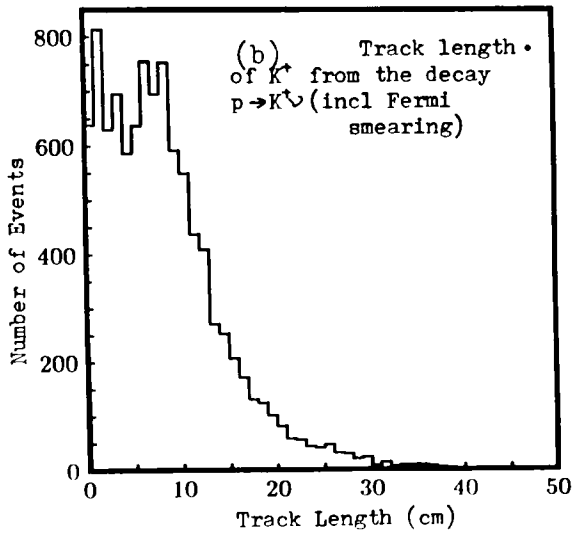

Fig 8.15 Proton Decay Event Track Length Distributions

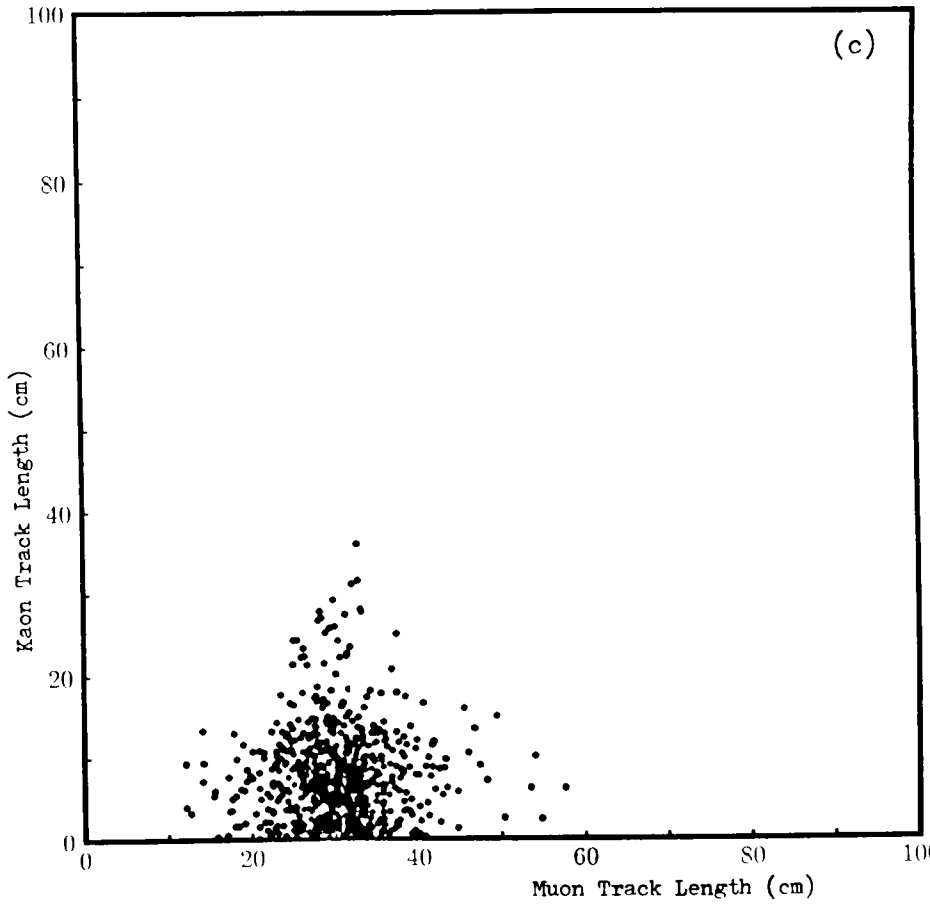

Scatter Plot of fig 8.15(a) vs fig 8.15(b)

Muon Cut	Kaon Cut (cm)	PDK Effic.	νevents/kT/year	Electron
None	4.0 to 22.0	68.4 %	28.1	
22.0 to 40.0	4.0 to 22.0	60.9 %	4.3	0.86
26.0 to 36.0	4.0 to 22.0	47.4 %	2.5	0.49

(3) The event can be rejected unless hits from the decay positron are seen at the end of the muon track. In a dense material such as iron, negative muons can be captured by a nucleus and absorbed. This reaction competes with the decay of the muon. The probability of capture is 8.2%, 25.5% and 90.9% for carbon, oxygen and iron [14]. For the detector composite, the average capture probability is 79.6% (compared with 22.7% for a water Cerenkov detector). Requiring that an electron is seen will preserve all the proton decay events and reduce the background by 79.6%. The number of neutrino events which still produce proton decay signatures are shown in right hand column of the table above.

(4) A quasielastic neutrino event has two unconstrained parameters (one if the neutrino energy is known, see chapter 7). Since cuts have been imposed on both the muon and proton track length, the angle between the tracks is constrained. Fig 8.16 shows the angle distributions for all events and for the events passing both muon and kaon track length cuts. Real proton decay events are expected to have isotropic distributions. The table below shows the overall efficiencies and background estimates if the angle between the two tracks is required to be less than 90 degrees. This includes the electron cut.

Muon Cut	Kaon Cut (cm)	Angle cut	PDK Effic.	ν events/kT/year
22.0 to 40.0	4.0 to 22.0	$< 90^{o}$	30.5 %	0.06
26.0 to 36.0	4.0 to 22.0	$< 90^{o}$	23.7 %	0.025

This overall set of cuts has reduced the background from quasielastic scattering to a few percent per kiloton year. The first three cuts will probably also be effective at removing background from other neutrino interaction channels, however, the angle cut which is

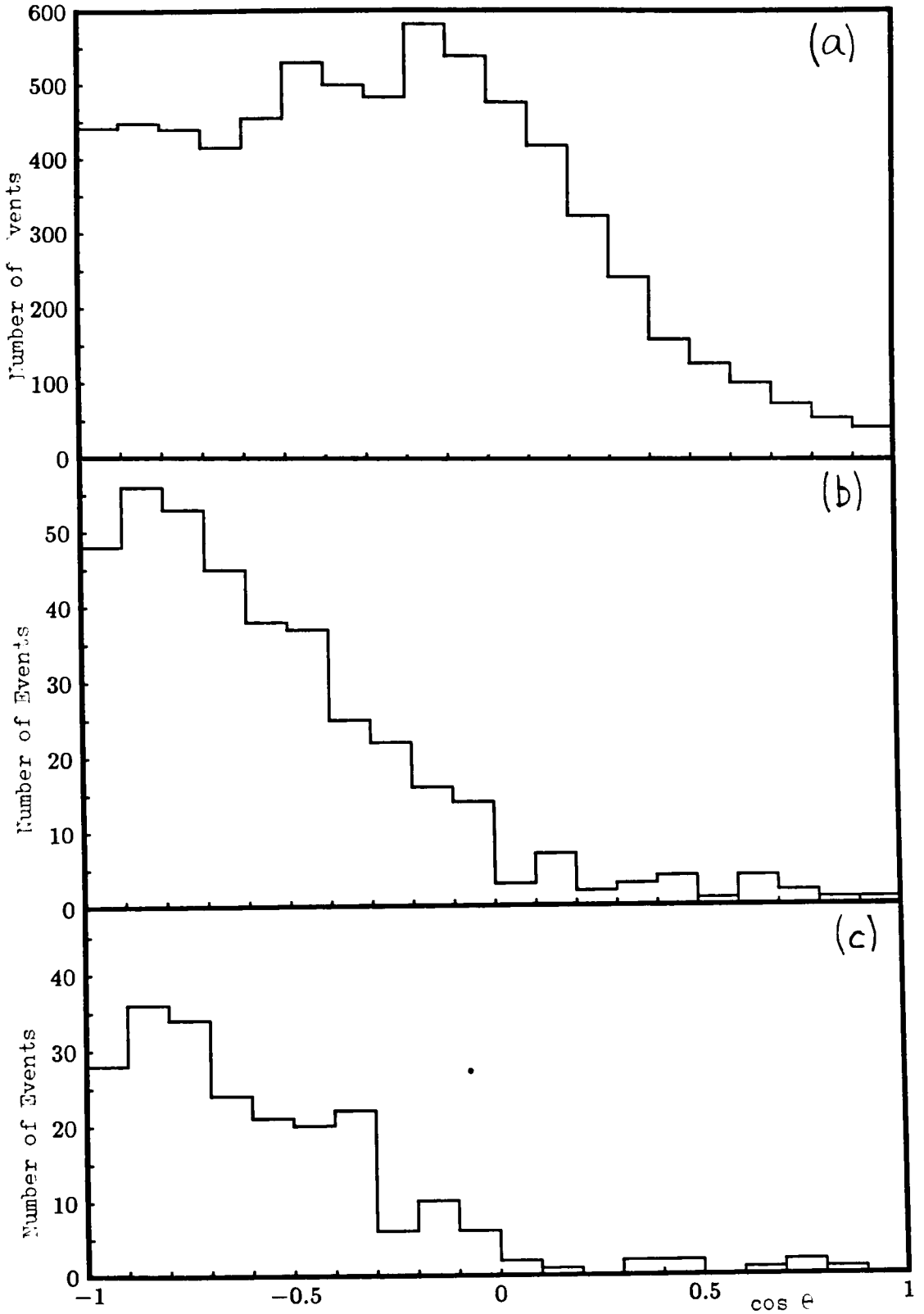

Fig 8.16 Distribution of angle between muon and proton in quasielastic neutrino events. (a) All events (b) Events which pass muon cut A and proton cut ((c) Events which pass muon cut B and proton cut

very effective on quasielastic events will not necessarily remove events from other background channels as they are not kinematically constrained in the same way. The backgrounds from other neutrino interactions are more difficult to calculate, since they must take into account the nuclear effects mentioned earlier in the chapter.

A real proton decay event does not involve a nucleus at the kaon decay vertex, so there must not be any visible fragmentation at that point. Also, since the kaon rarely interacts with the nucleus, it is unlikely that any nuclear breakup associated tracks should be seen at the proton decay vertex. A complete estimate of the background taking all these effects into account must wait until a portion of the detector has been exposed to a neutrino beam.

8.7 Conclusions

The effects of the spectator iron nucleons may significantly change the appearance of both proton decay and background events in the detector. This makes it more difficult to separate the two types of signal. Quantitative data on the reinteraction of secondary particles is difficult to find, since experiments which illuminate nuclei with a pion beam only produce interactions in the surface of the nucleus. A simple method has been used to estimate the interaction lengths and escape probabilities of pions and kaons. It is expected that interactions of K^+ and K^o may be neglected. An investigation of the possibility that the parent nucleus breaks up has been carried out. It is found that a significant number of breakup protons will be visible in the detector.

A sample calculation of the background to the decay mode $p \rightarrow K^+ \nu$ from quasielastic neutrino events has been studied. The background is dependent on the cuts made on the particle track lengths, which are subject to a calibration of the Monte Carlo. Cuts have been found which are 60% efficient to the proton decay signal for which the background is

expected to be 0.86 events/kT/year. In addition, a constraint on the angle between the kaon and muon tracks can be used to eliminate quasielastic events to a level of 0.025 events/kt/year while retaining 23.7% of the proton decay events, although it is likely that the background from other modes will be greater than this.

References

[1] A. Bodek and J. L. Ritchie Phys Rev D23 (1981) 1070.

[2] G. F. Pearce (unpublished), see routines DKNUCL, FBODEK, RSQ

[3] Ashery et. al. Phys Rev C 23 (1981) 2173.
I. Navon et. al. Phys Rev C 28 (1983) 2548.

[4] Ashery and Schiffer "Pion absorption in Nuclei".
Ann Rev Nucl Part Sci 36 (1986) 207.

[5] Petrouch, Carr and McManus "Scattering of e, N, as Probes of Nuclear Structure" Ann Rev Nucl Part Sci 36 (1986) 29.

[6] "Review of Particle Properties" Particle Data Group
Phys Lett 170B (1986)

[7] T. W. Jones (Private Communication).

[8] T. K. Gaisser, M. Nowakowski and E. A. Paschos
Phys Rev D33 (1986) 1233.

[9] R. A. Eisenstein "Kaon Elastic and Inelastic Scattering at 800 MeV/c" Proc. Kaon Factory Workshop, Vancouver TRI-79-1 (1979) 75.

[10] C. B. Dover "Nuclear Physics with Kaons"
Proc Kaon Factory Workshop Vancouver TRI-79-1 (1979) 4

[11] F. Bobisut Talk given at the III Telemark Conference on Neutrino Mass and Oscillations, Wisconsin, Oct 1984.

[12] A. Baldini. Ph. D. Thesis University of Pisa.

[13] It is interesting to consider whether the stopped positive kaon could capture an atomic electron from the iron to form a "kaonium" atom. This could then decay if the electron were captured by the kaon $K + e^- \rightarrow \pi^0 + \nu$. A calculation of this rate follows the same lines as for a muon capture beta decay calculation and yields a lifetime of 1700s. Since this is very much larger than the kaon lifetime, this effect will not be noticeable.

[14] J. C. Sens Phys Rev 113 (1959) 684

Chapter 9

SUMMARY AND CONCLUSIONS

The Soudan 2 detector is entering the data taking phase at a time when the current total nucleon decay detector exposure in the world is about 8 kT years. The detector has some capabilities which are not avaliable in any of the other detectors, namely its unique geometric structure, its fine tracking resolution and its dE/dx measurement. Although the Water Cerenkov detectors have only seen candidates at the rates expected by background calculations, to date the Frejus collaboration have seen one 'odd' event which is consistent with proton decay, NUSEX have a candidate which is difficult to explain as a neutrino event, and KGF have several events which they claim are nucleon decay. If events such as these appear in Soudan, the detector will have enough resolution to discover what they are. All of the detectors have candidate events which can also be interpreted as neutrino interactions.

Chapter 5 describes a trigger scheme which will allow a lower threshold to be set than in any other tracking detector. The Frejus collaboration quote a trigger efficiency of 19% for the mode $p \rightarrow K^{+}\nu$. Soudan 2 will be able to achieve 70% to 80% efficiency for the mode. In 0.9 kT years of exposure, Frejus has seen one candidate event. If we accumulate candidates at the same rate, we will obtain 4.4 per year.

The estimation of proton decay backgrounds from neutrino events has become the crucial issue in the search for proton decay. The present understanding of the neutrino flux at each site is good to about

20 to 30%. Neutrino interactions into low multiplicity final states are well understood in terms of the weak interaction model. These have been modelled in the neutrino event generator described in chapter 7. Events above 0.2 GeV will appear at a rate of 255 per kT year.

The largest area of uncertainty is the effects of performing the experiment with the nucleons bound in iron nuclei. Several possible effects have been discussed in chapter 8, although quantitative estimates of all of these can not be given. It is possible that the candidates seen in the other tracking detectors were produced by nuclear rescattering, since the nuclear reinteractions of pions is large.

To firmly establish evidence for proton decay, one of two methods of analysis may be used. (1) One or two events are seen in a configuration in which it has been firmly established that there is no background. (2) A large number of signatures are seen many standard deviations above background signals. Since Soudan 2 has a low fiducial mass and high resolution, it is most suited to an analysis of type (1). This requires that a simulation study to find background free configurations of proton decay signatures is carried out. This must then be followed by an experimental neutrino beam exposure to firmly establish that the configuration is background free.

The work for chapters 6 to 8 of this thesis represent the ground work of such a study. Furthermore, a configuration of $p \rightarrow K^{+}\nu$ has been found which has a tiny background from the neutrino interaction $\nu\, n \rightarrow \mu^{-} p$. This study must be extended to other types of neutrino interaction and then experimentally verified. This will require that the efficiency for distinguishing different particle types and track directions is studied in detail.

The short term prospects for contained event physics from Soudan 2 are quite limited, since it will be two years before the complete detector is running. The existence of unexpected events may be explored. The efficient trigger should enable smaller events to be detected than in any other tracking detector. In the longer term, the

detector will accumulate a significant fraction of the world's total nucleon decay detector exposure which will be compared with a library of accelerator neutrino events produced in a portion of the detector.

Appendix A

The Soudan 2 Collaboration
List of Collaborators

Oxford University, Oxford UK

W. Allison, G. D. Barr, C. B. Brooks, J. H. Cobb, L. Kirby-Gallagher, D. H. Perkins, P. D. Shield, N. West

Rutherford Appleton Laboratory, Chilton, Didcot UK

G. J. Alner, D. J. A. Cockerill, C. Garcia, P. J. Litchfield and G. F. Pearce

Argonne National Laboratory, Argonne, Ill 60439, USA

I. Ambats, D. S. Ayres, W. L. Barrett, J. W. Dawson, T. H. Fields, M. C. Goodman, F. Lopez, E. N. May, L. E. Price, J. L. Schlereth and J. L. Thron

University of Minnesota, Minneapolis, MN 55455, USA

H. Courant, U. Das Gupta, K Heller, S. Heppelman, K. Johns, T. Joyce, M. L. Marshak, E. A. Peterson, D. B. Rosen, K. Ruddick, M. Shupe and S. J. Werkema

Tufts University, Medford, MA 02155, USA

D. Benjamin, T. Kafka, J. Kochocki, A. Mann, R. Milburn, A. Napier, W. Oliver, B. Saitta, J. Schneps and N. Sundaralingam

Appendix B

The Density of the Detector and Range-Momentum Graphs

The Soudan 2 detector is made of a composite of Iron, Bandolier and Insert material. The mean range of an ionising particle may be computed using the Bethe-Bloch formula. The energy loss properties of a mixture of elements may be estimated by combining the elemental energy losses according to the partial densities of the constituents. Table B.1 summarises the partial densities of the different materials used in the construction of a module. Figures B.1 and B.2 show range-momentum and range-kinetic energy curves for each type of ionising particle, computed by numerical integration of the Bethe-Bloch formula.

The radiation length of the composite detector may be computed in a similar way. The radiation length of iron (mylar) is 13.84 (39.95) g/cm^2. The radiation length of the composite detector is 15.3 g/cm^2 or 9.7 cm.

Component	g/tube/layer/cm	Fraction by mass	Partial Density
Steel (BJ)	4.38	85 %	1.36 g/cm^3
Insert	0.30	6 %	0.09
Bandolier	0.45	9 %	0.14
Total	5.13	100 %	1.59 g/cm^3

Table B.1 Composition of the honeycomb area of a Soudan 2 module

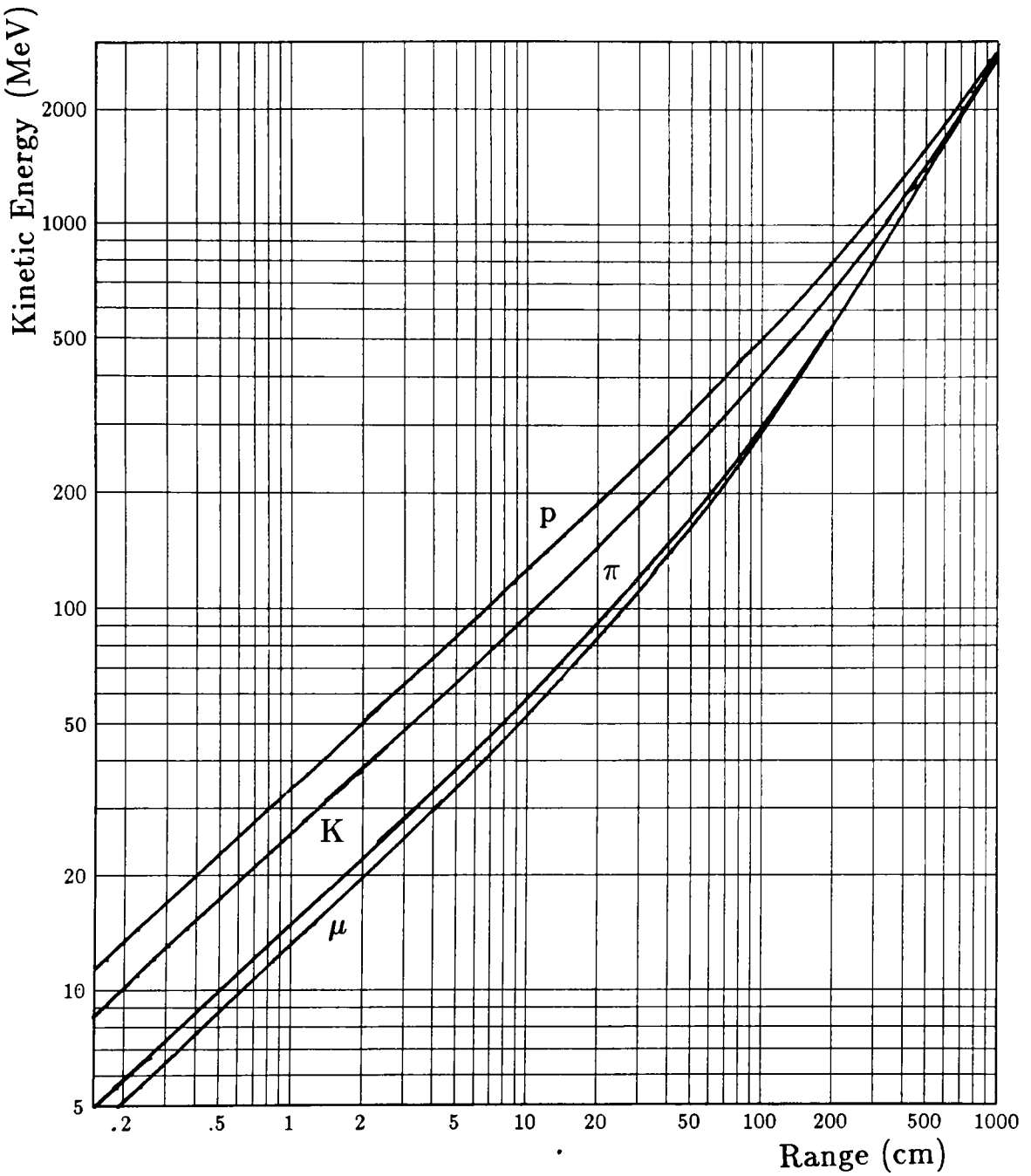

Fig B.1 Range – Kinetic Energy

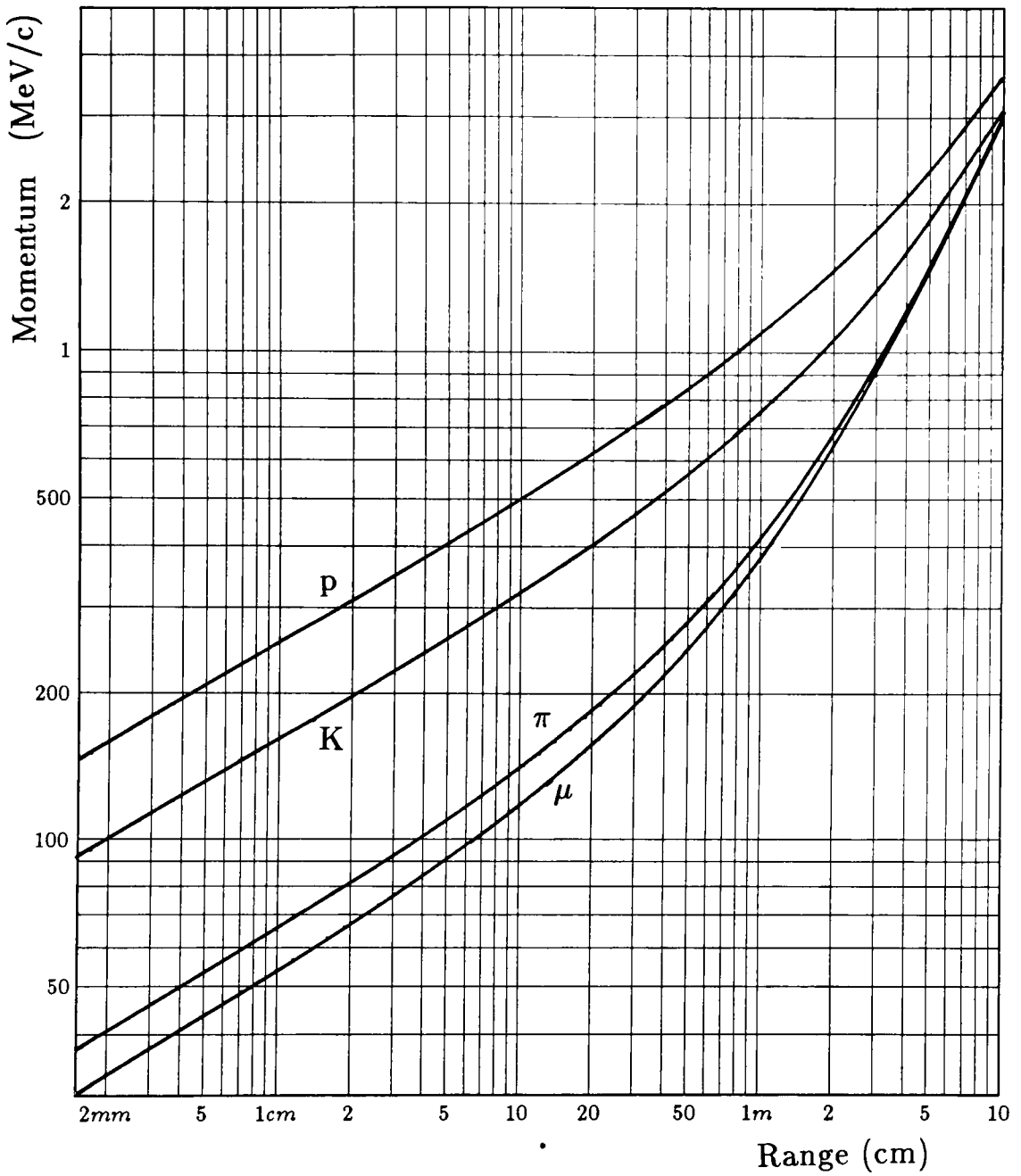

Fig B.2 Range – Momentum